An investigation into the influence of cardiovascular stent design on the development of restenosis using the finite element method

by

Caitriona Lally, BEng, MEng

A thesis submitted to the University of Dublin in partial fulfilment of the requirements for the degree of

Doctor in Philosophy

Trinity College Dublin

November 2004

Supervisor
Prof. P.J. Prendergast

External Examiner
Prof. James E. Moore Jr.
(Texas A&M University)

Internal Examiner
Dr. Ciaran Simms

DECLARATION

I declare that I am the sole author of this thesis and that the work presented in it, unless otherwise referenced, is my own. I also declare that the work has not been submitted, in whole or in part, to any other university or college for a degree or other qualification.

I authorize the library of Trinity College Dublin to lend or copy this thesis on request.

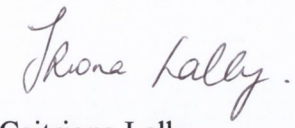

Caitriona Lally

August, 2004.

ACKNOWLEDGEMENTS

I am indebted to my supervisor, Prof. Patrick Prendergast, who has given me the opportunity to work in his group for the last four years during which time I have learned so much from him. He has inspired me to strive to answer many research questions and I hope to have the opportunity to work with him further in the future.

I would like to thank the many people from Medtronic AVE in Galway that helped me throughout this project. I would especially like to gratefully acknowledge the advice and support that Dr. Finbar Dolan gave me during this project.

Many thanks to Prof. Clive Lee from RCSI for providing both his knowledge and expertise when it came to the delicate matter of obtaining human arteries and Phillippa Marx from the Trinity Bioresources centre for her invaluable assistance in obtaining coronary arteries for testing. I would also like to thank Judith Brands from Eindhoven University for her assistance on the fatigue testing and Dr. Niall Mulvihill from St. James' Hospital who gave me a unique opportunity to see coronary stenting in practice and for this I am really grateful.

Thanks to Andy Bell from Marc/mentat for all his help, Alan Reid, Gabriel Nicholson and Peter O'Reilly, who helped to design and make the experimental devices for this project and Joan, Sheena and Nicole for all their assistance.

My time in Trinity College has been a very enjoyable one. This is due to the people I have worked with. Particularly, I would like to thank Mary, who has always been great company during all those coffee breaks, John B, Linda, Bruce, Danny, Laoise, JV, Alex, Richard, Paul, Kevin, Conor, John G, Susanne, Adriele, Seosamh, Toman, Fergal and all of the other postgrads.

I would also like to thank my friends outside Trinity College, Niamh, Tanja, Kathy and Gemma, who very patiently listened to all my woes even though they haven't the faintest clue what finite element analysis is.

Finally, I would like to thank my parents, Maria and Padraic, for all their support during my many years of research and for keeping their faith in me, my sisters and brothers, for their encouragement, and Fiachra, for his support and, of course, his patience.

This work was funded by Enterprise Ireland and Medtronic AVE
Project no: HE/2000/368

PUBLICATION AND PRESENTATIONS RESULTING FROM THIS STUDY

C. Lally, P.J. Prendergast, T.C. Lee, D. Quinn and F. Dolan. An investigation of the extent of tissue prolapse within various stent designs using the finite element method. In *Proceedings of the 7th Annual Conference of the Section of Bioengineering of the Royal Academy of Medicine in Ireland*, Louth, Ireland, p.21, 2001 [Presented January 28th, 2001, Louth, Ireland].

C. Lally, P.J. Prendergast, T.C. Lee, D. Quinn and F. Dolan. Finite element analysis to quantify tissue prolapse within three designs of cardiovascular stents. In *Technology and Health Care*, Volume 9, pp.110-112, 2001 [Presented at the European Society of Engineering in Medicine (ESEM) Conference, May 5th, 2001, Belfast, N. Ireland].

Lally, C, P.J. Prendergast, J.C. Messenger, S.J. Chen, A. Wu, J. Carroll and F. Dolan. Finite element analysis of the stress distribution within an atherosclerotic coronary artery during balloon angioplasty. In *Proceedings of the 8th Annual Conference of the Section of Bioengineering of the Royal Academy of Medicine in Ireland and the 16th Meeting of the Northern Ireland Biomedical Engineering Society*, Sligo, Ireland, p.88, 2002 [Presented January 26th, 2002, Sligo, Ireland].

C. Lally, P.J. Prendergast, F. Dolan. A biomechanical analysis of intravascular stenting of coronary arteries using the finite element method, In *Proceedings of the 5th Annual Sir Bernard Crossland Symposium*, Antrim, N. Ireland, pp.5-20, 2002 [Presented March 13th, 2002, Antrim, N. Ireland].

C. Lally, P.J. Prendergast, F. Dolan. 3D finite element analysis of an intravascular stenting procedure using a NIROYAL stent, In *Proceedings of the 4th World Congress of Biomechanics*, Calgary, Canada, 2002 [Presented August 5th, 2002, Calgary, Canada].

C. Lally, P.J. Prendergast, A.B. Lennon, D. Quinn, F. Dolan. Finite element analysis of tissue prolapse within intravascular stents calculated using a single repeating unit

of a stent and a full 3D model of a stent. In *Proceedings of the 13th European Society of Biomechanics, Acta of Bioengineering and Biomechanics*, 4 (Sppl. 1), pp.537-538, 2002 [Presented September 3, 2002, Wrocław, Poland].

C. Lally, P.J. Prendergast, T.C. Lee, D. Quinn and F. Dolan. Arterial tissue damage formation under cyclic loading and simulation of in-stent restenosis. In *Proceedings of the 9th Annual Conference of the Section of Bioengineering of the Royal Academy of Medicine in Ireland*, Cavan, Ireland, p.42, 2003 [Presented January 25th, 2003, Cavan, Ireland].

C. Lally, P.J. Prendergast. An investigation into the applicability of a Mooney-Rivlin constitutive equation for modelling vascular tissue in cardiovascular stenting procedures. In *Proceedings of the International Congress on Computational Biomechanics*, Zaragoza, Spain, pp.542-550, 2003 [Presented September 25, 2003, Zaragoza, Spain].

P.J. Prendergast, C. Lally, S. Daly, T.C. Lee, D. Quinn & F. Dolan. Analysis of prolapse in cardiovascular stents: a constitutive equation for vascular tissue and finite element modelling. *ASME Journal of Biomechanical Engineering*, 2003;125:692-699.

C. Lally, F. Dolan, P.J. Prendergast. A computational model of in-stent restenosis in response to mechanical stress. In *Proceedings of the 10th Annual Conference of the Section of Bioengineering of the Royal Academy of Medicine in Ireland*, Limerick, Ireland, p. 3, 2004 [Presented January 30th, 2004, Limerick, Ireland].

P.J. Prendergast, C. Lally. Simulation of in-stent restenosis and its relationship with cardiovascular stent design. In *Proceedings of the IUTAM Symposium on Mechanics of Biological Tissue*, Graz, Austria, 2004 [Presented July 1st, 2004, Graz, Austria].

C. Lally, F. Dolan, P.J. Prendergast. A comparison of the stress distribution in an atherosclerotic vessel stented with a flexible versus a rigid stent. In *Proceedings of the 14th European Society of Biomechanics*, 's-Hertogenbosch, The Netherlands, 2004 [Presented July 6th, 2004, 's-Hertogenbosch, The Netherlands].

C. Lally , A.J. Reid, P.J. Prendergast. Elastic behaviour of porcine coronary artery tissue under uniaxial and equibiaxial tension. *Annals of Biomedical Engineering*, October, 2004.

C. Lally, F. Dolan, P.J. Prendergast. Cardiovascular stent design and vessel stresses: a finite element analysis. *Journal of Biomechanics*, in press.

LIST OF FIGURES

LIST OF TABLES

NOMENCLATURE

Roman Letters

C_{ij}	Components of the right Cauchy-Green deformation tensor
$\dot{D}$	Rate of damage accumulation
E	Young's modulus
E_{ij}	Components of the Green-Lagrangian strain tensor
HD	Film coefficient (W/mm^2 K)
I_1, I_2, I_3	Stretch invariants
$K(D)$	Apoptosis/death rate of cells as a function of damage
N_f	The number of cycles to failure from fatigue tests
$P(D)$	Proliferation rate as a function of damage
S_{ij}	Components of the second Piola-Kirchoff stress tensor
T	Temperature (°C)
W	Strain energy
c	Constant relating damage to proliferation rate
s	Stiffness
t	Time (s)
q	Heat Flux (W/mm^2)

Greek Letters

ε	strain
γ_θ	Green-St.Venant circumferential strains
γ_z	Green-St.Venant longitudinal strains
κ	Diffusion coefficient of cells in arterial tissue (mm^2/day)
$\lambda_1, \lambda_2, \lambda_3$	Principal stretches
σ	stress
∇^2	Laplace operator

Abstract

Finite element models, which can determine the degree of vascular injury caused to a vessel by a stent and hence ascertain the propensity of that stent design to cause in-stent restenosis, would be a valuable tool for both medical device companies and interventional cardiologists. The basis of this thesis is to establish a preclinical testing methodology for stents, which can determine the degree of mechanical injury caused to a vessel by a particular stent design. The testing technique will enable stents to be designed to prevent or minimise vascular injury and hence restenosis. To achieve this goal, uniaxial and equibiaxial tensile tests on cardiovascular tissue were carried out to develop suitable Mooney-Rivlin constitutive models for arterial tissue. Three-dimensional models of different stent designs were generated and placed in their expanded states within models of coronary arteries. The established Mooney-Rivlin models were used to represent the materials of the artery. The mechanical loading induced within the stented vessels by the different stent designs was calculated to determine the stent design least likely to cause excessive vascular injury and hence in-stent restenosis.

Fatigue tests were carried out on coronary arterial tissue to determine a measure of damage accumulation within stented vessels at the elevated stresses imposed by stents on coronary arteries. The measured rate of damage accumulation within the tissue was used as a stimulus for in-stent restenosis in a computational model of the vascular healing process. The model was based on the predominant mechanism of the in-stent restenosis, SMC migration and proliferation. The propensity of the different stent designs to cause in-stent restenosis was determined from the computational model of the restenosis mechanism.

The in-stent restenosis model successfully predicted the stent design that is least likely to cause occlusive in-stent restenosis, by comparison to clinical restenosis data. It therefore supports the use of this method to analyse new stent designs. This method could ultimately be used as a preclinical test to determine the optimum bare-metal or drug-eluting stent design to prevent in-stent restenosis.

CONTENTS

CHAPTER 1

Introduction

Contents

1.1 Preclinical testing of stents

The ageing population, and an increased demand for healthcare, has made the medical device industry one of the largest and fastest expanding industries worldwide. More and more patients are benefiting from the use of innovative medical devices that have now become indispensable in the fight against disease and injury. Cardiovascular disease currently kills more Irish men and women of all ages than any other disease [Central Statistics Office Ireland, 2004]. About half of all deaths from cardiovascular disease are specifically from coronary heart disease [European Cardiovascular Disease Statistics, 2000]. In fact, by 2020, the World Health Organization estimates that nearly 25 million cardiovascular disease deaths will occur worldwide annually [Chockalingam and Balaguer-Vintro, 1999]. Balloon catheters and cardiovascular stents have been developed to treat cardiovascular disease and can significantly improve quality of life for a person with coronary heart disease. As a result of the prevalence of coronary cardiovascular disease, there are an estimated one million coronary stents implanted annually [Bioscorpio, 2004]. In the Republic of Ireland (population: 4 million), over 3,000 coronary stents were implanted in 2002 [Central Statistics Office Ireland, 2004; Hospital In-Patient Enquiry (HIPE) system and the National Perinatal Reporting System (NPRS) Unit, 2004].

Stent technology is not limited to use for treatment of coronary cardiovascular disease. Large artery stenting procedures are also performed to restore blood flow in stenosed carotid arteries whilst balloon-expandable, bifurcated stent grafts are used for endovascular aortic aneurysm repair. Small stents are implanted in cases of obstruction of the bile duct and for cerebral artery stenoses. Urethral stents have also been developed to facilitate bladder emptying in patients with spinal cord injury. All of these stents aim to achieve one objective; to restore patency to a fluid carrying vessel. However each stent type has different design considerations based on the size, function, and material properties of the host vessel, as well as the fluid being transported.

As a result of the prevalence of coronary cardiovascular disease, coronary stents are the most frequently used of all of these different stent types. Only 88 non-coronary stents were inserted in Ireland in 2002 [Hospital In-Patient Enquiry (HIPE) system and the National Perinatal Reporting System (NPRS) Unit, 2004]. Issues with

respect to the design of coronary stents include: (i) sufficient rigidity to resist the compressive forces from the vessel wall, (ii) sufficient flexibility to navigate tortuous vessels, (iii) scaffolding properties: stents must be able to hold open the vessel and scaffold the stenotic material (plaque) against the vessel wall, (iv) minimal longitudinal contraction when expanded, (v) minimal shearing between the stent and tissue during expansion because this denudes the vessel of its endothelial cell lining and finally but most importantly, (vi) minimal activation of the restenosis mechanism [Prendergast *et al.*, 2003]. Restenosis occurs when the blockage reforms around the stent; restenosis is the major obstacle to the long-term success of the procedure. In general, the propensity of a particular stent design to cause in-stent restenosis is determined from the results of time consuming and expensive animal and/or human clinical trials. Furthermore, there are issues associated with the use of animals in studies of in-stent restenosis since animals are not aged and the mechanism of atherosclerosis and/or in-stent restenosis in animals may not be the same as that in humans [Prendergast and Maher, 2001]. In many cases, therefore, the results from retrospective human clinical studies are the only available information on the success of a stent, and these results cannot be used to directly relate restenosis to particular aspects of stent design. One might say that the improvement of a stent's performance is more by trial-and-error than strategic device design.

Finite element analysis is a computational analysis tool that has been identified as an effective technique to preclinically test medical devices [Prendergast and Maher, 2001]. It can estimate the stresses and strains in very complex material and geometric models under a variety of loading patterns. It also has the advantage that it can incorporate simulations of tissue adaptations in response to the medical device. Therefore, in principle at least, the finite element method can be used to simulate the long-term performance of a medical device.

To-date the finite element method has been used extensively to analyse and optimise design characteristics of stents; namely to asses the longitudinal retraction (also called foreshortening) of stents, or to improve the expansion of a stent for different material choices and different stent geometries [Etave *et al.*, 2001; Tan *et al.*, 2001; Migliavacca *et al.*, 2002; Chua *et al.*, 2002; Chua *et al.*, 2003]. Numerous computational studies have also been carried out to investigate the structural and fatigue properties of stents for both balloon expanding stent designs [Dumoulin and Cochelin, 2000] and nitinol self-expanding stents [Whitcher, 1997]. However, there

are very few analyses which have investigated the interaction between the stent and the artery, even though mechanical vascular injury has been identified as the stimulus for restenosis of vessels [Schwartz and Holmes, 1994; Arakawa *et al.*, 1998]. In fact, no preclinical testing of stent designs using the finite element method have yet been published to determine the propensity of different stents to cause vascular injury and in-stent restenosis. Such tests would enable stents to be designed to reduce the risk of in-stent restenosis.

1.2 Atherosclerosis, stenting and restenosis

Atherosclerosis is an inflammatory disease of large and medium sized elastic and muscular arteries. It causes stenosis, or blockage, of the artery from the build-up of plaque within the vessel, see Figure 1.1 [Ross, 1999]. Risk factors include high blood cholesterol, high blood pressure, diabetes, male gender, obesity, smoking, physical inactivity, and an unhealthy diet [European Cardiovascular Disease Statistics, 2000]. Atherosclerosis occurring in the coronary artery is referred to as coronary heart disease and causes ischaemia of the heart. When left untreated it ultimately results in acute myocardial infarction.

Percutaneous transluminal coronary angioplasty (PTCA) is a non-surgical technique which was introduced in 1977 to restore blood flow within a stenosed coronary artery [Gruentzig *et al.*, 1979]. PTCA involves passing a radiographically guided catheter with a small balloon, over a guide wire, usually through the femoral artery into the narrowed section of the coronary artery. The balloon is then inflated to a high pressure for a short time within the vessel at the site of the stenosis. As a result, longitudinal and circumferential splits in the plaque are produced and the plaque is compressed against the artery wall [Meads *et al.*, 2000], see Figure 1.2. The technique has revolutionised the treatment of cardiovascular disease. Immediate patency is usually achieved, although restenosis or reformation of the occlusion occurs in 30-50% of patients [Nobuyoshi, 1991].

Because of elastic recoil of the vessel in PTCA, intravascular stents were developed in order to maintain vessel patency after balloon angioplasty. A balloon expandable stent is initially mounted in a crimped state over a balloon catheter and navigated to the site of arterial occlusion by means of a guide wire. Radiopaque

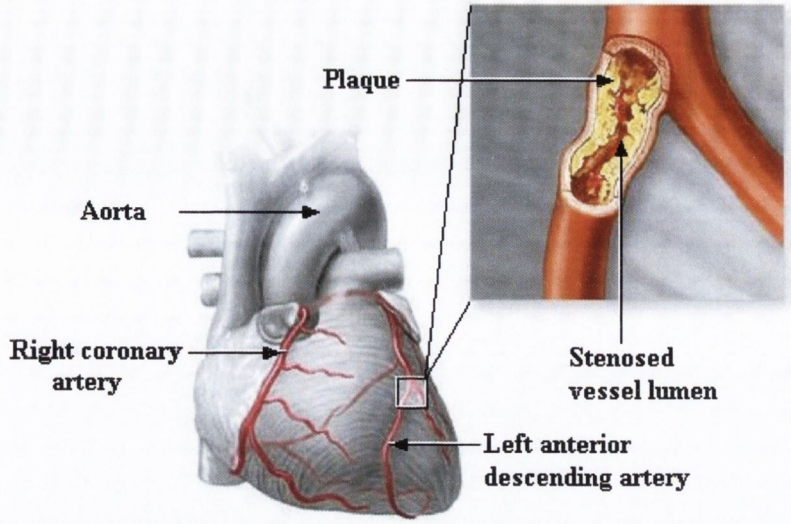

Figure 1.1 *Schematic of the human heart illustrating the locations of the left and right coronary arteries and coronary artery atherosclerosis [Website 1].*

markers at the ends of the angioplasty balloon enable accurate positioning of the stent at the site of the stenosis. The intravascular stenting deployment procedure first uses PTCA to plastically deform the stent at the site of the vessel stenosis, see Figure 1.2. The stent subsequently behaves as a scaffold for the artery wall and the compressed atherosclerotic plaque within the vessel, as shown in Figure 1.2(b).

Shape memory alloys such as nitinol may be used to make a stent; in that case the stent may be "self-expanding" and does not require balloon angioplasty to deploy it [Duerig *et al.*, 1999]. As the name suggests, shape memory alloys have the ability to recover their original shape. The superelastic material of a self-expanding stent can be shape-set to the expanded configuration, compressed into a catheter at room temperature and then pushed out of the catheter at the site of the stenosis. On removal from the catheter sheath the blood warms the device and it deploys automatically by recovering its original expanded shape. An advantage of the superelastic hysteresis of a nitinol stent is that it applies only a very light outward force against a vessel wall, but at the same time is highly resistant to crushing. There are also shape memory alloy stents that are not self-expanding and are deployed using a balloon catheter. The shape memory metal remains in its martensitic phase at all times and although the strength of the stent may be lower than conventional stainless steel stents, it has the advantage of superior MR compatibility and more uniform stresses and strains [Duerig *et al.*, 1999].

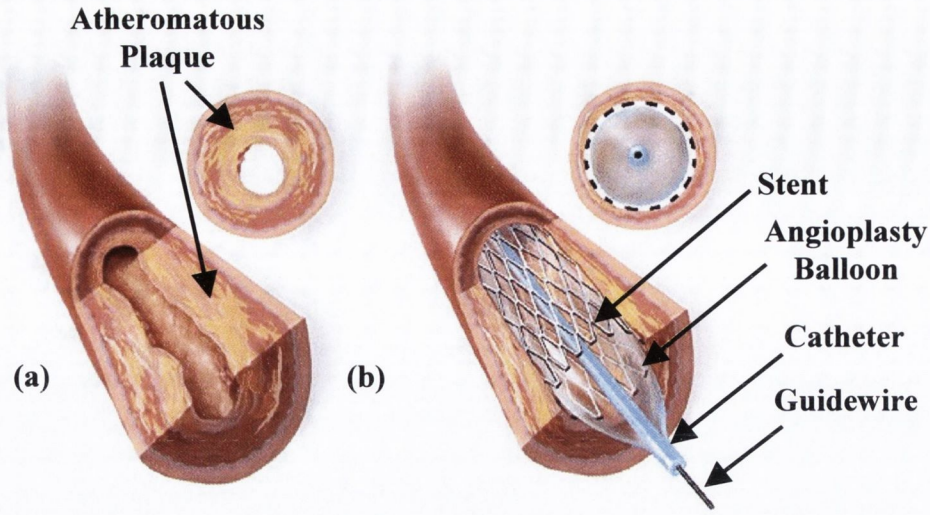

Figure 1.2 *A diseased coronary artery (a) before intervention, with stenotic atherosclerotic plaque and (b) with a deployed stent using balloon angioplasty [Website 2].*

Stents have improved the short-term outcome of PTCA alone, often called Plain Old Balloon Angioplasty (POBA). However, even with a stent, restenosis still remains a major limitation to the late outcome of the procedure, occurring in 20-50% of stented vessels [Grewe *et al.*, 2000]. Like restenosis post-POBA, *in-stent* restenosis results in renarrowing of the vessel lumen; however, it is a more chronic disease than restenosis from balloon angioplasty alone. The chronic nature of the disease is most likely due to the fact that the stent remains in the artery after deployment and may therefore act as a continuous source of vascular injury. As DeScheerder *et al.* [1999] state "Although the mechanisms underlying in-stent restenosis are not well understood, injury caused to the vessel during balloon angioplasty and subsequent stent implantation, and a foreign body reaction induced by the implant are considered to be the major contributing factors for in-stent restenosis".

In order to determine measures that can be taken to prevent or treat in-stent restenosis, it is necessary to have a detailed knowledge of the disease mechanism. Although, considerable research has been carried out to ascertain the cause of in-stent restenosis no complete solution to the problem has yet been found. The predominant mechanism of in-stent restenosis has been identified as neointimal proliferation, which is part of the vascular healing response to stent induced injury [Schwartz *et al.*, 1992; Edelman and Rogers, 1998].

In recent years, drug-eluting stents have emerged as an alternative to bare metal stents and are coated in an anti-proliferative drug (e.g. Sirolimus, Paclitaxel) to prevent in-stent restenosis. These stents have shown much promise since they can retard the predominant mechanism of in-stent restenosis – i.e. intimal cell proliferation. However, it is still generally accepted that the optimal approach to coronary revascularization lies in further developments in *both* the biomechanical and pharmacological aspects of stents, which can be related to stent design and drug-elution, respectively [Lepor *et al*, 2002; Palmaz, 2004]. The biomechanical aspects of stents alone may hold the answers to restenosis prevention since clinical studies have reported very different in-stent restenosis rates for different bare-metal stent designs [Colombo *et al*, 2002; McClean and Eigler, 2003].

1.2.1 Stimulus for restenosis

Abnormal values and variations of haemodynamic shear stresses have been identified as a likely stimulus for the formation of intimal hyperplasia at arterial bypass junctions and atherosclerosis within the vascular tree [Bassiouny *et al.*, 1992; Keynton *et al.*, 2001]. Consequently, alterations in vessel wall shear stress after stent implantation have also been postulated as a possible stimulus for in-stent restenosis [Wentzel *et al.*, 2000]. However, animal and human stenting trials have consistently identified a relationship between vascular injury and in-stent restenosis [Schwartz and Holmes, 1994; Arakawa *et al.*, 1998]. Studies have also identified a link between in-stent restenosis, as a result of vascular injury, and stent design [Rogers and Edelman, 1995; Kastrati *et al.*, 2000]. A relationship between vascular injury and the mechanical forces applied to the vessel by the stent can also be inferred because injury has been found to be a function of the aggressiveness of the stent deployment procedure [Hoffman *et al.*, 1999]. It therefore seems clear from these studies that vascular injury, or damage to the vessel wall, stimulates the restenosis mechanism. It is likely that haemodynamic shear stresses contribute to this damage, however, for this study only the damage due to stresses within the artery wall induced by the expanded stent will be considered, as they appear to be the dominant stimulus for in-stent restenosis.

The pattern of in-stent restenosis observed at the site of a stent also illustrates this relationship between injury and intimal cell proliferation. This is evident if both

the stenting deployment procedure and the response of the vessel to stenting are analysed. The stenting procedure begins with predilation of the stenosed vessel using balloon angioplasty and fractures may occur in the atherosclerotic plaque during this process, see Figure 1.3(a) and (b). The stent scaffolds open the vessel; however tissue prolapses between the stent struts, as shown in Figure 1.3(c). The first stage in the development of in-stent restenosis is an inflammatory response to the stent. It is initially focal in nature forming predominantly around the stent struts, as demonstrated schematically in Figure 1.3(d). As the restenosis process progresses neo-intimal hyperplasia, predominantly composed of smooth muscle cells, appears more concentric. However, the neointima is thicker where injury is more severe, i.e. at the stent struts, see Figure 1.3(e).

This characteristic pattern of in-stent restenosis has led to the hypothesis that damage may be induced within the artery wall by the stent as it scaffolds open the artery. It is conjectured that this damage, which is highly dependant on stent design, may be the stimulus for the vascular healing response within the vessel that ultimately results in excessive neointimal growth and consequently in-stent restenosis. The high mechanical stresses induced within a stented vessel, which would be far beyond the stresses experienced by a vessel under physiological conditions, superimposed on the cyclic loading of the vessel by the pulsing blood flow may cause localised damage formation to which the vessel responds by intimal proliferation.

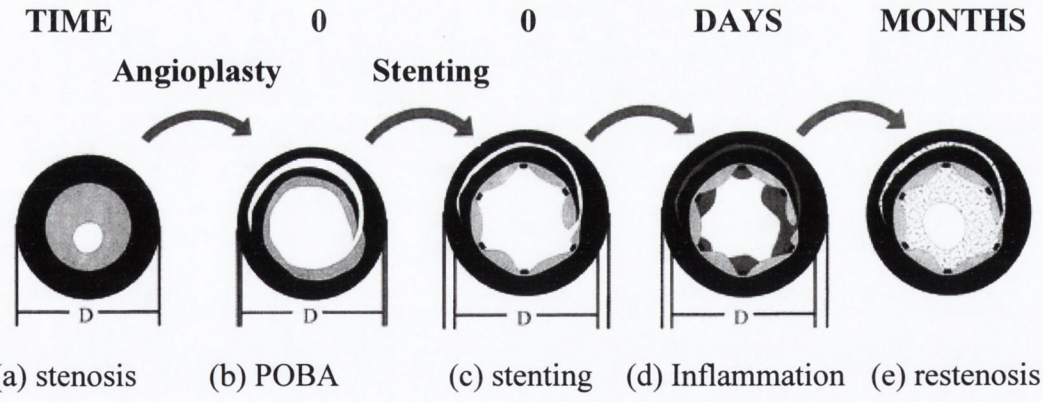

Figure 1.3 *Stent deployment after angioplasty enlarges the lumen by stretching the artery. Within hours to days after stenting, caps of thrombus infiltrated with inflammatory cells (dark grey) form over stent struts (black rectangles), particularly abundant at sites of deep injury. Over ensuing weeks, a neointima forms (speckled area), thicker where injury is more severe [adapted from Edelman and Rogers, 1996].*

1.3 Objectives of the thesis

In this thesis, the author will attempt to demonstrate that intravascular stents can be designed to prevent in-stent restenosis. This argument will be based on finite element simulations of restenosis within vessels stented with different stent designs. To have finite element models of in-stent restenosis whose results can be relied upon, it is necessary to;

(1) establish a suitable constitutive model for coronary arterial tissue,
(2) establish a finite element modelling approach whereby the level of vascular tissue loading and the damage caused during a stenting procedure by different stent designs can be ascertained,
(3) devise an algorithm to simulate in-stent restenosis, and apply it to stent designs known to have different restenosis rates.

If the simulations succeed in predicting the stent design which has the lowest propensity to cause in-stent restenosis, then the proposed methodology could be used to improve new stent designs.

In the future a restenosis model like this could be adapted for use with drug-eluting stents and patient-specific geometries to predict the clinical outcome of different stent designs. The complexity of the restenosis algorithm could be increased as animal and clinical studies offer further information on the restenosis mechanism and the response of the vascular wall to anti-proliferative drugs. It is necessary, however, to initially develop an algorithm which can successfully predict restenosis for different stents; later the technical challenges of using the algorithm for patient-specific geometries can be met.

CHAPTER 2

Literature Review

Contents

2.1 Introduction

This chapter begins with a detailed description of stenting and the mechanism of in-stent restenosis. In order to test the hypothesis that stents can be designed to reduce the risk of restenosis, it is necessary to simulate the outcome of different stenting procedures using a suitable design tool, such as the finite element method (FEM). To this end, it is important to understand the pathophysiology of the in-stent restenosis mechanism and the stimulus for the disease. Stresses in the vessel wall of the stented vessels can be estimated using FEM. However, the accuracy is highly dependant on the material model used to define the arterial tissue properties. It is therefore necessary to establish an appropriate material model for the coronary artery. The composition and biomechanical properties of arterial tissue are therefore discussed. Previous testing methods that have been used to determine the mechanical properties of arterial tissue are reviewed and constitutive models for arterial tissue are also presented. This chapter concludes with a review of studies that have been carried out to-date to simulate the intravascular stenting procedure using the finite element method.

2.2 Intravascular stenting and in-stent restenosis

As described in Chapter 1, percutaneous transluminal coronary angioplasty (PTCA) was introduced in 1977 to restore blood flow within stenosed coronary arteries [Gottsauner-Wolf *et al.*, 1996]. It involves expanding a balloon within the artery to compress the atherosclerotic plaque and permanently deform the stenosis. The lumen of the blood vessel is enlarged by the procedure and the blood flow restored within the vessel. However, elastic recoil of the vessel is noted clinically after deflation and removal of the balloon from the artery. In fact, there may be a substantial loss (up to 50%) of the arterial cross-sectional area from elastic recoil [Gottsauner-Wolf *et al.*, 1996]. The degree of elastic recoil is dependant on such factors as the lesion eccentricity and the amount of plaque within the vessel. When an artery with an eccentric lesion is dilated using a balloon, the non-diseased segment of the artery may expand under the pressure rather than the stiffer atherosclerotic plaque. Elastic recoil of the healthy artery occurs after expansion and the lesion may remain undeformed.

Therefore, the problem with expansion using the balloon alone is that the artery lumen diameter may not be permanently increased.

Stents were developed mainly to overcome this problem of elastic recoil. Stents have a significantly better long-term outcome than balloon angioplasty alone requiring fewer target lesion revascularization (TLR) procedures to be performed [Kiemeneij *et al.,* 2001]. This may be attributed to the fact that the increase in lumen diameter after stenting is much greater than after balloon angioplasty. However, coronary stenting causes greater levels of injury to the vessel and therefore causes relatively more intimal thickening than balloon angioplasty [Yutani *et al.*, 1999].

The probability of the development of occlusive in-stent restenosis in the coronary artery has been found to depend on the stent design as well as on the method of deployment of the stent [Edelman and Rogers, 1998; Arakawa *et al.*, 1998, Hoffmann *et al.*, 2004]. It is therefore highly dependent on mechanical factors. Although in-stent restenosis involves growth within the lumen of the stented artery and therefore causes further stenosis to the vessel in much the same way as stenotic atherosclerosis, it is a different process to atherosclerosis.

> *".. the pathophysiology of restenosis is a separate process from atherosclerosis. It follows an entirely different time course, has different histopathology, and comes from mechanical rather than biochemical injury in the arterial wall."* ~ [Schwartz and Holmes, 1994]

2.2.1 The biomechanical mechanism of in-stent restenosis

It is known that restenosis following balloon angioplasty is due to the formation of smooth muscle cell (SMC) rich intimal hyperplasia and vessel remodelling. However, the vascular response to balloon angioplasty with a stent takes a slightly different form.

> "*The more symmetric shape of the lumen imposed by the stent, as well localised disruptions of the vessel wall by the stent struts, compounded by the effects of an indwelling device, all lead to chronic, prolonged damage rather than only acute, time-limited injury.*" ~ [Edelman and Rogers, 1998]

The mechanism of in-stent restenosis is believed to be primarily the response of the vessel to vascular injury caused by the stent. Four different phases have been identified in the process of vascular repair after stent-induced injury [Edelman and Rogers, 1998].

(i) The first phase in the vascular response to stent-induced injury is a thrombotic response, whereby mural thrombus deposition occurs where the stent struts penetrate the vessel wall. The greater the extent of the injury caused to the vessel by the stent, the greater the resultant thrombotic response (Figure 2.1a).

(ii) The second phase involves an inflammatory reaction and takes place at the thrombotic sites (Figure 2.1b). Initially, surface adherent monocytes (SAM) are recruited, from the circulation and the adventitial vasa vasorum, to the injury site. These cells later migrate into the neointima as tissue infiltrating monocytes (TIM).

(iii) The third phase, tissue proliferation, coincides with the migration of these inflammatory cells to the neointima (Figure 2.1c). Both SMCs and the TIMs proliferate to develop intimal hyperplasia. It has been found that a linear

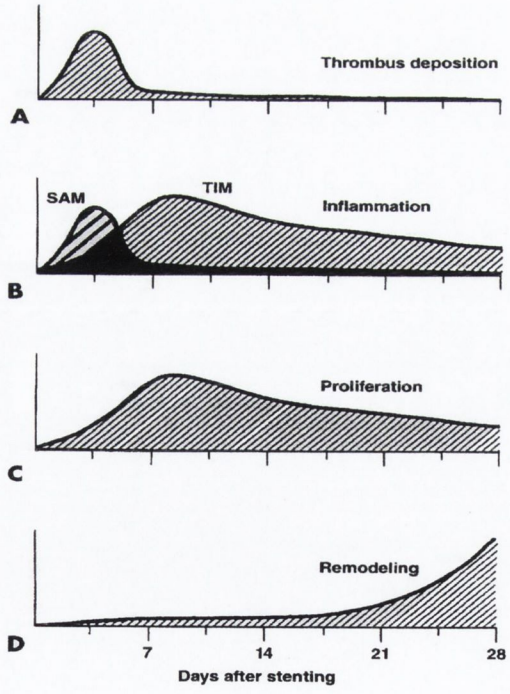

Figure 2.1 *The four phases of vascular repair after stent-induced arterial injury. SAM are surface adherent monocytes and TIM are tissue infiltrating monocytes [Edelman and Rogers, 1998].*

relationship exists between the number of inflammatory monocytes per artery and the extent of arterial intimal growth, as shown in Figure 2.2 (American Heart Association, 1996; cited in [Edelman and Rogers, 1998]). SMCs and extracellular matrix are the principal constituents of the stenotic material in stented vessels, which have partial or complete in-stent restenosis [Hoffman and Mintz, 2000].

(iv) The fourth and final phase in the vascular response to stent induced injury is remodelling of the vessel wall (Figure 2.1d). Remodelling is defined by changes in vessel size. After stenting the artery may shrink due to collagen deposition and fibrosis within the arterial wall. Although the stent limits elastic recoil of the vessel wall, it may not limit remodelling, since the arterial wall may squeeze through (or prolapse between) the stent struts [Edelman and Rogers, 1998; Ponde *et al.*, 1997]. In addition, arterial remodelling can potentially cause late stent radial recoil, which depends on the rigidity of the stent and the degree of increased collagen deposition within the artery [DeScheerder *et al.*, 1999].

The formation of a stenosis is a combination of tissue prolapse and superimposed neointimal tissue accumulation, see Figure 2.3 [Hoffman *et al.*, 1996]. Clearly, the highest contributing factor is the intimal hyperplasia formation within the lumen of the vessel post stenting.

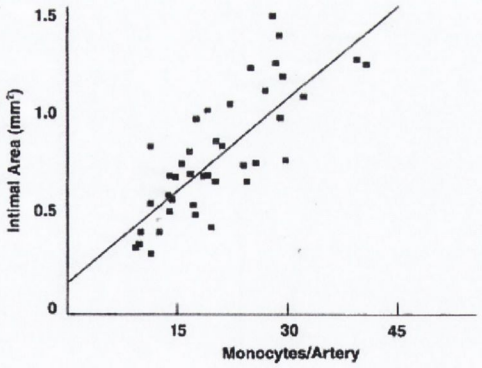

Figure 2.2 *Relationship between the number of monocytes in the vessel and intimal cell proliferation cross sectional area [Edelman and Rogers, 1998].*

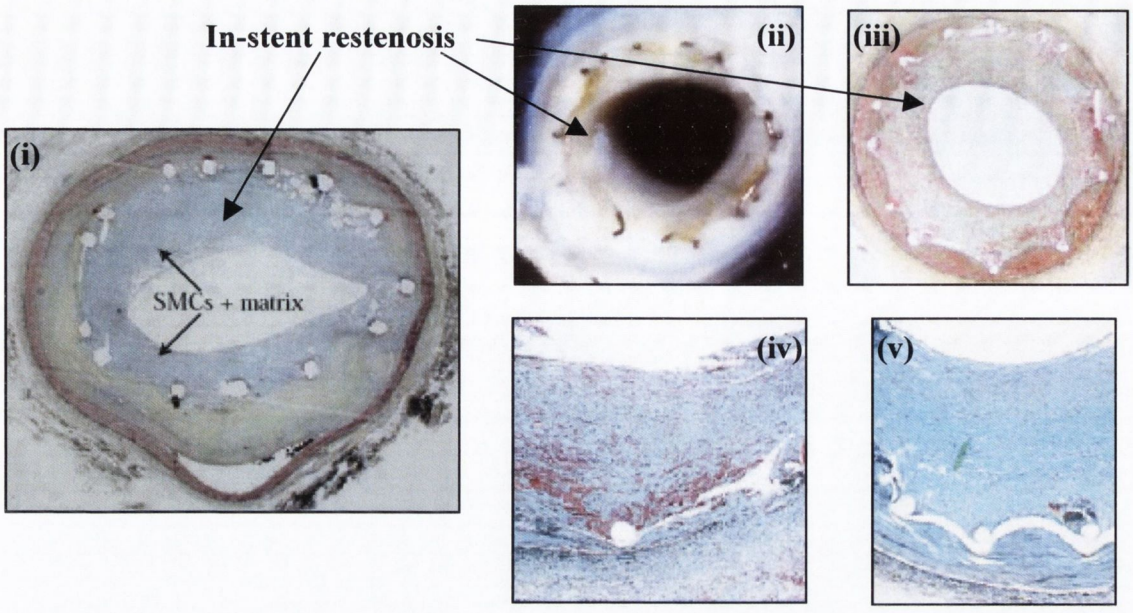

Figure 2.3 *i) Human stented coronary artery after 4 months, ii)-iv) Balloon expanded stents in Pig coronary artery at 2 weeks, v) at 4 weeks [Virmani, 2002].*

Intimal hyperplasia has been identified as the major mechanism of late lumen loss after stent implantation and hence the dominant mechanism of in-stent restenosis [Arakawa *et al.*, 1998; Schwartz *et al.*, 1994]. There is a strong correlation between late luminal loss in human stented arteries and the development of in-stent restenosis by the formation of intimal hyperplasia, see Figure 2.4.

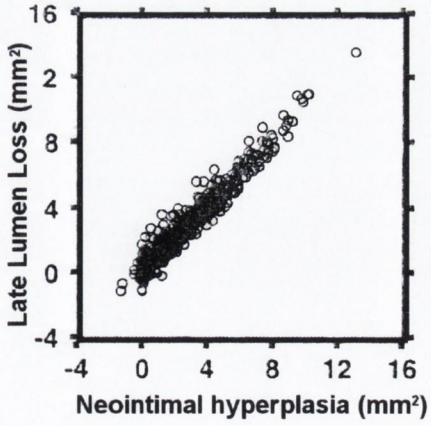

Figure 2.4 *Late lumen loss correlates very strongly with neointimal hyperplasia in human stented arteries [Hoffman et al., 1996].*

Although the vascular response to stent-induced injury can be observed in human and animal studies, the exact stimulus for this response has not yet been conclusively identified and therefore a stent design which limits the restenotic process has not yet been developed.

By looking in more detail at the main mechanisms of in-stent restenosis, the likely stimulus for restenosis can be hypothesised. Using biomechanical testing methods, it may then be possible to confirm or refute these hypotheses.

2.2.2 Thrombosis after stent implantation

Endothelial denudation after stent implantation exposes the thrombogenic constituents of the vascular subendothelium, promoting blood platelet adhesion, activation, aggregation and ultimately thrombus formation. The deep vascular injury imposed on the vessel by the implanted stent causes thick, platelet-rich mural thrombi to form at the stent struts [Orford *et al.*, 2000].

Currently available endovascular stents are extremely thrombogenic, and the prevention of thrombosis necessitates anticoagulation regimes [Yutani *et al.*, 1999]. Although thrombosis primarily affects the short-term outcome of stenting, it has also been hypothesised that extensive early thrombus, generated within days of stenting, may serve as a scaffold for subsequent intimal proliferation and neointimal hyperplasia [Edelman and Rogers, 1996; Orford *et al.*, 2000]. Activated and aggregating platelets produce a number of vascular SMC mitogens, which stimulate the synthesis of extracellular matrix as well as the migration and proliferation of SMCs [Orford *et al.*, 2000].

A study carried out by Rogers and Edelman [1995] investigated the thrombotic influence of two different stent materials and the effect that the thrombosis had on the formation of in-stent restenosis. The material of the stents was either stainless steel or stainless steel with a 3 μm anti-thrombotic polymer coating. Identical stent geometries were used and were implanted in the iliac arteries of New-Zealand white rabbits. The study found that considerably less acute thrombosis occurred in the polymer-coated stents. However, the stent coating did not influence the degree of chronic occlusive neointimal hyperplasia. The results from the study clearly demonstrated that the level of thrombosis is influenced by changes in the stent material in contact with the arterial wall. However, a correlation cannot necessarily be made between the thrombotic

response to the stent material and intimal hyperplasia, the predominant mechanism of in-stent restenosis.

Regarding the influence of stent geometry, Rogers and Edelman [1995], demonstrated that the thrombotic response of stented vessels to different stent geometrical configurations does vary, even when they are manufactured from the same material. They found that the level of thrombosis was dependent on the degree of vascular injury caused by the stent to the vessel and that increased thrombosis did correlate with increased intimal hyperplasia [Rogers and Edelman, 1995].

It may be necessary, therefore, to differentiate between the thrombotic response due to the presence of a foreign material and that which is as a result of vascular injury. Based on the observations by Rogers and Edelman [1995] it is proposed that the presence of a foreign material might not activate mitogens whereas vascular injury does. Mitogens play a key role in the proliferation of the SMCs. However, the response to a foreign material, although also apparently thrombotic, may not activate mitogens but rather may induce an inflammatory response. This inflammatory response may not affect the function of the SMCs.

2.2.3 Intimal proliferation

Neointimal growth after stenting consists of SMC proliferation in the intima and extracellular matrix, which supports the increased numbers of SMCs at the site of vascular injury [Gottsauner-Wolf *et al.*, 1996; Virmani, 2002]. At first, SMCs are activated in association with mural thrombi and growth factors. Then SMCs migrate from the media to the intima, where the cells change phenotype; they change from contractile to synthetic SMCs.

In the contractile phenotype, SMCs contain large quantities of fibrils and are incapable of responding to mitogens. Mitogens are the substances that stimulate mitosis (cell division). However, given sufficient stimulus the SMC looses its fibrous nature and changes phenotype to form a synthetic SMC, i.e. the cells differentiate. In this state the cell is capable of producing its own platelet derived growth factor and other mitogens and will respond to a large number of growth factors. The synthetic SMC plays a key role in restenosis via migration and intimal proliferation [Yutani *et al.*, 1999; Orford *et al.*, 2000]. Both clinical and animal studies have suggested that the deformation of the vessel wall is a principal determinant of the extent of intimal

proliferation as a response to arterial injury. To quote Yutani *et al.*, 1999, "*Substantial expansion and over expansion of the arterial lumen by a stent comes at the expense of a potent stimulus for SMC proliferation and neointimal hyperplasia*".

The cellular events in response to vascular injury by a stent that lead to restenosis are summarised in Figure 2.5 below.

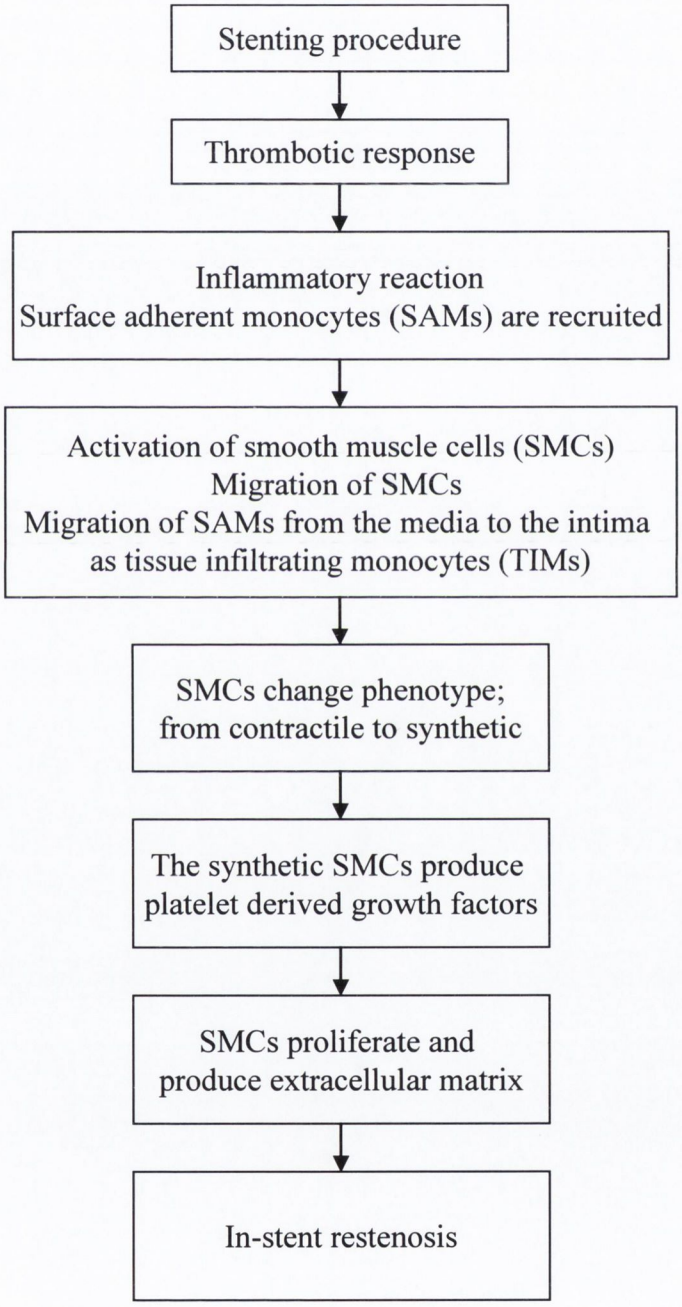

Figure 2.5 *Summary of cellular events post-stenting that lead to restenosis of a stented vessel.*

A grading scheme, or an injury score, whereby deeper injury is assigned a progressively higher score, has been developed to describe the degree of injury to a vessel by a stent [Schwartz *et al.*, 1994]. This scheme is summarised in Table 2.1 below. Using this scheme, the disruption caused by stent struts of purposefully over expanded stents to the arterial wall was determined in a porcine model. The study found the degree of vascular injury to correlate with neointimal hyperplasia, see Figure 2.6a and Figure 2.6b [Schwartz and Holmes, 1994].

The 'injury score' system was also used to determine the relationship between stent induced vascular injury in rabbit iliac arteries [Rogers and Edelman, 1995]. Two different stent designs were deployed within the arteries and the observed injury score was found to correlate with neointimal hyperplasia. Greater injury and neointimal thickening was found to occur in the stent design with the higher number of strut-strut intersections. A close linear relationship was found between monocyte adhesion and both vascular injury and neointimal hyperplasia. The findings from the study support the hypothesis that neointimal formation is provoked by mechanical vascular disruption, to which monocytes respond, rather than by an inflammatory response to the stent material.

Score	**Degree of vascular injury**
0	The stent causes endothelial denudation and medial compression but no disruption of the internal elastic lamina
1	Disruption of the internal elastic lamina
2	Laceration of the tunica media
3	Disruption of the external elastic lamina

Table 2.1 *Vascular Injury Scoring Scheme [Schwartz and Holmes, 1994].*

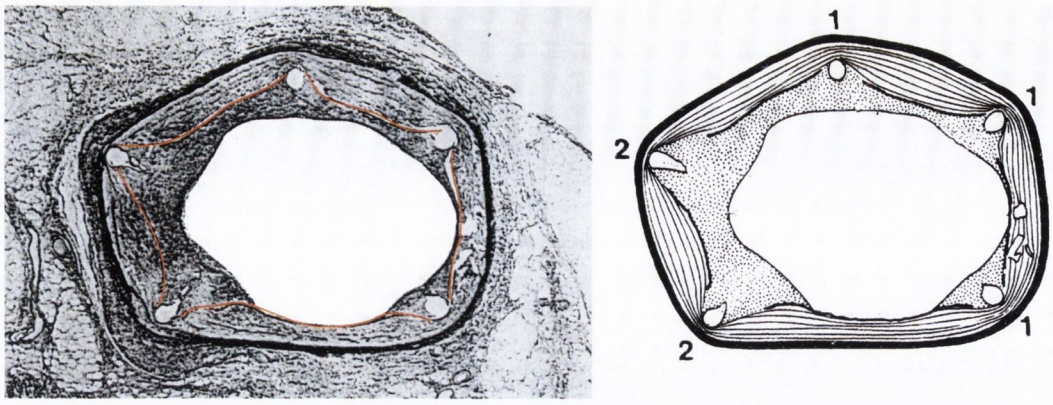

Figure 2.6 *(a) Photomicrograph of a pig coronary artery injured by an oversized stent, 28 days after injury. (b) Different wires have created different depths of injury. The depths of injury are assigned an injury score. The extent of neointimal hyperplasia is seen to correlate with the depth of injury [Schwartz and Holmes, 1994].*

It is therefore hypothesised that the increased intimal hyperplasia in stented vessels relative to vessels that have undergone angioplasty alone may not be due to the presence of a foreign material but rather that leaving the stent behind in the artery may cause a more severe vascular injury. This injury may provide a chronic stimulus for smooth muscle cell proliferation and neointimal hyperplasia. However, it should be noted that the response to stent induced vascular injury is a self-limiting process, which ceases once the site of injury has been re-endothelialised. This re-endothelialisation process occurs within 21-56 days in animal models, but has been found to take at least 3 months in humans. In fact, the time course of in-stent restenosis after coronary intervention in humans ranges from 3-18 months after stent implantation, with peak angiographic restenosis typically detected between the first and third month after the procedure [Orford *et al.*, 2000]. The greatest proliferative activity occurs in the first 7 days after stenting, see Figure 2.1 [Edelman and Rogers, 1998].

In summary, the predominant mechanism of in-stent restenosis is lumen loss from SMC proliferation occurring as a healing response to vascular injury. In order to minimise restenosis, therefore, the optimum stent design should be sufficiently rigid to prevent lumen loss from remodelling whilst minimising injury to the vessel.

2.3 Arterial adaptation

Proliferation of the intima has been found to occur in arterial bifurcations and graft-artery bypass junctions to restore abnormal haemodynamic wall shear stresses to baseline levels [Glagov *et al.*, 1995]. Arterial thickening has also been identified in arteries in response to hypertension [Fung, 1993]. Arterial adaptive modelling processes may also cause intimal thickening after stent implantation in order to restore normal tensile or compressive stress or strain induced in the vessel wall from the stent implantation. Therefore, in-stent restenosis may be a growth mechanism that is a response to stress induced vascular injury in the vessel wall. A study, by Fu *et al.* [1997], demonstrates the ability of canine saphenous arteries to adapt to a constant long-term applied strain on the vessel. Silicone balloon expanders were inflated in the saphenous arteries under different pressures and they were left for different durations within the vessel. Short-term pressure inflation altered the arteries' properties considerably, such that the vessel was stiffer in uniaxial tension. However, long-term lower pressure inflation allowed the arteries to adapt to the applied pressure and restore the original vessel properties by vessel wall thickening. In the same way, the permanent strain induced on a stented artery may initially cause collagen deposition and stiffening of the vessel whilst the long-term healing process of in-stent restenosis may be an attempt to restore the original vessel properties by intimal thickening.

Although abnormal values and variations of haemodynamic shear stresses have been identified as a likely stimulus for the formation of intimal hyperplasia at arterial bypass junctions and within the vascular tree [Bassiouny *et al.*, 1992; Keynton *et al.*, 2001], it seems clear from the extensive studies carried out on restenosis that it is vascular injury or damage to the vessel wall which is the predominant stimulus for the restenosis mechanism.

2.4 Injury as a stimulus for in-stent restenosis

2.4.1 Relationship with stent design

Many clinical studies have been carried out to investigate stent performance. Among the findings from these studies has been that different stents have different in-stent restenosis rates [Kastrati *et al.*, 2000; McClean *et al.*, 2002; Colombo *et al.*, 2002].

Hoffman *et al.* [1999] conducted a study to determine the effects of stent-induced injury on the formation of restenosis within human coronary arteries. They found that tissue proliferation within and surrounding stents is dependent on the 'aggressiveness' of the stent implantation technique. The aggressiveness of the procedure was defined by an aggressiveness score. However, unlike the injury score defined by Schwartz and Holmes [1994], the aggressiveness score was determined from the magnitude of the product of the balloon/artery diameter ratio and the final inflation pressure of the balloon. They used IVUS imaging to quantify the degree of tissue proliferation at follow-up. In-stent and peri-stent intimal hyperplasia thickness within the vessels correlated significantly with the aggressiveness ratio, with greater tissue proliferation found at higher values. In addition, the degree of surface monocyte cell adhesion and infiltration into the stented arteries was found to correlate with the degree of injury and intimal hyperplasia.

Vascular injury caused to a vessel by the implantation of a stent, whether defined by the depth of penetration of the stent wires into the host artery wall or by an aggressiveness score, has consistently been found to determine the degree of restenosis [Schwartz *et al.*, 1994; Rogers and Edelman, 1995; Arakawa *et al.*, 1998; Hoffman *et al.*, 1999]. Histological studies have also indicated that intimal hyperplasia thickness after stent placement is related to vessel trauma during stent placement [Carter *et al.*, 1994]. The level of vascular injury, therefore, depends on the balloon/artery ratio, the inflation pressure of the balloon and also the material properties and configuration of the stent. These parameters also determine the stress and strain induced in the stented vessel wall.

It should be noted that, in the study by Hoffman *et al.* [1999], a larger balloon/artery ratio and a higher balloon inflation pressure did not mean a larger final lumen diameter at follow-up because in-stent restenosis had narrowed the vessel lumen. In other studies, greater intimal hyperplasia has been noted in over-expanded vessels but often there has been a corresponding increase in the lumen diameter and therefore the vessel has been able to accommodate the restenotic tissue without complete stenosis occurring. This has led to the 'bigger is better' approach in stenting, i.e. intentional over-expansion of the vessel by the stent to ensure that the restenotic material will be accommodated and not cause complete stenosis [Goldberg *et al.*, 1998]. However, Hoffman *et al.* [1999] found a higher incidence of complete stenosis with increased aggressiveness of the procedure.

Arakawa *et al.* [1998] found a correlation between higher vessel stretch by stenting and intimal hyperplasia in human coronary arteries after stenting. In the study, higher stent-to-vessel CSA ratio at stenting resulted in more neointimal proliferation 6 months after stenting. They found the optimum stent-to-vessel CSA ratio to be 0.7 in order to minimise restenosis. This indicates that stent deployment protocols may need to consider optimal rather than maximal lumen diameters to limit vascular injury.

However, if the stent-to-vessel diameter ratio were the only factor which dictated in-stent restenosis, then no single stent design would be superior provided that the stent/artery diameter ratios were the same. Rogers and Edelman [1995] compared stainless steel stents with two geometries: slotted-tube and corrugated ring–type stents at 2 weeks after implantation in denuded rabbit iliac arteries. Both stent configurations were of identical mass, surface area, and surface finish. The ring stents, however, were associated with significantly less vascular injury, having a 42% lower vascular injury score; significantly less thrombosis (15% versus 42%); and significantly less neointimal hyperplasia (38% lower). The reduced risk of restenosis associated with the corrugated ring stents was postulated to be due to the fact that they had 29% fewer strut-strut intersections compared to the slotted-tube stents, and they did not flare at the ends. Therefore, we can conclude from the study by Rogers and Edelman [1995] that: (i) the geometrical configuration of the stent alone can determine the degree of vascular injury and subsequent restenosis, and (ii) the rigid strut-strut intersections of a stent would be likely to exert more injury to the vessel during vasoconstriction of the artery after stenting than the body of the stent.

Some stents may even induce a different response at different points along the length of the stent. Greater luminal loss after stent implantation has been observed at the edges and at the central articulations of the Palmaz-Schatz stent, see Figure 2.7 [Hoffman *et al.*, 1996; Dusaillant *et al.*, 1995; Ikari *et al.*, 1995]. At the articulation point, the artery may not be sufficiently supported by the stent and so prolapse of the tissue may contribute significantly to luminal loss. However, the edges of the Palmaz-Schatz stent dilate more than the body during normal inflation. As a result, the stent edges may be more deeply embedded in the vessel wall than the body causing more severe injury to the vessel. Therefore, intimal hyperplasia is most likely greater at the edges of the stent as a consequence of greater injury to the vessel. In addition, the junctions of stented and native arterial segments are subject to abrupt transitions in

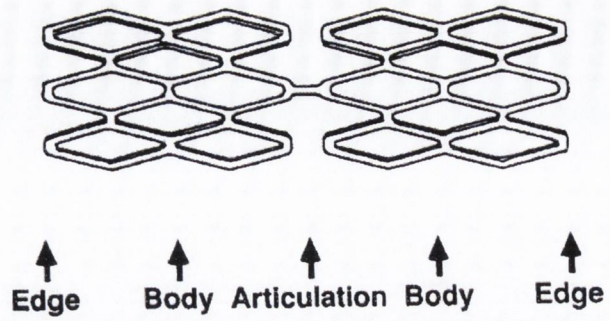

Figure 2.7 *A section of a Palmaz-Schatz stent [Hoffman et al., 1996]*

diameter, contour and rigidity [Edelman and Rogers, 1996], which may induce non-physiological, high concentrated stresses in the vessel wall at the stent edges. Although an atherosclerotic artery would be relatively stiff compared with a healthy artery, it would be still considerably more compliant than the stented segment of the vessel. This is because stents are designed to withstand vasoconstriction pressures of up to 450 mmHg (~60 kPa) [Serruys *et al.*, 1998], whereas physiological pressures are only in the range of 80-120 mmHg (10-16 kPa).

It is hypothesised therefore that the stresses induced in the artery walls by the implantation of a stent may determine the degree of injury caused to the vessel and hence the degree of restenosis. The stresses induced within a stented vessel can be estimated using FEM, provided that information on the vessel and stent material properties are known along with the boundary conditions of the problem.

2.4.2 Measures of arterial damage

As discussed in the previous section, vascular injury caused to a vessel by a stent may be used as a stimulus for restenosis. To use this idea for biomechanics it is necessary to have a quantitative measure of damage.

Damage accumulation under cyclic loading leading to fatigue failure has been found to occur in soft tissues in much the same way as bone [Wang *et al.*, 1995]. For example, fatigue tests were carried out on lengths of wallaby tendons at different stress levels and different frequencies to determine the rate of damage accumulation within the tendon tissue. Plots of force versus displacement for selected cycles of the fatigue tests showed a gradual decrease in stiffness throughout each test. The falling

stiffness of the wallaby tendon tissue was deemed a symptom of the accumulation of damage within it.

The characteristic pattern of in-stent restenosis and the observations of Wang *et al.* [1995] and Ker and Zioupos [1997] have led the author to hypothesise that cyclic loading of another soft tissue, the arterial wall, may also result in localised damage accumulation. Damage may be induced within a stented vessel when the expansion stress created by the stent is superimposed on the cyclic load due to blood pressure. The elevated stresses generated within the vessel wall by the stent scaffolding open the artery may cause localised damage accumulation around the stent struts, which may cause a healing response and consequently restenosis. The rate of damage accumulation within arterial tissue can be ascertained at the elevated stress levels imposed by the stent by determining the reduction in stiffness of the tissue during fatigue tests in a similar way to that carried out by Wang *et al.* [1995] on wallaby tendon test specimens. Fatigue damage could act as a stimulus for tissue repair, in the form of SMC proliferation and consequently intimal hyperplasia thus narrowing the lumen of the stented vessel and ultimately causing in-stent restenosis.

The idea of fatigue damage accumulation within arterial tissue at elevated stress levels will be investigated as part of this thesis.

2.5 Previous experimental tests to determine the elastic behaviour of arterial tissue

2.5.1 Anatomy of the artery wall

Arteries are the blood vessels in the body that carry oxygenated blood to the organs and cells of the body. They may be divided into two categories; elastic arteries and muscular arteries. The elastic arteries of the body are the largest vessels and include the aorta, the carotid and the iliac arteries. Muscular arteries include the coronary and femoral arteries. All of the arteries in the body comprise three concentric layers; the tunica intima, the tunica media and the tunica adventitia, see Figure 2.8.

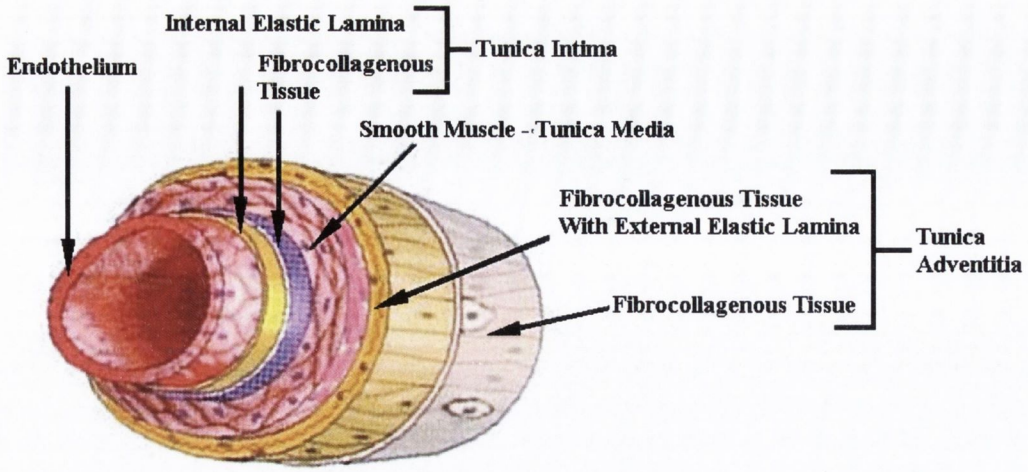

Figure 2.8 *Schematic of a human muscular artery [adapted from Website 3].*

The intima of large arteries is composed of a monolayer of endothelial cells and a thin underlying layer of fibrocollagenous tissue. A band of elastin, called the internal elastic lamina, separates the intima from the media of the artery. The media contains smooth muscle cells in an extracellular network of elastin and collagen [Humphrey, 2002]. Elastic arteries have a thick, highly developed media of which elastin fibres are the main component. These are gathered together in sheets arranged in concentric layers throughout the thickness of the media. Muscular arteries have a media composed of more smooth muscle and collagen and less elastin than the elastic arteries. The large elastic arteries gradually merge into muscular arteries by losing most of their medial elastic sheets. Usually only two elastin layers remain in muscular arteries; the internal elastic lamina and the external elastic lamina at the junction of the media with the intima and adventitia, respectively, see Figure 2.8.

The adventitia of large blood vessels mainly consists of collagen fibres, which are initially undulated in the unloaded state [Humphrey, 2002]. The adventitia also carries the blood vessels that supply the smooth muscle cells and fibroblasts with oxygenated blood [Martini, 2001].

Arteries exhibit both active and passive mechanical behaviour. The active mechanical behaviour of arterial tissue is determined from the degree of contraction of the smooth muscle cells within the artery wall [Holzapfel *et al.*, 2000]. The passive mechanical properties of arteries, whether elastic or muscular, are dependent on the

composition of the artery, namely the amount of elastin and collagen present in the vessel wall. This is demonstrated in Figure 2.9 where the fresh tissue illustrates the characteristic J-shaped non-linear stress-stretch response observed when arterial tissue is uniaxially loaded in tension.

The response of the fresh human iliac artery is non-linear and stress stiffening; illustrating a low stiffness on initial loading and higher stiffness as the load is increased, see Figure 2.9. Linear elastic elastin fibres ($E \cong 3 \times 10^5$ Pa) predominantly bear the load at low loads giving rise to the large extensions of the arterial tissue at low loads. The initially undulated stiffer collagen fibres ($E \cong 10^8$ Pa) are gradually straightened and begin to bear the load as the tissue is stretched [Hastings, 1992]. The non-linearity of the tissue is due to the gradual recruitment of the collagen fibres to bear the load on the arterial tissue. The final slope of the curve, which is also almost linear, represents the elasticity of the tissue when all of the collagen fibres are recruited. The low stiffness of the elastin fibres and the relatively high stiffness of the collagen fibres has been demonstrated by tensile tests on iliac artery segments. In the test, the two constituents were selectively digested away allowing the stress-stretch characteristics of each component to be determined separately, see Figure 2.9 [Burton, 1962].

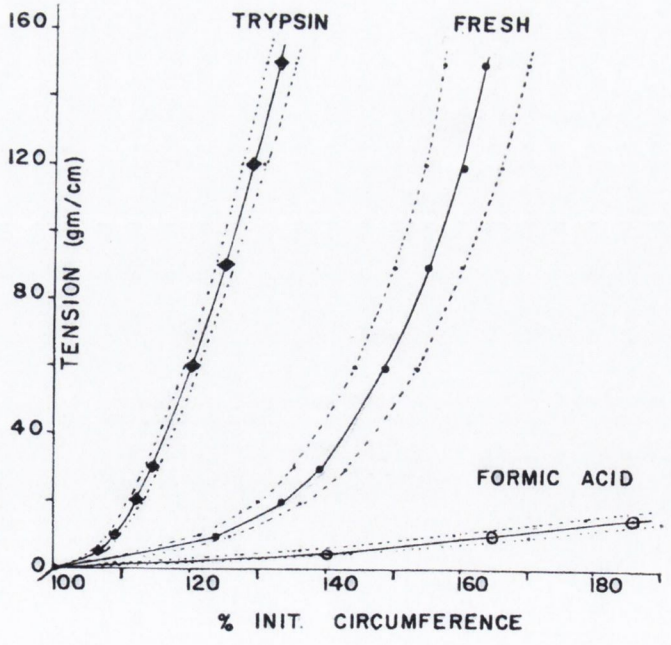

Figure 2.9 *Tension-length diagrams for the wall of human iliac arteries, after selective digestion of elastin fibres (trypsin), and of collagen fibres (formic acid) [From Burton, 1962].*

There are different amounts of elastin and collagen in different arteries in the human body with the amount of elastin reducing and the amount of collagen increasing with distance from the heart. This can be illustrated by comparison to canine arteries where the collagen/elastin ratio has been measured and found to be 1.58, 1.89 and 3.12 in the abdominal aorta, femoral and coronary arteries, respectively [Fisher and Llaurado, 1966, cited in Humphrey, 2002].

For the purpose of developing a preclinical test on coronary intravascular stents, a constitutive model of human coronary arterial tissue is required. Suitable constitutive models, which can be implemented in finite element codes, are discussed in the following section.

2.5.2 Constitutive models of arterial tissue

A constitutive model which includes the contribution of the smooth muscle of the artery, in its active state, to the mechanical properties of arterial tissue has been developed by Rachev and Hayashi [1999]. Most constitutive models, however, have been established to describe the passive properties of arterial tissue. For investigating the interaction between the arterial system and intravascular devices, the passive properties of the tissue are of most interest.

To model the complex non-linearity and stress-stiffening passive behaviour of arterial tissue some assumptions are made. The first assumption is that of homogeneity. Histologically an arterial segment can be considered to have a reasonably uniform structure in the longitudinal and circumferential directions, but not in the radial direction [Wolinsky and Glagov, 1964]. Therefore, the wall properties may be considered uniform at least in the longitudinal and circumferential directions. In the radial direction, they will reflect only the average properties through the three layered vessel if a one layer model is used. It should be noted, however, that the media of the vessel bears most of the load in an expanded blood vessel since the adventitia and intima may, in fact, constitute less than 10% of the thickness of the vessel wall [Humphrey, 2002]. Another implication of the assumption of homogeneity is that no distinction is made between the specific contributions made by the different constituents of the wall such as elastin and collagen. However, it is the overall mechanical behaviour of the arterial tissue, and the contribution of all constituents of the vessel, that is of interest here. Therefore, for the purpose of investigating stent

induced vascular injury, the artery wall may be adequately represented by a material model that assumes homogeneity.

Another assumption is that of incompressibility. Rubber-like materials, which are materials capable of undergoing large deformations, show a very low degree of compressibility, i.e. they resist volume changes to a much greater extent than they do shape changes. Carew *et al.* [1968] considered the issue of incompressibility in the context of arterial tissue and reported that "for most practical purposes" the assumption of incompressibility can safely be made. Dobrin and Rovick (1969) also later corroborated this finding.

Although many constitutive models of arterial tissue are isotropic, it is well known that the arterial wall is anisotropic given the three-layered nature of arteries and the various constituents of the vessel wall. It has been shown, however, that there exists an elastic symmetry about the planes perpendicular to the principal axes. This indicates that blood vessels may be considered to be cylindrically orthotropic, having elastic symmetry about the planes perpendicular to the r, θ and z directions [Patel and Fry, 1969].

Tickner and Sacks (1967) were the first to present a theory for the study of arterial elasticity based on finite deformation of rubber-like incompressible materials. The theory assumes the existence of a strain energy density function, W, for the material that is a function of the principal stretches (λ_1, λ_2, λ_3) or the stretch invariants (I_1, I_2, I_3). A constitutive model based on defining a strain energy density function is termed a hyperelastic material. For a hyperelastic material:

$$S_{ij} = \frac{\partial W}{\partial E_{ij}} = 2\frac{\partial W}{\partial C_{ij}} \tag{2.1}$$

where: S_{ij} = components of the second Piola-Kirchoff stress tensor

E_{ij} = components of the Green-Lagrangian strain tensor

C_{ij} = components of the right Cauchy-Green deformation tensor

Arterial tissue is not strictly an elastic material but displays viscoelastic behaviour; therefore, it is strain rate dependant and exhibits hysteresis. The concept of a pseudoelastic strain energy density function was developed to describe this behaviour [Fung, 1993]. Unique pseudoelastic strain energy density functions can be defined for the loading and unloading of a viscoelastic material. This function also refers to the strain energy density function of the arterial tissue after the tissue has

been preconditioned at a specific strain rate. Preconditioning involves cyclically loading and unloading the arterial tissue for a number of cycles until a steady state is reached where no further change occurs in the material stress-stretch curve. The upper limit of the loading cycle is usually about 20% of the expected ultimate tensile strength of the arterial tissue. For arteries, 3-5 cycles is usually enough to precondition the tissue and remove hysteresis [Fung, 1993]. Arteries thus preconditioned can be treated as being pseudoelastic and their response during loading or unloading can be described by one strain energy density function for a specific strain rate [Fung, 1993]. The representation of the mechanical properties of an artery by a pseudoelastic function, where the arterial tissue has been preconditioned, can be justified by the fact that arterial tissue *in vivo* is under a constant cyclic load and is therefore in a preconditioned state.

Several forms of strain energy functions, in terms of the principal strains or stretches, have been proposed to fit to experimental data from tests on arterial tissue. Patel and Vaishnav [1972] used a polynomial strain energy function given by:

$$W = A\gamma_\theta^2 + B\gamma_\theta\gamma_z + C\gamma_z^2 + D\gamma_\theta^3 + E\gamma_\theta^2\gamma_z + F\gamma_\theta\gamma_z^2 + G\gamma_z^3 \qquad (2.2)$$

where: A, B, ...G are material constants and γ_θ and γ_z are the Green-St.Venant circumferential and longitudinal strains, respectively. They used this form of the strain energy density function to fit to experimental data from the aorta which was assumed to be incompressible and orthotropic. They demonstrated that this third order polynomial containing seven material constants gave a good fit.

Fung *et al.* [1979] employed an exponential form of the strain energy density given by:

$$W = \frac{C}{2}\exp[a_1 E_{\theta\theta}^2 + a_2 E_{zz}^2 + 2a_4 E_{\theta\theta} E_{zz}] \qquad (2.3)$$

where: C, a_1, a_2, a_4 are material constants and $E_{\theta\theta}$, E_{zz} are circumferential and axial Green-Lagrange strains, respectively. Fung *et al.* [1979] applied this form of the strain energy density function to study the properties of rabbit arteries from different parts of the arterial tree and obtained a good fit with experimental data. Both the methods by Patel and Vaishnav [1972] and Fung *et al.* [1979] are essentially two dimensional and orthotropic, since the vessel walls are assumed to be thin (i.e. the radial stresses are

uniform) and the stresses in the circumferential and longitudinal directions are much greater than in the radial direction.

One general polynomial form of the strain energy density function in terms of the stretch invariants, given by Maurel *et al.* [1998] for an isotropic hyperelastic material is:

$$W(I_1, I_2, I_3) = \sum_{i,j,k=0}^{\infty} a_{ijk} (I_1 - 3)^m (I_2 - 3)^n (I_3 - 3)^o, a_{000} = 0 \tag{2.4}$$

where a_{ijk} are the hyperelastic constants. If the principal stretches of the material are denoted λ_1, λ_2 and λ_3, then the stretch invariants for the material are:

$$I_1 = \lambda_1^2 + \lambda_2^2 + \lambda_3^2 \tag{2.5a}$$

$$I_2 = \lambda_1^2 \lambda_2^2 + \lambda_1^2 \lambda_3^2 + \lambda_2^2 \lambda_3^2 \tag{2.5b}$$

$$I_3 = \lambda_1^2 \lambda_2^2 \lambda_3^2 \tag{2.5c}$$

$I_3 = 1$ for an incompressible material. Many other strain energy functions have been formulated to model incompressible hyperelastic materials. Some of these are summarised below:

Mooney-Rivlin [Mooney, 1940]

$$W(I_1, I_2) = \sum_{i,j=0}^{\infty} a_{ij} (I_1 - 3)^m (I_2 - 3)^n, a_{00} = 0 \tag{2.6}$$

where a_{ij} are material constants.

Vito [Vito, 1980]

$$W_1 = \sum_{k=1}^{k \leq 4} b_k (I_1 - 3)^k \tag{2.7}$$

where b_k is a material constant.

Ogden [Ogden, 1984]

$$W(\lambda_1, \lambda_2, \lambda_3) = \sum_{p=1}^{N} \frac{\mu_p}{\alpha_p} (\lambda_1^{\alpha_p} + \lambda_2^{\alpha_p} + \lambda_3^{\alpha_p} - 3) \tag{2.8}$$

where μ_p and α_p are material constants.

Fung [Fung, 1993]

$$W(E_{ij}) = \frac{1}{2}\sum_{i,j,k,l=1}^{3}\alpha_{ijkl}E_{ij}E_{kl} + \beta_0 \sum_{m,n,p,q=1}^{3}\beta_{mnpq}E_{mn}E_{pq}e^{\alpha}$$
$$\alpha = \sum_{i,j=1}^{3}\nu_{ij}E_{ij} + \frac{1}{2}\sum_{i,j,k,l=1}^{3}\gamma_{ijkl}E_{ij}E_{kl} + \ldots.. \qquad (2.9)$$

where E_{ij} is the Green-Lagrange strain tensor. This model also applies to an anisotropic hyperelastic material. (For further strain energy density functions, see Maurel *at al.*, 1998).

Holzapfel *et al.*, 2000 have recently developed a three dimensional anisotropic multi-layer strain energy density function for application to arterial tissue given by:

$$W(C, A_1, A_2) = W_{iso}(I_1) + W_{aniso}(I_4, I_6) \qquad (2.10)$$

where C is the right Cauchy-Green deformation tensor, A_1 is given by the tensor product $a_{01} \otimes a_{01}$, and A_2 is given by $a_{02} \otimes a_{02}$. a_{0i}, i = 1,2, represent two direction unit vectors defined as

$$a_{01} = \begin{bmatrix} 0 \\ \cos\beta \\ \sin\beta \end{bmatrix} \qquad \text{and} \qquad a_{02} = \begin{bmatrix} 0 \\ \cos\beta \\ -\sin\beta \end{bmatrix}$$

where β is the angle between the collagen fibres and the circumferential direction of the artery. $W_{iso}(I_1)$ represents the isotropic contribution to the strain energy of the material, due primarily to the elastin bearing the load at low lumen pressures. $W_{iso}(I_1)$ is defined by the neo-Hookean form of the strain energy density function, i.e.

$$W_{iso}(I_1) = \frac{c}{2}(I_1 - 3) \qquad (2.11)$$

where c is a material constant obtained from experimental data fit.

$W_{aniso}(I_4, I_6)$ represents the anisotropic contribution to the strain energy function which is caused by the orientation of the collagen fibres in the arterial tissue which bear the load at high lumen pressures [Burton, 1962] .

$$W_{aniso}(I_4, I_6) = \frac{k_1}{2k_2} \sum_{i=4,6} \left\{ \exp\left[k_2 (I_i - 1)^2\right] - 1 \right\} \qquad (2.12)$$

where I_4 and I_6 are invariants of the tensors C, A_1 and A_2 given by:

$I_4 = C : A_1$ and $I_6 = C : A_2$

k_1 and k_2 are material constants established from experimental data fit.

In order to apply these models, and many similar ones, to the study of arterial tissue the material constants have to be obtained from tests on arterial tissue. Although this has been done for different arterial tissue types from different species the application of these models to computational models of cardiovascular stenting and angioplasty procedures is very limited [Vito and Dixon, 2002]. Some of the computational models to-date represent the vascular wall as linear elastic [Loree *et al.*, 1992; Rogers *et al.*, 1999] or as an isotropic hyperelastic material based on uniaxial data alone [Hayashi and Imai, 1997; Auricchio *et al.*, 2001]. Only one study has modelled the arterial tissue as an anisotropic hyperelastic material model [Holzapfel, 2002].

The best deformation modes for testing, to determine the hyperelastic material constants for any of the above models, are those that are the dominant modes of deformation in the application of interest for the material defined by the model. A stented vessel undergoes primarily uniaxial and biaxial tension where the arterial tissue drapes between the stent units, and uniaxial compression where the stent contacts with the artery wall. However, for an incompressible material uniaxial compression creates the same deformation as equibiaxial tension (see Fig. 2.10) and therefore, it is not necessary to test an arterial tissue in both uniaxial compression and equibiaxial tension in order to characterise the tissue. An accurate model for arterial tissue in cardiovascular stenting applications would be a constitutive equation based on fitting to experimental data from uniaxial tension and equibiaxial tension tests or data from inflation tests of arteries, which combine arterial lumen pressure with axial tension.

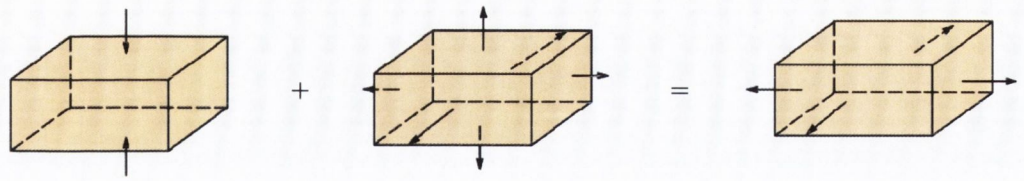

Uniaxial Compression **Hydrostatic Tension** **Equibiaxial Tension**

Figure 2.10 *Equivalent modes of deformation for an incompressible material [Ansys Theory manuals]*

Of most interest for stenting applications with the potential to be used in preclinical tests are hyperelastic material models which can represent adequately the large deformations of arterial tissue whilst also being easy to implement in finite element codes. Models that are available in commercially available finite element codes are limited to isotropic models and always include a form of the Mooney-Rivlin model and the Ogden model. High order Ogden models are generally weaker than the Mooney model and can cause numerical instabilities. On the other hand, many different forms of the more stable generalized Mooney-Rivlin model are available in commercial finite element analysis codes which can, or so it is claimed, accurately fit experiment data. The strain energy function W, given by Mooney [1940] in Eqn. 2.6, can be expanded to obtain the special cases of the two, five or nine-parameter strain energy density functions:

$$W = a_{10}(I_1 - 3) + a_{01}(I_2 - 3) \tag{2.13}$$

$$\begin{aligned} W = {} & a_{10}(I_1 - 3) + a_{01}(I_2 - 3) + a_{20}(I_1 - 3)^2 \\ & + a_{11}(I_1 - 3)(I_2 - 3) + a_{02}(I_2 - 3)^2 \end{aligned} \tag{2.14}$$

$$\begin{aligned} W = {} & a_{10}(I_1 - 3) + a_{01}(I_2 - 3) + a_{20}(I_1 - 3)^2 \\ & + a_{11}(I_1 - 3)(I_2 - 3) + a_{02}(I_2 - 3)^2 \\ & + a_{30}(I_1 - 3)^3 + a_{21}(I_1 - 3)^2(I_2 - 3) \\ & + a_{12}(I_1 - 3)(I_2 - 3)^2 + a_{03}(I_2 - 3)^3 \end{aligned} \tag{2.15}$$

These equations represent first, second, and third order models respectively. When the first order model is reduced to $W = a_{10}(I_1 - 3)$ it is called the neo-Hookean form of the strain energy function and it is the simplest hyperelastic constitutive model [Treloar, 1943]. The deformation modes of a hyperelastic material can, in principle, be more accurately modelled as the order of the expression for W is increased. When a suitable form of the strain-energy function is chosen, the parameters a_{ij} are found by non-linear regression. Many of the hyperelastic models available in commercial finite element analysis codes are special cases of the Mooney-Rivlin nine-parameter model, such as the third order model used by Hayashi and Imai [1997].

Since, the assumption of isotropy for arterial tissue does not represent the arterial tissue exactly, the use of an isotropic material may lead to errors in the analysis of the inflation response of vessels. However, if an isotropic Mooney-Rivlin model is established based on experimental data of the deformation modes of interest it may be used to model arterial tissue without a large error in the case where the tissue has an initial prestretch (see Appendix A for a more detailed discussion of the use of an isotropic model).

2.5.3 Uniaxial tensile tests

In uniaxial tensile testing, longitudinal and circumferential specimens, usually in a rectangular shape, are gripped and pulled lengthways and the force-elongation relationship recorded. There have been many studies, which have measured the non-linear stress-strain relationship in uniaxial tension of different arterial tissues from different species as well as from different areas in the arterial tree (Sharma, 1974; Patel and Fry, 1969; Bergel, 1972; Mohan and Melvin, 1982; Fung 1993).

The complex organisation of the constituents of arterial tissue, namely the collagen and elastin, means that the deformation response of arteries is strongly coupled in the principal directions, i.e. the radial, longitudinal and circumferential directions. This requires simultaneous multiaxial testing, e.g. biaxial testing. Unlike other biological orthotropic materials, like bone, multiple uniaxial tests are insufficient due to nonlinear interactions in arterial tissue, i.e. an applied axial strain in arteries alters the circumferential stress-strain curve [Humphrey, 2002]. Therefore, uniaxial testing does not describe the deformation of the arterial tissue adequately,

especially for applications where the tissue undergoes complex deformation modes, such as during stenting procedures.

2.5.4 Biaxial tensile tests

If arterial tissue may be considered to be incompressible, three-dimensional mechanical properties can be obtained from two-dimensional data. This has encouraged a number of studies to estimate the biaxial response of arterial segments. A review of biaxial testing of soft tissues has been recently published by Sacks [2000], whilst a review of constitutive models and relevant experimental testing to establish these models specifically for blood vessels has been written by Vito and Dixon [2002]. The main challenge in biaxial testing is to control two boundary conditions. The edges of a biaxially loaded sample need to be free to expand since the sample is loaded in two principal orientations. This excludes the use of solid clamping grips in biaxial testing. In addition, the gripping of the sample by numerous grips, to allow lateral extension, necessitates the use of non-contact strain measurement in a central region of the test specimen far from the specimen edges to avoid the localised affect of the grips.

Biaxial testing has been carried out primarily on the following soft tissues; arterial tissue [Manak, 1980; Vito, 1980; Vaishnav *et al.*, 1973], skin [Lanir and Fung, 1974], heart valve tissue [Billiar and Sacks, 2000] and pericardium [Sacks and Chuong, 1998; Choi and Vito, 1990].

To test skin under biaxial loading, Lanir and Fung [1974] floated square skin specimens in saline solution and applied biaxial forces by means of silk threads attached to the tissue by small staples, see Figure 2.11(a). An actuator, which was controlled via a function generator, applied the loads in the principal material directions. Strains were measured using two orthogonally positioned video dimensional analysers to simultaneously measure the strain in both principal stretch directions. Other studies have used a similar technique to load square arterial tissue specimens but have also incorporated complex feedback mechanisms to control the stress/stretch in the two orthogonal principal directions. The strain in the samples was measured using non-contact video extensometers mounted above the test specimens [Vaishnav *et al.*, 1973; Fronek *et al.*, 1975; Vito, 1980, Zhou and Fung, 1997].

Alternative gripping techniques have also been used whereby alligator grips were used to grip the tissue samples, see Figure 2.11(b).

Although a number of investigations into the biaxial behaviour of arterial tissue have been carried out, the availability of this data in a format suitable for implementation in preclinical tests is limited. Although arterial tissue is anisotropic,

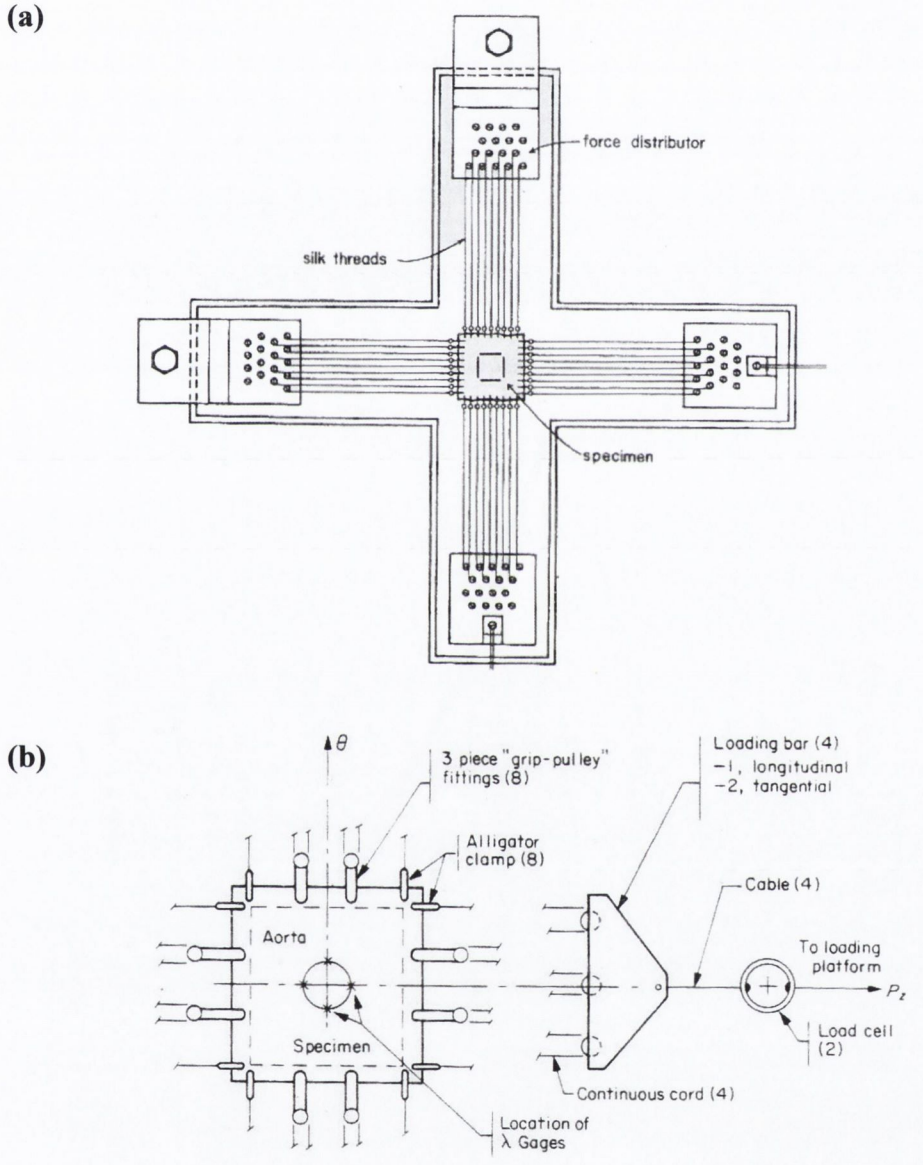

Figure 2.11 *Gripping techniques for biaxial testing; (a) biaxial testing of skin samples [Fung et al., 1974] and (b) gripping for thoracic aorta tissue samples [Manak et al., 1980].*

tests that apply an equal force to the four sides of a square tissue specimen can be devised. The resultant stress-stretch response in the two orthogonal directions can then be averaged to give the equibiaxial response of the tissue. No data of this nature was found in the literature which could be used to define a hyperelastic constitutive material model for coronary arterial tissue.

An alternative method to testing planar excised arterial tissue specimens involves inflation tests on intact arterial segments. Inflation tests on arterial tissue, whereby both a longitudinal force and an internal pressure are applied to a cylindrical vessel, have been carried out in the past [Vito, 1980; Fung *et al.*, 1979; Ogden and Schulze-Bauer, 2000, van Andel *et al.*, 2003]. This method has the particular advantage of avoiding traumatic excision and the mechanical properties are closer to physiological loading conditions. However, the use of data from these experiments on cylindrical specimens to define a constitutive model which can be implemented in finite element codes is not straight forward given the complex loading patterns and the anisotropic nature of the vessel.

Ideally, numerical studies on intravascular stents should use a material model defined from data from fresh human coronary arteries. However, fresh human coronary arteries are very difficult to obtain for testing because they are necessary for the embalming process of cadavers[1]. The coronary artery would have to be replaced by a bypass graft to enable the heart to be embalmed in a cadaver where the coronary arteries are harvested. In fact, harvesting the coronary artery alone is a complicated surgical procedure that requires extensive dissection [Humphrey, 2002]. Consequently, until very recently, the only available data on coronary arteries were uniaxial tensile tests of segments of human coronary arteries [Yamada, 1950] and a study which published the relationship between lumen pressure and axial and circumferential strain for one intact human and one porcine coronary artery [Carmines *et al.*, 1992]. However, van Andel *et al.* [2003] have now carried out a study of the inflation response of a number of human coronary and porcine coronary vessels and found that the porcine arteries have up to three times greater elasticity than the human coronary arteries. This result is to be expected since the human coronary tissue was taken from aged patients and atherosclerosis was present in all of the vessels.

[1] Personal communication with Prof. Clive Lee, Dept. of Anatomy, Royal College of Surgeons in Ireland.

Data are currently available on the mechanical properties of human aortic atherosclerotic plaques, which were collected during autopsies [Loree *et al.*, 1994]. This data defines the uniaxial tensile properties of calcified intimal aortic plaque and may therefore be used to define a hyperelastic constitutive equation to represent this material in finite element analyses, see Figure 2.12.

However, no data exist on the uniaxial and equibiaxial properties of human coronary arteries, which could be used to define a hyperelastic model for the computational preclinical tests to be proposed in this thesis.

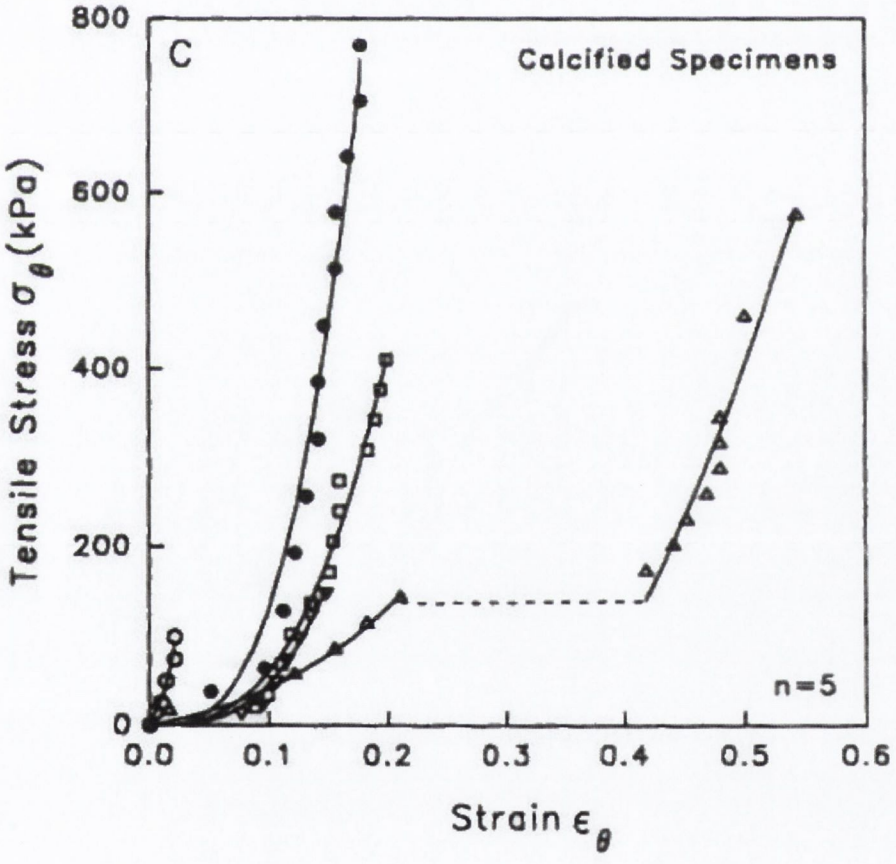

Figure 2.12 *Uniaxial stress-strain data for calcified human aortic plaques [Loree et al., 1994]*

2.6 Biomechanical analysis of stents using the finite element method

Since the emergence of stents nearly 20 years ago, research to assess their performance has been based almost solely on clinical trials. Preclinical tests on the biomechanical performance of different stent designs and materials have only emerged in the last 5 years with the dramatic increase in computing capabilities. An early *in-vitro* preclinical test was carried out by Peacock *et al.* [1995]. However, the study was solely concerned with flow disturbances induced by different coronary stent designs. Peacock *et al.* postulated that in-stent restenosis is a similar mechanism to intimal hyperplasia at graft-artery anastomoses and that it was due to flow instabilities and altered shear stresses induced by stenting. This theory has also been proposed and investigated by other researchers since this early study, using both *in-vitro* and computational techniques [Berry *et al.*, 2000; Wentzel *et al.*, 2001]. Endothelial cell migration onto metal stent surfaces under static and flow conditions was also investigated by Sprague *et al.* [2000] but little research has been done to assess the biomechanical properties of stents.

One of the first such finite element analyses was carried out to assess the fatigue behaviour of a nitinol self-expanding stent. The area of maximum tensile stress and expected fatigue failure of the Symphony stent design was determined [Whitcher, 1997]. The finite element model in this study by Whitcher [1997] had some limitations, especially in the geometric representation of the stent. The stent was modelled as a planar segment rather than a radial segment. This paper was, however, the beginning of a new surge in research on stents using finite element analysis, which included computational assessment of the expansion mechanisms, recoil, fatigue life and collapse of balloon-expandable and self-expanding stents [Dumoulin and Cochelin, 2000; Etave *et al.*, 2001; Tan *et al.*, 2001; Migliavacca *et al.*, 2002; Chua *et al.*, 2003]. As previously discussed in Section 2.4, stent design has been found to dictate the degree of in-stent restenosis [Colombo *et al.*, 2000] and has been linked to vascular injury [Rogers and Edelman, 1995], the probable stimulus for in-stent restenosis. However, numerical analyses that investigate the interaction between the stent and the artery are very limited.

Edelman and Rogers [1998] have used the finite element method to carry out a 2D analysis to investigate balloon-artery interactions during stent placement. The study has shown that factors such as the balloon inflation pressures, stent-strut

openings and balloon compliance can influence the contact stresses between the balloon and the arterial tissue between the stent struts and hence vessel injury. However, the study by Edelman and Rogers [1998] was limited to a 2D analysis and furthermore used linear elastic material properties to model the arterial tissue. A fully three dimensional model has been developed by Auricchio *et al.* [2001], to assess improvements to a stent design. However, the arterial tissue properties used were based on a hyperelastic material defined by uniaxial data from the aorta of Japanese white rabbits and so the stresses in the artery wall were not reported and injury caused to the vessel wall was not assessed.

The most detailed numerical model to-date of a cardiovascular intervention is that by Holzapfel *et al.* [2002]. They have developed a full 3D model of a realistic iliac artery vessel geometry using FEM. The material model for the vessel is orthotropic and multi-layered and is based on experimental data taken directly from tests on a human iliac cadaveric artery. The stresses induced within the vessel during balloon angioplasty and a Palmaz-Schatz stenting procedure were estimated. The limited mesh density of the vessel, however, meant that the localized stresses around the stent struts could not be computed. These are the important stresses because they would be the most likely site of vascular injury and therefore provoke in-stent restenosis. Consequently, it would not be possible to determine differences in the level of vascular injury as a function of stent design from their study. No doubt, however, these researchers will make rapid advances in the future.

Models which include patient specific information, such as that contained in the model reported by Holzapfel *et al.* [2002], offer valuable information on the level of stresses within a realistic vessel geometry. The specificity of the model to one vessel however, which in this case is a cadaveric iliac artery, and the limited mesh density possible given the complexity of the material model may limit the use of this type of analysis. A model such as this is difficult to use to compare and contrast different stent designs, the stent biomechanics or the influence of the stent design on vessel wall injury localised around the stent struts. The stent biomechanics and localised vessel wall injury should be of great concern to stent manufacturers and clinicians since they are main determinants of the major long-term failure mechanism of stents; in-stent restenosis.

Immediate patency is always achieved with commercially available stents; however, it is the propensity to cause restenosis that is unknown and of interest. Some

theoretical models of restenosis or vascular remodelling have been developed to-date [Taber *et al.*, 1998; Rachev *et al.*, 2000]. More recently, a computational model of restenosis in grafts has also been developed [Yang *et al.*, 2003]. The theoretical restenosis model by Taber [1998] used both fluid shear and wall stresses as the stimuli for growth in an aorta. This growth model was used to predict the changes in the thickness of a rat aorta during early development and following the sudden onset of hypertension. The study succeeded in developing a model which showed good agreement with published data on aortic growth in rats. This model was one of the first to develop a theoretical framework to model the observed adaptation of arteries to hypertension. The ability of arteries to respond and adapt to hypertension has been well documented [Fung, 1993]; however, in-stent restenosis is a more localised acute response to arterial injury than the chronic response observed in arteries subjected to hypertension.

The restenosis model developed by Rachev *et al.* [2000] used the stress concentrations at the artery-stent or artery-graft junction as the stimulus for arterial intimal thickening. In the mathematical model developed intimal thickening was allowed to form which was proportional to the magnitude of the circumferential and axial stress deviations from the baseline stresses. The baseline stresses were taken as the arterial wall stresses at a region far from the artery-stent or artery-graft junction. The remodelling process defined by this mathematical model was found to be self-limiting and caused local thickening in the stented vessel that gradually decreased with distance from the edge of the stent/graft. This model clearly demonstrated how a localised response of arterial tissue to altered wall stresses could cause intimal thickening and restenosis. However, the theoretical model was limited to a very simplified representation of an artery-graft or artery-stent junction. It assumed the artery to be a long circular cylindrical shell and the stent or graft joined to the artery was simply represented by clamping the artery at one end.

Yang et al., [2003] have recently developed a computational growth model for restenosis in grafts. The model developed uses only fluid shear stresses as the stimulus for intimal thickening. As stated earlier, alterations in fluid shear stresses may contribute to in-stent restenosis; however, vascular injury has consistently been identified as the most significant contributor to the onset of in-stent restenosis. Cleary, the optimum restenosis model should include the effects of both stimuli.

2.7 Conclusion

The mechanism of in-stent restenosis is clearly a complex one, involving a sequence of cellular events in response to vascular injury. It begins with an inflammatory and thrombotic response and is followed by smooth muscle cell proliferation and eventual restenosis. Although acute thrombosis in stented vessels needs to be addressed by using anticoagulation drugs, its overall ability to deliver a long-term solution to the problem of in-stent restenosis is not yet proven. Stent coatings can minimise acute thrombosis but vascular injury also causes a thrombotic response. It has been found that the thrombotic response to stent materials alone may not be the main influence on the predominant mechanism of in-stent restenosis, i.e. smooth muscle cell proliferation and intimal hyperplasia formation, but rather that vascular injury needs to be kept to a minimum. It is therefore anticipated that further exploration of the mechanism of stent-induced vascular injury and subsequent restenosis may lead to stent deployment protocols and stent designs that consider optimal rather than maximal lumen diameters so as to limit vascular injury. Gottsauner-Wolf *et al.* [1996] summed this up where they stated "Smooth muscle cell proliferation may be conceptualised as part of a useful and needed healing process after arterial injury. Stopping this healing process at a point where restoration of the endothelial surface is achieved, yet before a haemodynamically important reduction in vascular cross-sectional area occurs, is the basis of efforts to reduce restenosis". Clearly therefore, the ideal stent design should have a low propensity for in-stent restenosis by minimising damage to the wall during deployment whilst still maintaining sufficient vessel patency.

The contention of this thesis is that a stent can be designed and preclinically tested to achieve this objective. Although numerous numerical models exist for describing the non-linear and anisotropic behaviour of arterial tissue the anisotropic models cannot be easily implemented in commercial environments. The anisotropic models also require information on collagen fibre angles within the arterial tissue, an average value of which can be obtained from cadaveric tissue. Given the variability in the mechanical properties of biological tissue it may be reasonable to use an isotropic hyperelastic model to describe the non-linear stress-stiffening behaviour of arterial tissue. Isotropic hyperelastic models have also the advantage that they are easy to implement as they are readily available in all commercially available finite element

codes and are not very computationally expensive. This is a necessity for any preclinical testing technique if it is to find broad applicability in the medical device industry. Whilst an anisotropic model would be more accurate in a specific case, it is proposed that an isotropic hyperelastic model which describes the non-linear stress-stiffening behaviour of arterial tissue and is based on both uniaxial and equibiaxial experimental data presents an appropriate balance between the complexity of anisotropic modelling and the hyperelastic models based on uniaxial data alone.

Although in-stent restenosis represents the major limitation to the long-term success of stent implantations, there is currently no preclinical means for stent designers or manufacturers to predict it. Some techniques exist for predicting intimal thickening within arteries subjected to abnormal fluid shear stresses and/or abnormal wall stresses. Clearly, therefore, there remains a need for a preclinical testing methodology which can be easily implemented and used to determine the vascular injury caused to a vessel by a stent, can be correlated to clinical restenosis rates and can subsequently be used to determine the propensity of different stent designs to cause in-stent restenosis.

CHAPTER 3

Materials and Methods

Contents

3.1 Introduction

This chapter describes all of the experimental and computation methods used in this thesis to determine if stents can be designed to prevent restenosis. Finite element models of arteries in which cardiovascular stents were deployed were developed to achieve this objective. The finite element models were used to compute the stress and hence the level of vascular injury caused to a vessel by different stent designs and to determine if the development of in-stent restenosis may be attributed to the degree of vascular tissue loading.

Uniaxial and equibiaxial tension tests were carried out on both human femoral arterial tissue and porcine coronary arterial tissue to obtain the stress-stretch characteristics of tissue in the deformation modes that arterial tissue undergoes during a stenting procedure. This experimental data was used to define a Mooney-Rivlin hyperelastic constitutive model for each tissue type. These hyperelastic models were implemented in a finite element code and used to define the coronary arterial tissue in the finite element models of the stented vessels.

Fatigue tests were also performed to ascertain if damage accumulates within arterial tissue under cyclic loading and, if so, the rate of damage accumulation. Using this damage as the stimulus for in-stent restenosis, the finite element models were used to test a computational model of the in-stent restenosis mechanism.

3.2 Determination of the elastic behaviour of arterial tissue

Tensile test data were obtained for both human femoral arterial tissue and porcine coronary arterial tissue. Human femoral arterial tissue, although less muscular than human coronary arterial tissue, is susceptible to atherosclerosis and was therefore tested to represent aged atherosclerotic tissue similar to human coronary tissue. The cadaveric femoral arterial tissue obtained had varying levels of atherosclerotic disease present. Porcine coronary tissue was also tested to represent the mechanical properties of healthy human coronary arterial tissue. Porcine coronary arterial tissue was selected for testing because the porcine coronary artery is anatomically similar to that of humans, and is widely available [Swindle, 1992].

It is recognised that planar equibiaxial tensile tests on arterial tissue specimens apply non-physiological loads. However, the data from these tests are needed to

develop Mooney-Rivlin constitutive models that can be used to predict multi-axial deformations of the kind that occur in vascular tissue as a result of cardiovascular stenting.

3.2.1 Human femoral arterial tissue tests

Human femoral arterial tissue was obtained from cadavers in the Royal College of Surgeons in Ireland. Samples were stored in antibiotic solution at 4°C until testing. The protocol used for preparation of the antibiotic solution is given in Appendix B. All samples were prepared under sterile conditions, and any visible connective tissue was removed from the surface of the vessel before it was cut along its length, gently pressed flat, and sectioned. Lengths of tissue were prepared for uniaxial testing and areas of 25 mm square were prepared for biaxial testing. The thickness of each sample was measured with a Vernier calipers at several locations and an average taken. Each sample was marked to indicate its circumferential/longitudinal orientation. Both uniaxial and biaxial stress-stretch data were obtained as described in Sections 3.2.1.1 and 3.2.1.2 below. In both tests a strain rate of 60% min^{-1} was used. Specimens were continuously irrigated with 0.9% saline solution during testing and tests were carried out a room temperature. Preconditioning of the samples was carried out to a maximum load of 1 N at a strain rate of 60% min^{-1}. There was some variation in the thickness of the femoral artery tissue specimens, which were 1.5 +/- 0.5 mm.

A strain rate of 60% min^{-1} was chosen for all tests as it represents the rate at which an artery would be circumferentially expanded in a typical stenting procedure, i.e. an artery initially 2.2 mm diameter (3.5 mm vessel with 60% area stenosis), expanded to 3.5 mm diameter in 60 seconds, would be subjected to a circumferential strain rate of 60% min^{-1}.

3.2.1.1 Uniaxial testing

Custom made stainless steel grips with rubber coatings and emery paper to prevent slippage during loading were mounted on a 1011 Instron (displacement controlled) tensile testing machine. Specimens were longitudinal in the *in vivo* orientation. Extension of the specimen was taken to be the crosshead displacement. The tests were stopped when tearing began at either the grips or along the length of the specimen. The stress was determined by dividing the load by the instantaneous cross sectional

area and the stretch was obtained by dividing the instantaneous length by the original length.

3.2.1.2 Equibiaxial testing

The biaxial rig was designed so that it could be used on a standard uniaxial testing machine and comprised a number of working assemblies, as shown in Figure 3.1. The biaxial tests on femoral arterial tissue were carried out on a displacement controlled Instron 1011 tensile testing machine. The biaxial loading device consisted of a balanced set of levers or rotating beams of equal length which were free to pivot on polished stainless steel shoulder screws [one such lever is indicated by Point 5 in Figure 3.1]. Oil-impregnated bushes were used to minimize frictional forces between the screws and the beams. These balance beams ensured an equal force was applied to the four sides of a square test specimen. The levers are attached to a central block [Point 4 in Figure 3.1] by four horizontal beams and the central block fixed to the machine crosshead. The base plate of the assembly had four brackets and was secured to the base of the testing machine such that each bracket was directly below the ends of two adjacent balance beams. The main function of the bracket-pulley assemblies were to turn the vertical cable network through 90° and guide them toward the square specimen of cardiovascular tissue positioned centrally on the base plate. High strength fishing line (50 lb breaking strain) was used for the cable network. The route taken by the thread can be seen in Figure 3.1. Each line was connected to the balance beam, then around the curved beam ends, through the pulley-bracket fixture on the base plate [Point 10 in Figure 3.1], and then through the loading bracket [Point 9 in Figure 3.1] before returning via a similar route to the end of the adjacent balance beam. In this way the cables and rotating balance beams ensured that if one of the principal directions was stiffer than the other that the beams could rotate to allow a different value of stretch in each of the principal directions whilst maintaining an equal force.

The loading bracket transferred the loads from the line to the specimen. The jaw ends of crocodile clips were used to grip the sample and the other ends were linked to vertical dowel pins on the Perspex loading brackets.

Validation of the biaxial test device was carried out by measuring the equibiaxial stress-stretch response of a square, 1mm thick, silicone specimen. The isotropic silicone sample exhibited an isotropic response with equal forces maintained on the four sides of the sample and a resulting equibiaxial strain condition.

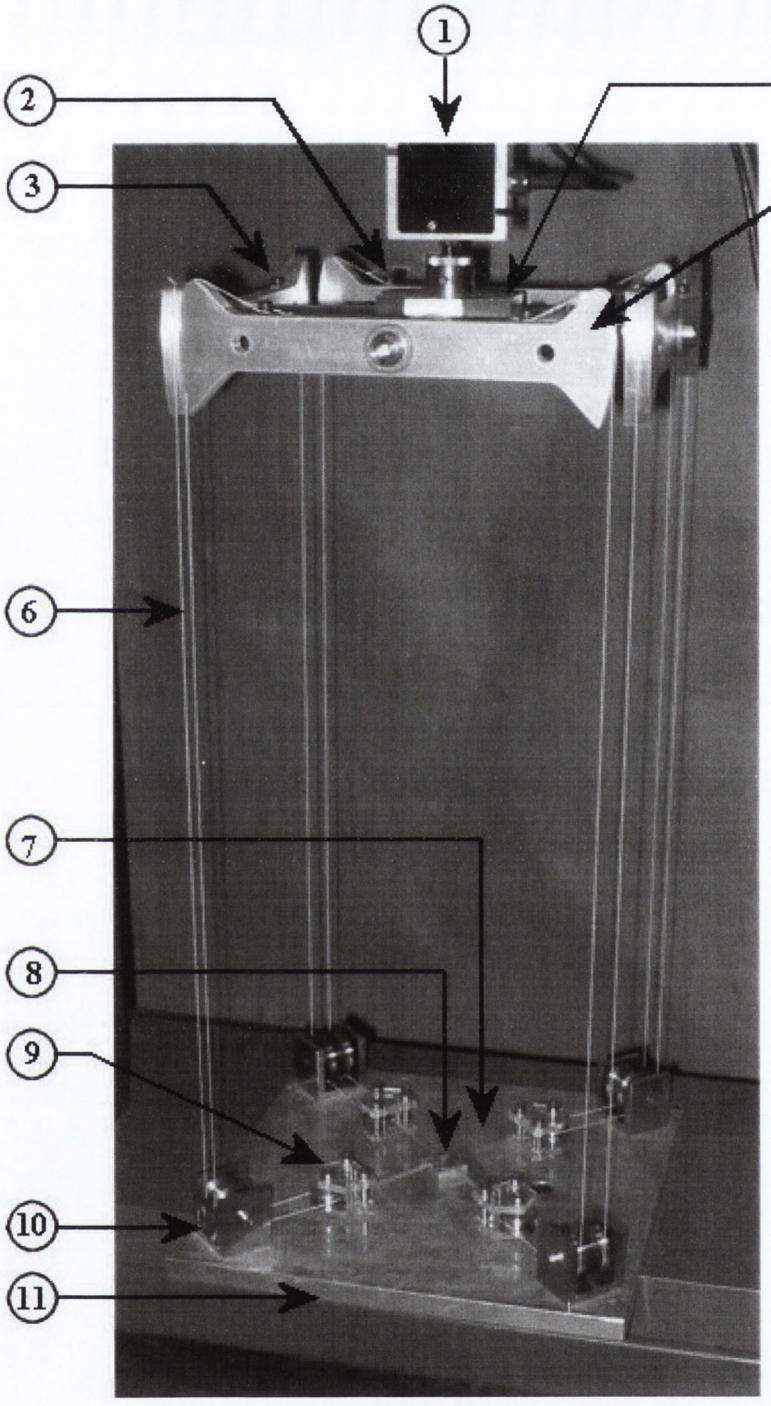

1) **Load cell**
2) **Initial connection point of tension line to balance beam**
3) **Final connection point of tension line to balance beam**
4) **Central block**
5) **Rotating beams**
6) **High strength thread tension lines**
7) **Threads with hooks at ends**
8) **Tissue test specimen**
9) **Loading bracket**
10) **Pulley bracket**
11) **Base plate**

Figure 3.1 *The equibiaxial testing device.*

A 3 × 3 array of dots was printed on the inner surface of the blood vessel using a rubber stamp and water resistant, oil-based, quick drying ink. A typical such sample is shown in Figure 3.2. The distance between each dot was approximately 5 mm. Two crocodile clips were attached at each side as shown in Figure 3.2. The clips were adjusted to ensure that each jaw remained firmly locked during the test.

The sample was then placed in the centre of the rig and the metallic clips hooked between the Perspex loading brackets and the crocodile clips. The crosshead of the Instron was advanced until any slack was eliminated from the specimen. The tests were stopped when tissue tearing or slippage began at the jaws of the crocodile clips.

A high-resolution colour digital camera (JAI CV-950, Vortex Vision, UK) mounted above the test specimen was used to take images of the tissue at one second intervals during the test. Each image was edited to remove the background and to isolate the markers. The image was then thresholded and brought into UTHSCSA Image Tool (University of Texas).

The strain of the tissue in the principal directions was then determined from the movement of the centroid of these four central dots on the specimen from picture to picture as the load increased. The first step in calculating the engineering stress was to divide the load cell reading by two, to determine the load in each of the principal directions. The load in each principal direction was then divided by the initial cross-sectional area. The cross-sectional area was taken as the product of the gauge length and the thickness of the sample. The gauge length was taken as the distance between the ends of the crocodile grips, determined using image analysis, and was averaged for the two principal directions.

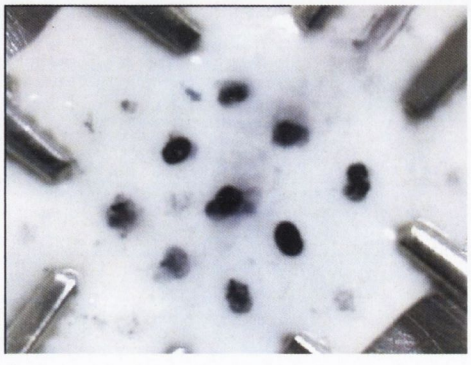

Figure 3.2 *Close-up view of a human femoral biaxial specimen with the array of dots used to measure stretch, and the crocodile clips used to clamp the tissue.*

3.2.2 Porcine coronary arterial tissue tests

Porcine left, right and circumflex coronary arteries were harvested within 3 hours of death from the hearts of adult domestic pigs, which were obtained from an abattoir. The arteries were stored in an antibiotic solution at 4°C prior to testing to preserve the tissue properties, and were tested within 4 weeks of harvesting. All samples were prepared under sterile conditions, and any visible loose connective tissue was removed from the surface of the vessel before it was cut along its length using a coronary artery scissors, pressed flat gently by hand, and sectioned. Longitudinal rectangular shaped strips of tissue were prepared for uniaxial testing and 5 mm square samples were prepared for biaxial testing. The thickness of tissue adjacent to each sample was measured after mounting the specimen on a glass slide and by viewing the edge of the sample under a microscope fitted with an eyepiece with a digital measuring graticule. The tissue thickness was recorded at three different locations along the edge of the sample and an average taken. The mean standard deviation of the three thickness measurements for each individual sample was 0.06 mm. Sections 3.2.2.1 and 3.2.2.2 below outline the details of the uniaxial and equibiaxial tensile testing of this tissue type. In both tests a strain rate of 60% min^{-1} was used. Specimens were continuously irrigated with 0.9% saline solution during testing and tests were carried out a room temperature.

3.2.2.1 Uniaxial testing

Pneumatic grips, the gripping faces of which were covered with emery paper to prevent slippage during loading, were mounted on a Zwick Z005 displacement controlled tensile testing machine. Nine samples from nine different pigs were tested. Each test section was cut to a width of 3.5 mm using a custom-made cutter comprising of two scalpel blades 3.5 mm apart and loaded in the longitudinal direction. Extension of the specimen was taken to be the crosshead displacement. Preconditioning of the samples was carried out to a maximum load of 1 N at a strain rate of 60% min^{-1} of the initial gauge length, determined at a preload of 0.05 N. Five preconditioning cycles were performed and a steady state was reached where no further change occurred in the material stress-stretch curve after the five cycles. A strain rate of 60% min^{-1} was used to test the sample to failure after the preconditioning cycles. The tests were stopped when tearing began at either the grips

or along the length of the specimen. The stress was determined by dividing the instantaneous load by the original cross sectional area. The stretch was obtained by dividing the instantaneous length by the original length. The original length of each specimen was taken as the gauge length after test specimen preconditioning, and at a load of 0.05 N.

3.2.2.2 Equibiaxial testing

The same equibiaxial test rig as that described in Section 3.2.1.2 was used to test the porcine coronary arterial tissue specimens. It was mounted on a Zwick Z005 testing machine and the significantly smaller size of the test specimens necessitated a number of modifications to the test set-up. High strength thread was used for the cable network, as the loads were much lower than those applied in the equibiaxial tests on human femoral arterial tissue.

The loading bracket transferred the load from the line to the specimen via threads of equal length with fishing hooks attached. For small tissue specimens, these hooks proved superior to the crocodile grips used to grip the larger human femoral specimens in Section 3.2.1.2 above. Four fishing hooks were attached to each side of the square test specimen, as shown in Figure 3.3.

A specially designed gripping jig was used to ensure that the hooks were placed an even distance apart when gripping the small tissue specimens, see Figure 3.4.

(a) 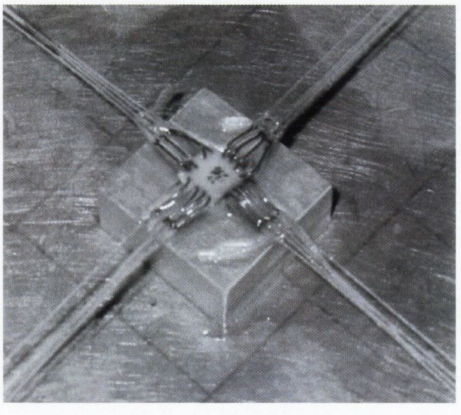 **(b)** 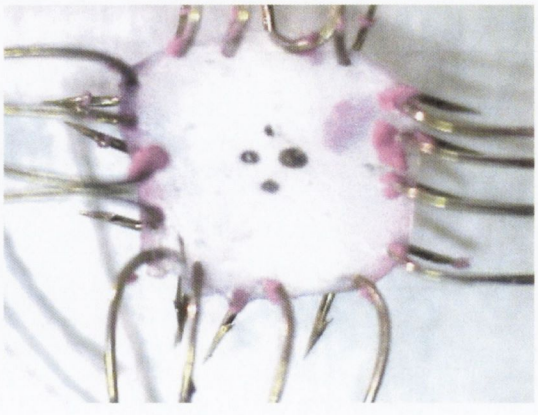

Figure 3.3 *Close-up view of a biaxial test specimen (a) illustrating the fishing hooks used to grip the tissue and (b) illustrating the strain measurement markers.*

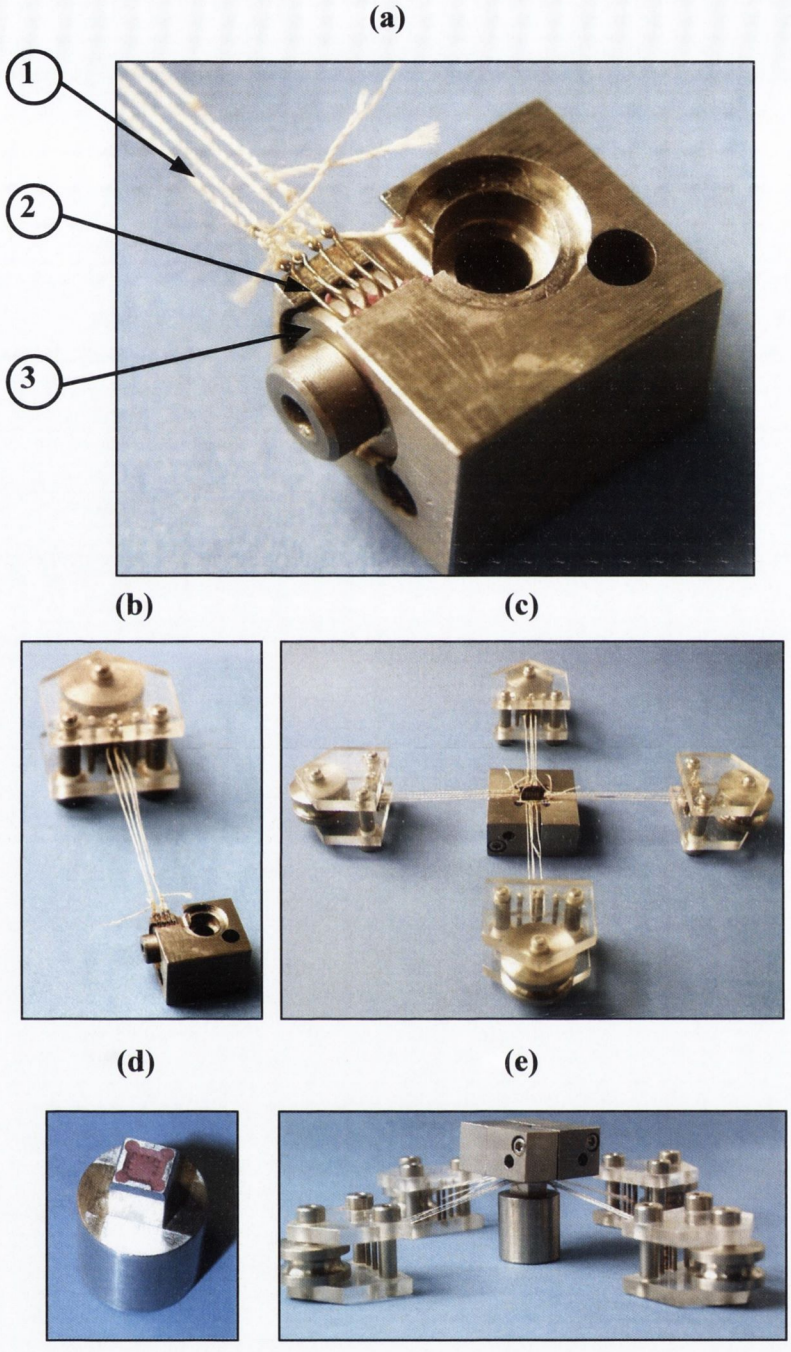

Figure 3.4 *The biaxial test specimen gripping jig; (a) Individual gripping block illustrating: 1. Threads from loading bracket, 2. Hook placement and 3. hook spacers, (b) Loading bracket and gripping block, (c) The four gripping blocks together, (d) Tissue platform, (e) Gripping jig fitted over tissue platform to place hooks in tissue.*

The gripping jig comprised of four identical gripping blocks. Four hooks, which were attached to a loading bracket via threads, were placed in each block and tightened into position using four stainless steel spacers an equal distance apart, see Figure 3.4(a) and Figure 3.4(b). The blocks were tightly screwed together such that all of the hooks faced upwards, Figure 3.4(c). The square tissue specimen was then placed on a custom-made stainless steel platform, shown in Figure 3.4(d). The gripping jig was pushed down over the platform and the hook spacers released to allow the hooks to remain in the tissue, see Figure 3.4(e). The loading brackets, with the gripped tissue specimen, were initially placed at set marked positions on the base plate. This ensured that each pair of brackets was lined up to load the tissue in the circumferential and longitudinal directions only and the specimen was in the centre of the base plate. The load reading on the load cell was corrected to account for the load required to pull the pulleys (0.5 N).

Eight specimens taken from five different pigs, each 5 mm square, were cut from arteries using a custom-made cutter comprising of two scalpel blades 5 mm apart. Each sample was marked using vegetable dye to indicate its *in vivo* circumferential/longitudinal orientation. Arterial tissue has been identified as a curvilinear orthotropic material such that stresses in the circumferential, longitudinal and radial direction produce only normal strains [Weisacker and Pinto, 1988]. As a result these directions were taken as the principal directions and a no-shear condition was assumed in all other directions. For biaxial testing, dots were printed on the inner surface of the blood vessel using a pin and water resistant, oil-based, quick drying ink. A typical such sample is shown in Figure 3.3 (b). Preconditioning of the samples was carried out to a maximum total load of 0.5 N at a strain rate of 60% min^{-1} of the initial gauge length. Five preconditioning cycles were performed, see Figure 3.5. After preconditioning, the tissue was loaded to failure at a constant strain rate of 60% min^{-1} of the initial gauge length. Testing was stopped when the tissue began to tear at the fishing hooks. The test specimens were moistened throughout the test with 0.9% saline solution.

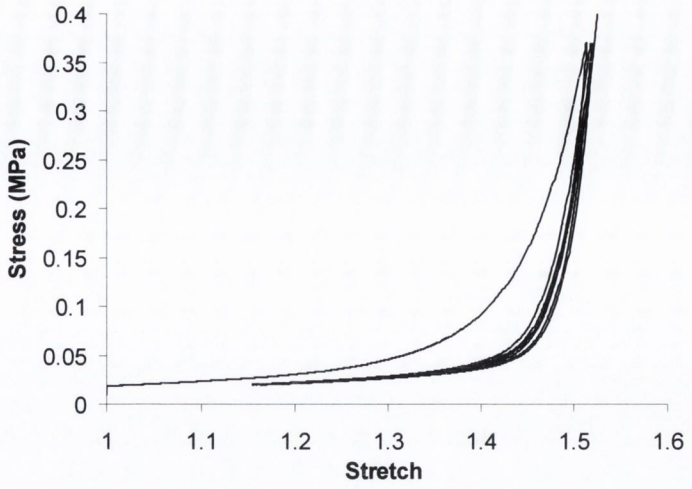

Figure 3.5 *A typical preconditioning curve showing the reduction in the hysteresis loops during five preconditioning cycles.*

As with the femoral arterial tissue test, a digital camera mounted above the test specimen was used to take an image of the tissue every second during the test. Each image was thresholded in Scion Image (Maryland, USA) and the vertical and horizontal distance between two pairs of central markers was determined for each image. The strain of the tissue in the principal directions was then determined from the increase in distance between the markers on the specimen, in both the vertical and horizontal directions, from picture to picture as the load increased. The engineering stress was calculated by dividing the load cell reading by two, to determine the load in each of the principal directions. This load value was then divided by the initial cross-sectional area of the specimen. Each cross sectional area was taken as the product of the gauge length in each principal direction and the thickness of the specimen. The gauge length was taken as the distance between the hooks in the direction orthogonal to the loading direction and an average value was found for the two principal directions using image analysis.

3.3 Mooney-Rivlin constitutive model

Since the objective of this study is to provide a means to preclinically test intravascular stents, it is important to use a material model which includes the key features of arterial tissue including its stiffening non-linearity, incompressibility and the capability to undergo large deformations. As reviewed in Chapter 2, Section 2.5.2,

much work has been done on developing complex constitutive models capable of describing arterial tissue. However, ease of implementation of the numerical model within various commercially available finite element codes is also a necessary feature of any preclinical test. The Mooney-Rivlin model, or a derivative of it, is a widely available hyperelastic material model and is included in most finite element analysis software codes. The hyperelastic constants, a_{ij}, in the strain energy density function, for a specific Mooney-Rivlin constitutive material model, are calculated by using a regression routine to obtain the best fit to experimental test data for a non-linear, incompressible elastic material such as arterial tissue.

The third order Mooney-Rivlin strain energy function W given in the Literature Review (Eqn. 2.9) can be reduced to obtain the special case of the third order deformation hyperelastic model whereby the strain energy density function is given by:

$$W = a_{10}(I_1 - 3) + a_{01}(I_2 - 3) + a_{20}(I_1 - 3)^2 + a_{11}(I_1 - 3)(I_2 - 3) + a_{30}(I_1 - 3)^3 \qquad (3.1)$$

A non-linear regression routine to determine the parameters, a_{ij}, of the third order deformation model is available in Marc/Mentat (MscSoftware, Santa Ana, CA, USA) so as to obtain the model that best fits both the uniaxial and equibiaxial data. The least squares error to be minimised during data fitting can be based on absolute or relative errors and are defined as follows [Marc/Mentat manuals]:

$$\text{Relative error} = \sum_i \left[1 - \frac{\text{data measured}(i)}{\text{data calculated}(i)} \right] \qquad (3.2)$$

$$\text{Absolute error} = \sum_i [\text{data measured}(i) - \text{data calculated}(i)]^2 \qquad (3.3)$$

To determine the hyperelastic constants, one uniaxial and one equibiaxial stress-stretch curve were input into Marc/Mentat and the constants of Eqn. 3.1 established using the non-linear regression routine for both absolute and relative error to fit to the data. The constants, a_{ij} of Eqn. 3.1, that yielded the closest stress-stretch behaviour to that of the experimental data were determined. In some cases it may be

found that the predicted non-linear elasticity is unaffected by a particular hyperelastic constant and therefore that constant is redundant and may be set to zero.

However, it is important to ensure that the uniaxial and biaxial data fits produce curves which are positive definite as well as the best fit to the data. In many cases the curves are not positive definite on extrapolation beyond the experimental data in which case it may be necessary to constrain the hyperelastic constants to have only positive values [Truesdell, 1952]. Alternatively, a lower order model may be used to determine a constitutive model which best fits the data, if the higher order model is not suitable. A second order model, the Signiorini model, is also available in Marc/Mentat [James *et al.*, 1972]. It is a reduced form of the third order deformation model whereby the strain energy density is given by:

$$W = a_{10}(I_1 - 3) + a_{01}(I_2 - 3) + a_{20}(I_1 - 3)^2 \tag{3.4}$$

The constants for this model were also established in cases where the third order model given in Eqn. 3.3 did not yield a constitutive equation which remained positive definite on extrapolation beyond the range of the experimental data.

3.4 Damage accumulation within coronary arterial tissue

3.4.1 Experimental set-up and arterial tissue preparation

Porcine coronary arterial tissue was tested to ascertain damage accumulation under cyclic loading. Porcine coronary arteries are anatomically similar to that of humans and, in fact, the porcine circulatory system is a more similar animal system to that of humans than any other animal [Swindle, 1992]. In addition, porcine coronary arterial tissue is easily obtained.

The porcine coronary arterial tissue was obtained from the abattoir and prepared in the same way as that described for the uniaxial tests in Section 3.2.2. However, for these tests the arterial tissue was punched into dog-bone shaped test specimens using a punch as shown in Figure 3.6.

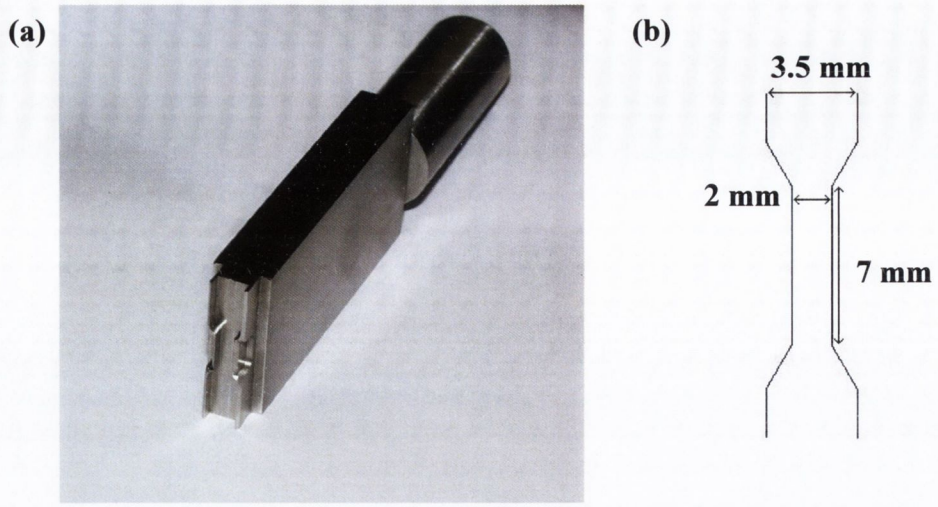

Figure 3.6 *(a) The punch used to obtain arterial test specimens in a dog-bone shape, and (b) the shape and dimensions of the arterial test specimens.*

The reason for this particular shape, rather than rectangular shaped specimens, is to prevent premature failure of the sample occurring at the grips due to high stress concentrations. This is a common occurrence in soft tissues and was also found to occur during tensile and fatigue tests of tendons [Ker and Zioupos, 1997]. The dog-bone shaped specimens result in a more homogenous distribution of stress across the sample and therefore usually result in failure of the sample in the central narrower region. In addition, the tabs at the ends of each specimen were gripped with clamps coated with emery paper to increase the maximum tensile force that could be obtained before slippage of the tissue specimens in the grips.

The remainder of the artery, after punching out the test specimen, was used to determine the thickness of the sample. The thickness of tissue adjacent to each sample was measured after mounting the specimen on a glass slide and by viewing the edge of the sample under a microscope fitted with an eyepiece with a digital measuring graticule. The tissue thickness was recorded at three locations along the edge of the sample and an average taken. The mean standard deviation of the three thickness measurements for each individual sample was found to be 0.06 mm. The test specimen grips consisted of a top plate fixed to a bottom base plate, with the artery placed between them, see Figure 3.7.

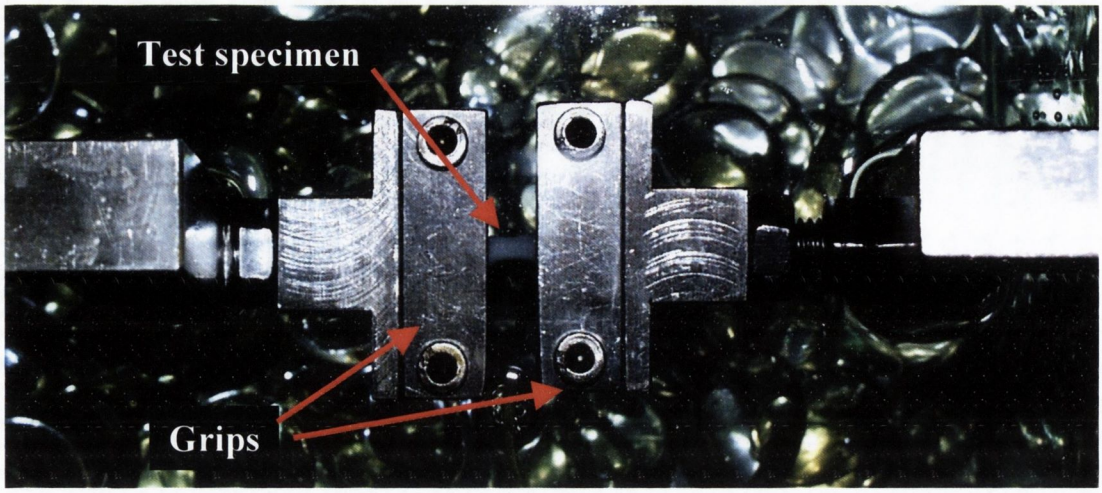

Figure 3.7 *The two stainless steel grips with a specimen gripped, viewed from above.*

The tensile and fatigue testing machine used for these tests was a MTS Tytron 250, which has a pneumatic actuator and a 250 N load cell. Two bridges were attached to the load cell and the actuator and a grip attached to each to allow the test specimens to be immersed in a custom-built glass water tank, see Figure 3.8. The load cell was aligned with the actuator and the grips were placed horizontally at equal heights, as shown in Figure 3.8.

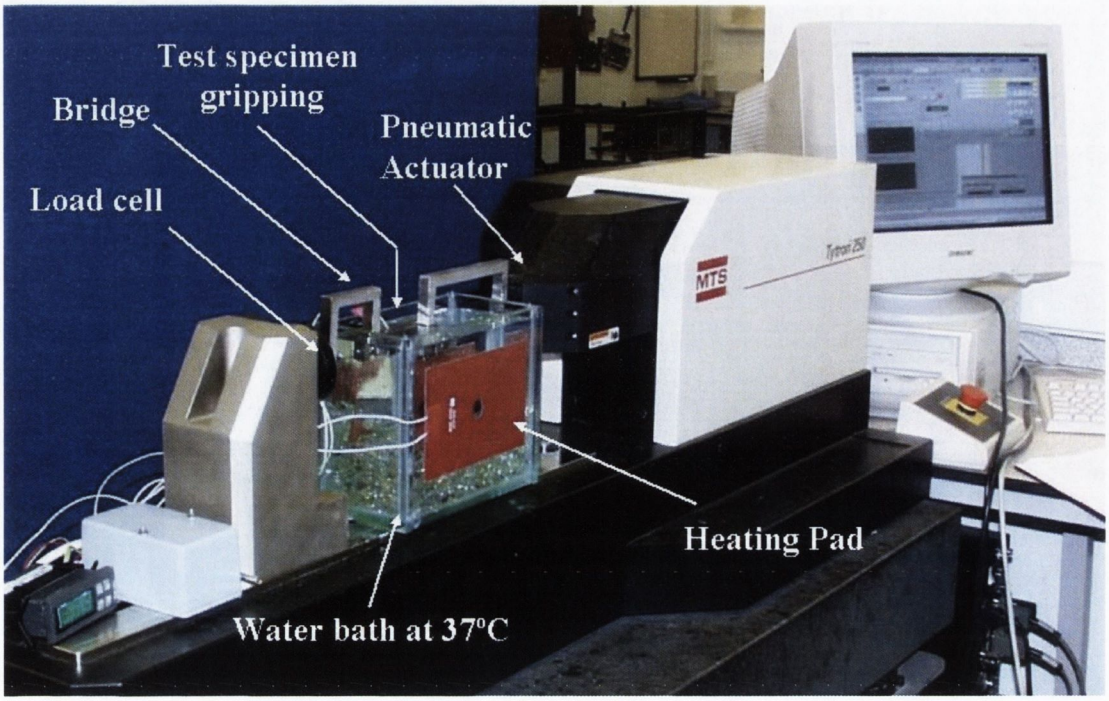

Figure 3.8 *The tensile and fatigue testing experimental set-up.*

The water bath was filled with 0.9% saline solution. The test specimen and clamps were immersed in the bath. Stainless steel was used for the clamps and bridges to prevent corrosion. The temperature of the solution was maintained at 37°C, i.e. body temperature, by two heating pads placed on the sides of the water bath. To reduce the quantity of water in the tank it was partially filled with glass stones (these are visible in Figure 3.7) with the same heat conducting properties as the water tank.

3.4.2 Tensile tests to obtain the ultimate tensile strength of porcine coronary arterial tissue

Using the test set-up outlined in the previous section tensile tests were carried out to determine the ultimate tensile strength (UTS) of the arterial tissue. In order to set the maximum and minimum loads in the fatigue tests, the UTS of the tissue was determined. Since coronary arterial tissue is a visco-elastic material the specimen had to be preconditioned before each tensile test. Five preconditioning cycles with a displacement of 0 to 3 mm were performed; five were chosen because a steady state was reached where no further change occurred in the material stress-stretch curve. The Tytron testing machine cannot be changed from displacement control to force control until a minimum load of 0.3 N is reached. Therefore the preconditioning limits had to be set as displacement limits rather than force limits.

Before preconditioning, an initial preload of 0.03 N was applied to the tissue, to ensure the tissue was in tension. The initial length of the test specimen was measured using a Vernier calipers. Twelve arterial specimens were tested. The tissue was tested at a constant strain rate chosen to be 60% min^{-1}.

After preconditioning, the specimen was stretched to failure at 60% min^{-1} strain rate. The stress level at which the specimen failed was recorded as the ultimate tensile strength (UTS) of the tissue. The water bath was not used for these tests as it was found not to influence the UTS of the tissue. Given the short duration of the tensile tests, the test specimens were easily kept moist by dropping 0.9% saline solution on the samples during the tests, which were carried out at room temperature.

3.4.3 *Fatigue tests to determine the rate of damage accumulation within porcine coronary arterial tissue*

Fatigue tests of longitudinal segments of the porcine coronary arterial tissue were performed to determine the S-N curve of arterial tissue. The MTS Tytron with the experimental protocol described above was used. The test specimens were placed in the water bath filled with 0.9% saline solution, maintained at 37°C, for 15 minutes before starting the test and remained immersed in the bath during the tests. As in the tensile tests, the initial length of the specimen was measured at a preload value of 0.03 N. The distance between the grips was determined using a microscope. The pneumatic actuator of the MTS Tytron requires tuning to adaptively compensate for the stiffness of the material being tested (See MTS Tyron 250 manual). It is therefore necessary to establish different tuning parameters for different materials, and the tuning value is input into the MTS test software. Tuning of the MTS Tytron was carried out for each individual specimen before the fatigue test on the specimen was done. The loading frequency was 1 Hz.

The fatigue tests were performed at three stress levels. The loading levels were percentages of the UTS, which was determined based on the results of the tensile tests described in section 3.4.2 above. The loading levels were 10%-20%, 10%-30% and 10%-40% of the UTS. Nine test specimens were tested at each of these load levels.

The tests were run until the test specimen failed by tearing or until the machine started to oscillate. The actuator of the fatigue testing machine mainly oscillated during tests that ran for many hours. During these tests the stiffness of the arterial tissue alters, presumably due to the accumulation of damage. The consequence of this change in stiffness of the arterial tissue is that the tuning values of the specimen become less accurate resulting in oscillations of the machine and hence failure of the sample. These samples are included in the data set, since the material stiffness altered sufficiently for the machine to oscillate and hence the tissue stiffness had reduced sufficiently that it can be assumed to have failed.

At any stage in the fatigue test, a stiffness ratio, s_r, which has been previously defined for tendons by Ker and Zioupos [1997], can be defined as:

$$s_r = \frac{s}{s_0} = \frac{E}{E_0} \tag{3.5}$$

where s_0 and E_0 are the initial values of stiffness and Young's modulus, respectively and s and E are the instantaneous values of stiffness and Young's modulus, respectively. Ker and Zioupos [1997] further defined the following:

$$D = (1 - s_r) \tag{3.6}$$

where D denotes the fractional reduction in stiffness and may therefore be considered a measure of damage.

However, following Miner's rule [Miner, 1945] the number of cycles to failure at different stress levels also indicates damage is accumulating within the tissue and ultimately causing failure. In fact, the S-N (stress versus number of cycles to failure) curve for the arterial tissue may also be used to get a measure of the rate of damage accumulation within the coronary arterial tissue under cyclic loading.

In conclusion, the results of these tests will show whether or not arterial tissue accumulates damage under cyclic loading. In addition, the number of cycles applied to the tissue before failure of each specimen, at each loading stress amplitude, enables an S-N curve for porcine coronary arterial tissue to be obtained, and the S-N curve can be used to compute the rate of damage accumulation within the tissue under cyclic loading at different stress levels.

3.5 Finite element models of stenting procedures

3.5.1 Introduction

This section describes the finite element modelling approach used to compute the stress in a stented vessel, and hence to investigate the degree of injury caused to a vessel by a stent. Models of repeatable units of different stent designs were developed which enabled the magnitude of tissue prolapse within four different stent designs to be quantified and an estimation of the stresses around the stent units to be determined.

Full three-dimensional models, which incorporated contact between the stent and the artery were then developed to assess more realistically the stress levels induced within stenosed coronary arteries scaffolded open by three different stent designs.

To generate these numerical simulations the finite element method requires a number of inputs; the geometry and material properties of the stent and blood vessel, and appropriate loading conditions to simulate the stenting procedure, all of which are described in detail below.

3.5.2 An investigation of the degree of tissue prolapse within different "repeating unit" designs

To establish the magnitude of tissue prolapse within different stent designs, the geometry of one repeating unit of the fully expanded stents was determined. The finite element model geometry is of the area of arterial tissue scaffolded by each stent repeating unit. The stent measurements were obtained by taking pictures of the fully expanded stent under a LEICA MZAPO microscope using a JVC digital ½ inch colour CCD camera and LEICA QWIN standard software. A line of known length was incorporated into each image. The line length was determined from a calibration plate used with the microscope. The images were imported into WINDIG where coordinates to define the cell area of each stent were obtained by defining points on the stent wire. The coordinate values were then imported into ANSYS Version 5.5 (Canonsburg, PA, USA) and projected onto a 3.5 mm diameter cylinder to define the geometry of one repeating unit of each stent design. Four stent designs were analysed: (BeStent 2, *Medtronic AVE*; NIR, *Boston Scientific*; VELOCITY, *Cordis;* and the TETRA, *Guidant*), see Figure 3.9.

Three-dimensional finite element models of arterial tissue within four different stent designs were generated numerically using ANSYS. The area defining the tissue within one unit of each stent design was extruded in the outward normal direction. The element used was a 3D 8-noded isoparametric element (HYPER58, a mixed U-P hyperelastic solid element). Eight elements were employed through the thickness of the vessel wall. This choice was made based in the results of a mesh convergence study (see Appendix C). The thickness of the arterial tissue in the numerical studies was taken as 0.5 mm, based on the average thickness of the human coronary artery wall [Burton, 1962]. Fig. 3.9 shows the finite element mesh of each of the four repeating units.

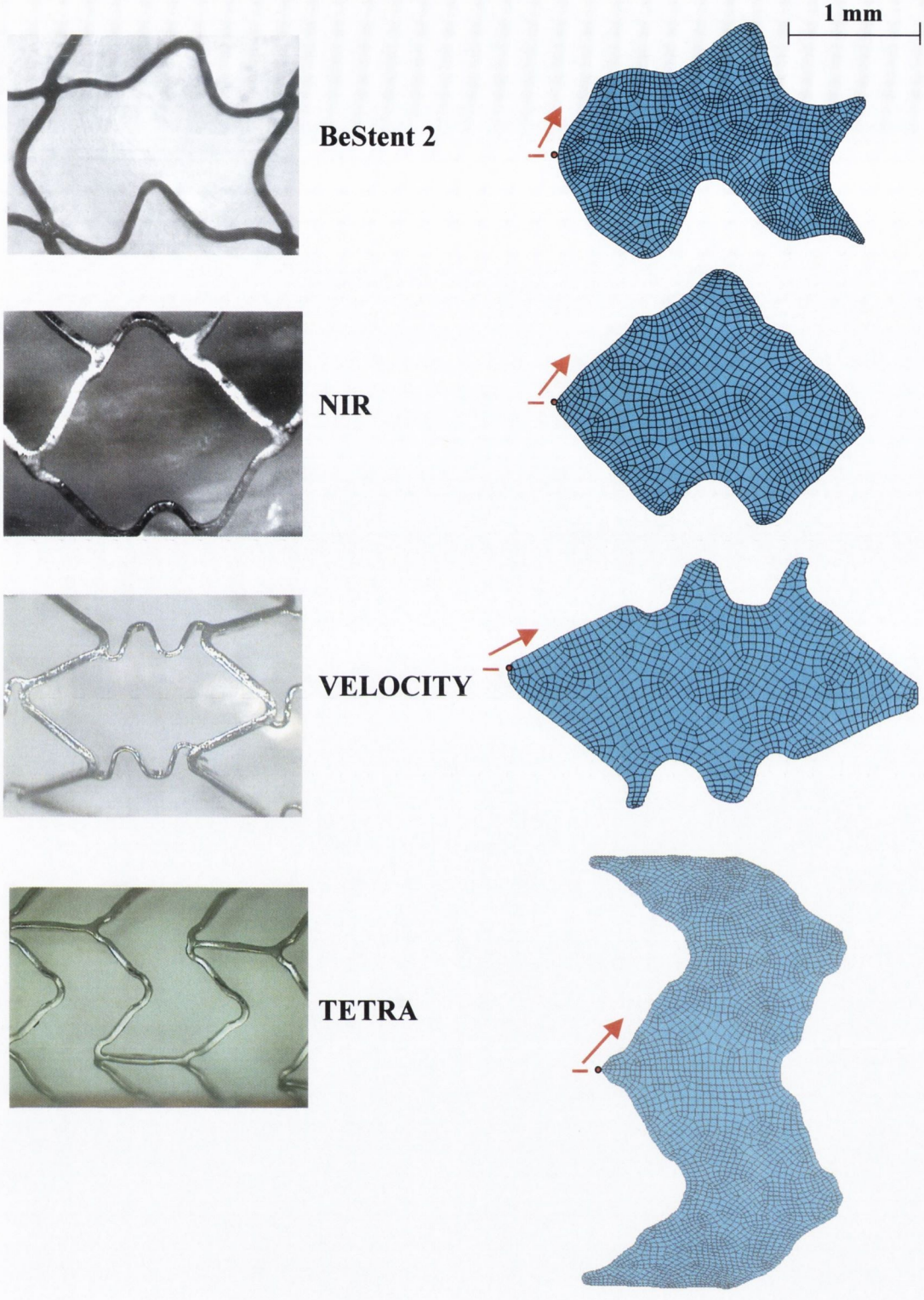

Figure 3.9 *Four types of stent analysed; (BeStent 2, Medtronic AVE; NIR, Boston Scientific; VELOCITY, Cordis, and TETRA Stent, Guidant). The arrow indicates the direction and the start point from which the distance around the periphery of the stent is taken for reporting the stress (Given in the Results Chapter (Section 4.4.1), Figure 4.18, page103)*

The mesh densities used were the following; BeStent 2: 12104 elements (14733 nodes); NIR: 8096 elements (10017 nodes); VELOCITY: 8112 elements (10080 nodes); TETRA: 23520 elements (28224 nodes).

The models were restrained around the edges of the stent repeating unit to represent the constraint of the stent wire. Such a restraint was considered to be adequate since the stent wire thickness (approximately 0.1 mm) is much less than the thickness of the tissue (0.5 mm). To simulate the *in vivo* deformation of the vessel wall around the stent wires (see Figure 3.10), consider that, in the ideal case, a cylindrical vessel [*c.f.* Figure 3.10 (b)] is deformed by the radial motion of the stent wires into a shape represented schematically in Figure 3.10 (c). The expanded vessel with a surface pressure applied to it will have a similar deformation to that illustrated in Figure 3.10 (c).

According to Serruys and Kutryk [1999], a maximum pressure a stent is expected to sustain *in vivo* is 450 mmHg (~60 kPa) and this value was applied to the outer vessel wall in the finite element model. The vessel wall was modelled using the Mooney-Rivlin hyperelastic constitutive equation established based on the uniaxial and equibiaxial tensile properties of human femoral arterial tissue. The constants for this Mooney-Rivlin hyperelastic constitutive equation are given in the Results Chapter (Section 4.2.3).

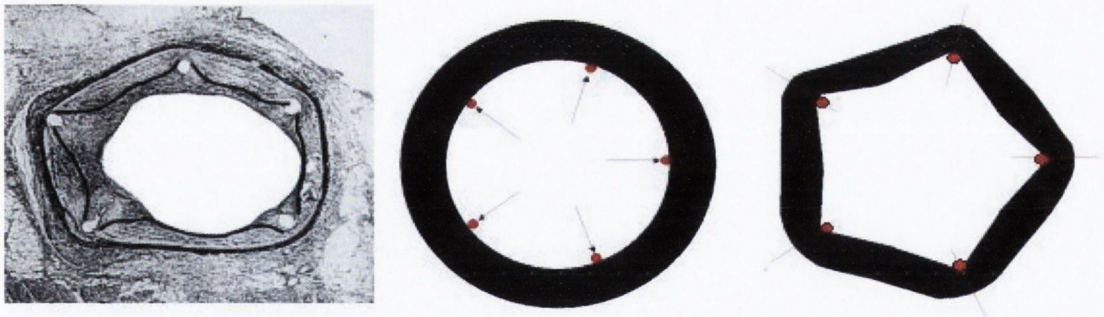

(a) **(b)** **(c)**

Figure 3.10 *(a) Luminal tissue prolapse within a stented vessel (indicated by black lines), taken from Schwartz et al.[1994], (b) A 2D schematic of a stented vessel before stenting with the vessel wall ideally cylindrical and (c) After stenting where the tissue drapes between the stent wires.*

3.5.3 Full three-dimensional models of stenting procedures

For the full three-dimensional models the finite element software used was MSC Marc/Mentat (Santa Ana, CA, USA). Although ANSYS was found to be adequate for the analyses described in Section 3.5.2 above, it was found not to be suitable for solving analyses that combined the use of a hyperelastic material and contact.

In the three-dimensional models the stent geometry had to be defined since the models include both the vessel and the stent and simulate the stenting procedure by modelling the contact between the two. The 3D geometry of the repeatable units of the fully expanded 3.5 mm diameter NIR and S7 stents was determined using the coordinate measurement technique outlined in Section 3.5.2. The thickness of the struts was 0.1 mm. Using the repeating unit geometry of each stent design solid models of the full stents were generated. A hypothesised 'simple' stent design was also developed and used to compare to the two commercially available stent designs.

The solid models initially generated of all three stents were of the stents in a planar state, i.e. the geometry of the stents if they were cut longitudinally and flattened out. The stent solid models was then meshed and wrapped into a cylindrical shape by transferring the nodal coordinates from a Cartesian coordinate system into a cylindrical coordinate system. In this way, finite element meshes were generated for each stent design as shown in Figure 3.11. The two commercially available stent designs differed greatly; the NIR is a slotted tube laser-cut stent with 7 crowns whilst the S7 is a modular stent with a circular cross-section, 10 crowns and welded joints. The 'simple' stent design is a slotted tube laser-cut stent with 5 crowns. 'Crown' is the term used by medical device companies to describe the number of circumferentially repeating units in a stent. All three stents had an outer diameter of 3.5 mm and an inner diameter of 3.3 mm (i.e. a wire thickness of 0.1 mm).

The stent material was modelled as isotropic linear elastic 316L stainless steel, with $E = 200$ GPa, $\nu = 0.3$. The element type used for the stents was a reduced integration, three-dimensional eight-node isoparametric arbitrary hexahedral element (Type 117 in Marc/Mentat).

The healthy vessel wall material in the models was modelled using the Mooney-Rivlin hyperelastic constitutive equation for human femoral arterial tissue whilst the hyperelastic constitutive model used to represent the plaque tissue of the vessel wall, representing the stenosis, was determined by fitting to published data for

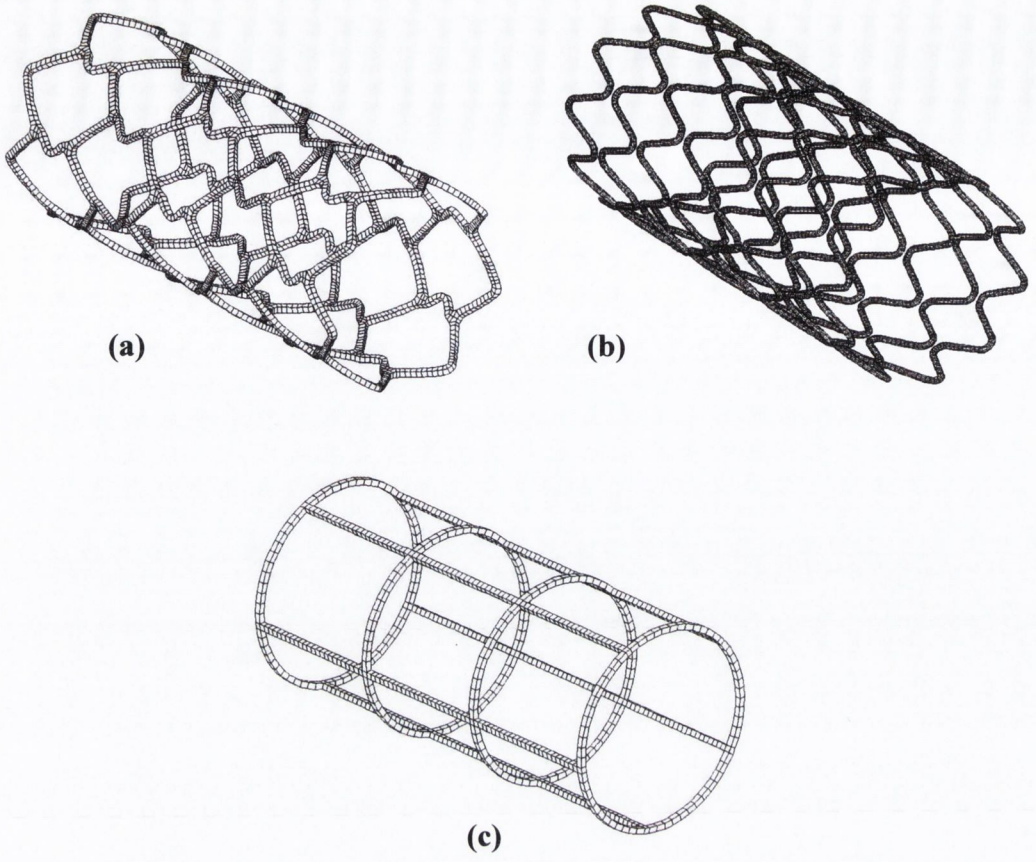

Figure 3.11 *Finite element meshes of the expanded stents; (a) NIR, (b) S7 and (c) the 'simple' stent design used for comparison purposes.*

human calcified plaques published by Loree *et al.* [1994]. The constants for both Mooney-Rivlin hyperelastic constitutive equations are given in the Results Chapter (Section 4.2.3). The vessel wall was represented by three different geometries for the stenting procedures simulated.

(1) The vessel was represented as a perfect cylinder with an inside diameter of 3 mm. The vessel thickness was taken as 0.5 mm, based on the average thickness of the human coronary artery wall [Burton, 1962], see Figure 3.12(a). Three elements were assigned through the thickness of the vessel wall, 91 along the length (6.5 mm) and 140 elements around the circumference of the cylinder.

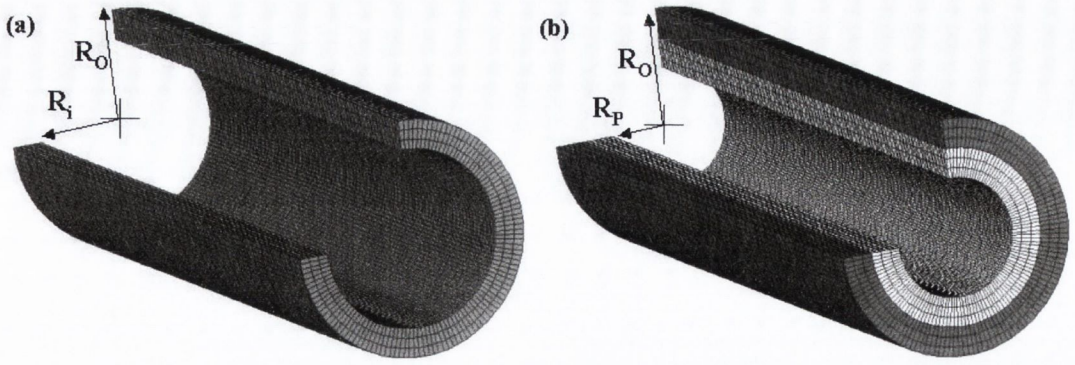

Figure 3.12 *Cylindrical coronary vessel geometries; Artery outer radius, R_O =2 mm, Non-stenosed artery inner radius, R_I =1.5 mm, Stenosis inner radius, R_P=1 mm. (One quarter of the vessel is cut away for visualisation)*

(2) The vessel geometry was represented by a perfectly cylindrical stenotic vessel, whereby the inner lumen diameter was 2 mm whilst the inner diameter of the healthy vessel was 3 mm and the outer diameter of the stenosed vessel was 4 mm, see Figure 3.12(b). The same mesh density was used for the circumference and vessel length as for the cylinder geometry described in (1) above with 6 elements assigned through the vessel thickness.

(3) The final vessel geometry was that of an atherosclerotic coronary artery with a localised stenosis. This was represented by a cylinder with an outside diameter of 4 mm and had a localised crescent-shaped axisymmetric stenosis with minimum lumen diameter of 2 mm, see Figure 3.13. The mesh density used for the cylinder was the same as that used in (1) above. 300 elements were used to represent the area of the crescent shaped atherosclerotic plaque which protruded into the vessel lumen whilst 140 elements were again used in the circumference.

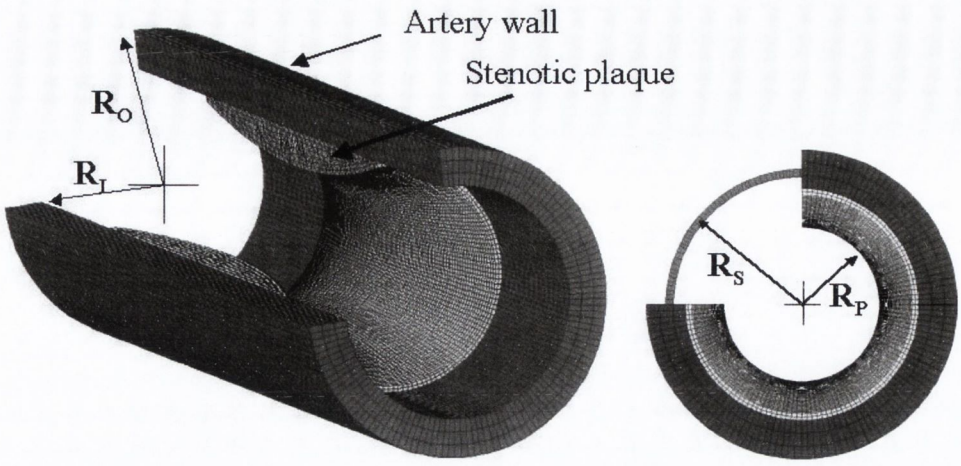

Figure 3.13 *Atherosclerotic coronary vessel geometry; Artery outer radius, R_O =2 mm, Non-stenosed artery inner radius, R_I =1.5 mm, Stenosis inner radius, R_P=1 mm, Stent radius, R_S = 1.75 mm. (One quarter of the vessel is cut away for visualisation)*

The element type used for the arterial tissue and atherosclerotic plaque was a full integration, three-dimensional eight-node isoparametric arbitrary hexahedral element (Type 7 in Marc/Mentat). Use of this element type to model large deformation hyperelastic materials necessitates the use of the updated Lagrangian framework in Marc/Mentat to solve for true (Cauchy) stresses and logarithmic strains in the updated configuration. To activate this method a combination of the following parameters is required: LARGE DISP, UPDATE, FINITE and CONSTANT DILATATION, which enforces the incompressibility condition necessary for a Mooney-Rivlin material.

For all three vessel geometries the loading and restraint conditions were applied to the stent-artery construct in two steps. It involved use of the feature that exists in Marc/Mentat (and many other finite element codes as well) that allows elements to be activated and deactivated during an analysis (called 'element birth and death'). In the first step, the stent elements were deactivated and the vessel was expanded to a diameter greater than that of the expanded stent by applying a sufficient internal pressure to the vessel. In the second step, the elements of the stent were activated and the pressure on the inner lumen of the artery was gradually reduced to a value of 13.3 kPa, corresponding to mean blood pressure of 100 mmHg. Due to the

elastic nature of the hyperelastic arterial tissue the vessel contracted around the stent with the stent behaving as a scaffold within the vessel.

Frictionless contact between the stent and the artery was assumed. The contact algorithm implemented in Marc/Mentat was the direct constraint method. In this procedure, the motion of the bodies are tracked, and when contact occurs, direct constraints are placed on the motion using boundary conditions – both kinematic constraints on transformed degrees of freedom and nodal forces. Deformable-deformable contact was used to describe the contact between the two contact bodies, i.e. the stent and the artery. Both contact bodies were mathematically defined as analytical (NURB) surfaces. This leads to a more accurate solution than using the individual element faces because the normal to the contact surface is recalculated each iteration based upon the current surface position.

A longitudinal stretch of 1.2 was applied to the arteries to simulate the longitudinal tethering observed on coronary arteries *in vivo* [Ogden and Schulze-Bauer, 2000; Weizsacker *et al.*, 1983]. The importance of applying longitudinal tethering on the vessel to model more accurately the material properties of the arterial tissue is discussed in detail in Appendix A. Analyses were solved of the stented cylindrical vessels both with and without tethering and the stresses generated within the vessel in each case obtained (see Results section, Figure 4.20, pg. 106). This demonstrated the effect of applying longitudinal tethering on the stresses induced in the artery wall.

Axial restraints were applied to one end of the vessel. During the analysis the stent was restrained at one node in the circumferential direction to prevent rigid body rotations. Because of cyclic symmetry it was not necessary to model the entire stented vessel but rather only segments of the stented artery had to be modelled. Using the cyclic symmetry capability in Marc/Mentat, the nodes on the two cyclically symmetrical faces were coupled or tied [Marc manual, Volume A: Theory and User Information, page 9-32]. This allows out of plane motion (unlike planar symmetry constraints) and was therefore valid for representing a cyclically repeating segment of the stented vessel (See Appendix D for a comparison of analyses using a complete model, a model using cyclic symmetry and one using planar symmetry constraints).

The NIR stent was represented by a cyclically repeating one-seventh segment whilst the S7 could only be represented by half cyclic symmetry due to the position of the welds on the stent. A cyclically repeating one-fifth segment represented the simple

stent design. The one-seventh segment of the NIR stent was adequately represented by 125 elements and 470 nodes. For the half model of the S7, 5040 elements and 9021 nodes were necessary to model the circular cross-section of the stent whilst only 62 elements and 252 nodes were necessary to represent the one-fifth segment of the simple stent design. The mesh densities given earlier for the vessel geometries describe the number of elements in the circumference for a full cylinder. Only cyclic segments of the stents were used and, as a result, a corresponding segment of the cylinder had to be used to represent the vessel wall. The element number in the circumference of the vessel meshes therefore reduced accordingly to one-seventh, one-half or one-fifth of the full cylinder mesh density for the NIR, S7 and simple stent designs, respectively.

The adaptive meshing capability within Marc/Mentat was used in all of the models for the arterial tissue to allow the mesh to adapt and refine at contact areas. This enabled the elements in the region of highest stress gradients to subdivide and the finer mesh allowed for more accurate stress and strain evaluation in these critical regions. The mesh adaptivity criterion was chosen based on obtaining a mesh refinement to adequately estimate the areas of high stress gradients around the stent struts, as well as maintaining the element number low in areas where the stress gradients were low and thus limiting the time to run the models.

3.6 Development of a computational model of in-stent restenosis

It has been argued in Chapter 2 that in-stent restenosis develops in response to injury, or damage, in arterial tissue. Therefore, the computational restenosis model is based on the hypothesis that this injury stimulates new material to be laid down within the artery. The development of damage within the stented vessel is a function of the stresses induced within the vessel wall. This can be calculated from a contact analysis simulating the stenting procedure as described above. Following methods used in mechanobiology (van der Meulen and Huiskes, 2002), an algorithm to simulate in-stent restenosis can be developed as an iterative process simulating, each day, the total distribution of new tissue formed, see Figure 3.14.

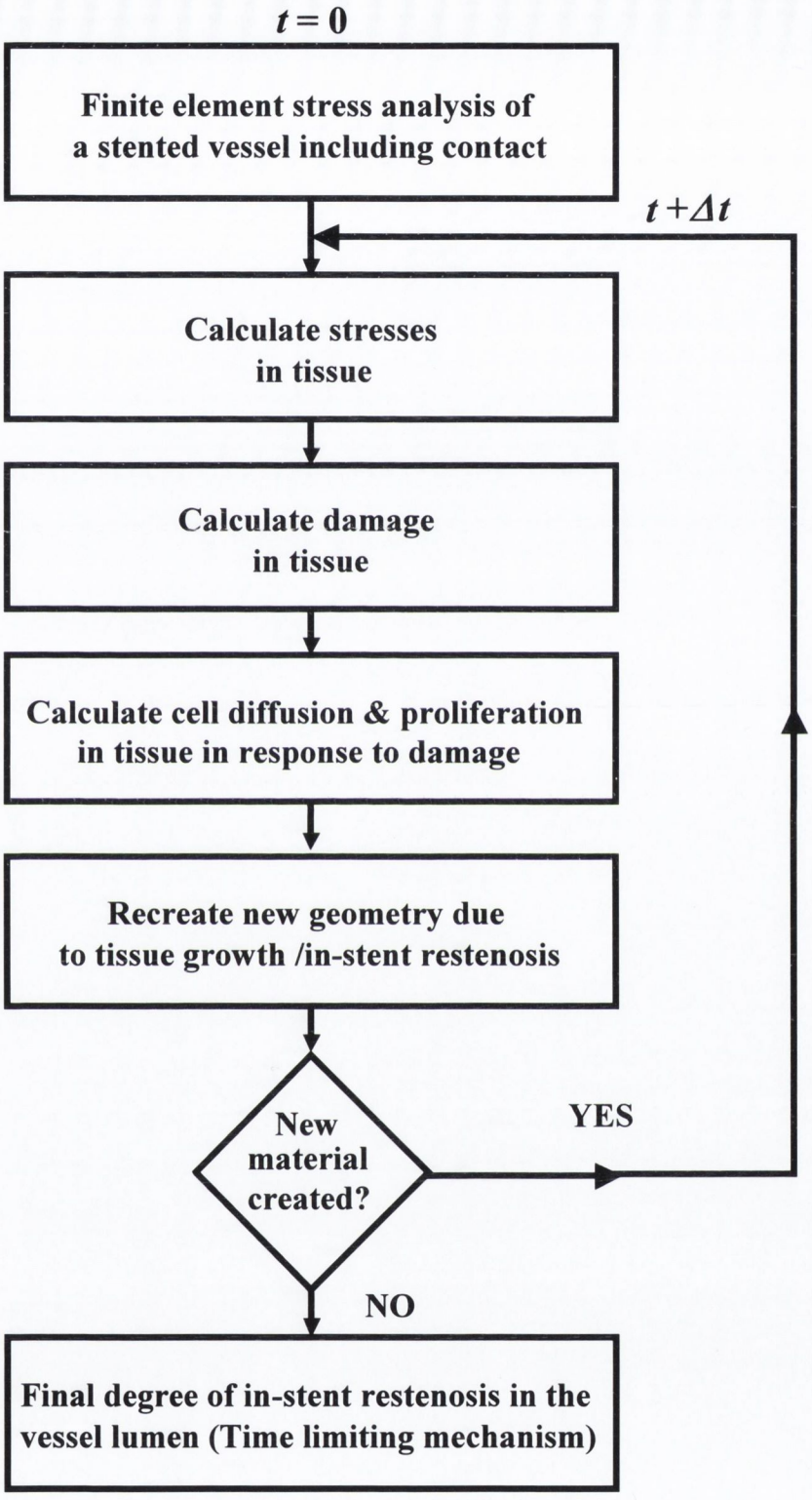

Figure 3.14 *The iterative process regulating in-stent restenosis; the stresses within the artery wall determine the level of damage in the tissue, and hence the degree of in-stent restenosis formed within the stented vessel.*

3.6.1 Restenosis algorithm - Mathematical description

A measure of damage within porcine coronary arterial tissue was determined using the data from the fatigue tests described in Section 3.4. The fatigue tests were used to determine the rate of damage accumulation within the arterial tissue of the stented vessel, $\dot{D}$, where from the S-N curve:

$$N_f = f(\sigma) \tag{3.7}$$

$$\dot{D} = \frac{1}{N_f} \tag{3.8}$$

where N_f is the number of cycles to failure from the fatigue tests and σ is the stress level at which damage is calculated.

The effect of the stress measure on the simulated restenosis was investigated by calculating a damage stimulus due to;

(i) the maximum principal stress magnitudes,

(ii) the minimum principal stress magnitudes,

(iii) both the maximum and minimum principal stress magnitudes separately and then summing the damage.

The maximum and minimum principle stresses were chosen as the damage inducing stimuli since they correspond to the maximum tensile and compressive stresses induced within the artery and, hence, they represent the circumferential and radial stresses, respectively. It is the elevation of these stresses beyond the baseline circumferential and radial stresses that are deemed to induce damage within the artery which then acts as the stimulus for restenosis.

Eqn. 3.8 assumes a linear relationship between damage accumulation and the number of cycles to failure (Miner's Law [Miner, 1945]) and has been used previously for bone adaptation studies [Prendergast and Taylor, 1994].

Let $\dot{R}$ be the repair rate, which may be considered to be the damage generation rate under physiological loading [Prendergast and Taylor, 1994]. Therefore,

$$\dot{R} = \dot{D}_{physiol} \tag{3.9}$$

$$\text{where } \dot{D}_{physiol} = \frac{1}{f(\sigma_{physiol})} \tag{3.10}$$

The accumulated damage, ΔD, will be the stimulus for in-stent restenosis. The accumulated damage is given by

$$\Delta D = \int_{t_0}^{t} (\dot{D} - \dot{R}) dt \ . \tag{3.11}$$

However, since the stress in the tissue surrounding a stent is an order of magnitude greater than the physiological stress (*c.f.* Chapter 4) we may write

$$\dot{D} >> \dot{R}, \tag{3.12}$$

and Eqn. 3.11 may be reduced to

$$\Delta D = \int_{t_0}^{t} \dot{D} dt \ , \tag{3.13}$$

It is acknowledged that integration here would increase the error introduced by ignoring the repair rate, $\dot{R}$. However, $\dot{R}$ would be very low at physiological stresses compared with the elevated stresses observed in stented vessels.
Eqn. 3.13 may now be put in numerical form as

$$\Delta D = \sum_{i=0}^{n} \dot{D}_i \Delta t \ , \tag{3.14}$$

but, since we may assume that the tissue is undamaged initially (i.e. at $t = t_0$), then

$$D = \sum_{i=0}^{n} \dot{D}_i \Delta t \tag{3.15}$$

It is assumed that the damage, *D*, stimulates cell proliferation. It is the proliferation of cells that creates the new volume of material observed as in-stent restenosis. The migration of the cells may be modelled using the diffusion equation [Murray, 1989]. If the number of cells in a region (e.g. a finite element) that is filling

with stenosis is denoted n, then the increase in the number of cells in that region is given by

$$\frac{dn}{dt} = \kappa \nabla^2 n + P(D) - K(D) \tag{3.16}$$

where κ is the diffusion coefficient of cells in arterial tissue, ∇^2 is the Laplace operator, $P(D)$ denotes the proliferation rate as a function of damage and $K(D)$ denotes the apoptosis/death rate of cells ~ in this case $K(D) = 0$. If a linear association between the damage and proliferation is assumed, then

$$P(D) = cD \tag{3.17}$$

where c is an empirical constant which relates the cell proliferation rate to the accumulated damage. Since c may vary between individuals, a number of different values were used in the restenosis model.

3.6.2 Restenosis algorithm – Implementation in finite element models

The diffusion coefficient, κ, in Eqn. 3.16 was calculated from the parameters published for human coronary in-stent restenosis in Hoffman *et al.* [2002]. Hoffman *et al.* [1999] obtained measurements at follow-up of the neointimal thickness in human coronary arteries stented with different stent designs, see Table 3.1. Given the area of the neointima and the number of days of neointimal growth, the diffusion coefficient for the cell migration was determined from the neointimal growth generated per day (per iteration in the model), i.e. the average neointimal growth was calculated to be 0.016 mm^2/day (Table 3.1). Therefore, the diffusion coefficient, κ, in the finite element models was set to 0.016 mm^2/day.

The constant, c, in Eqn. 3.17, was determined for each analysis such that the restenosis process was time limiting. This constant was uniquely determined for each of the three different measures of stimuli within the artery used to calculate the damage stimulus, i.e. it was different for (i) the maximum principal stress, (ii) the minimum principal stress, and (iii) combined maximum and minimum principal stress. However, the same value of c was used for the three different stent designs.

Stent	Inflow SS	Inflow Au	Multi-link	Palmaz-Schatz	NIR SS	NIR Au
Mean follow-up (months)	6.0	6.0	5.7	6.4	6.1	6.1
Mean IH CSA (mm^2)	3.1	3.7	1.8	2.6	2.9	3.4
IH Growth (mm^2/day)	0.0172	0.0206	0.0105	0.0135	0.0158	0.0186
Mean IH growth (mm^2/day)			0.016			

Table 3.1 *Neointimal growth following stenting. SS =Stainless steel; Au=Gold [Hoffmann et al., 2002].*

To model the ingrowth of tissue into the lumen of the vessel in the finite element model, a finite element mesh of 'deactivated' elements was created inside the vessel with elements that could be activated as restenosis progressed, see Figure 3.15. The deactivated grid within the lumen of the vessel defined the extent of the potential neointimal growth material. The material was initially deactivated in the model by setting the material stiffness low enough that it did not contribute to the structural behaviour of the vessel, E = 0.05 MPa. Elements of this restenotic tissue were activated if the number of cells within the element reached a critical value. This value was obtained by averaging the calculated cell densities, which have been reported for human restenotic specimens at several time points after balloon angioplasty [Schwartz *et al.*, 1996]. The average cell density value was found to be 1.93×10^3 cells/mm^2. It was assumed that cell density is uniform in all directions and therefore the cell density in the three-dimensional models was taken to be the square root of 1.93×10^3 cells/mm^2 cubed giving a critical value of cell number n of $n = 84.79 \times 10^3$ cells/mm^3. Activation was achieved by raising the Young's modulus to 1 MPa. This value was chosen to represent the stiffness of arterial tissue under low loads, as obtained from the uniaxial tensile tests on human femoral and porcine coronary tissue (see Results section, Figures 4.4-5, pg. 88)

A thrombotic layer (see Figure 3.15), which is a thin layer (0.1 mm thick) of tissue covering the inner lumen of the artery, was assigned as an active material immediately after stent placement to simulate the acute thrombotic response of a vessel to the presence of the stent [Edelman and Rogers, 1998].

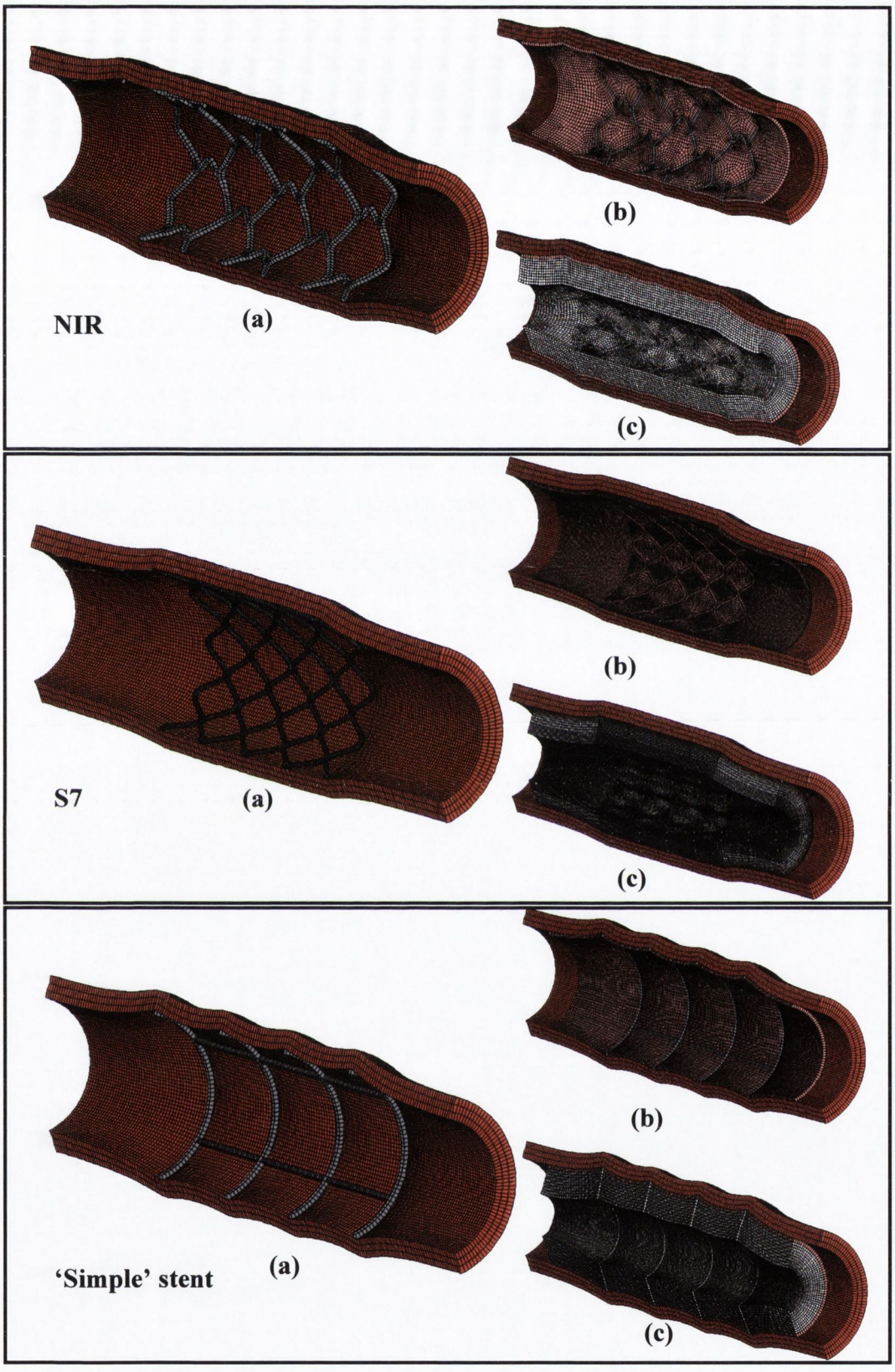

Figure 3.15 *(a) Segments of the stented vessels illustrating the thrombotic elements (pink) in (b) and the potentially restenotic tissue growth within the artery lumen surrounding the stent (white) in (c). (Pre-stented artery inner radius, R_I =1.5 mm, Artery outer radius, R_O=2 mm; Axial stretch applied to the artery, λ_z=1.2)*

3.6.3 Details of implementation in Marc/Mentat

The analyses were performed in Marc/Mentat (MscSoftware, Santa Ana, CA, USA) using the coupled thermal-mechanical job specification. This allows the cell diffusion, represented by temperature in the thermal analysis, to be coupled with the stress analysis of the stenting procedure. A separate routine was written to allow cell generation (modelled as a cell source) and diffusion to be damage dependant. Following the algorithm laid out in Figure 3.14, the finite element analysis was solved initially to determine the maximum and minimum principal stresses induced within the artery wall. The damage was then calculated using the *S-N* curve established from the fatigue data at that stress level, cells were generated according to Eqn. 3.17 and migrated and proliferated from areas of damage according to Eqn. 3.16. If the cell number within any of the deactivated elements reached the critical value of $n = 84.79 \times 10^3$ cells the element was activated. Once elements were activated there was then new material in the model and the stress distribution was altered. Therefore an iteration process is required, as shown in Figure 3.14.

The tissue in the thin thrombotic layer and the arterial tissue were the only sites of new cell generation in the first week of the time-course of the in-stent restenosis simulation. For the remaining time of the restenosis process in the simulation, i.e. 93 days, only cells in the thrombotic layer and the activated restenotic material within the lumen of the vessel were allowed to divide and proliferate. This was to simulate the migration of smooth muscle cells from the arterial wall into the lumen of the vessel, whereupon these cells proliferate and diffuse out further from areas of damage, as has been noted in studies of the in-stent restenosis mechanism [Edelman and Rogers, 1998]. Cells could migrate by diffusion through all of the materials at any time during the simulation. Cell concentrations in all of the materials were set to zero at the beginning of the simulation.

The restenosis algorithm applied a luminal pressure of 100 mm/Hg to the inner surface of the lumen, which would be the surface of the newly formed restenotic tissue if it had formed. This simulates the blood pressure. To apply this luminal pressure on the continually-changing inner surface of the active material, the user subroutine FORCEM was used. This subroutine looped through all element faces to determine the active elements and then applied the pressure to the inner surface of the active elements. To ensure that the pressure was not superimposed on the pressure

applied in the previous increment of the analysis it was necessary to use the total Lagrangian framework as opposed to the updated Lagrangian framework used in the previously described stenting analyses (Section 3.5.3). The element type used for the arterial tissue in the restenotic models was therefore a full integration, three-dimensional nine-node isoparametric hexahedral element with mixed formulation (Type 84 in Marc/Mentat). It is an eight-node, isoparametric element with an additional ninth node for the pressure. Use of this element type to model large deformation hyperelastic materials with the total Lagrangian framework in Marc/Mentat outputs second Piola-Kirchhoff stress and Green-Lagrange strain. Although the total Lagrange method is based on the initial element geometry, the incremental stiffness matrices are formed to account for previously developed stress and changes in geometry and when used with the FOLLOW FOR parameter, which ensures all distributed loads are on the basis of the current geometry, it yields the same results as the updated Lagrangian framework.

As with the FE stenting procedure outlined in Section 3.5, it was possible to represent the restenosis model of the NIR stent by a cyclically repeating one-seventh segment whilst the 'simple' stent design was represented by one-fifth segment. Due to the high mesh density required for the restenosis model of the S7 stent design, a cyclically repeating one-tenth segment, as opposed to half of the stenting procedure, was used to represent it. The circular cross section of the S7 stent required a higher mesh density and hence a high mesh density was required for the restenotic material, since the meshes of the two structures had to be compatible, see Figure 3.15. The mesh densities used for the simulations of restenosis are summarised in the following table:

Material	**NIR**	**S7**	**Simple stent**
Stent	136 elements 492 nodes	1152 elements 5932 nodes	62 elements 252 nodes
Restenotic tissue within each vessel	13746 elements 21488 nodes	45008 elements 53948 nodes	35078 elements 40248 nodes

Table 3.2 *Mesh densities of the stent and restenotic tissue in the in-stent restenosis simulations.*

The cylindrical artery was represented by 3 elements (0.5 mm) in the thickness and 91 in the length (6.5 mm). In the circumference of the cylindrical vessel, the element numbers used were 20, 14 and 28 to represent the one-seventh, one-tenth and one-fifth segments of the NIR, S7 and 'simple' stent designs, respectively.

The stent, and the restenotic material surrounding the stent, formed one contact body, whilst the artery formed the other contact body in the contact analysis. 'Glued' contact was used between the two deformable contact bodies. Cell movement was enabled across the interface of the two contacting bodies to simulate the migration of cells from the artery into the restenotic material. This was achieved by assigning a heat film on the outer contacting surface of each contact body. In fact, for a coupled thermal-stress analysis heat fluxes are automatically created on all the boundaries of the deformable-bodies and two film coefficients are assigned to each contact body. One corresponds to free convection and is used whenever the boundary is free. The other is a contact film, and is used whenever the boundary is in contact with another body. In these cases, the heat flux, q, across the interface is given by:

$$q = HD\,(TD - T) \tag{3.18}$$

where T is the surface temperature, HD is the film coefficient between the two surfaces and TD is the temperature of the same contact location, as obtained from interpolation of nodal temperatures of the body being contacted (Marc/Mentat user manuals; Volume A). A film coefficient of 200 W/mm^2 K was assigned to describe the heat flux between the two contact bodies and on the outer surface of the artery. This value was chosen to ensure that the cells generated at the site of arterial damage migrated into the lumen of the vessel. The number of cells (actually temperature in the finite element model) on the two surfaces in contact was the same and did not alter if HD was increased to greater than 200 W/mm^2 K. Using a lower value, however, would have meant that the cell number on the artery contact surface would have been higher than the contacting surface of the stent/restenosis contact body. Assigning the film coefficient on the outer surface of the artery at the adventitia enabled the cells to diffuse out in every direction and not to be stored in the artery. If the cells were not able to diffuse out at the free outer boundary of the artery a high concentration of cells would have been stored in the artery and would have had the ability to migrate into the intima long after the proliferation within the artery wall had ceased.

As regards material properties, the arterial tissue in the restenotic models was defined using the hyperelastic constitutive equation established for porcine coronary arterial tissue since the fatigue tests to measure damage accumulation were conducted on porcine coronary arterial tissue.

3.7 Summary

This chapter has detailed the methods used to investigate the performance of cardiovascular stents. Finite element modelling is to be used to simulate stenting procedures. The models include the important property that the vessel wall is non-linearly elastic. When this thesis began (2000) there was no satisfactory constitutive model of the non-linear elasticity of coronary arterial tissue presented in the literature; therefore, it was found necessary to conduct experiments, and the methodology for these experiments has been given in detail in this chapter. This experimental data will be used to construct a Mooney-Rivlin constitutive model in the next chapter. Most importantly in the context of this thesis, to investigate if stents can be designed to prevent in-stent restenosis, is the 'restenosis algorithm' which is presented in Section 3.6 of this chapter. This algorithm will be used in the following chapter to show that in-stent restenosis can be predicted in preclinical tests.

CHAPTER 4

Results

Contents

4.1 Introduction

This chapter begins with a description of the results from the uniaxial and equibiaxial tensile tests on human femoral arterial tissue and porcine coronary arterial tissue. From this data, hyperelastic models of these two tissue types are defined. The results obtained from the fatigue tests on porcine coronary arterial tissue are given.

Finite element models of stenting procedures, using the hyperelastic constitutive equation established from the experimental tests on *human femoral arterial tissue*, are then shown. As an initial approach to understanding the problem, the simplified finite element models of one repeating unit of four different stent designs are compared by computing the degree of tissue prolapse and the stresses surrounding the stent units. Next, the stresses induced within the vessel wall for the full 3D finite element analyses of stenting procedures for three different stent designs are presented.

Finally, using the fatigue test data and the hyperelastic model for *porcine coronary tissue*, in conjunction with the full 3D finite element models of the artery stented with the three different stenting procedures, in-stent restenosis is simulated within the stented vessels.

4.2 Experimental testing and constitutive models

To define Mooney-Rivlin models to represent both the human femoral and porcine coronary arterial tissue types, it was necessary to establish just one biaxial stress-stretch curve to define the equibiaxial properties of the arterial tissue. This is due to the fact that the Mooney-Rivlin model assumes the material to be isotropic; therefore an average stress-stretch curve was determined from the stress-stretch curves in both the circumferential and longitudinal directions in the equibiaxial tests.

4.2.1 Human femoral arterial tissue

The elastic behaviour of the femoral arterial tissue was found to be non-linear to high strains on both uniaxial and biaxial loading, see Figure 4.1. It is clear that variation occurs in the elastic behaviour of the various samples. Larger extension ratios are achieved in the uniaxial than the biaxial loading. In addition, the tissue is stiffer and less non-linear under biaxial loading.

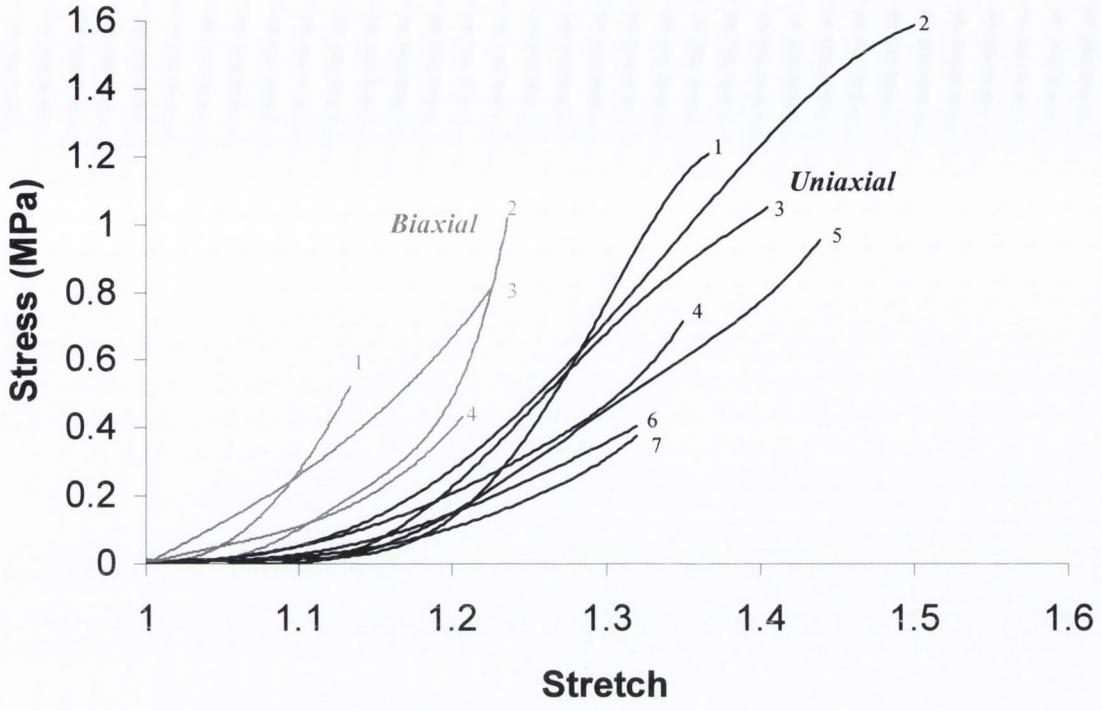

Figure 4.1 *Uniaxial and biaxial stress-stretch data for the human femoral arterial tissue. Each curve is numbered for later discussion.*

4.2.2 Porcine coronary arterial tissue

The uniaxial and biaxial elastic behaviour of the porcine arterial tissue was also found to be noticeably non-linear to high strains, see Figure 4.2 and Figure 4.3. It is again noteworthy with the porcine tissue that significant variation occurs in the elastic behaviour of the various samples. The uniaxial tests carried out on dog-bone shaped porcine coronary specimens, to obtain the ultimate tensile strength of the tissue as described in Section 3.2.1, are included in Figure 4.2 in red. By comparison, it can be seen that there is no significant difference between the variability of the samples' stress-stretch behaviour when tested as rectangular samples or as dog-bone shaped specimens. Larger extension ratios are achieved in the uniaxial specimens than the biaxial test specimens; compare Figure 4.2 and 4.3. Furthermore the tissue is stiffer and less non-linear under biaxial loading.

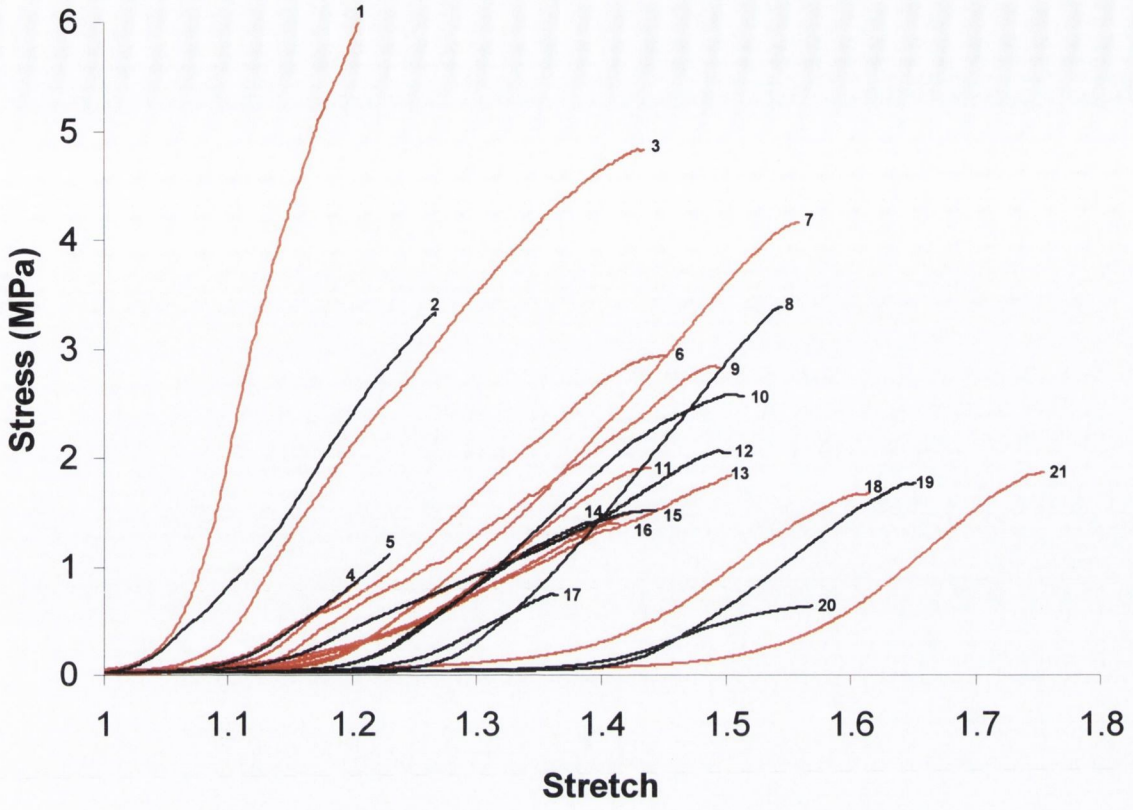

Figure 4.2 *Uniaxial stress-stretch data for the porcine coronary arterial tissue; rectangular test specimens are shown in black and dog-bone specimens in red.*

Comparing the response of the vessel in the circumferential and longitudinal directions illustrates the anisotropy of the porcine coronary arterial tissue, see Figure 4.3. There is clearly a great deal of variability in the uniaxial and equibiaxial tensile properties of the arterial tissue. The uniaxial data is most variable in the magnitude of the strain at which the toe region of the J-shaped non-linear curve occurs. The final slope of the curves can be seen to be very similar for all of the uniaxial curves.

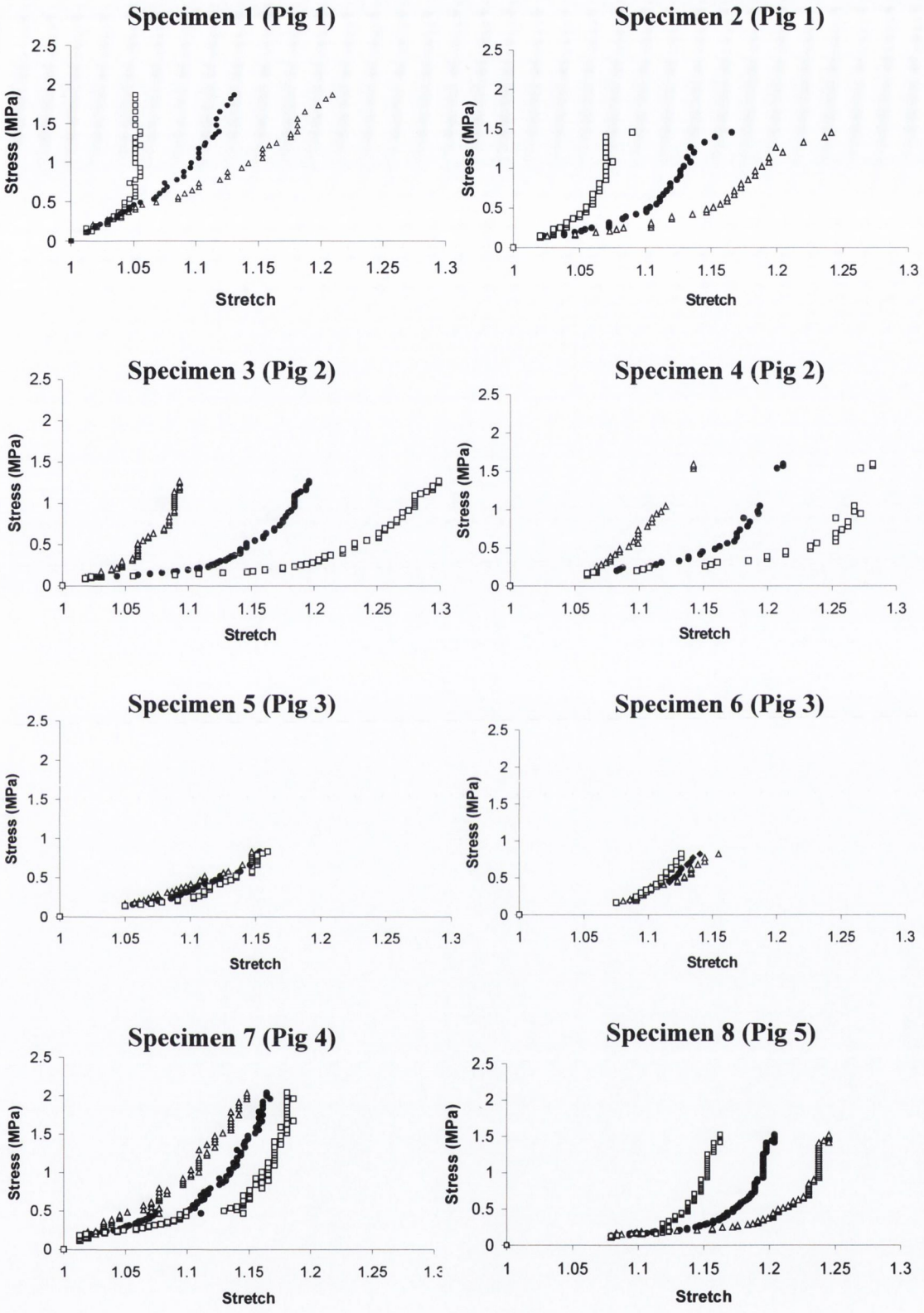

Figure 4.3 *The circumferential (△), average (●) and longitudinal (□) stress-stretch data from the equibiaxial tests on the porcine coronary arterial tissue.*

4.2.3 Mooney-Rivlin constitutive models

Using the uniaxial and equibiaxial experimental data the constitutive models to describe each material were determined. Only one uniaxial and one averaged equibiaxial curve can be used to define each constitutive material model. The uniaxial and equibiaxial behaviour of the constitutive equation to define the material properties of the human femoral arterial tissue are given in Figure 4.4. The uniaxial and equibiaxial curves chosen, to which the material model was fit, are marked with an asterisk, see Figure 4.4.

The uniaxial stress-stretch behaviour of the constitutive equation, which defines the material properties of the porcine coronary arterial tissue, is given in Figure 4.5. The uniaxial curve chosen, to which the constitutive material model was fit, is curve number seven and is marked with an asterisk, see Figure 4.5.

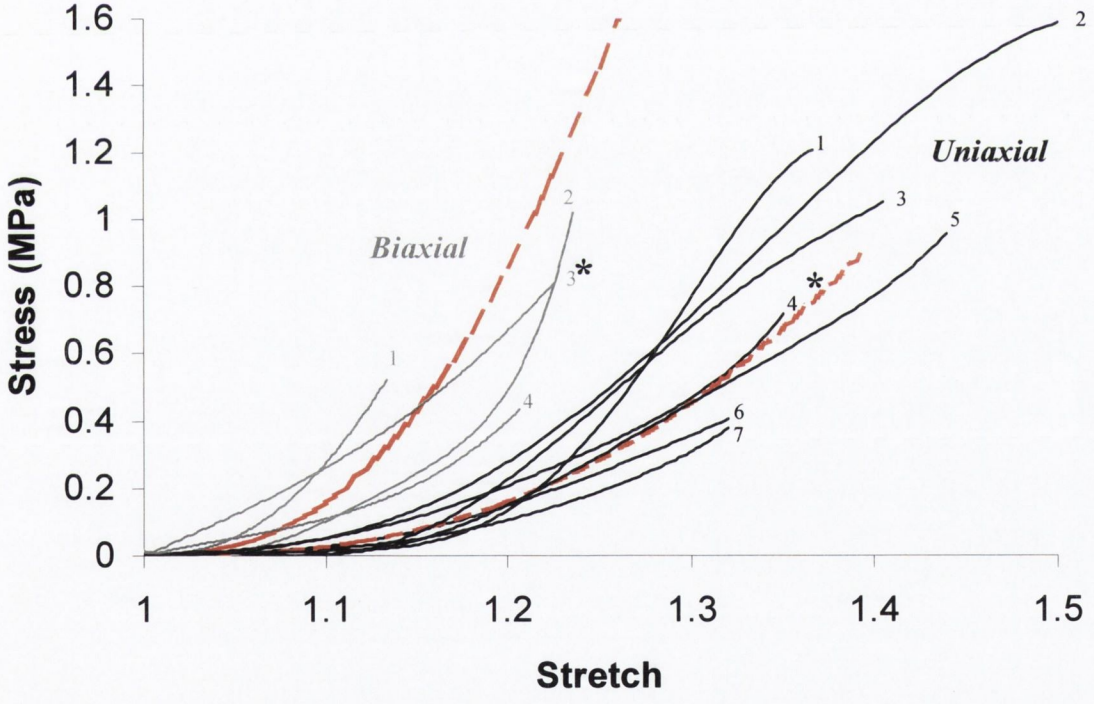

Figure 4.4 *Uniaxial and biaxial data for the human femoral arterial tissue with the fitted uniaxial and biaxial behaviour of the constitutive model (red dashed lines), see Table 4.1.*

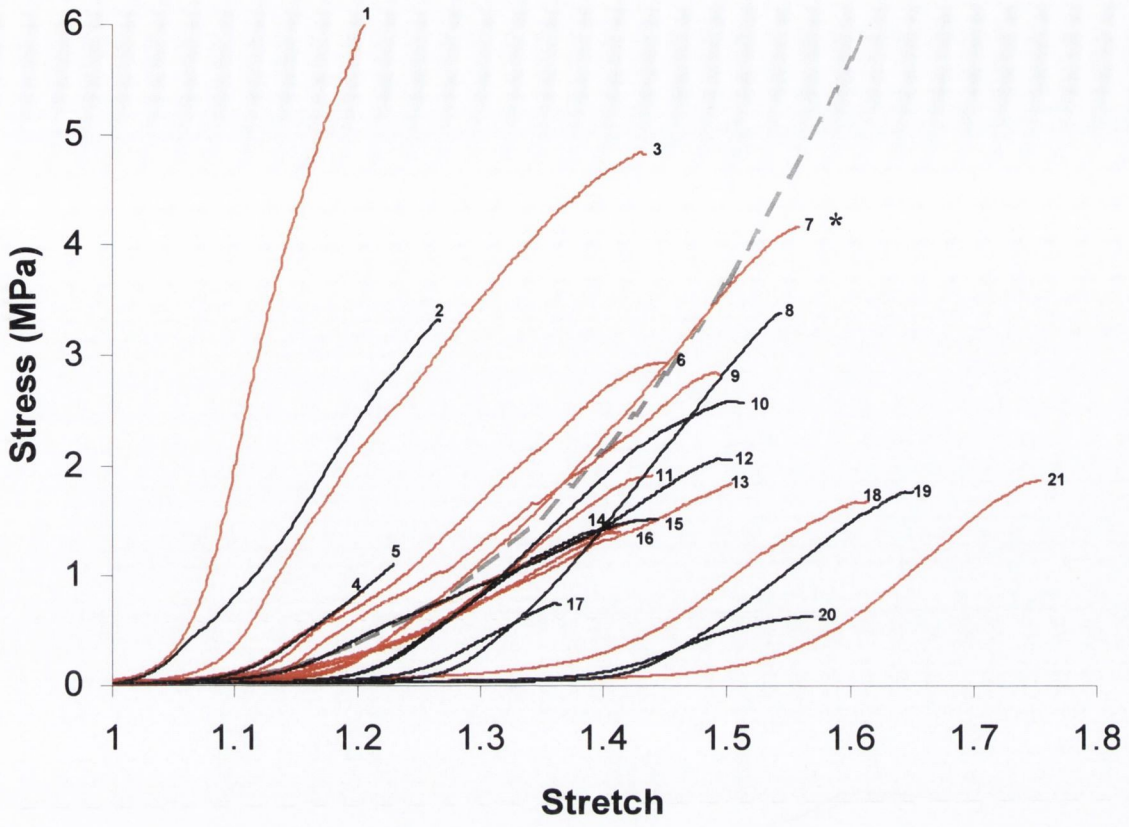

Figure 4.5 *Uniaxial data for the porcine coronary arterial tissue with the fitted uniaxial behaviour of the constitutive model (dashed line), see Table 4.1. The red lines are the stress-stretch curves obtained from the tests on dog-bone shaped tissue samples to obtain the UTS of porcine coronary tissue and the black lines are those from the standard uniaxial tensile tests.*

The equibiaxial behaviour of the same constitutive equation is given in Figure 4.6. The stress-stretch properties of each arterial tissue specimen in the longitudinal and circumferential directions were averaged and one average biaxial curve chosen, to which the material model was fit. The curve chosen is marked with an asterisk, see Figure 4.6. It can be seen that the constitutive model fits the chosen curves very well and represents the average properties of the uniaxial and equibiaxial data sets.

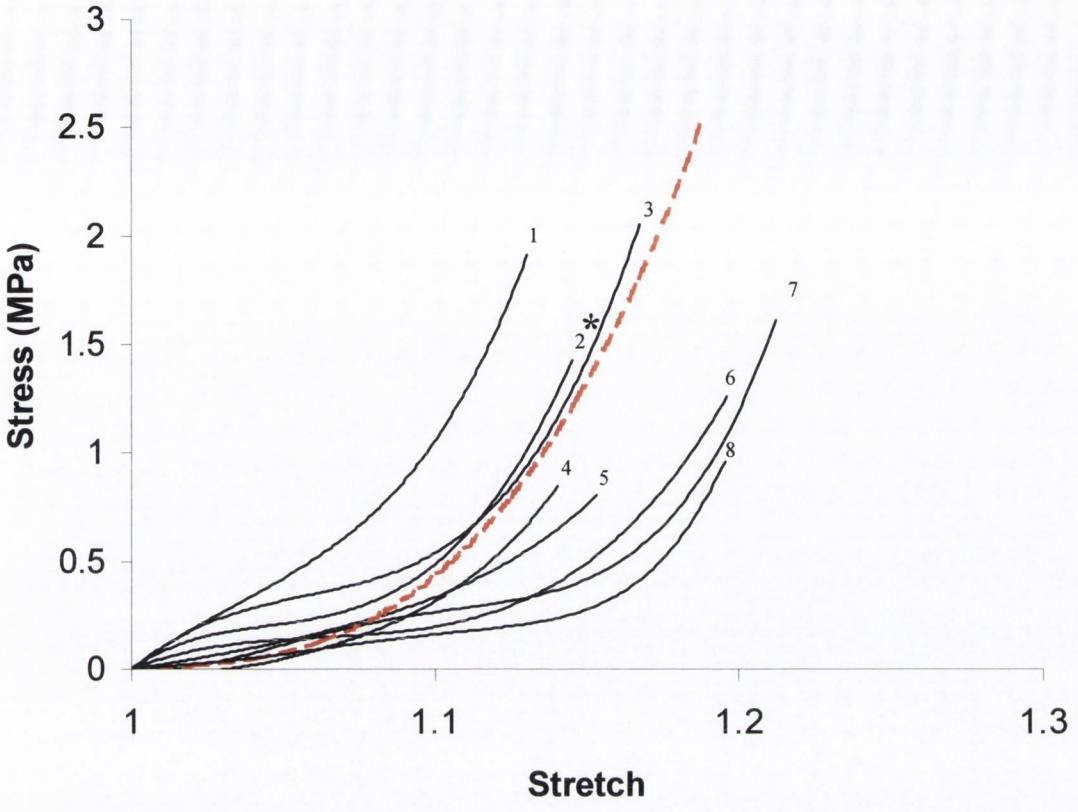

Figure 4.6 *Average biaxial data for the porcine coronary arterial tissue with the fitted biaxial behaviour of the constitutive model (red dashed line), see Table 4.1.*

A hyperelastic constitutive equation to represent the stress-stretch behaviour of atherosclerotic plaque was also determined by fitting to available published data on calcified human atherosclerotic plaques [Loree *et al.*, 1994]. The published data is limited to uniaxial stress-stretch data; therefore a constitutive equation was determined by fitting to only uniaxial data. However, the biaxial behaviour predicted by the constitutive equation was also assessed to ensure it was typical of arterial tissue and followed the trend observed in the experimental biaxial data obtained for human femoral and porcine coronary arterial tissue. The constitutive equation models the tissue as stiffer in equibiaxial tension than uniaxial tension, which is in accordance with the experimental data obtained for other two arterial tissue types, see Figure 4.7. The constants to define the Mooney-Rivlin strain energy density functions of the material models are given in Table 4.1, and all three models are shown together in Figure 4.8.

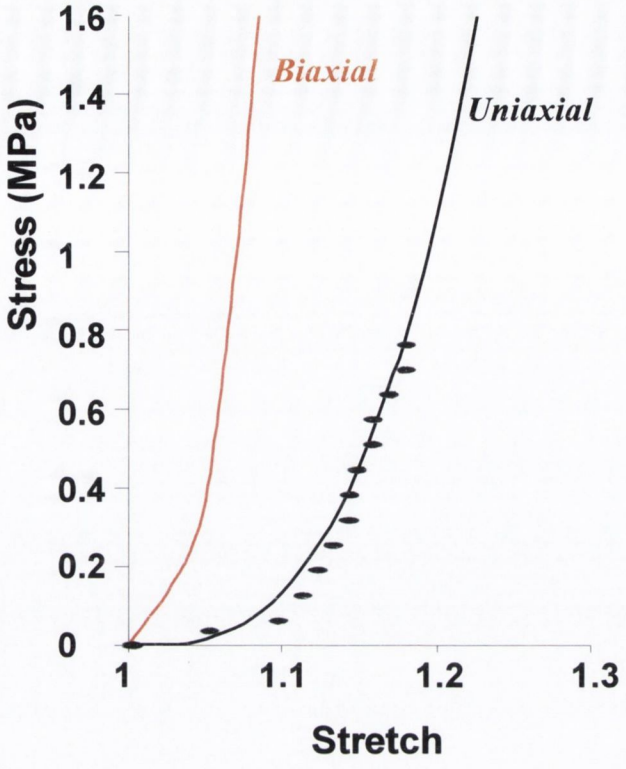

Figure 4.7 *Human calcified plaque properties (data points), adapted from Loree et al. [1994], and the fitted uniaxial and biaxial behaviour of the constitutive model (solid lines), see Table 4.1.*

	Human femoral arterial tissue (kPa)	Porcine coronary arterial tissue (kPa)	Stenotic plaque tissue (kPa)
a_{10}	18.90	11.44	-495.96
a_{01}	2.75	21.30	506.61
a_{20}	85.72	601.25	1193.53
a_{11}	590.43	1205.26	3637.80
a_{30}	0	0	4737.25
Error	3.08 (relative)	5.21 (absolute)	0

Table 4.1 *Hyperelastic constants to describe the human femoral arterial tissue, the porcine coronary arterial tissue and stenotic plaque non-linear elastic behaviour. The parameters describe a Mooney-Rivlin model of the form given in Eqn. 3.1.*

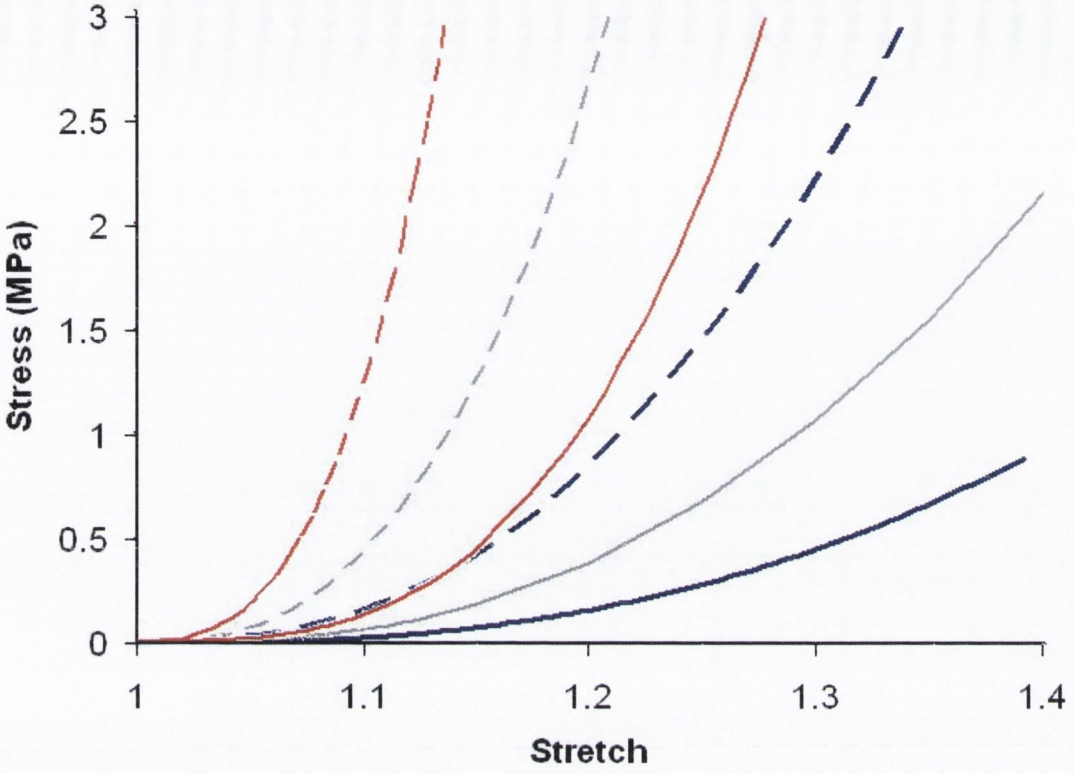

Figure 4.8 *The Moony-Rivlin constitutive models (Table 4.1) used to describe the human femoral arterial tissue (blue), the porcine coronary arterial tissue (grey) and stenotic plaque non-linear elastic behavior (red). The solid lines represent uniaxial behaviour and the dashed lines represent the biaxial behaviour of the tissue.*

4.3 Damage accumulation within coronary arterial tissue

4.3.1 Tensile tests to obtain the ultimate tensile strength of porcine coronary arterial tissue

The elastic behaviour of all twelve specimens tested was found to be highly non-linear to high strains, see Figure 4.9. The stress-stretch data show a significant degree of variation; however the final slopes of the curves are all very similar. The ultimate tensile stretch of the tissue is seen to range between 1 MPa and 6.5 MPa. The average UTS of the tissue corresponds to 4 MPa and is represented by sample 5, which failed in the centre of the sample between the grips.

4.3.2 Fatigue tests to determine the rate of damage accumulation within porcine coronary arterial tissue

Twenty-seven fatigue tests were carried out in total. The data of one of the fatigue tests will be thoroughly discussed here. The test chosen was carried out from 10-30% of the UTS. The test results illustrated exhibit the key characteristics of the all of the

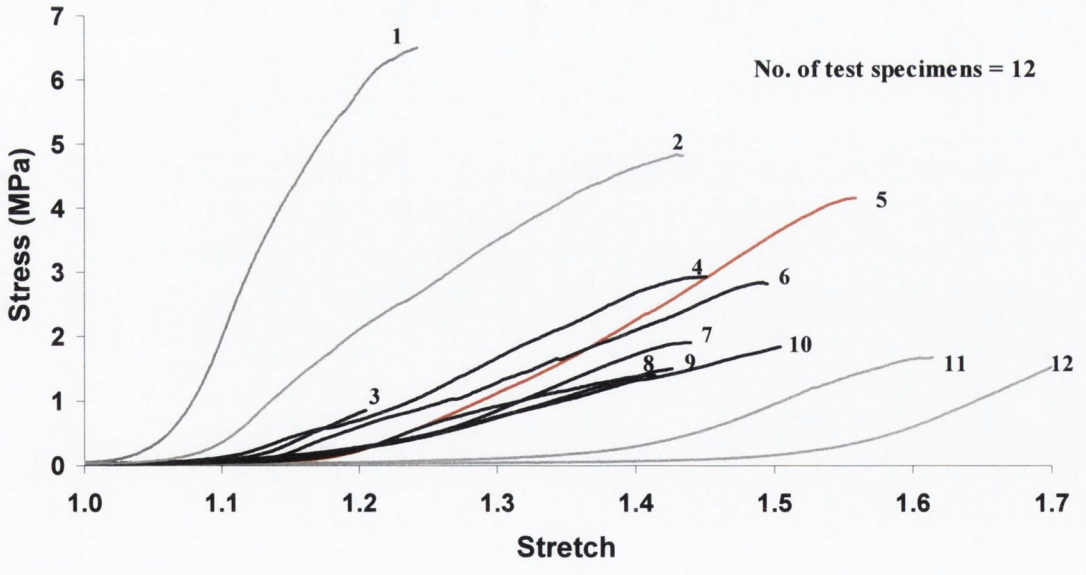

Figure 4.9 *Uniaxial stress-stretch data for porcine coronary arterial issue to obtain the UTS of the tissue.*

fatigue tests carried out on the porcine coronary arterial tissue (Further results from these tests are available from Brands, 2003).

Figure 4.10 illustrates one complete fatigue test, including preconditioning. As observed in the uniaxial tensile tests it can be seen that, after approximately five cycles, the tissue is preconditioned since it reaches a steady state response, see Figure 4.10. The preconditioning can clearly be seen in the first few cycles where the loading and unloading curves for each cycle are distinctly different from the previous cycles. Looking at these first few cycles, there is also a difference in the amplitude of the loading and unloading curve compared to the rest of the curves. The force amplitude of the preconditioning cycles is lower than the amplitude of the successive curves.

After the initial preconditioning cycles, the successive loading and unloading curves are indistinguishable from one another. Although the loading and unloading curves almost overlap the displacement of the sample is clearly increasing, illustrating that the arterial tissue is extending due to its viscoelasticity.

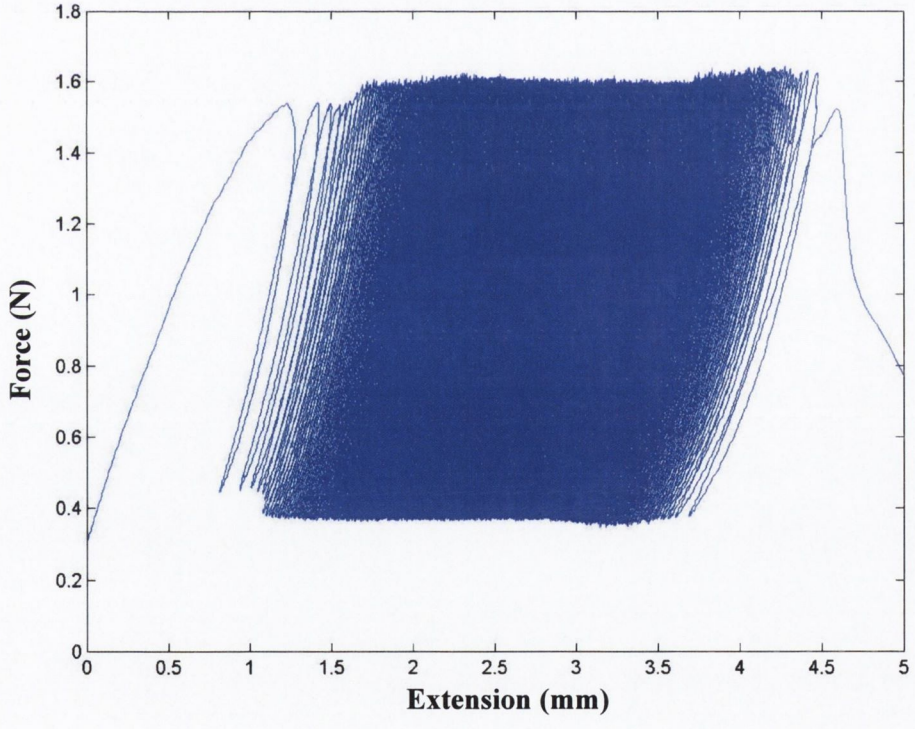

Figure 4.10 *The displacement versus applied force of a fatigue test on porcine coronary arterial tissue carried out at 10-30% of the UTS.*

The mean extension of the arterial tissue specimen increases with increasing number of applied cycles, see Figure 4.11. To better understand what is actually occurring within the arterial tissue it is necessary to look at the displacement amplitude and the force amplitude during the test as the number of cycles is increased, see Figure 4.12.

It is evident that creep is occurring in this viscoelastic material; however, damage is also accumulating within the tissue, which is evident by the fact that the displacement amplitude increases as the number of cycles increases, whilst the force amplitude remains the same, see Figure 4.12. This indicates that the arterial tissue is lowering in stiffness with increasing number of cycles, demonstrating damage accumulating within the tissue.

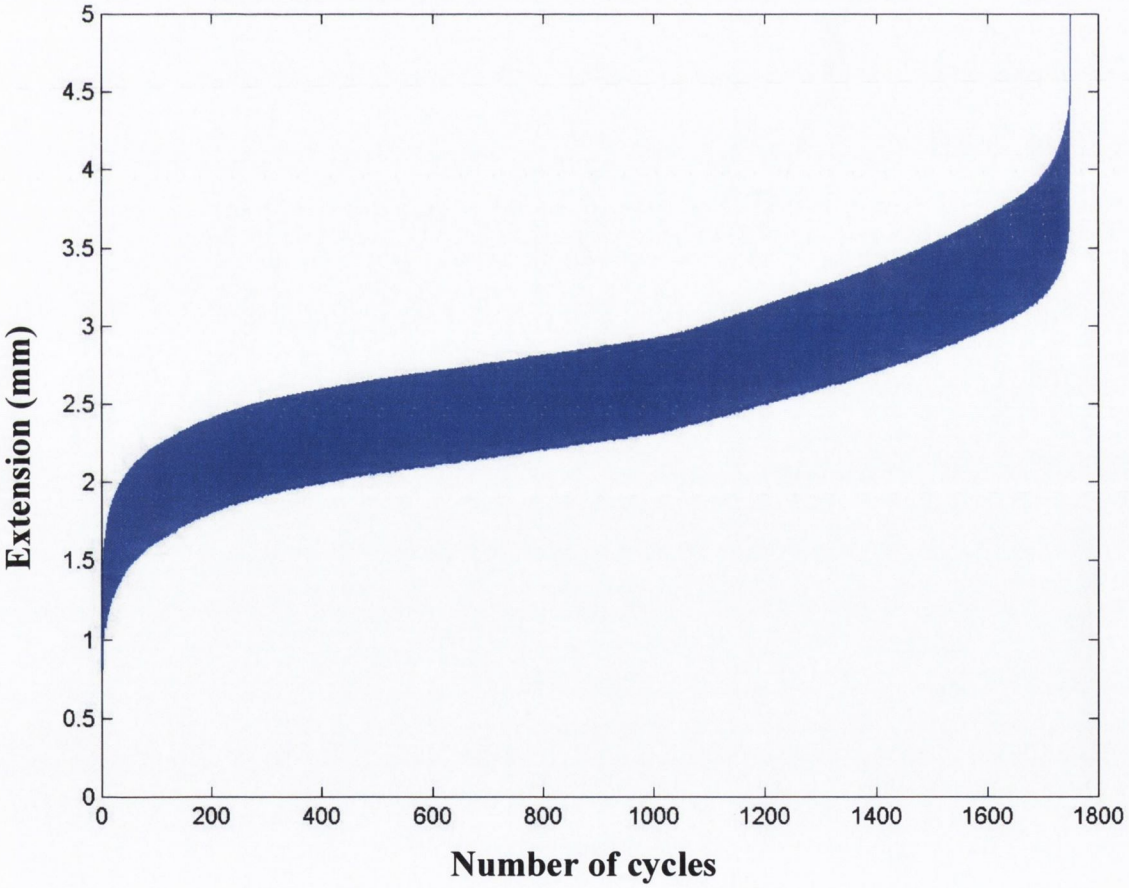

Figure 4.11 *The displacement versus number of cycles for a fatigue test on porcine coronary arterial tissue carried out at 10-30% of the UTS.*

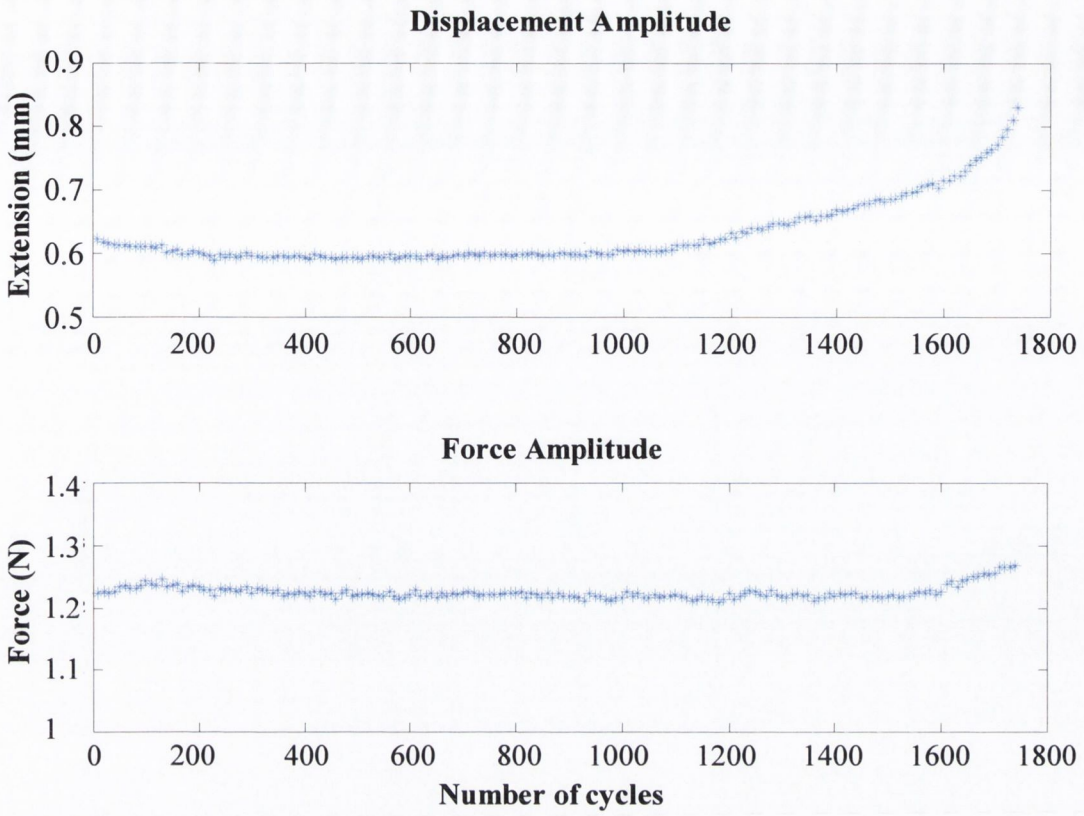

Figure 4.12 *The amplitude of the displacement and force of a fatigue test on porcine coronary arterial tissue carried out at 10-30% of the UTS.*

Plotting the stiffness of the tissue at intervals throughout the fatigue test further illustrates the accumulation of damage within the arterial tissue, see Figure 4.13. "Stiffness" is a structural property, denoting the tangent to the load-extension curve. Ker *et al.* [1997] used it to investigate damage accumulation within wallaby tendon tissue.

Finally, the mean stress level and the number of cycles to failure recorded for each fatigue test was used to generate an *S-N* curve for porcine coronary arterial tissue, see Figure 4.14. The three increasing stress levels correspond to the loading amplitudes of 10%-20%, 10%-30% and 10%-40% of the ultimate tensile strength, respectively. Assuming that arterial tissue will have an infinite life at zero stress an exponential curve can be fitted through the average value of N_f for each stress level, as shown in Figure 4.14.

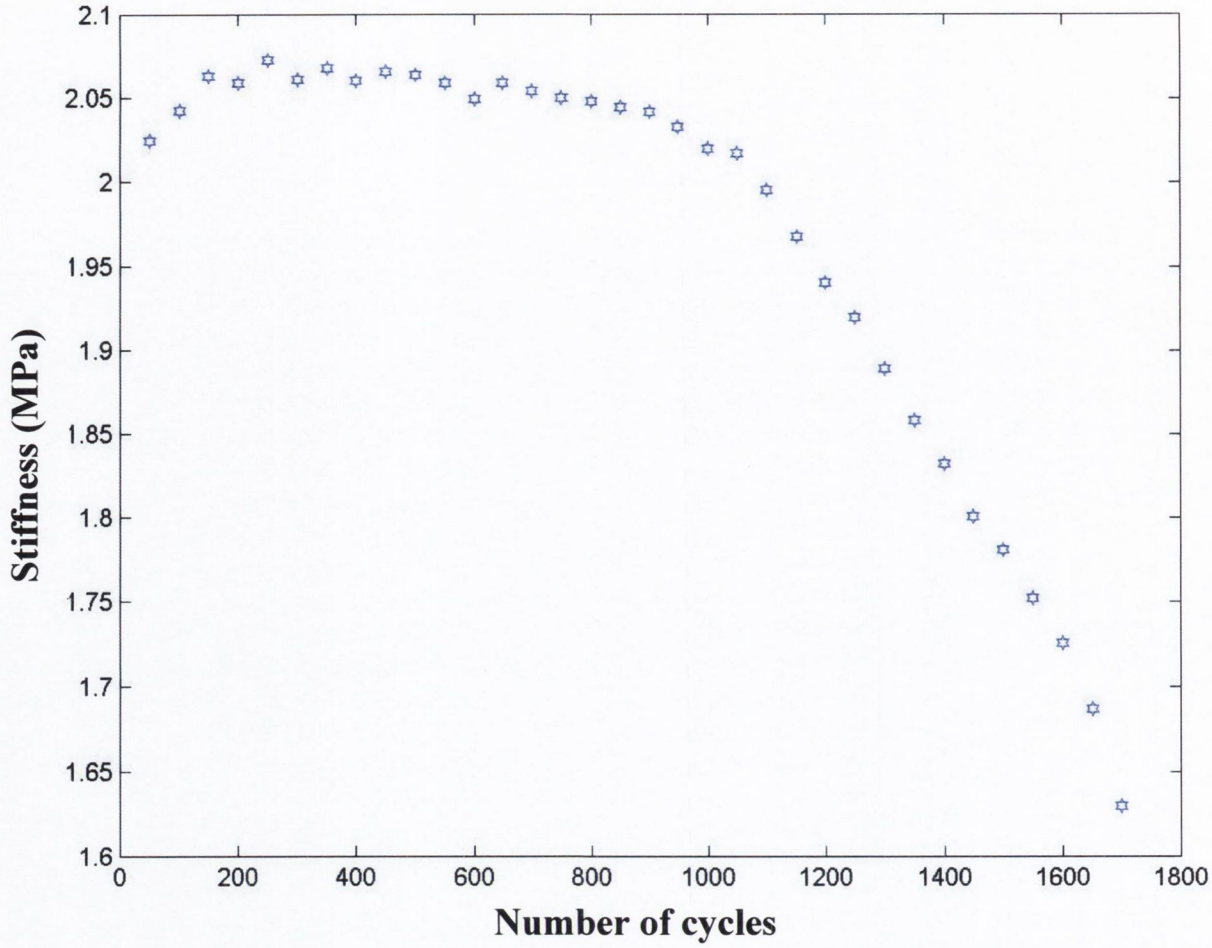

Figure 4.13 *The arterial stiffness at intervals during a fatigue test carried out at 10-30% of the UTS.*

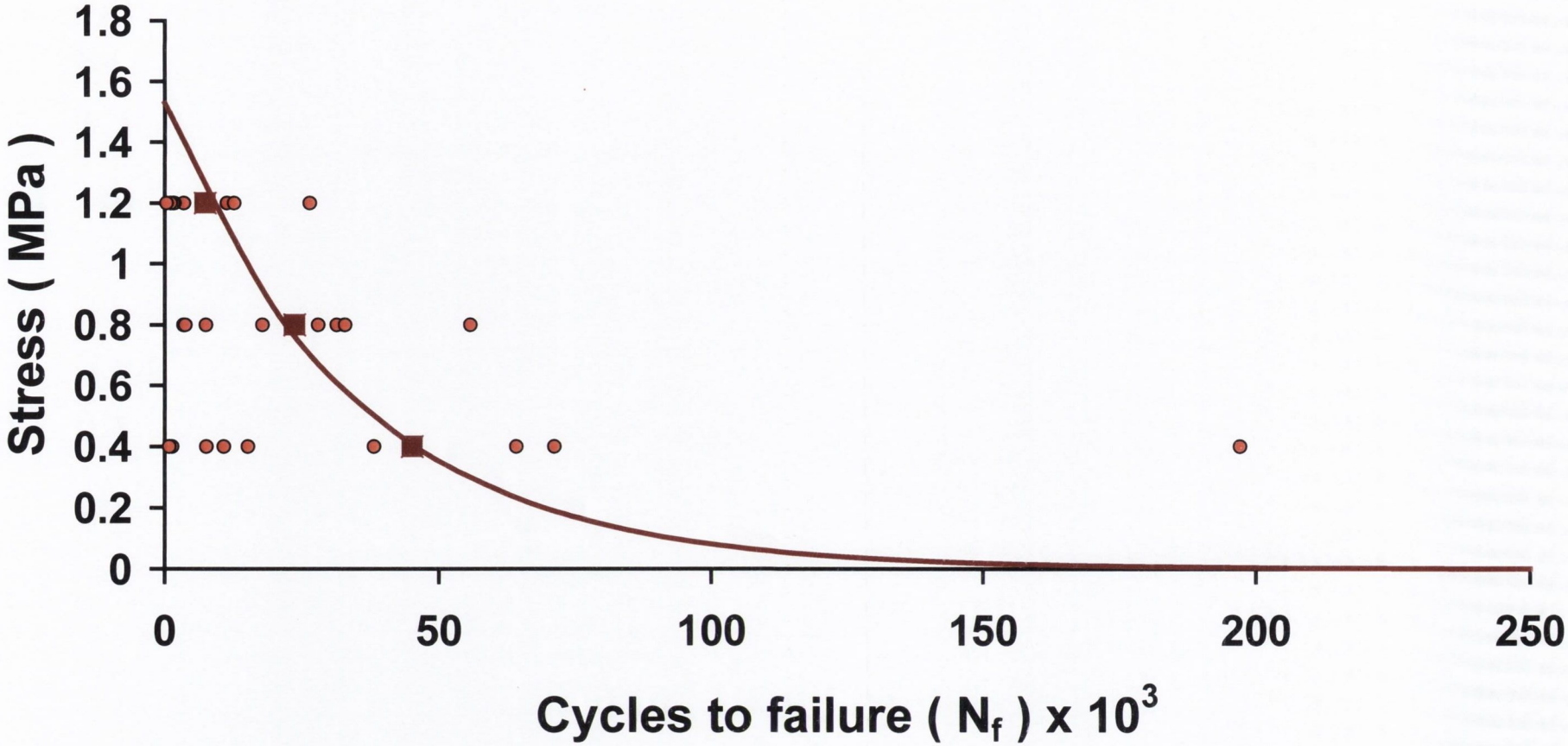

Figure 4.14 *The S-N curve for porcine coronary arterial tissue. The circles represent test data whilst the squares are the represent the average number of cycles to failure at each stress level.*

The equation of the exponential curve, shown in Figure 4.14, through the average value for the number of cycles to failure at each stress level is given by:

$$\sigma = 1.52e^{-2.93\times10^{-5}N_f} \qquad (4.1)$$

For $\sigma > 1.52$ MPa, $N_f = 0$

For $\sigma = 0$, $N_f = \infty$

To relate this to damage recall Eqn. 3.8, $\dot{D} = \frac{1}{N_f}$. The damage may be calculated as a function of stress, σ, as follows:

$$\dot{D} = \frac{1}{N_f} = \frac{-2.93\times10^{-5}}{\ln|\sigma| - \ln(1.52)} \qquad (4.2)$$

For $\sigma \geq 1.51$ MPa, $\dot{D} = 1$ i.e. for $\sigma \geq 1.51$ MPa, $N_f = 1$

This relationship between the rate of damage accumulation and the magnitude of the absolute value of the maximum or minimum principal stresses generated within porcine arterial tissue may be represented by a non-linear curve, see Figure 4.15.

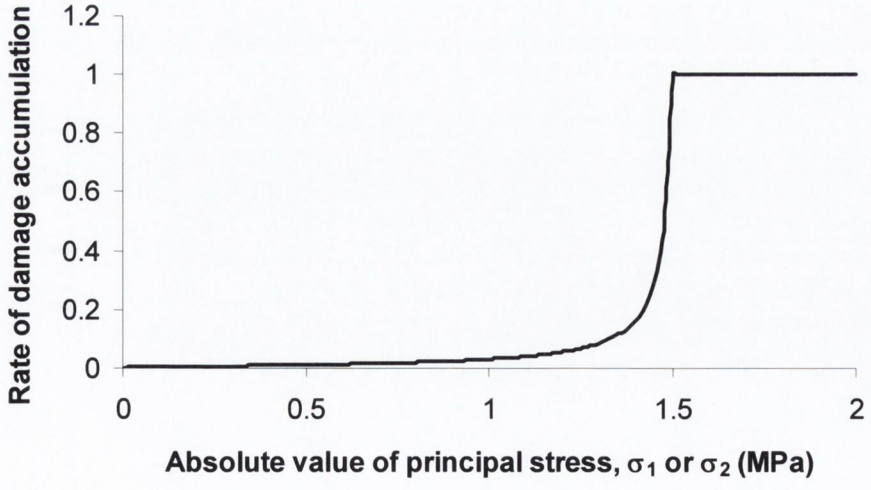

Figure 4.15 *The non-linear relationship between the rate of damage accumulation within porcine arterial tissue and the mean stress level within the tissue at which the tissue is cyclically loaded.*

4.4 Finite Element Models

4.4.1 Prolapse Study

The finite element analyses to assess the degree of tissue prolapse (i.e. the maximum radial displacement of the tissue) within one repeating unit of four different stent designs illustrated that the stent unit configuration has an effect on the scaffolding properties of the stent. These analyses were, in fact, carried out for both human femoral arterial properties and porcine aortic tissue properties [Prendergast *et al.*, 2003]. However, the same ranking was found for the analyses using both tissue types. The results of the analyses found that the degree of tissue prolapse was in increasing order, as follows: the least prolapse was in the BeStent 2 unit, next was the TETRA stent, then the NIROYAL, and the highest predicted prolapse was in the unit of the VELOCITY stent, see Figure. 4.16 and Figure 4.17.

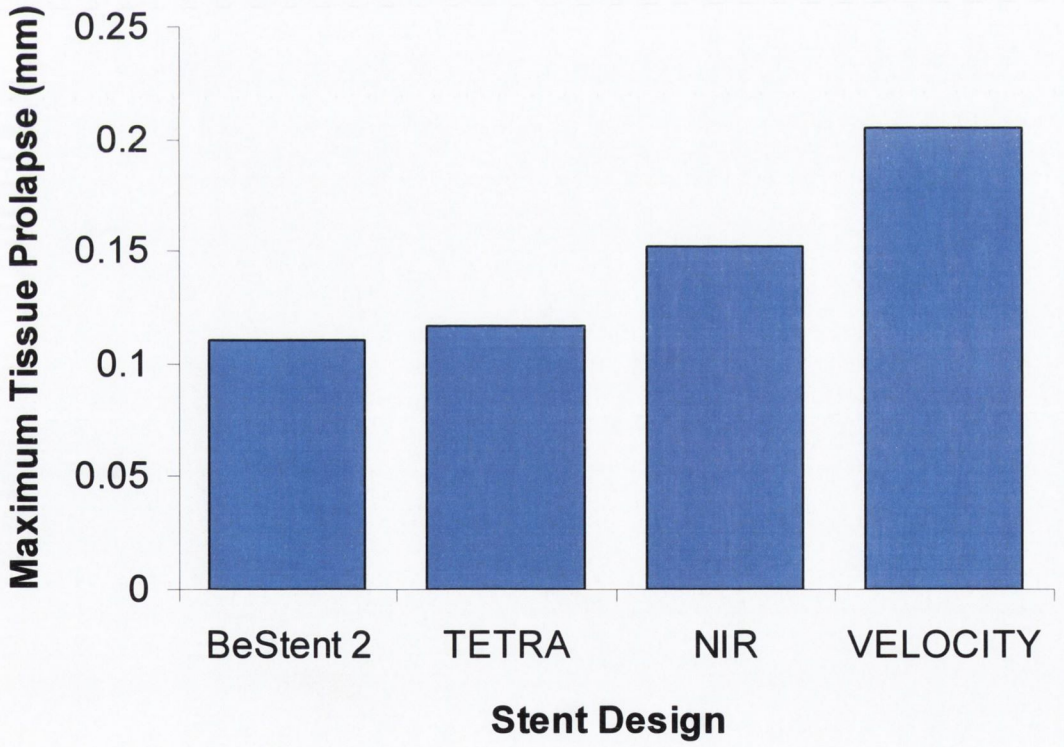

Figure 4.16 *The maximum prolapse of the vascular tissue within the repeating unit of the four stents analysed using human femoral arterial properties.*

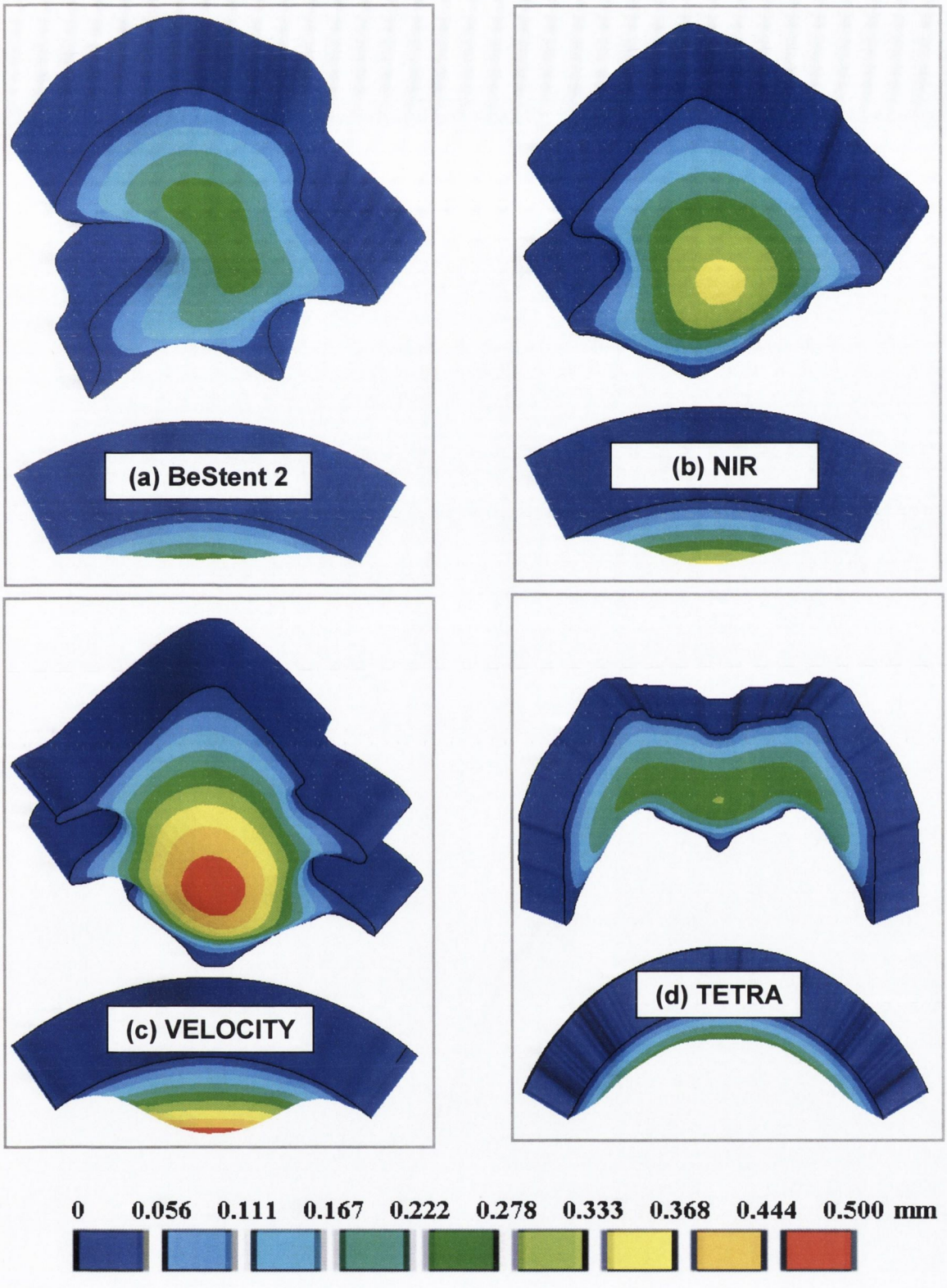

Figure 4.17 *Prolapse of the four stents: Contour plot of the radial displacements in the BeStent 2,* Medtronic AVE*; the NIR,* Boston Scientific*; the VELOCITY,* Cordis*; and the Tetra Stent,* Guidant, *for porcine aortic tissue properties.*

The prolapse data should be 'normalised' if a proper comparison of the four stent designs is to be achieved. A small repeating-unit will allow little draping but it may cause problems for the other design objectives for cardiovascular stents, e.g. a high stent-vessel contact area is likely to increase the risk of thrombosis and endothelial denudation during deployment. In this respect, a repeating-unit is in some way superior if it can minimize prolapse despite having a large area. When the prolapse is normalised for the area of the repeating unit, the TETRA stent and BeStent 2 perform best (Table 4.2). A similar conclusion is reached if the predicted prolapse is normalised by the length of the periphery of each stent repeating unit (Table 4.2).

Since it is the stresses within the vessel wall induced by the stent that are hypothesised to cause damage and subsequent intimal hyperplasia and restenosis, a measure of the stresses in the media layer directly above the stent are shown in Figure 4.18. It can be seen that the highest stresses are provoked by the VELOCITY stent.

Design	Maximum prolapse (mm)	Expanded area of repeating unit (mm^2)	Maximum prolapse per unit area (mm/mm^2)	Length of periphery of expanded repeating unit (mm)	Maximum prolapse per unit length (mm/mm)
BeStent 2	0.253	2.34	1.08×10^{-1}	8.24	0.031
TETRA	0.279	4.35	0.64×10^{-1}	12.60	0.022
NIR	0.348	2.12	1.64×10^{-1}	6.52	0.053
Velocity	0.480	3.71	1.29×10^{-1}	10.5	0.046

Table 4.2 *Maximum prolapse per unit area of the repeating unit, and per length of the periphery of the repeating unit.*

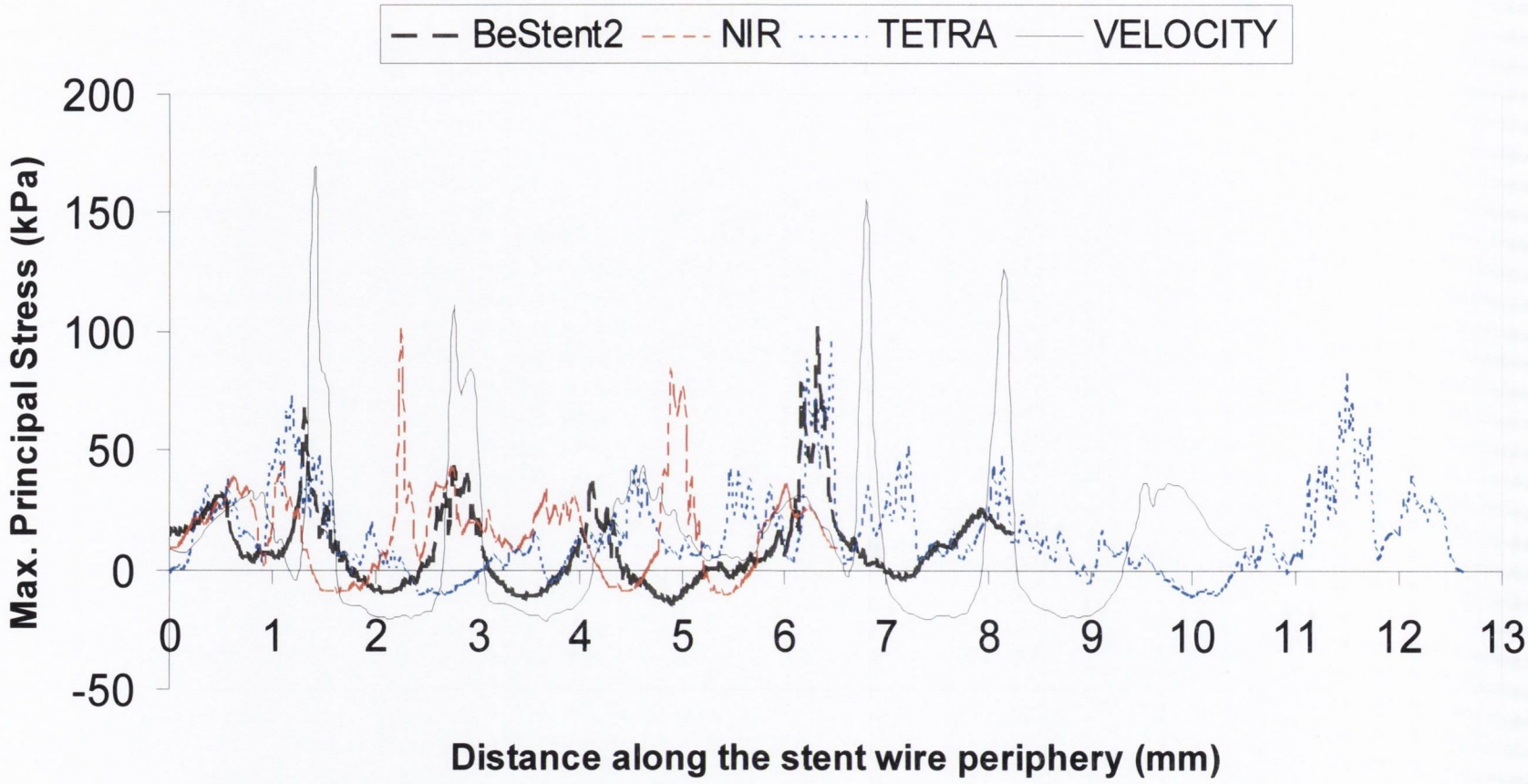

Figure 4.18 *Maximum principal stresses in the mid-layer of the vessel around the periphery of the repeating-unit (i.e. directly above the stent wire). High stresses are indicative of a likelihood of tissue damage and intimal hyperplasia. Note that the starting point for each stent wire is indicated on Figure 3.9.*

4.4.2 Full 3D Models

To investigate the stresses induced within the arterial wall of stented vessels more fully and hence ascertain the propensity of different stent designs to cause in-stent restenosis, full 3D models of stented vessels were generated. The degree of tissue prolapse within the stent struts and the maximum and minimum principal stresses generated within the artery wall were determined, as well as the radial retraction of the stents. These values were compared for the three different stent designs, i.e. the NIR stent (*Boston Scientific)*, S7 stent (*Medtronic AVE)* and a 'simple' original stent design, to determine which design would cause the least damage to the artery wall whilst maintaining vessel patency.

4.4.2.1 Cylindrical Vessels – no plaque

Cylindrical vessels without any plaque were stented with the three different stent designs, see Figure 4.19. The vessel had an initial inner diameter of 3 mm and was 0.5 mm thick.

An axial stretch of 1.2 was applied to all of the vessels in the stenting simulations. However, the effect that applying this stretch, simulating the stretch an artery experiences *in vivo*, can be seen by comparing the stresses induced within the vessel wall during a stenting simulation with and without the axial stretch applied, see Figure 4.20. It can be seen that the stresses induced within the arterial tissue, both maximum and minimum principal stresses, of a NIR stented vessel increase dramatically when an axial stretch is applied to the vessel. The regions of highest stresses, however, are the same in both simulations, i.e. the vessel wall at the stent ends.

The maximum and minimum principal stress induced with the idealised cylindrical vessels are considerably higher in both the NIR and 'simple' stent designs than in the vessel stented with the S7 stent, see Figures 4.21 and 4.22. The lower stresses in the S7 may be attributed to the radial retraction of the stent, which is higher than that of the other two stents, see Figure 4.23.

Figure 4.19 *Deformed geometry of the cylindrical stented vessels without stenotic plaque, axial stretch applied (λ_z=1.2) and original vessel lumen diameter of 3 mm.*

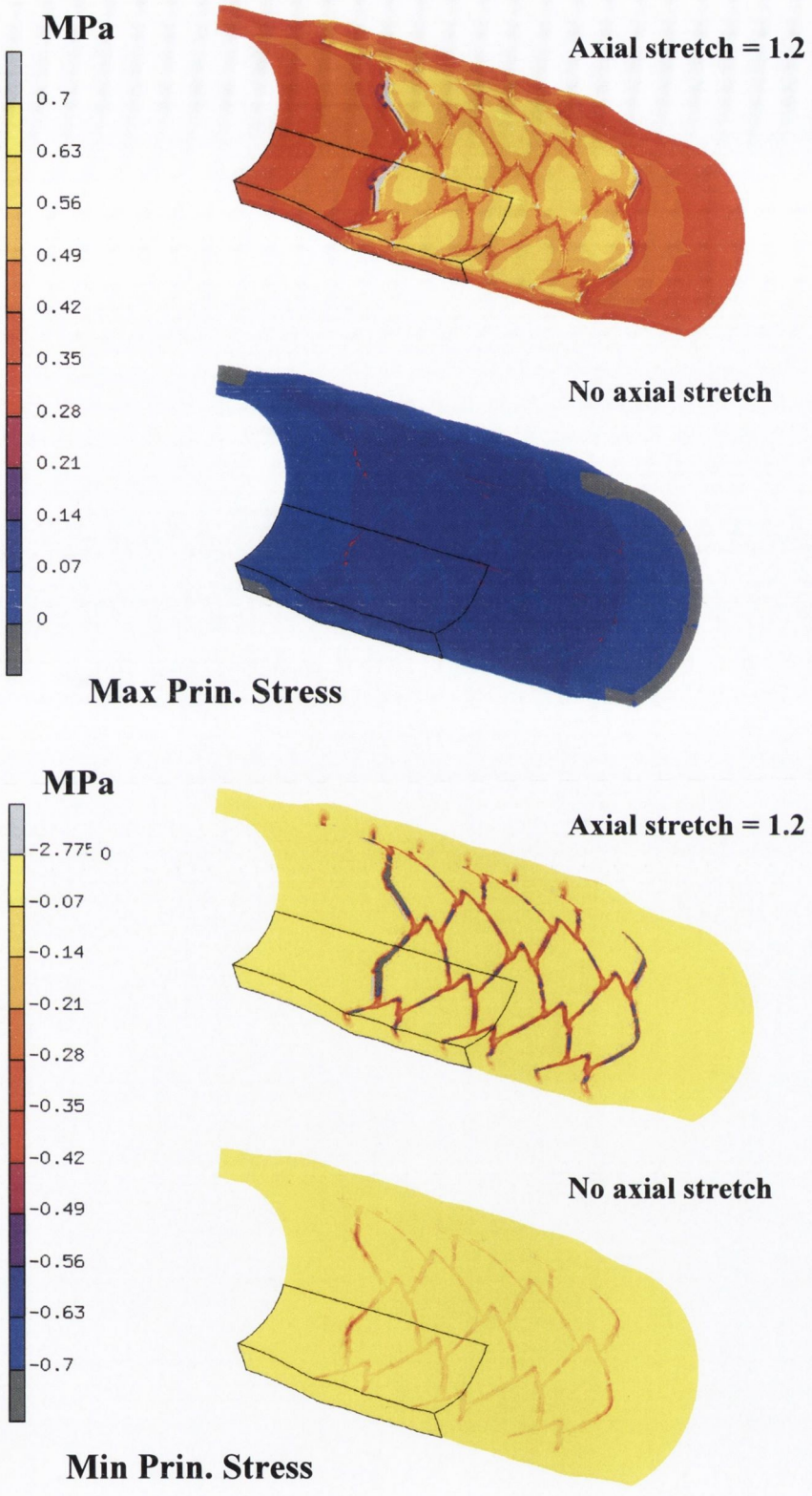

Figure 4.20 *Cylindrical vessel segment, stented with the NIR stent, with and without axial stretch applied and with an original vessel lumen diameter of 3 mm.*

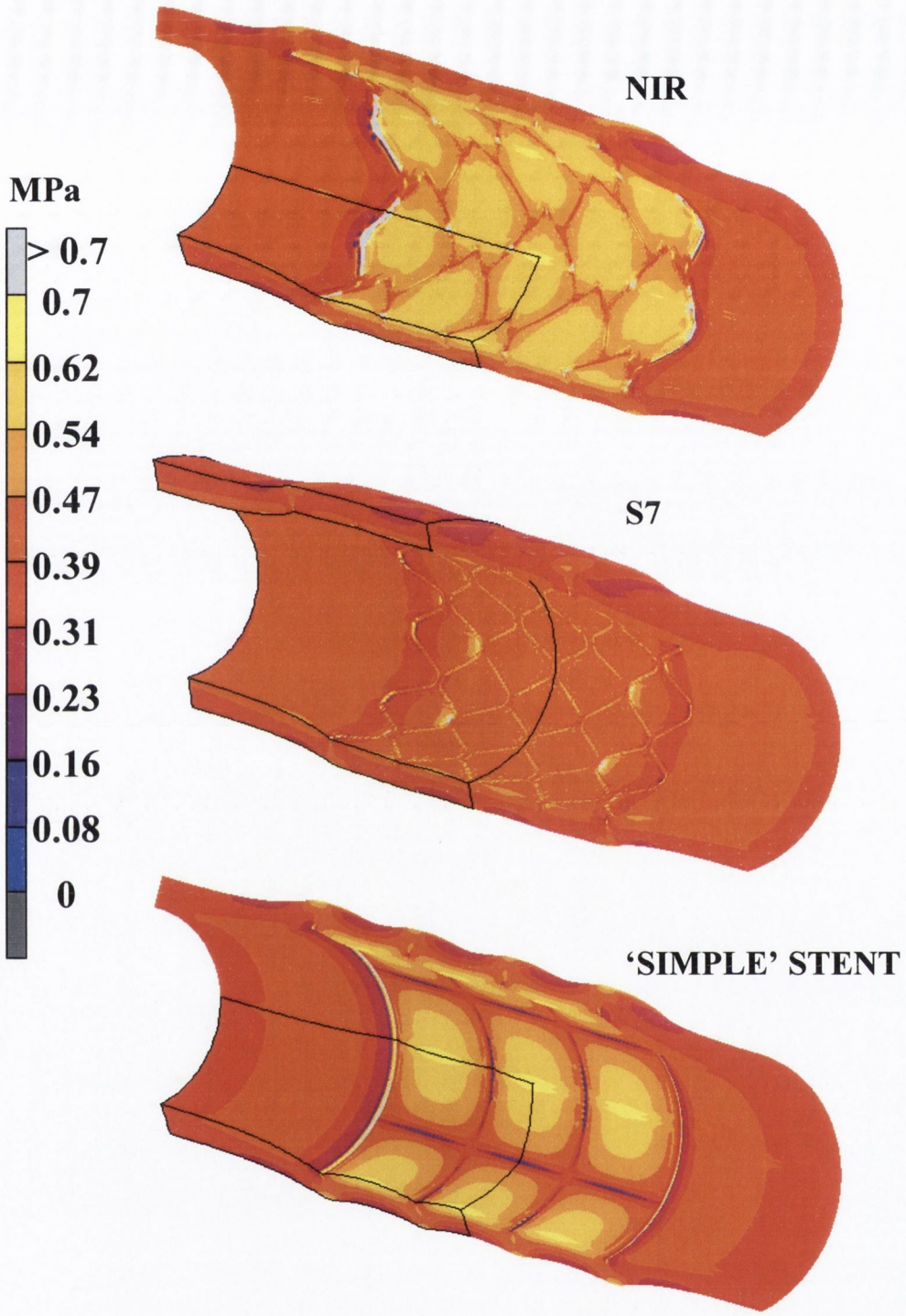

Figure 4.21 *Maximum principal stresses induced within segments of idealised cylindrical vessels stented with the NIR, S7 and 'simple' stents, axial stretch applied (λ_z=1.2) and original vessel lumen diameter of 3 mm.*

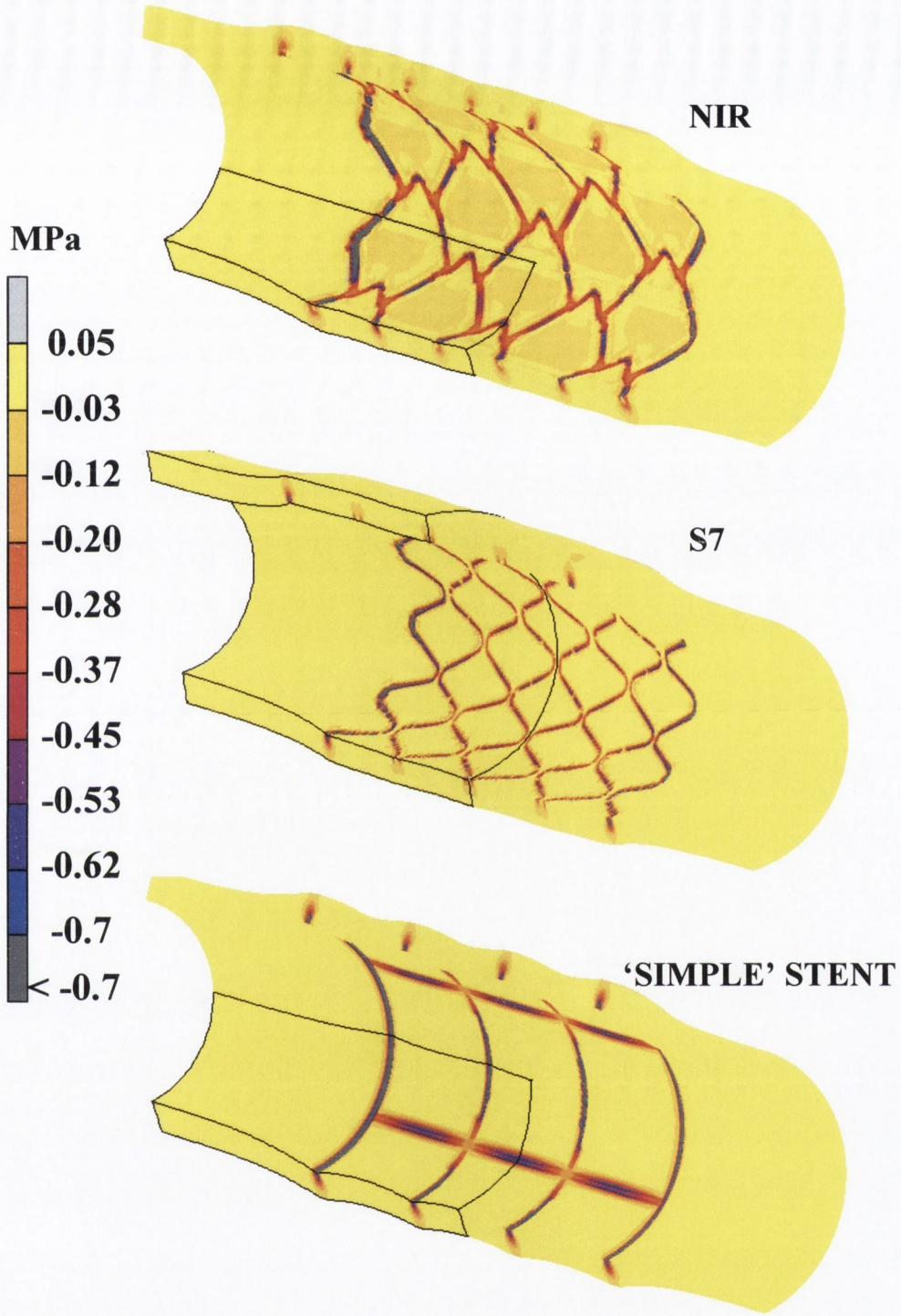

Figure 4.22 *Minimum principal stresses induced within segments of idealised cylindrical vessels stented with the NIR, S7 and 'simple' stents, axial stretch applied (λ_z=1.2) and original vessel lumen diameter of 3 mm.*

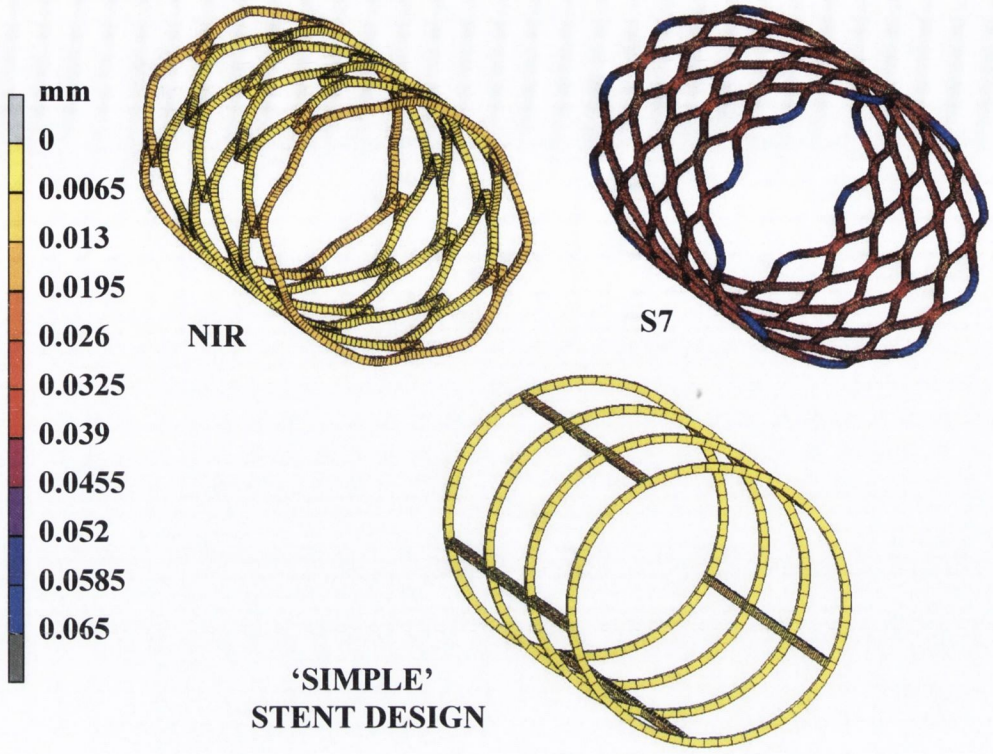

Figure 4.23 *Radial retraction during the NIR, S7 and 'simple' stenting procedures within the idealised cylindrical vessels.*

It can be seen that the S7 has the lowest tissue draping within the struts of the stent and hence it has the best scaffolding properties, see Figure 4.24. The final minimum lumen diameter of the stented vessels was found to be 3.38 mm, 3.29 mm and 3.25 for the NIR, S7 and 'simple' stents, respectively.

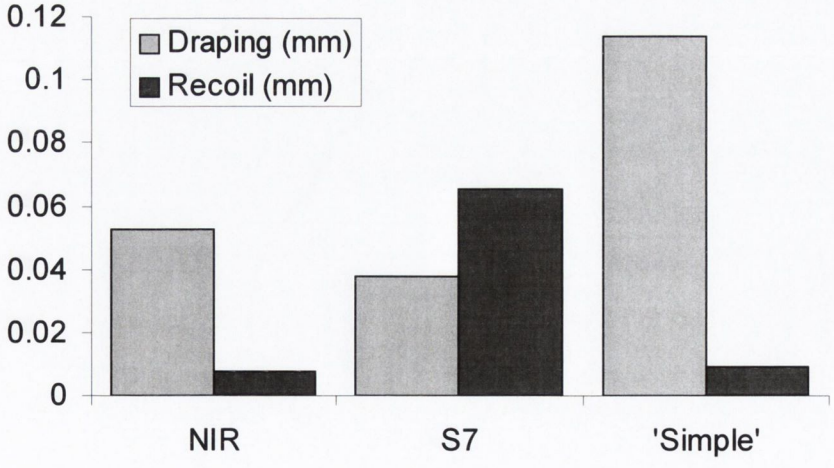

Figure 4.24 *The magnitude of the maximum draping within the struts of the NIR, S7 and 'simple' stent and the maximum radial retraction of the stents during the stenting procedures in the idealised cylindrical vessels.*

4.4.2.2 Atherosclerotic Vessels – cylindrical stenotic lesion

The NIR, S7, and 'simple' stent designs were also deployed within cylindrical vessels with a concentric cylindrical lesion, see Figure 4.25. The vessel had an initial inner diameter of 2 mm, with plaque material within the vessel of 0.5 mm thick and healthy arterial tissue of 0.5 mm thick. The maximum and minimum principal stress induced within the cylindrical vessels with a concentric cylindrical lesion are again higher in both the NIR and 'simple' stent designs than in the vessel stented with the S7 stent, see Figures 4.26 and 4.27. The stresses are highest in the centre of the vessel and around the stent struts. The lower stresses in the S7 may be attributed to the greater radial retraction of the stent, which is higher than that of the other two stents, see figure 4.28. However, the scaffolding of the S7 stent is still superior to the other two designs within this stenosed vessel, see Figure 4.29.

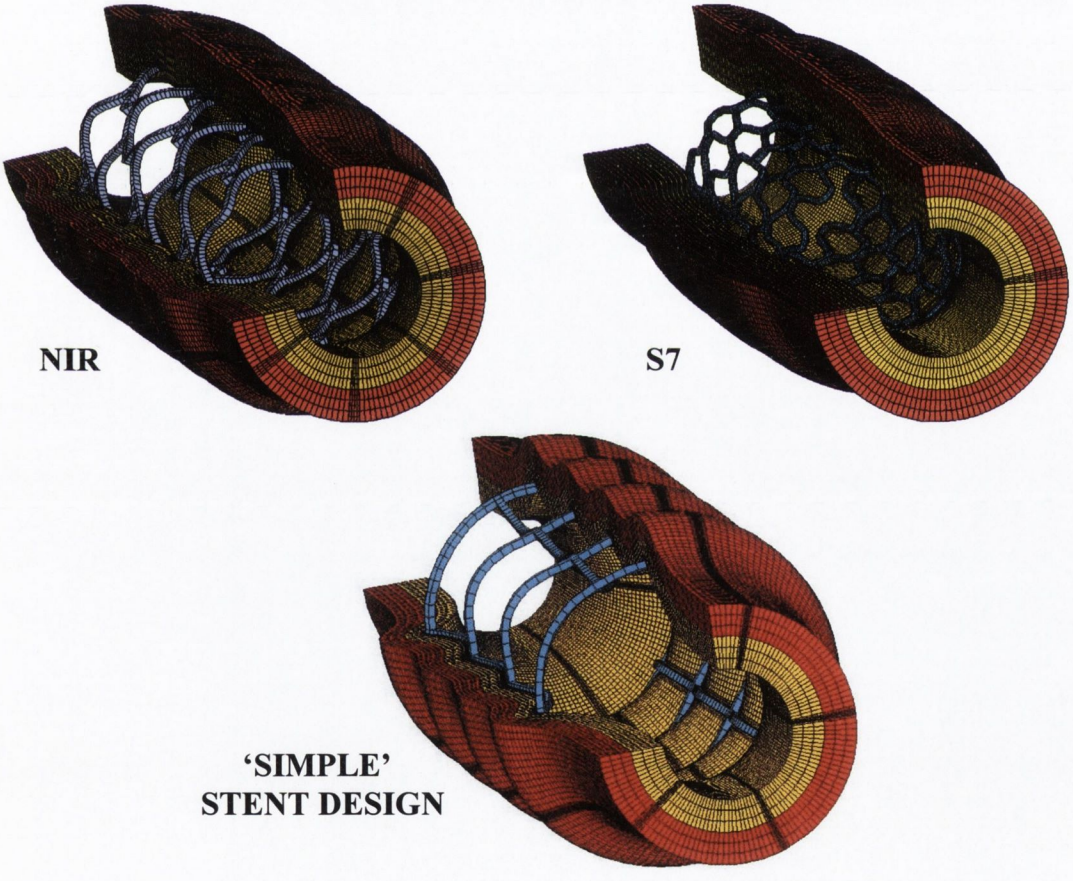

Figure 4.25 *Deformed geometry of the cylindrical stented vessels with symmetrical cylindrical stenotic plaque (yellow), axial stretch applied (λ_z=1.2) and original vessel lumen diameter of 2 mm.*

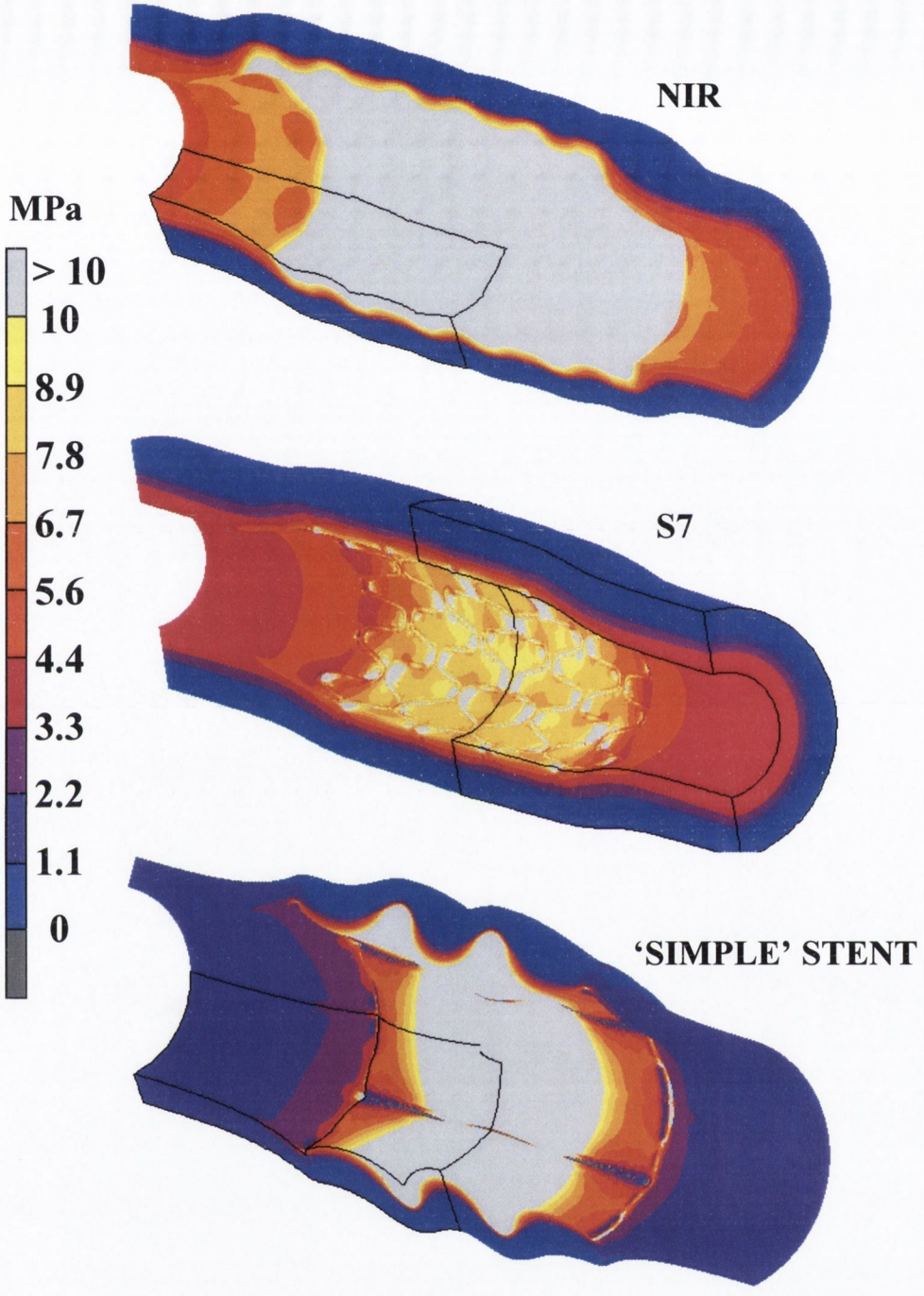

Figure 4.26 *Maximum principal stresses induced within segments of idealised cylindrical stenosed vessels stented with the NIR, S7 and 'simple' stents, axial stretch applied (λ_z=1.2) and original vessel lumen diameter of 2 mm.*

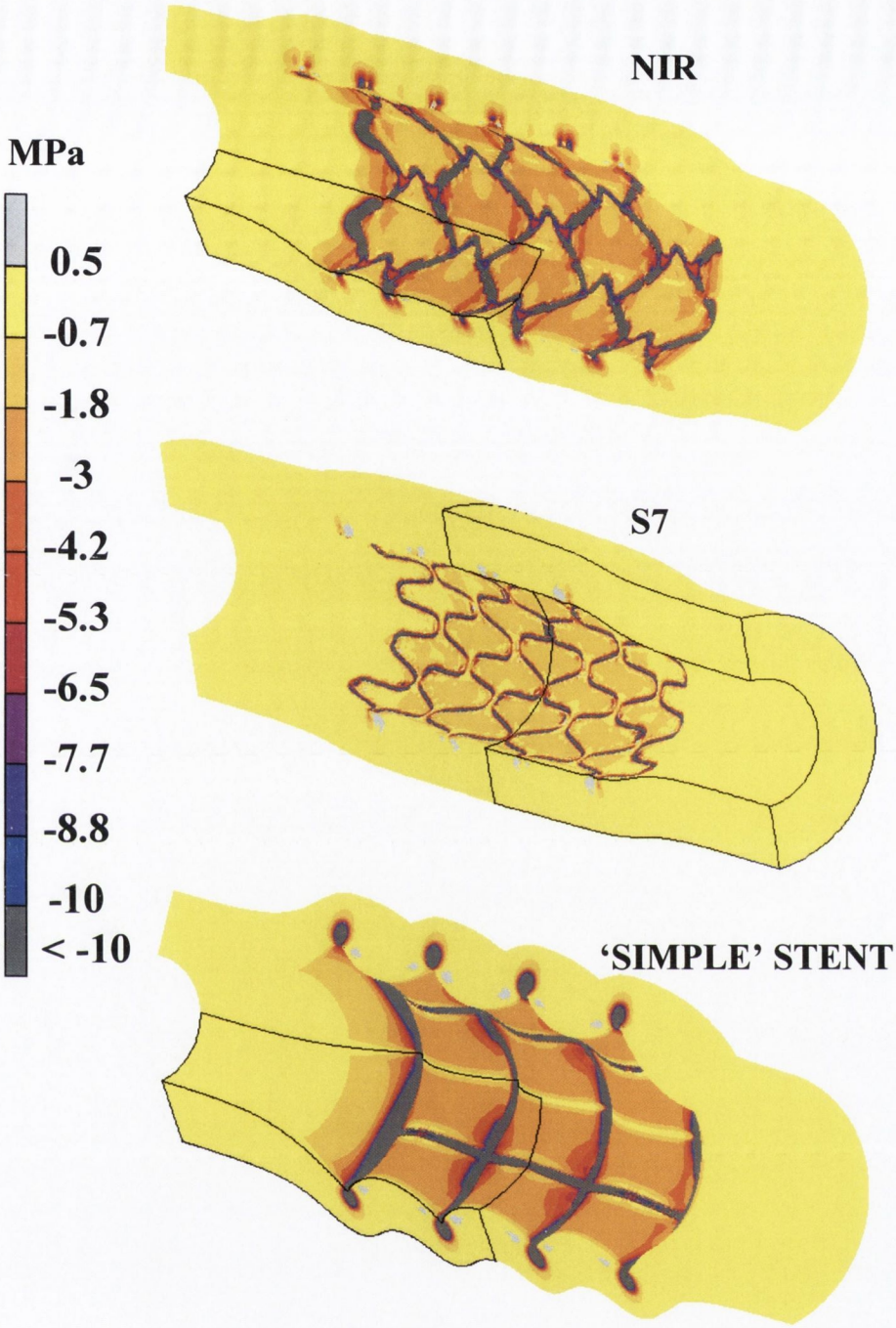

Figure 4.27 *Minimum principal stresses induced within segments of idealised cylindrical stenosed vessels stented with the NIR, S7 and 'simple' stents, axial stretch applied (λ_z=1.2) and original vessel lumen diameter of 2 mm.*

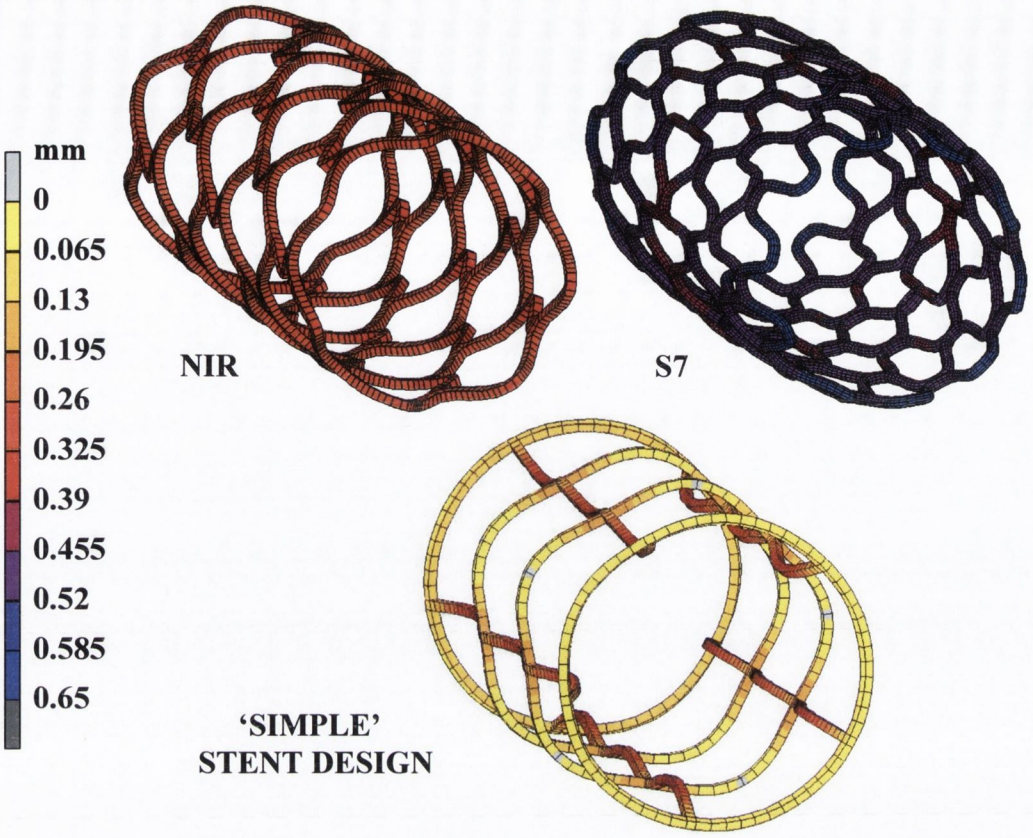

Figure 4.28 *Radial retraction during the NIR, S7 and 'simple' stenting procedures within the idealised cylindrical stenosed vessels.*

The final minimum lumen diameter of the stented vessels was found to 2.7 mm, 2.53 mm and 2.76 for the NIR, S7 and 'simple' stents, respectively.

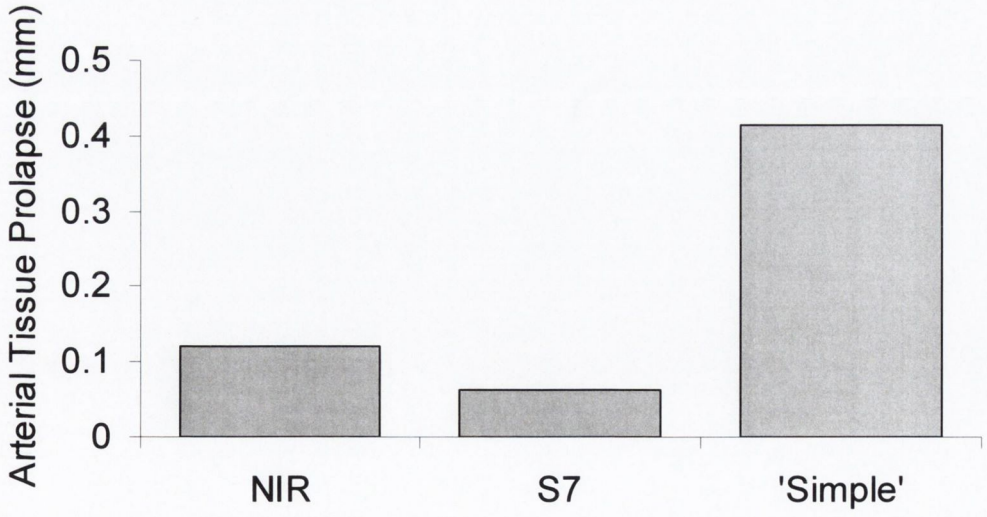

Figure 4.29 *Maximum arterial tissue draping/prolapse within the struts of the NIR, S7 and 'simple' stenting procedures in the idealised cylindrical stenosed vessels.*

4.4.2.3 Atherosclerotic Vessels - Localised lesion

The NIR, S7, and 'simple' stent designs were deployed within cylindrical vessels with a crescent shaped concentric lesion, see Figures 4.30-4.32. The vessel had a minimum initial inner diameter of 2 mm, with plaque material within the vessel of maximum thickness of 0.5 mm and healthy arterial tissue of 0.5 mm thickness. The deformed stented vessels illustrate tissue prolapsing within the struts and hence the scaffolding properties of each stent design (Figures 4.30-4.32).

As with the previous vessel geometries, the maximum and minimum principal stress induced within the cylindrical vessels with the localised lesion are considerably higher in both the NIR and 'simple' stent designs than in the vessel stented with the S7 stent, see Figures 4.33 and 4.34. The stresses are highest in the centre of the vessel at the region of maximum stenosis and also around the stent struts. The lower stresses, and lower volume of material stressed at high levels, in the vessel stented with the S7 stent is due to the greater radial retraction of the S7 stent, see Figure 4.35.

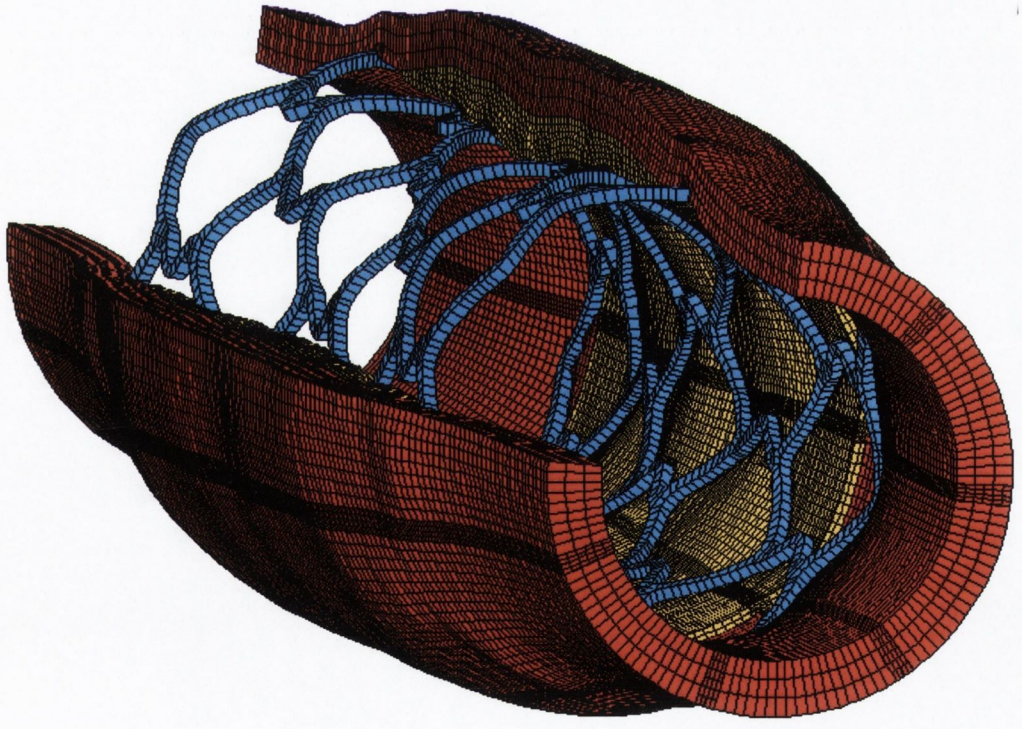

Figure 4.30 *Cylindrical vessel with a localised lesion (yellow) stented with the NIR stent.*

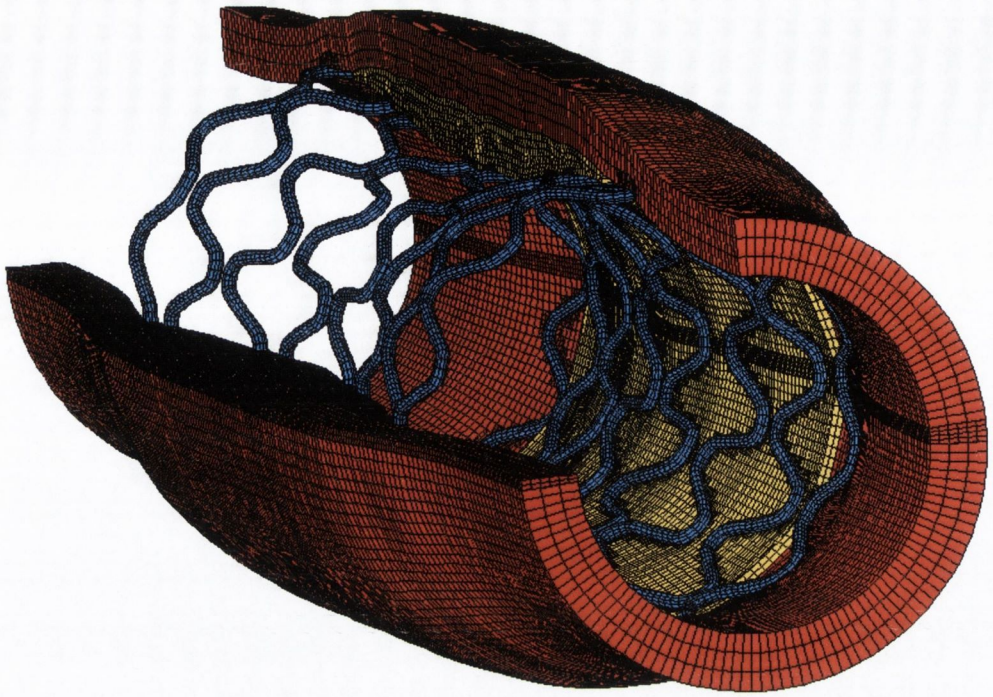

Figure 4.31 *Cylindrical vessel with a localised lesion (yellow) stented with the S7 design.*

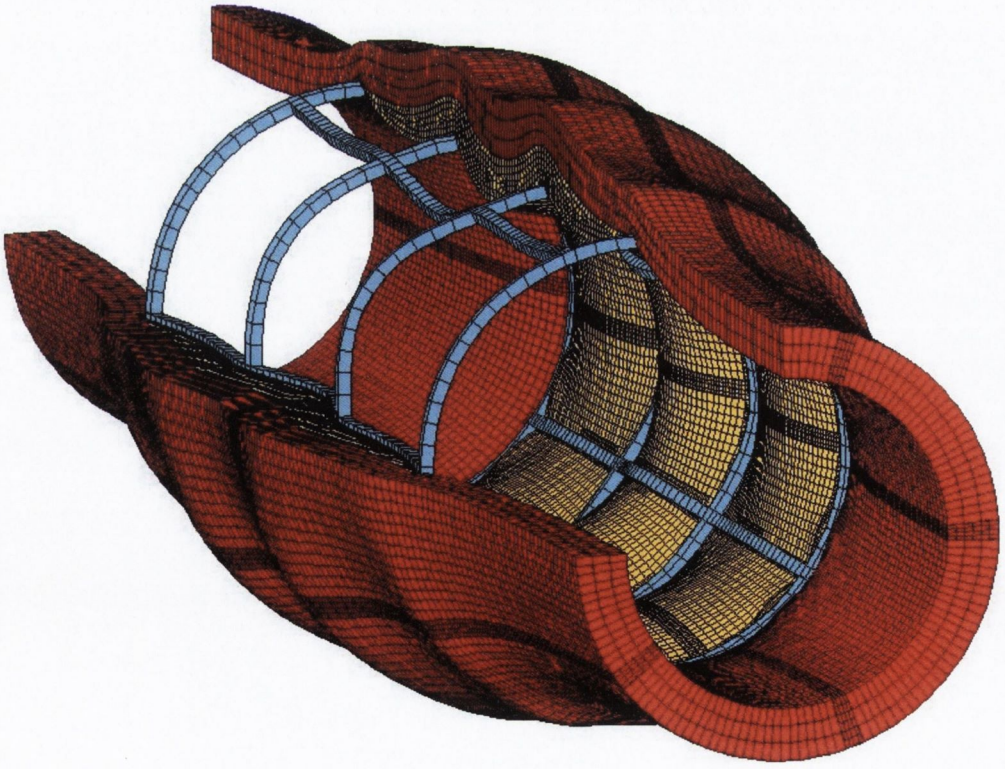

Figure 4.32 *Cylindrical vessel with a localised lesion (yellow) stented with the 'simple' stent design.*

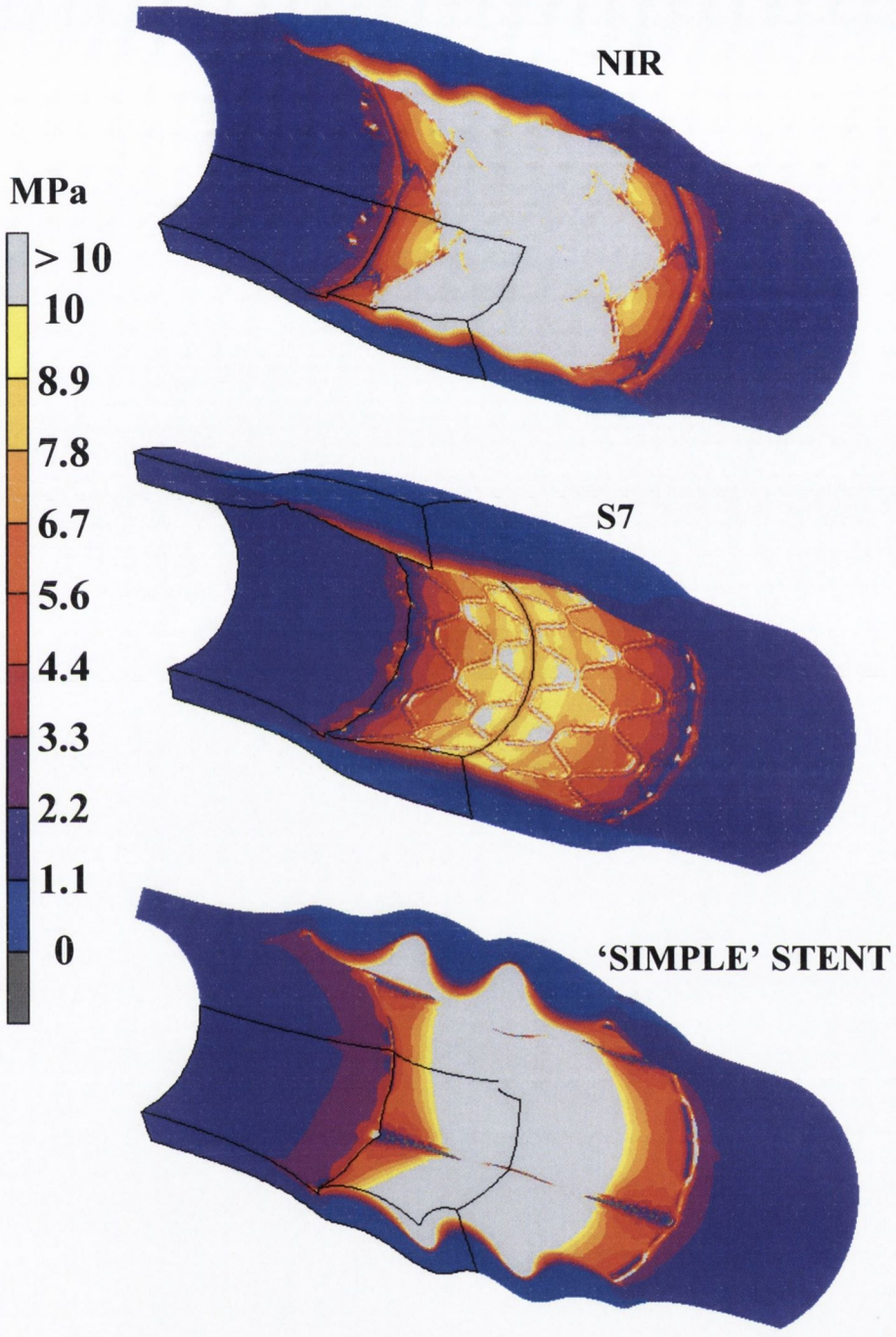

Figure 4.33 *Maximum principal stresses induced within segments of vessels, with a localised lesion, stented with the NIR, S7 and 'simple' stents, axial stretch applied (λ_z=1.2) and original vessel minimum lumen diameter of 2 mm.*

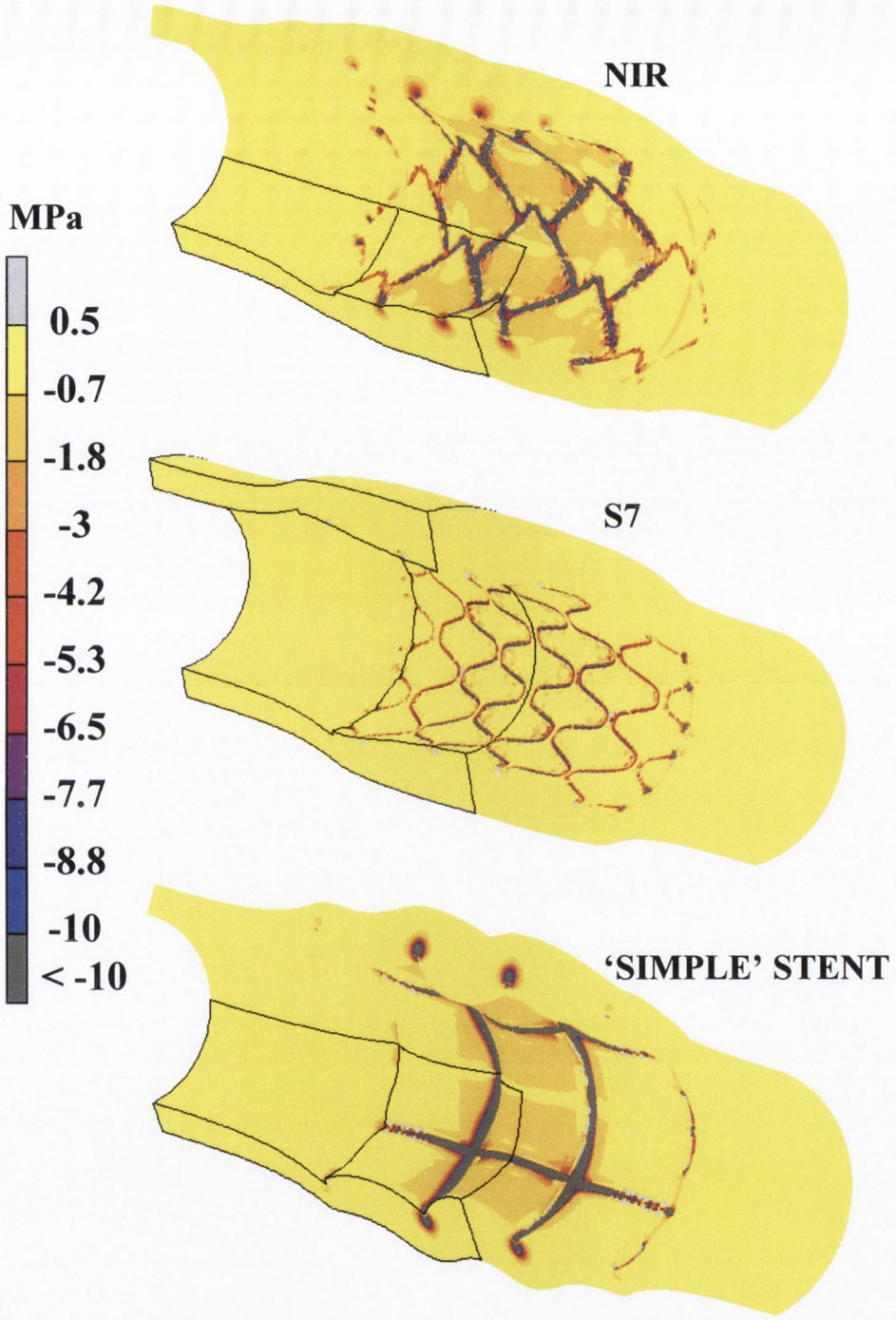

Figure 4.34 *Minimum principal stresses induced within segments of vessels, with a localised lesion, stented with the NIR, S7 and 'simple' stents, axial stretch applied (λ_z=1.2) and original vessel minimum lumen diameter of 2 mm.*

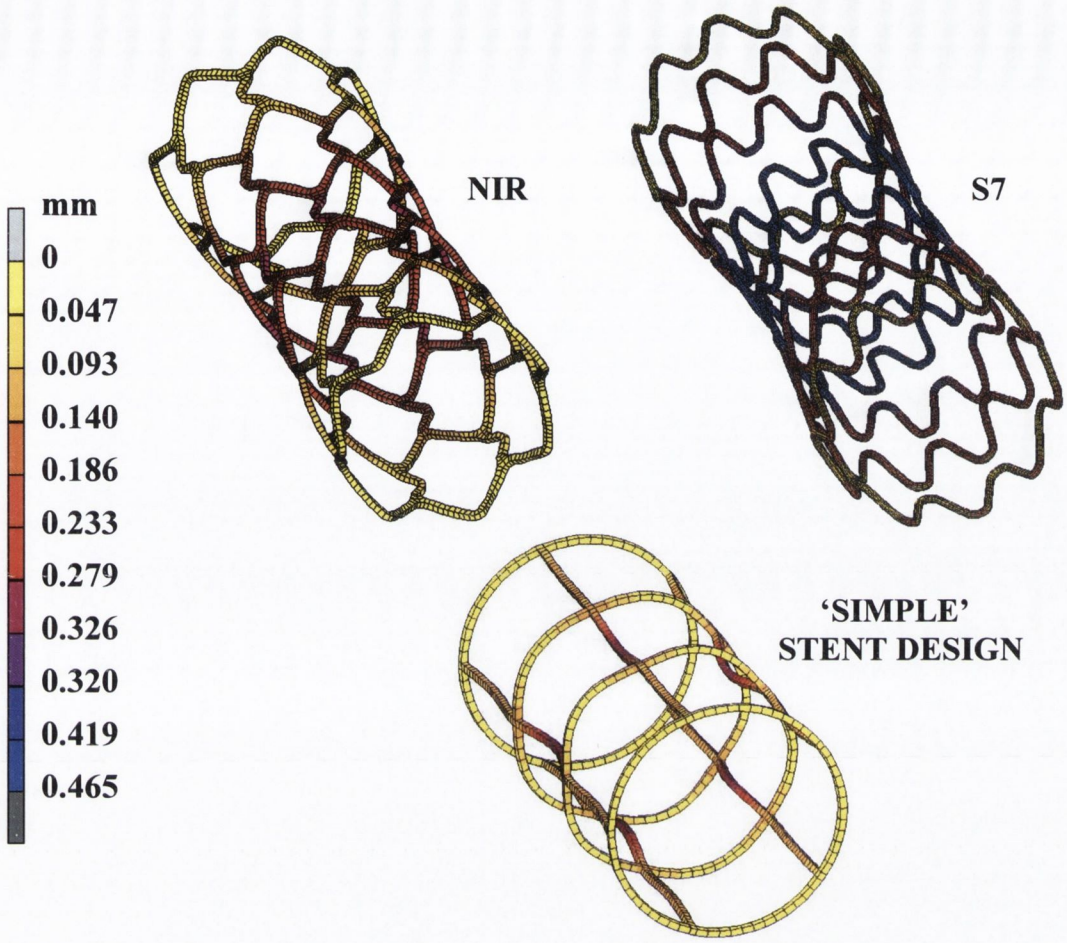

Figure 4.35 *Radial retraction during the NIR, S7 and 'simple' stenting procedures within the atherosclerotic vessels with a localised lesion.*

The flexibility of the modular S7 stent, as opposed to the other two more rigid laser cut type stents, allows the stent to conform to the altering contours of the inner lumen of the vessel with the localised lesion. This manifests itself in greater retraction of the S7 stent during the stenting procedure in these finite element analyses. By retracting, the stent maintains the stresses in the vessel at a lower level than in the vessels stented by the other two stents, see Figures 4.33 and 4.34. The S7 stent also stresses less volume of the arterial wall to high stress levels compared with the NIR and the 'simple' stent design, see Figure 4.36. Vessel patency is still achieved by the S7 stent, which exhibits superior scaffolding properties to the other two stents in a vessel with a localised lesion, see Figure 4.37.

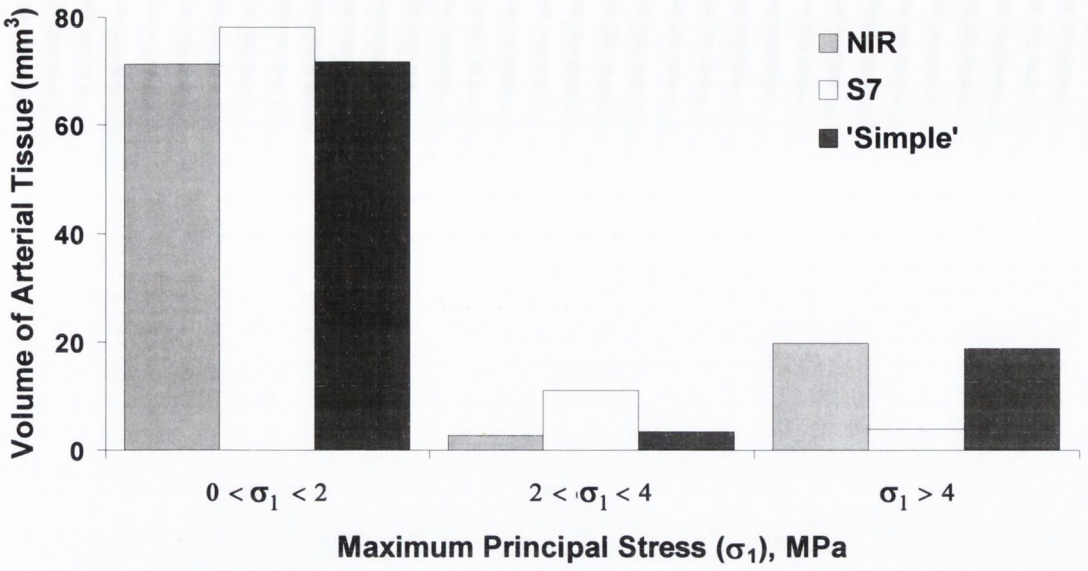

Figure 4.36 *Maximum principal stress volumes for the arterial tissue in the atherosclerotic vessel stented with a NIR, S7 and 'simple' stent.*

The final minimum lumen diameter of the stented vessels was found to 2.79 mm, 2.63 mm and 2.71 at the vessel stenosis for the NIR, S7 and 'simple' stents, respectively.

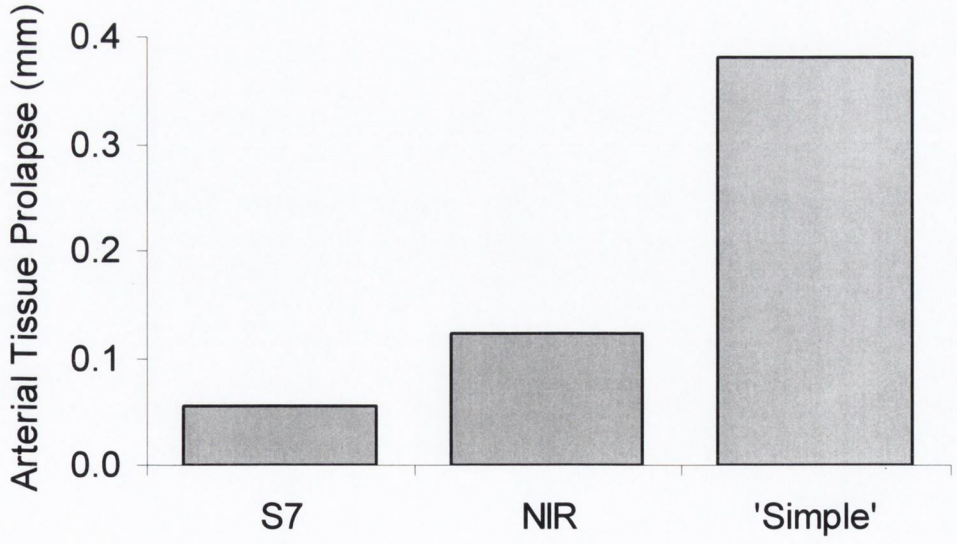

Figure 4.37 *Maximum arterial tissue draping/prolapse in the atherosclerotic vessel stented with a NIR, S7 and 'simple' stent.*

Finally it should be noted that for all of the analyses the contact area between the stent and the artery was found to be 13.9 mm^2 for the NIR stent, 11.3 mm^2 the S7 stent, and 8 mm^2 for the 'simple' stent design.

4.5 Computational Model of In-Stent Restenosis

This section presents the results obtained for the computational model of in-stent restenosis within an idealised cylindrical vessel stented with the three different stent designs. The vessels stented were idealised cylindrical vessels the same as those shown in Section 4.4.2.1 (page 104).

As stated previously, the damage stimulus was calculated based on either (i) the maximum principal stress, (ii) the minimum principal stress, or (iii) both the maximum and minimum principal stress. The relationship between the rate of damage accumulation and the magnitude of the absolute value of the maximum or minimum principal stresses was obtained from the fatigue test data (shown in Section 4.3.2, Figure 4.14). The constant, c, in Eqn. 3.17 (Chapter 3, Section 3.6.1), which relates the number of proliferating smooth muscle cells to the damage present was determined for each stimulus such that the restenosis process converged as outlined in Chapter 3. This constant was uniquely determined for each of the stimuli from (i) to (iii) above and was calculated to be 1.75×10^6, 1.6×10^6 and 9.52×10^5 for the three stimuli, respectively.

Each analysis was carried out over time with a maximum of 100 days allowed for restenosis to develop within the lumen of the vessel. Colour coding is used throughout the following results to distinguish each different material type in the analyses, see Figure 4.38.

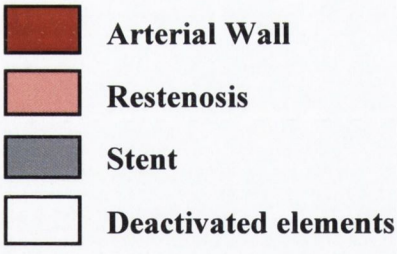

Figure 4.38 *Material colour coding in the in-stent restenosis models.*

4.5.1 Stimulus: Maximum principal stress

The idealised cylindrical vessel was stented with the NIR stent (Figure 4.39) with an active thrombotic layer and potential restenotic growth within the lumen of the vessel (Figure 4.40).

Figure 4.39 *Deformed geometry of a segment of the idealised cylindrical vessel stented with the NIR stent (λ_z= 1.2).*

Figure 4.40 *Deformed geometry of a segment of the idealised cylindrical vessel stented with the NIR stent illustrating the thrombotic layer (pink) and all of the potential restenotic growth within the lumen of the vessel (white elements).*

Many of the layers of potential restenotic material within the lumen of the vessel did not activate during the in-stent restenosis analysis. These layers are removed to enable the pattern of restenosis in the NIR stented vessel to be seen more clearly (Figure 4.41). The in-stent restenosis growth was time limiting and stopped after 20 days in the NIR stented vessel. The maximum restenotic growth can clearly be seen to be concentrated within the struts of the stent when the stimulus chosen was maximum principal stresses within the arterial wall, see Figures 4.41 and 4.42. Restenosis developed gradually over the 20 days to converge to the final outcome shown in Figure 4.41-4.43. The pattern of restenosis in a transverse cut through the vessel illustrates the maximum restenosis is between the stent struts and significantly narrows the vessel lumen, see Figure 4.43.

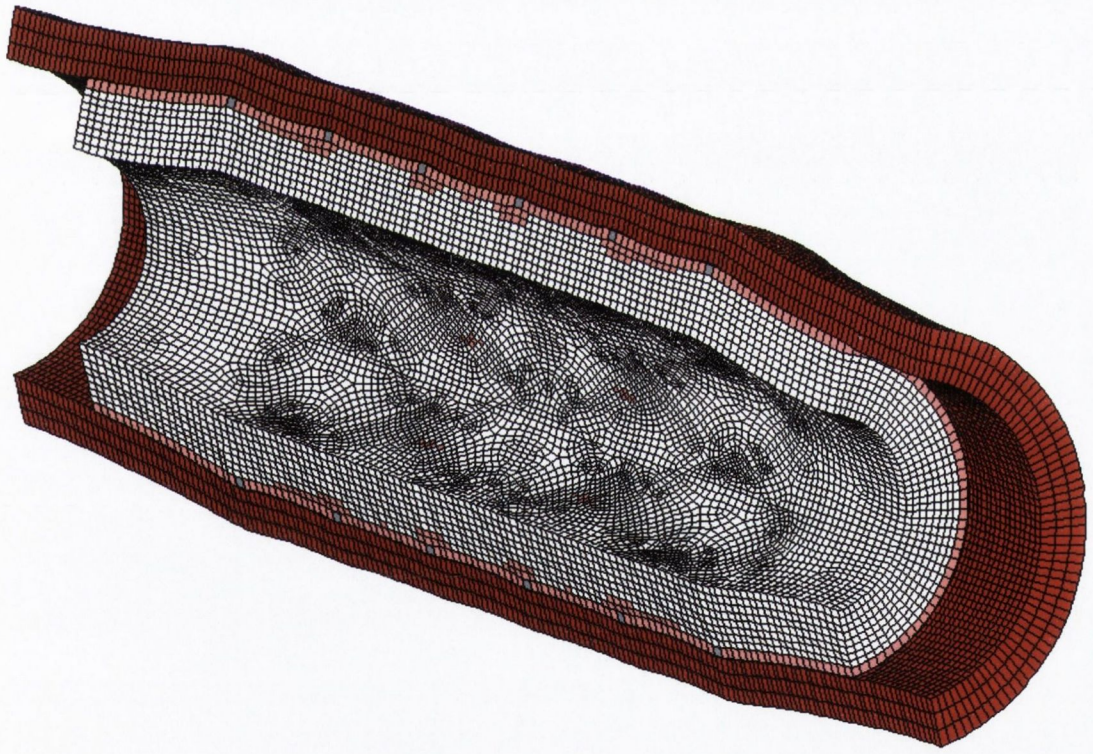

Figure 4.41 *Deformed geometry of a segment of the idealised cylindrical vessel stented with the NIR stent with completely deactivated layers of potential restenotic tissue removed.*

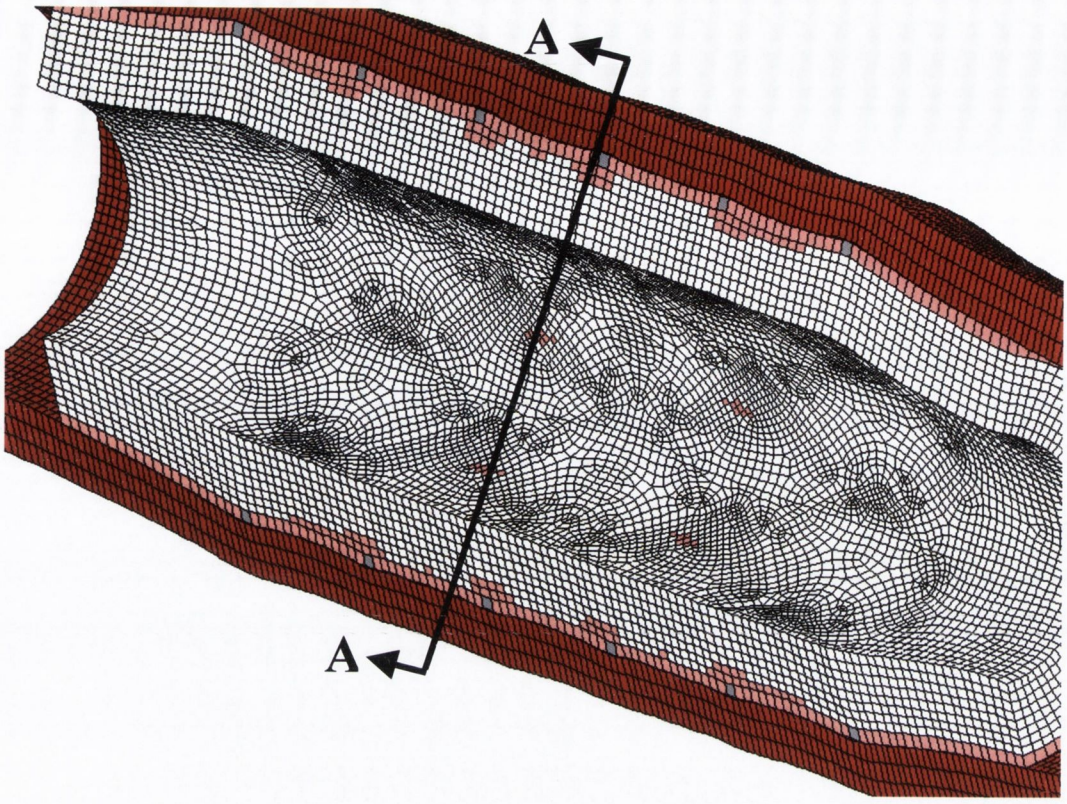

Figure 4.42 *Close-up view of the deformed geometry shown in Figure 4.41 with completely deactivated layers of restenotic tissue removed.*

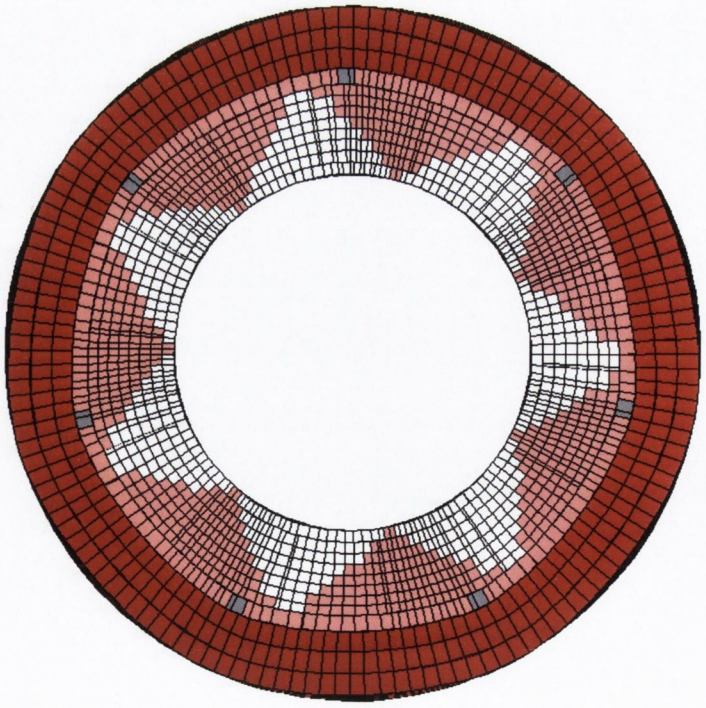

Figure 4.43 *Section A-A shown in Figure 4.42, the cross-section of maximum restenosis in the cylindrical vessel stented with the NIR stent.*

The idealised cylindrical vessel was also stented with the S7 stent (Figure 4.44) with an active thrombotic layer and potential restenotic growth within the lumen of the vessel (Figure 4.45). Again, many of the layers of potential restenotic material within the lumen of the vessel did not activate during the in-stent restenosis analysis in the S7 stented vessel. These layers are removed to enable the pattern of restenosis in the S7 stented vessel to be seen more clearly (Figure 4.46). The in-stent restenosis growth was time limiting and stopped after 10 days in the S7 stented vessel. The maximum restenotic growth can clearly be seen to be concentrated within the struts of the stent when the stimulus chosen was maximum principal stresses within the arterial wall, see Figures 4.46 and 4.47. Restenosis developed gradually over the 10 days to converge to the final outcome shown in Figure 4.46-4.48. The pattern of restenosis in a transverse cut through the vessel illustrates the maximum restenosis is between the S7 stent struts; although it is two layers inside the initially activated thrombotic layer, see Figure 4.48.

Figure 4.44 *Deformed geometry of a segment of the idealised cylindrical vessel stented with the S7 stent (λ_z= 1.2).*

Figure 4.45 *Deformed geometry of a segment of the idealised cylindrical vessel stented with the S7 stent illustrating the thrombotic layer (pink) and all of the potential restenotic growth within the lumen of the vessel (white elements).*

Figure 4.46 *Deformed geometry of a segment of the idealised cylindrical vessel stented with the S7 stent with completely deactivated layers of potential restenotic tissue removed.*

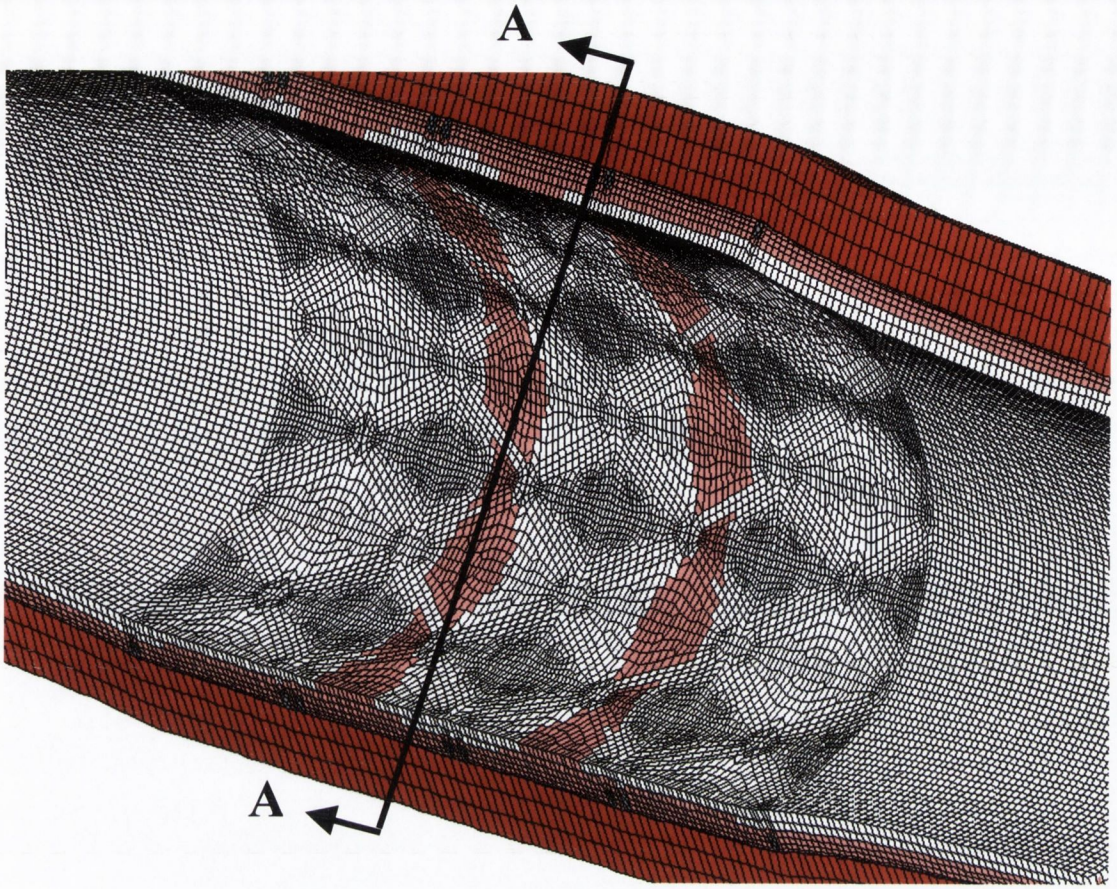

Figure 4.47 *Close-up view of the deformed geometry shown in Figure 4.46 with completely deactivated layers of restenotic tissue removed.*

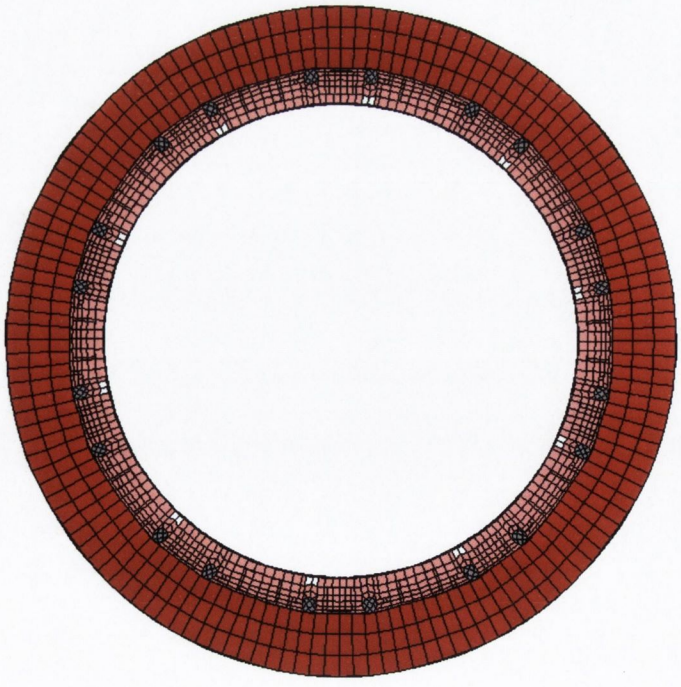

Figure 4.48 *Section A-A shown in Figure 4.47, the cross-section of maximum restenosis in the cylindrical vessel stented with the S7 stent.*

The idealised cylindrical vessel was stented with the 'simple' stent (Figure 4.49) with an active thrombotic layer and potential restenotic growth within the lumen of the vessel (Figure 4.50). The layers of potential restenotic material within the lumen of the vessel that did not activate during the in-stent restenosis analysis in the 'simple' stented vessel were again removed to enable the pattern of restenosis in the 'simple' stented vessel to be seen more clearly (Figure 4.51). The in-stent restenosis growth was time limiting and stopped after 11 days in the vessel stented with the 'simple' stent. The maximum restenotic growth can clearly be seen to be concentrated between the central struts of the stent when the restenosis stimulus was maximum principal stresses within the arterial wall, see Figures 4.51 and 4.52. Restenosis developed gradually over the 11 days to converge to the final outcome shown in Figure 4.51-4.53. The pattern of restenosis in a transverse cut through the vessel illustrates the maximum restenosis is around the struts of the 'simple' stent; although, it is only three layers inside the initially activated thrombotic layer, see Figure 4.53.

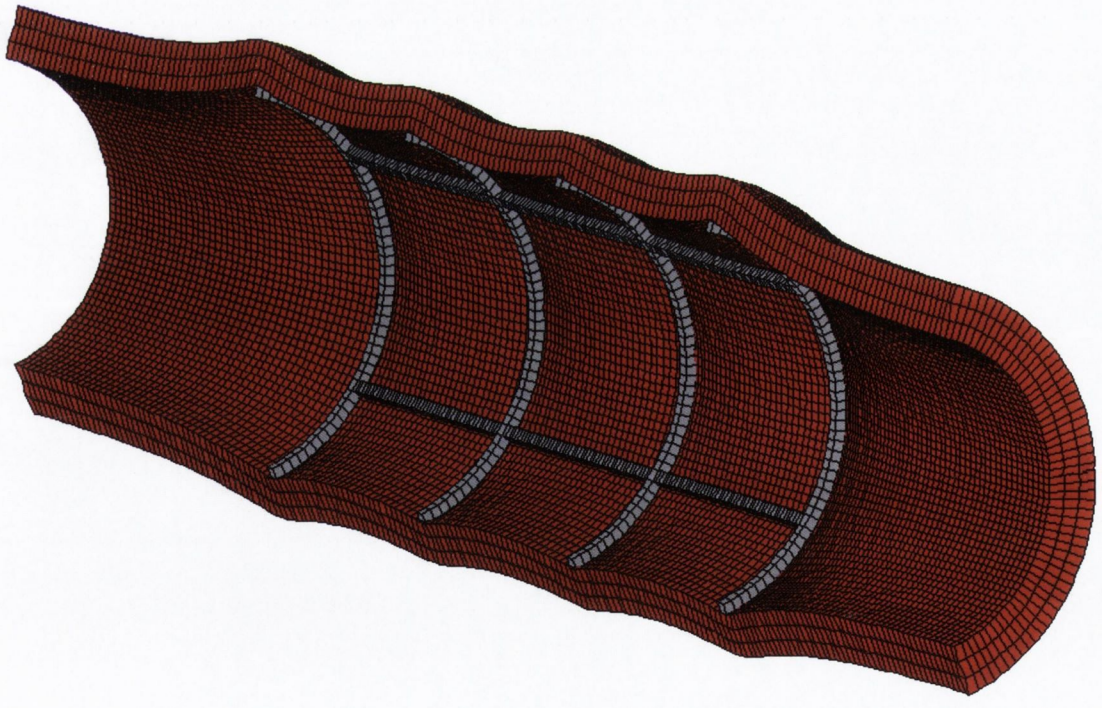

Figure 4.49 *Deformed geometry of a segment of the idealised cylindrical vessel stented with the 'simple' stent (λ_z= 1.2).*

Figure 4.50 *Deformed geometry of a segment of the idealised cylindrical vessel stented with the S7 stent illustrating the thrombotic layer (pink) and all of the potential restenotic growth within the lumen of the vessel (white elements).*

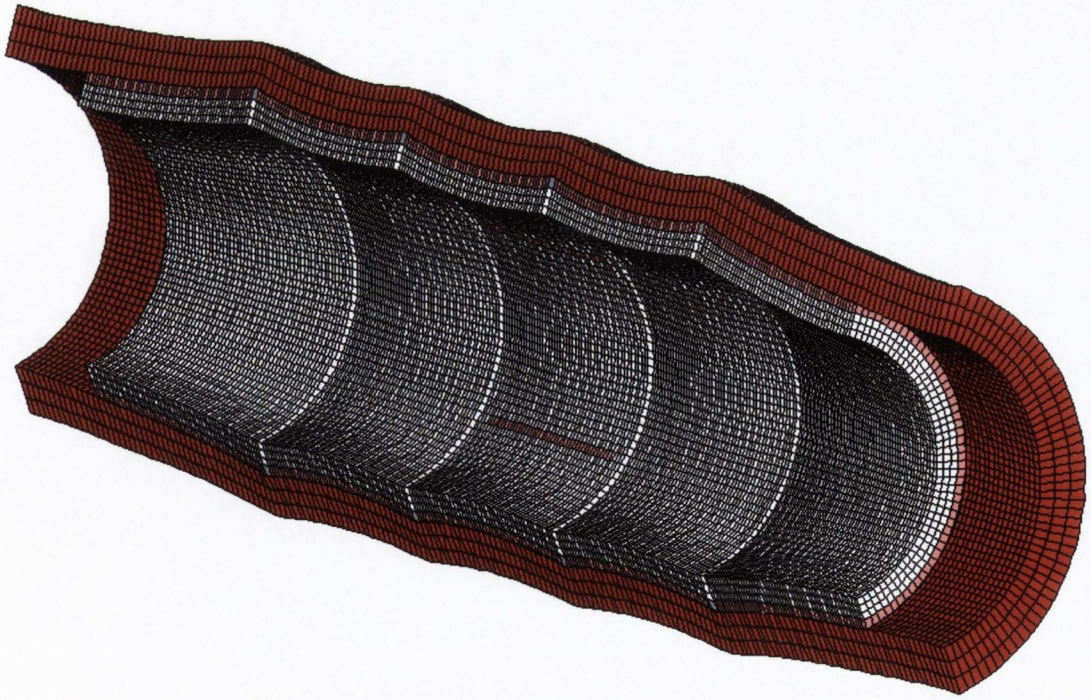

Figure 4.51 *Deformed geometry of a segment of the idealised cylindrical vessel stented with the 'simple' stent with completely deactivated layers of potential restenotic tissue removed.*

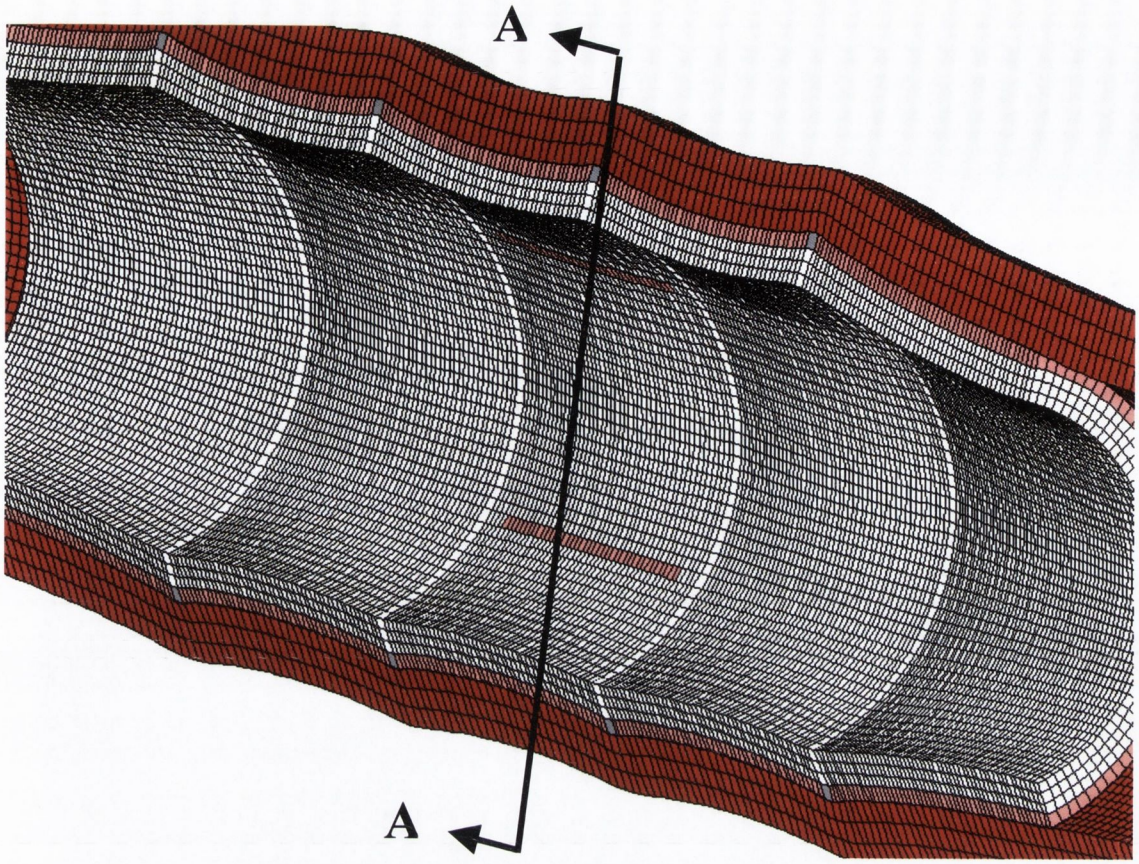

Figure 4.52 *Close-up view of the deformed geometry shown in Figure 4.51 with completely deactivated layers of restenotic tissue removed.*

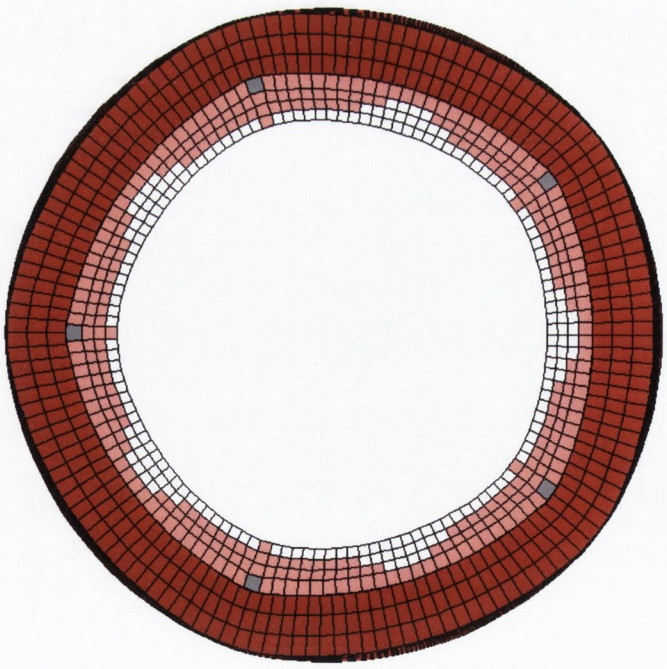

Figure 4.53 *Section A-A shown in Figure 4.52, the cross-section of maximum restenosis in the cylindrical vessel stented with the 'simple' stent.*

Comparing the restenotic growth within the lumen of the three stented vessels it can be seen that the NIR stent would have the greatest intimal growth compared with the other two stents, if the stimulus for restenotic growth is taken as the maximum principal stress in the arterial tissue, see Figure 4.54. The growth would also be concentrated between the stent struts for this stimulus rather than around the struts of the stents, see Figure 4.54.

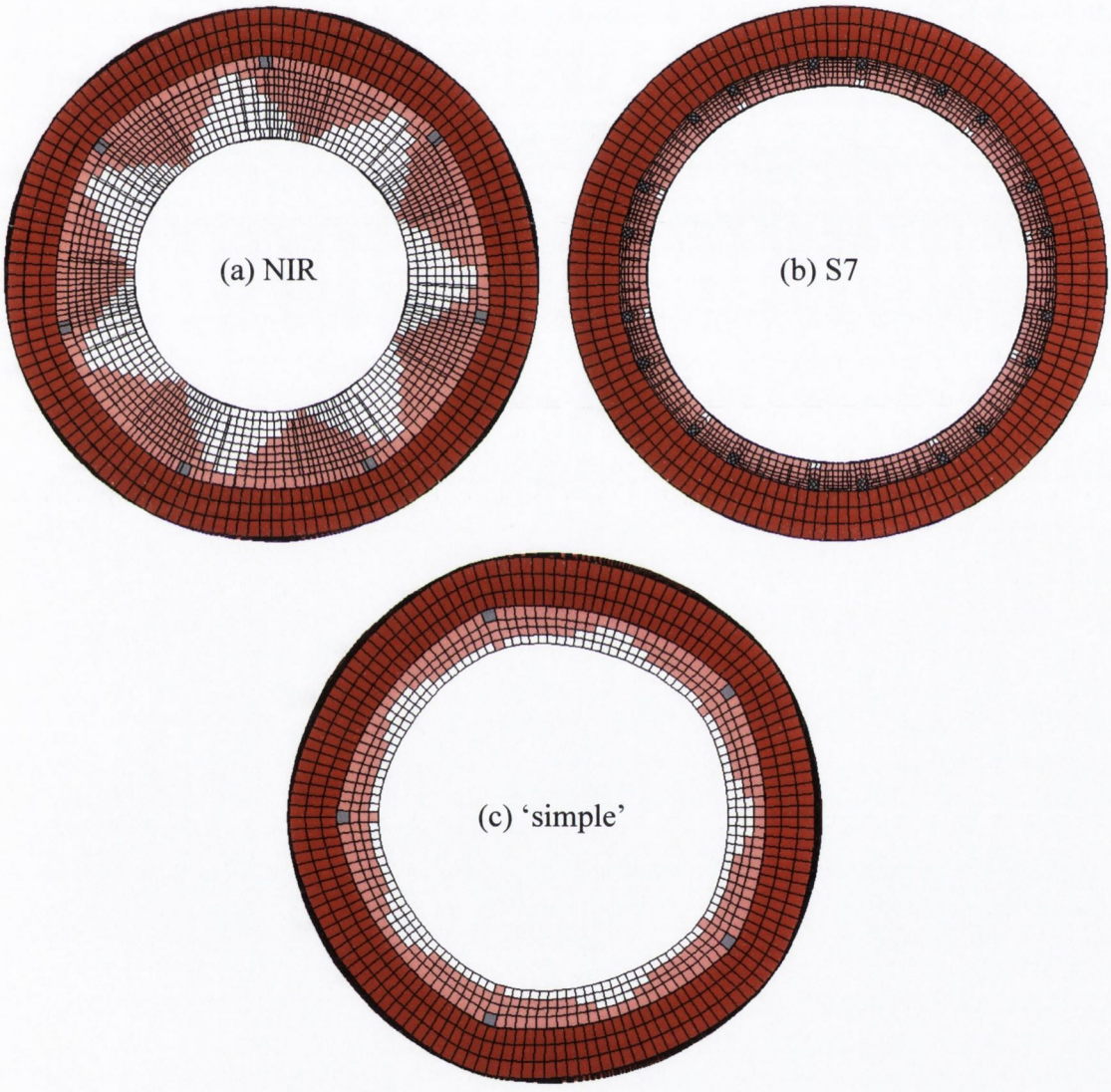

Figure 4.54 *Sections A-A (shown in Figures 4.43, 4.48 and 4.53). The cross-section of maximum restenosis in the cylindrical vessel stented with (a) the NIR stent, with restenosis growth completed at 20 days, (b) the S7 stent, with restenosis growth completed at 10 days and (c) the 'simple' stent, with restenosis growth completed at 11 days.*

4.5.2 Stimulus: Minimum principal stress

In-stent restenosis was allowed to develop within the idealised cylindrical vessel stented with the NIR, S7 and 'simple' stents using the minimum principal stresses induced within the arterial wall as the damage stimulus.

The NIR stented vessel generated restenosis within the lumen of the vessel as a response to damage, based on the magnitude of the minimum principal stresses in the vessel. The restenotic growth was found to be localised around the stent struts and greatest at the ends of the stent, see Figure 4.55. The pattern of restenosis in the S7 and 'simple' stented vessels as a response to damage, based on the magnitude of the minimum principal stresses in the vessels, also illustrate restenotic growth localised around the stent struts and at a maximum at the ends of the stents (see Figures 4.58-4.60 for the S7 stented vessel and Figures 4.61-4.63 for the 'simple' stented vessel).

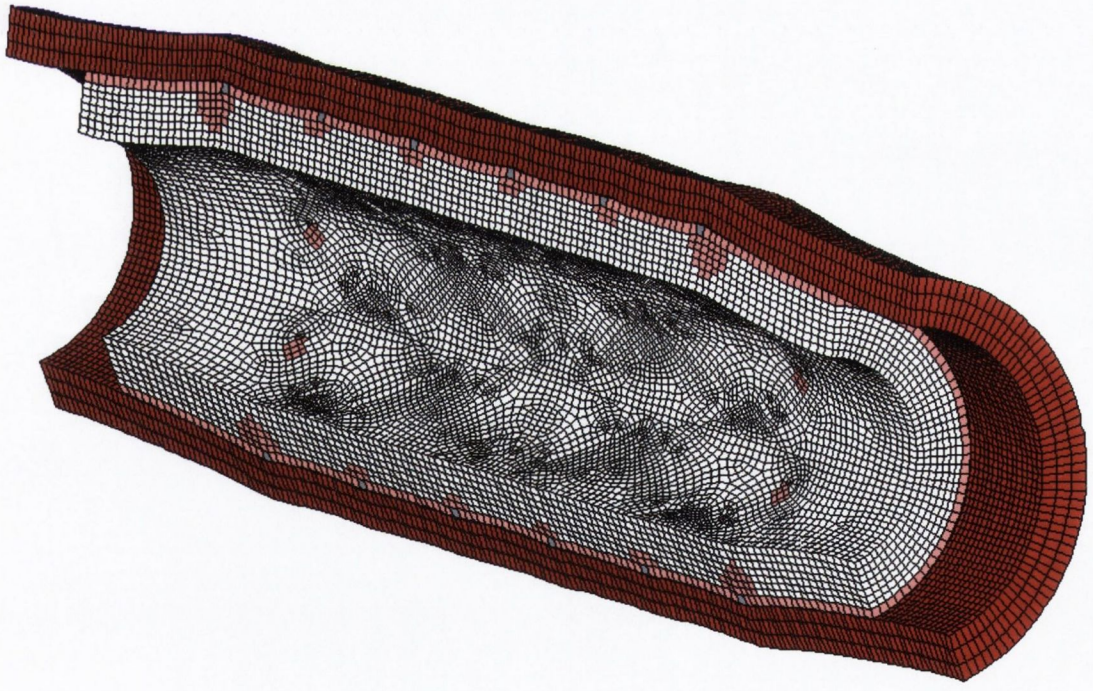

Figure 4.55 *Deformed geometry of a segment of the idealised cylindrical vessel stented with the NIR stent with completely deactivated layers of potential restenotic tissue removed.*

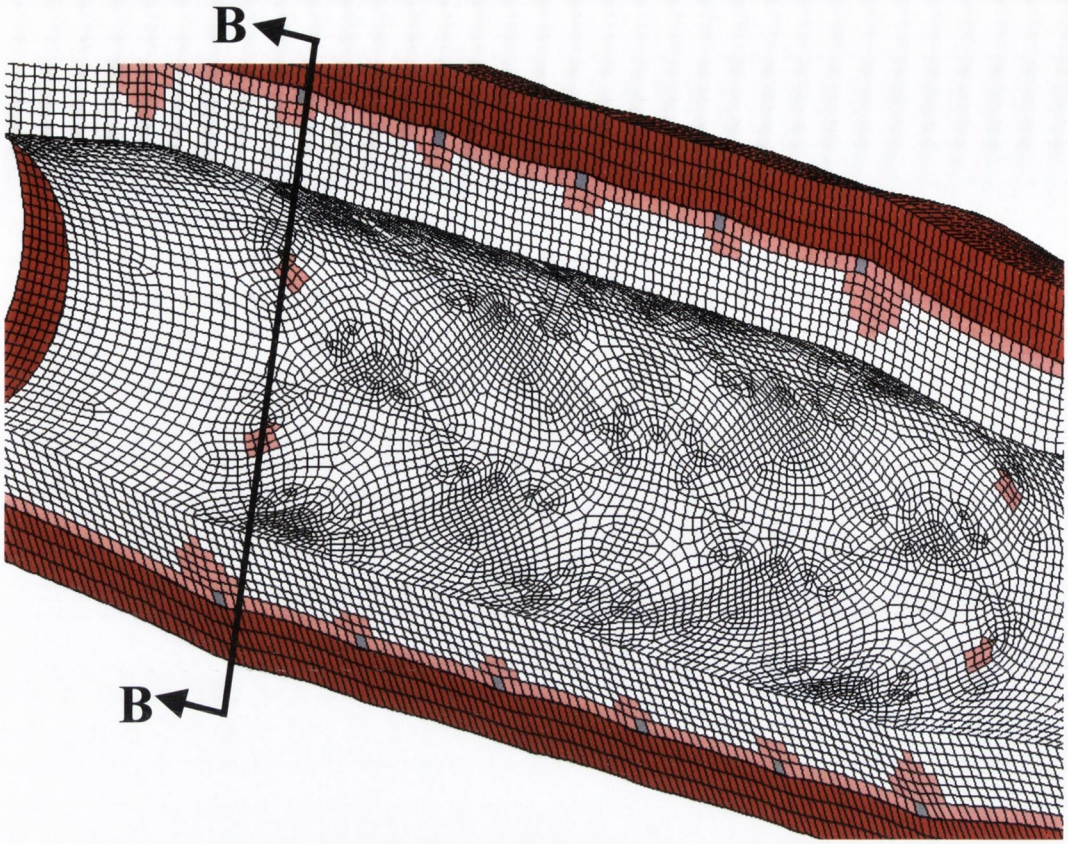

Figure 4.56 *Close-up view of the deformed geometry shown in Figure 4.55 with completely deactivated layers of restenotic tissue removed.*

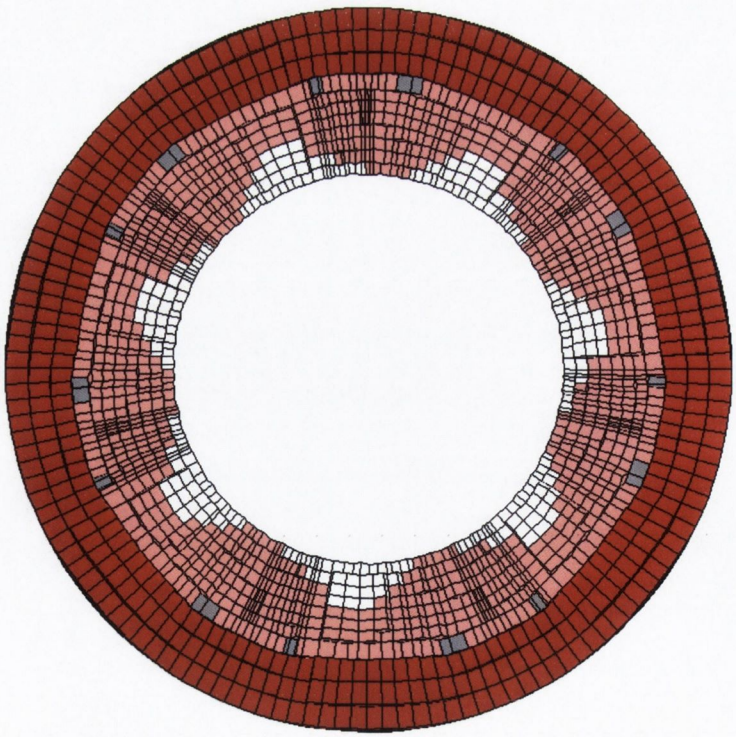

Figure 4.57 *Section B-B shown in Figure 4.56, the cross-section of maximum restenosis in the cylindrical vessel stented with the NIR stent, i.e. the end of the stent.*

Figure 4.58 *Deformed geometry of a segment of the idealised cylindrical vessel stented with the S7 stent with completely deactivated layers of potential restenotic tissue removed.*

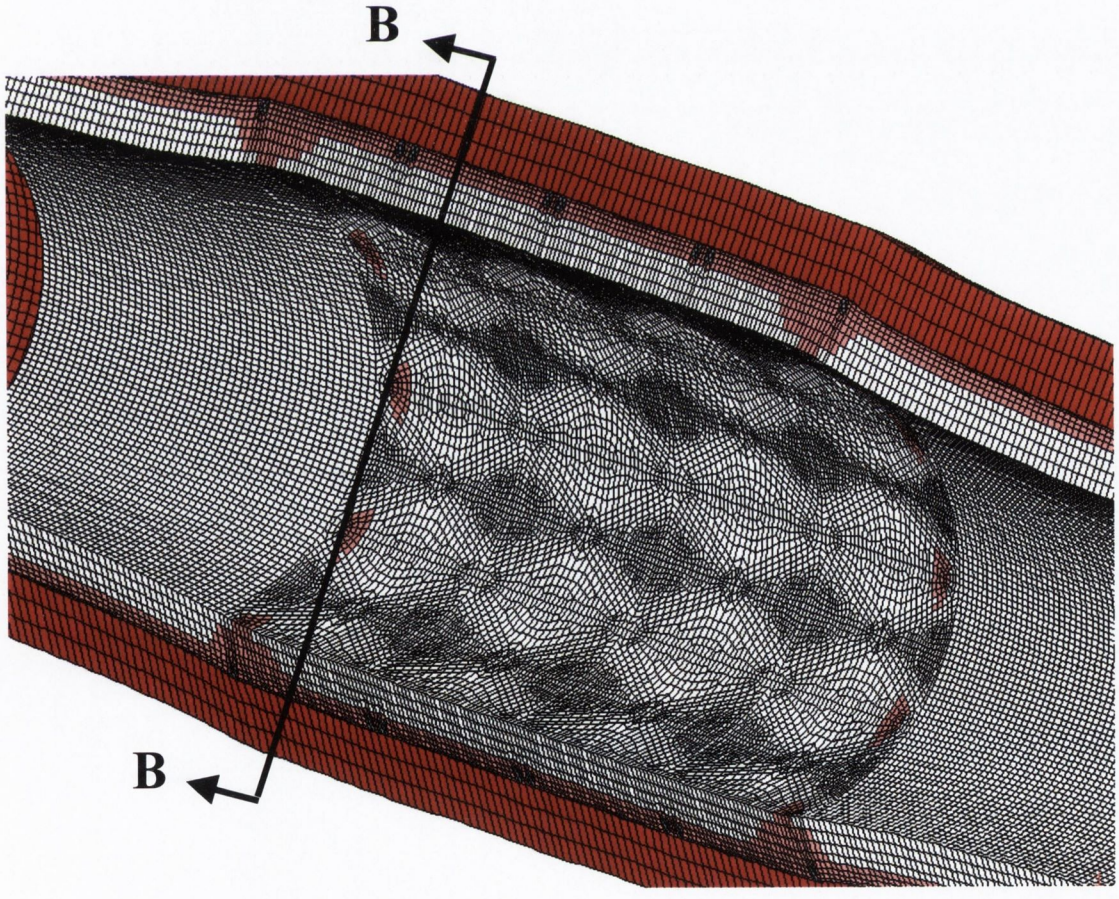

Figure 4.59 *Close-up view of the deformed geometry shown in Figure 4.58 with completely deactivated layers of restenotic tissue removed.*

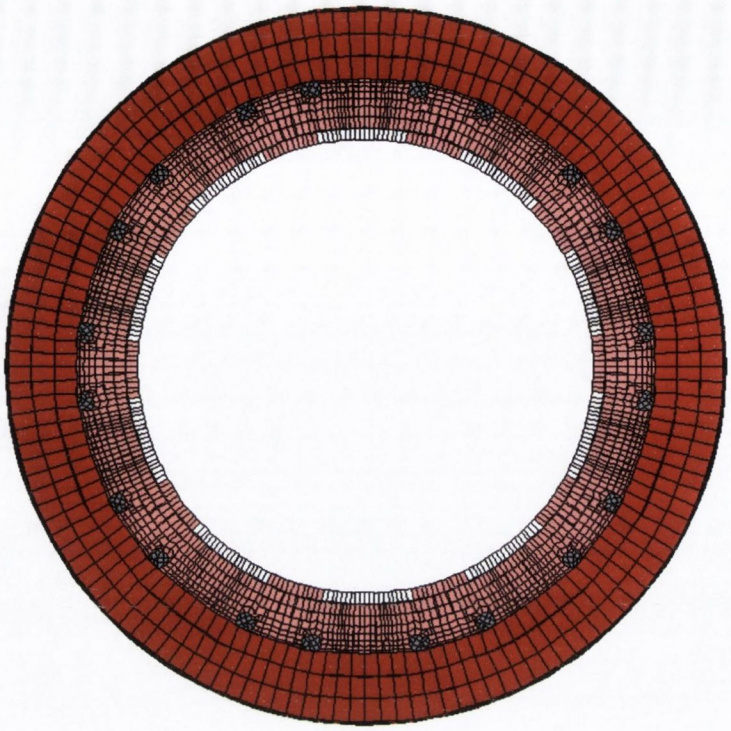

Figure 4.60 *Section B-B shown in Figure 4.59, the cross-section of maximum restenosis in the cylindrical vessel stented with the S7 stent, i.e. the end of the stent.*

Figure 4.61 *Deformed geometry of a segment of the idealised cylindrical vessel stented with the 'simple' stent with completely deactivated layers of potential restenotic tissue removed.*

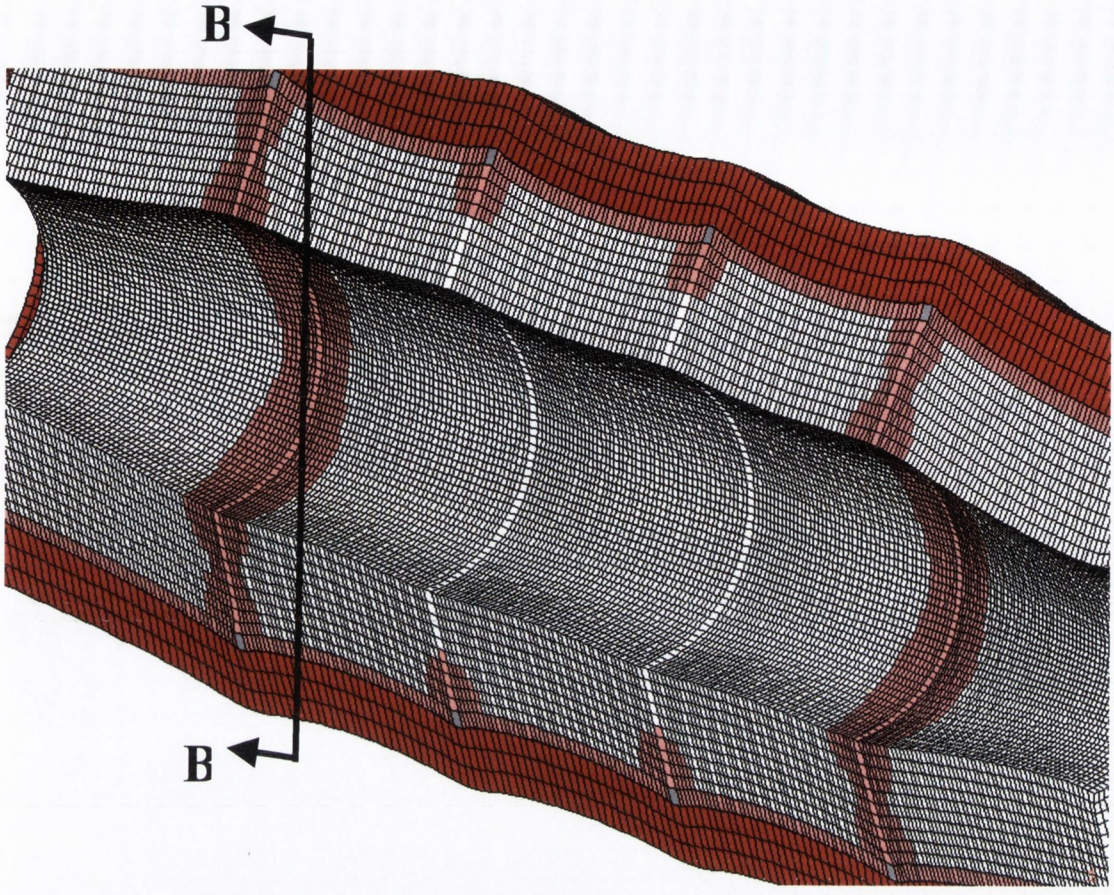

Figure 4.62 *Close-up view of the deformed geometry shown in Figure 4.61 with completely deactivated layers of restenotic tissue removed.*

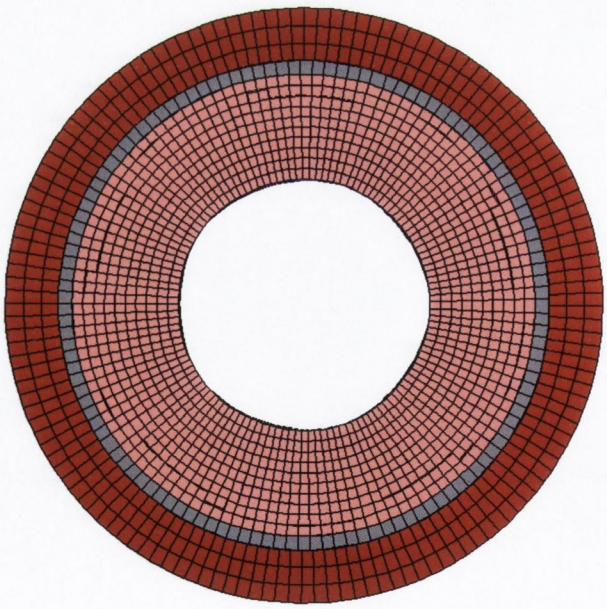

Figure 4.63 *Section B-B shown in Figure 4.61, the cross-section of maximum restenosis in the cylindrical vessel stented with the 'simple' stent, i.e. the end of the stent.*

Comparing the restenotic growth within the lumen of the three stented vessels it can be seen that the NIR and 'simple' stents would have the greatest intimal growth compared with the S7 stent, if the stimulus for restenotic growth is taken as the minimum principal stress in the arterial tissue, see Figure 4.64. Also, it can be seen that using this stimulus that the restenotic growth is concentrated in areas around the stent struts.

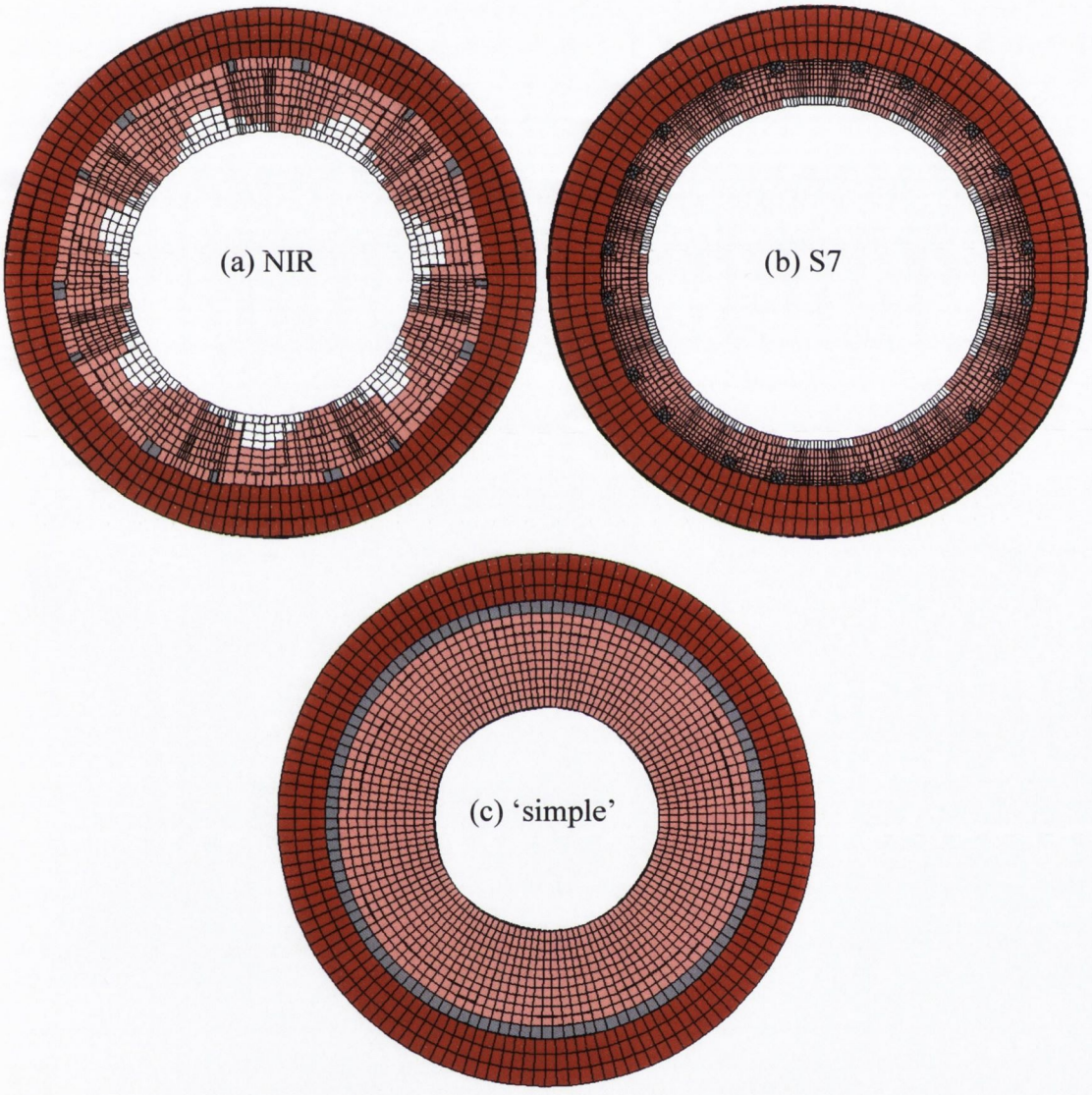

Figure 4.64 *Sections B-B (shown in Figures 4.57, 4.60 and 4.63). The cross-section of maximum restenosis in the cylindrical vessel stented with (a) the NIR stent, with restenosis growth completed at 13 days, (b) the S7 stent, with restenosis growth completed at 12 days and (c) the 'simple' stent, with restenosis growth completed at 32 days.*

4.5.3 Stimulus: Both maximum and minimum principal stress

In-stent restenosis was also allowed to develop within the idealised cylindrical vessel stented with the NIR, S7 and 'simple' stents using the sum of damage generated due to the maximum *and* minimum principal stresses induced within the arterial wall as the stimulus (the damage generated due to each stress stimulus was calculated and the two damage values summed).

The NIR stented vessel generated restenosis within the lumen of the vessel as a response to damage, based on the magnitude of both maximum and minimum principal stresses in the vessel. The restenotic growth was again found to be localised around the stent struts and greatest at the central struts and the ends of the stent, see Figure 4.65. The pattern of restenosis in the S7 and 'simple' stented vessels as a response to damage, based on the magnitude of both the maximum and minimum principal stresses in the vessels, also illustrate restenotic growth localised around the stent struts and for the S7 stent the maximum restenosis occurred at the ends of the stents (see Figures 4.68-4.70 for the S7 stented vessel and Figures 4.71-4.73 for the 'simple' stented vessel).

Figure 4.65 *Deformed geometry of a segment of the idealised cylindrical vessel stented with the NIR stent with completely deactivated layers of potential restenotic tissue removed.*

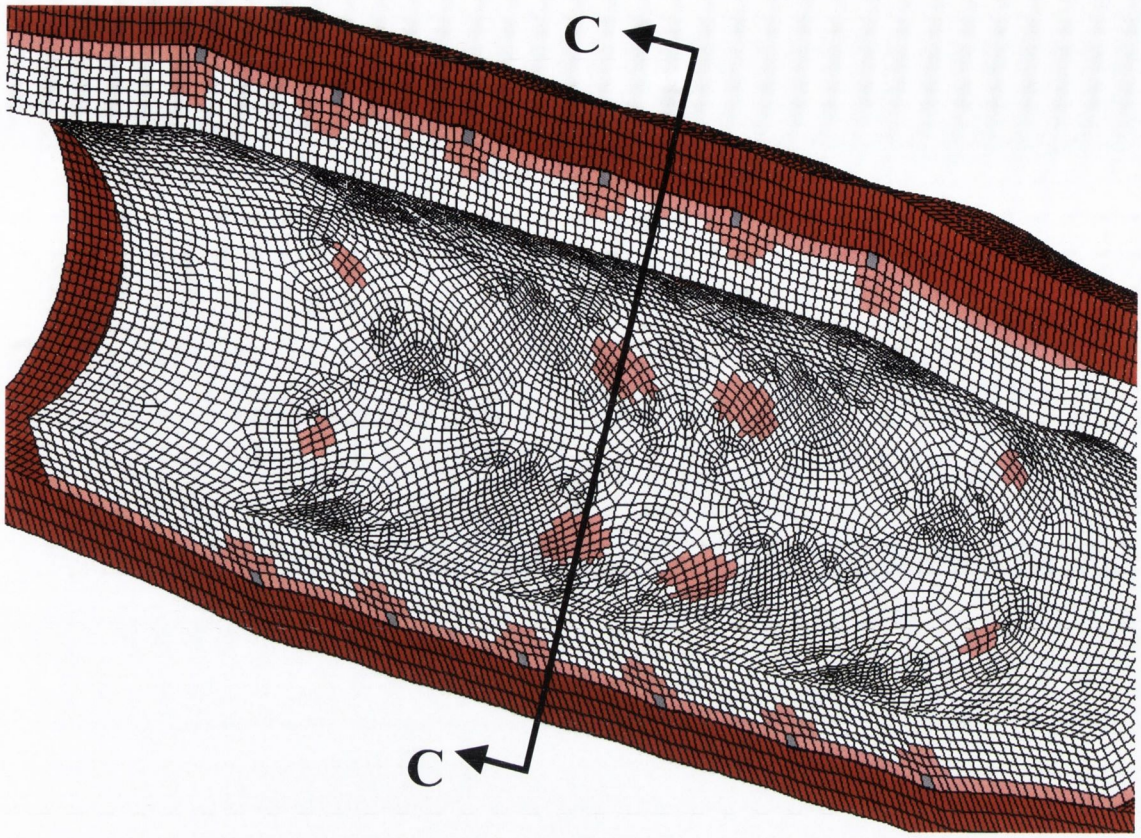

Figure 4.66 *Close-up view of the deformed geometry shown in Figure 4.65 with completely deactivated layers of restenotic tissue removed.*

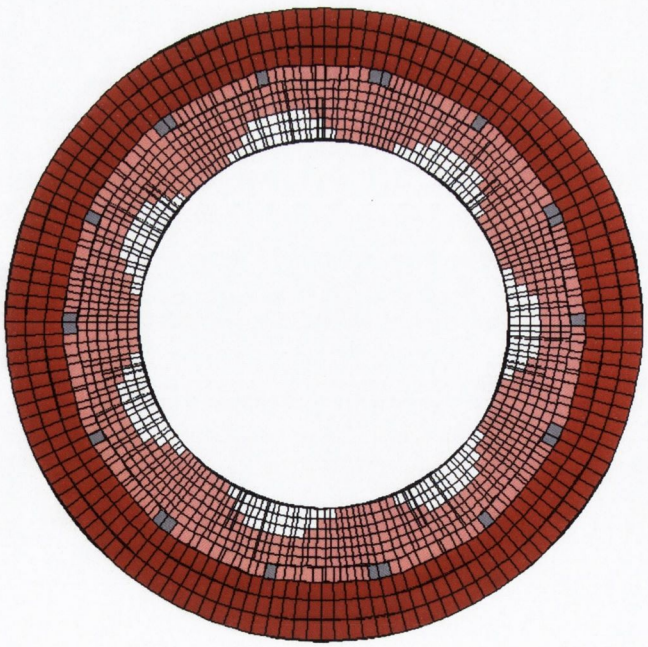

Figure 4.67 *Section C-C shown in Figure 4.66, the cross-section of maximum restenosis in the cylindrical vessel stented with the NIR stent, i.e. the middle of the stent.*

Figure 4.68 *Deformed geometry of a segment of the idealised cylindrical vessel stented with the S7 stent with completely deactivated layers of potential restenotic tissue removed.*

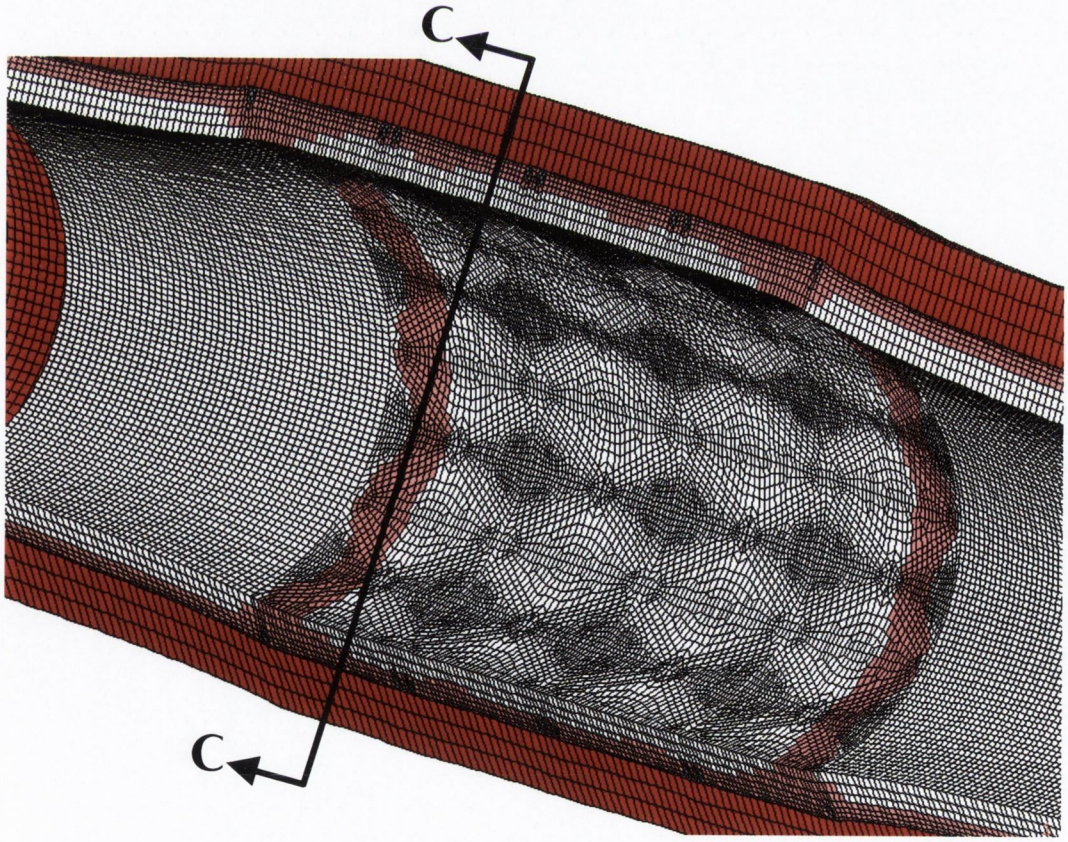

Figure 4.69 *Close-up view of the deformed geometry shown in Figure 4.68 with completely deactivated layers of restenotic tissue removed.*

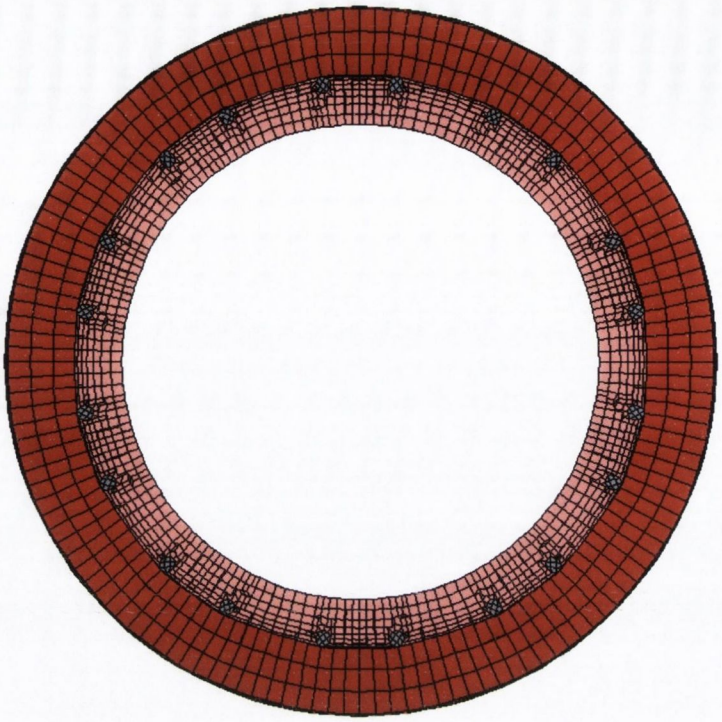

Figure 4.70 *Section C-C shown in Figure 4.69, the cross-section of maximum restenosis in the cylindrical vessel stented with the S7 stent, i.e. the end of the stent.*

Figure 4.71 *Deformed geometry of a segment of the idealised cylindrical vessel stented with the 'simple' stent with completely deactivated layers of potential restenotic tissue removed.*

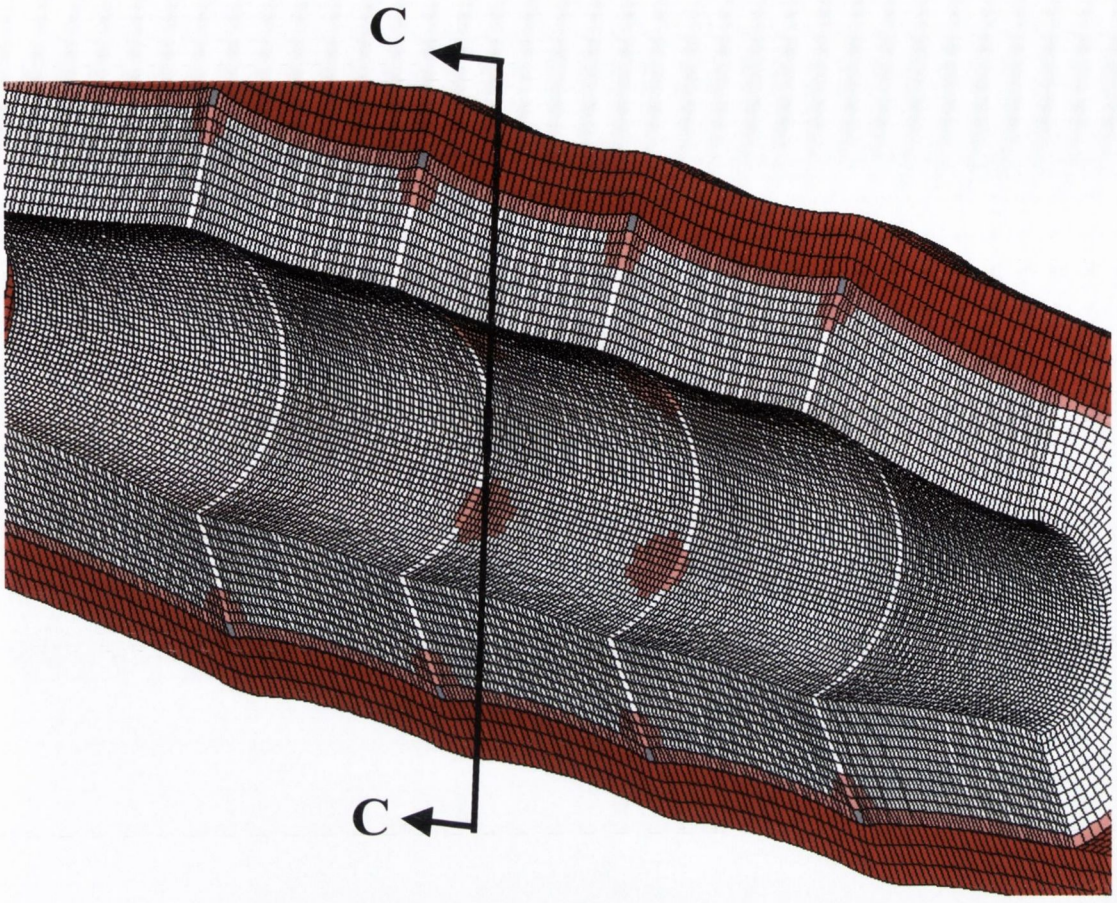

Figure 4.72 *Close-up view of the deformed geometry shown in Figure 4.71 with completely deactivated layers of restenotic tissue removed.*

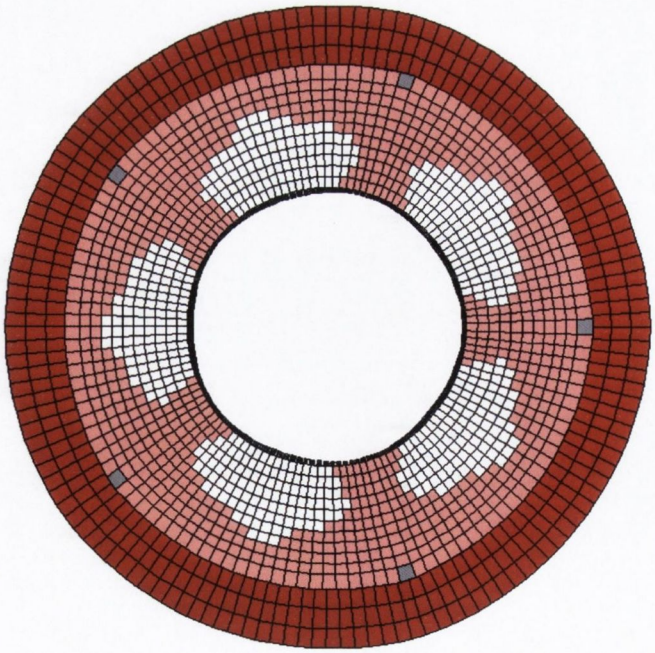

Figure 4.73 *Section C-C shown in Figure 4.72, the cross-section of maximum restenosis in the cylindrical vessel stented with the 'simple' stent, i.e. the mid strut-strut intersections of the stent.*

Comparing the restenotic growth within the lumen of the three stented vessels it can be seen that the NIR and 'simple' stents would again have the greatest intimal growth compared with the S7 stent, if the stimulus for restenotic growth is taken as the maximum *and* minimum principal stresses in the arterial tissue, see Figure 4.74. Also, it can be seen that using this stimulus that the restenotic growth is concentrated in areas around the stent struts.

Figure 4.74 *Sections C-C (shown in Figures 4.67, 4.70 and 4.73). The cross-section of maximum restenosis in the cylindrical vessel stented with (a) the NIR stent, with restenosis growth completed at 19 days, (b) the S7 stent, with restenosis growth completed at 12 days and (c) the 'simple' stent, with restenosis growth completed at 24 days.*

The pattern of in-stent restenosis in the models clearly depends upon the stimulus used to calculate the damage within the arterial tissue. The final volume of restenosis within the lumen of the vessels also depends upon the damage stimulus but even more importantly it is clearly dependent on stent design, see Figure 4.74. Regardless of the damage stimulus used, the S7 stent causes the least damage to the artery wall and hence the least in-stent restenosis when compared with the NIR and 'simple' stents.

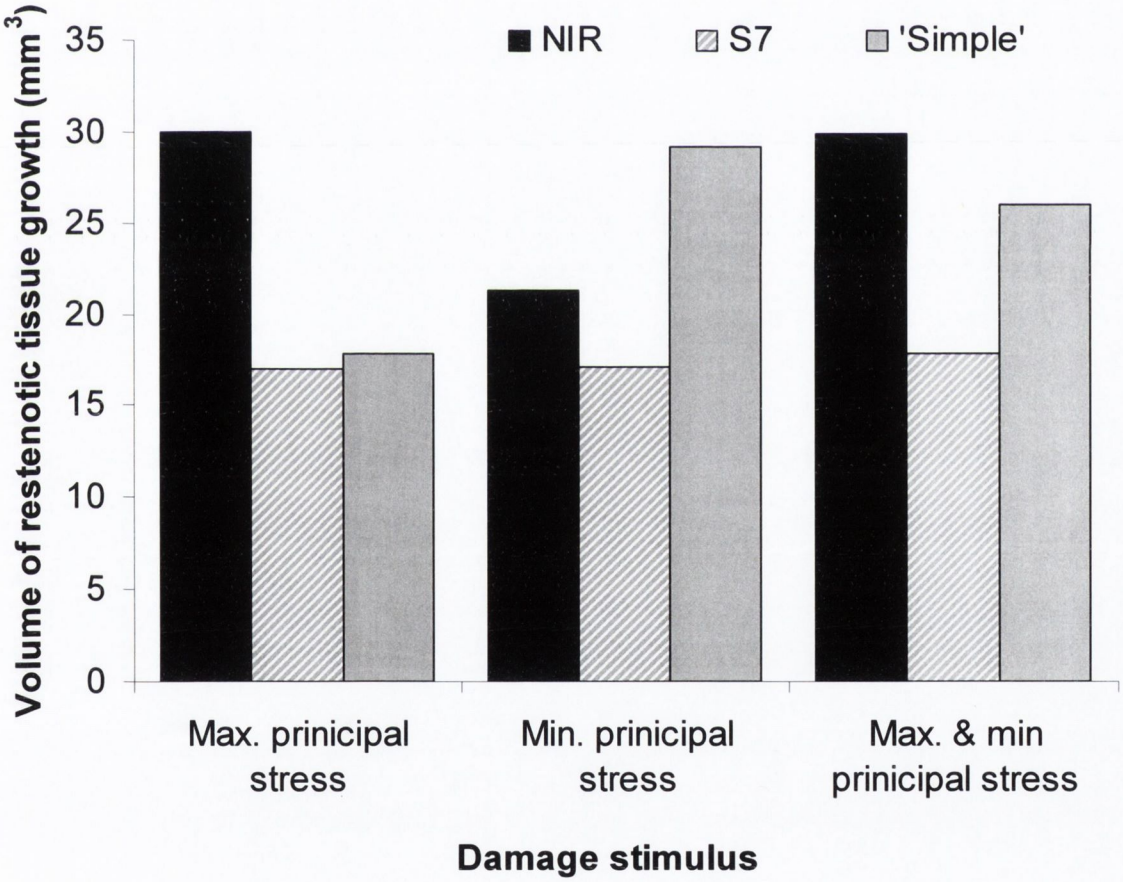

Figure 4.74 *Final volume of restenotic tissue growth within each of the stented vessels for the three different damage stimuli.*

CHAPTER 5

Discussion

Contents

5.1 Introduction

The primary objective of this thesis was to advance the biomechanical analyses that could be brought to bear on the design and preclinical testing of cardiovascular stents. Finite element analyses of vessels stented with different stents were performed using a suitable Mooney-Rivlin hyperelastic material model that had been determined from both uniaxial and equibiaxial tests. A computational algorithm to predict binary in-stent restenosis was also developed. The algorithm was devised and applied to stent designs known to have different restenosis rates. The algorithm is deemed useful as a preclinical test only if the stenting simulations and the in-stent restenosis algorithm succeed in predicting the stent design with the lowest propensity to cause in-stent restenosis. In addition, the pattern of restenosis in the stented vessels predicted by the algorithm is also important to support the use of this methodology in developing or testing new stent designs.

In this chapter, the assumptions and limitations of the constitutive model, the finite element models of the stenting procedures, and the restenosis algorithm are discussed first. The results of the stress analyses and the restenosis algorithm will then be compared to published clinical data on restenosis for stenting procedures. By comparison of predicted and observed restenosis patterns, the most likely mechanical stimulus responsible for the development of in-stent restenosis can be identified. The ability of the restenosis algorithm to predict in-stent restenosis will be discussed and subsequently the suitability of using this algorithm as a design and preclinical testing tool for stents.

5.2 Limitations of the numerical models

5.2.1 Geometry

The main limitation of the finite element models of the stenting procedures is the idealised representation of stenosed coronary arteries. It is hypothesised, however, that the tortuosity of a realistic coronary artery model would only serve to further demonstrate the lower stresses generated by a flexible stent that can conform well to the vessel curvature relative to a stiffer stent. A more tortuous arterial geometry might also show that a rigid stent would cause even higher stress concentrations and hence

vascular injury at the ends of the stent which could embed in the artery wall due to the relative non-conformability of the stent.

5.2.2 Constitutive Laws

The constitutive equation used in the finite element models was of the Mooney-Rivlin type. This model is an isotropic hyperelastic model and is therefore not the most accurate representation of arterial tissue since arterial tissue has been identified as cylindrically orthotropic [Patel and Fry, 1969]. To understand the limitation that this poses in the calculation of stresses, it is important to discuss the stress-stretch response of the arterial tissue.

The experimental data obtained for both the human femoral and the porcine coronary arterial tissue and used to define the Mooney-Rivlin models illustrate the key characteristics of the non-linear stress-stretch behaviour of soft tissue. Each stress-stretch curve, whether uniaxial or biaxial, clearly comprises of three distinct regions; (i) an initial linear region with high extension at low stresses, which corresponds to the stretch of the tissue when the elastin component of the artery predominantly bears the load, (ii) a toe region where the slope of the curve alters dramatically and which corresponds to the recruitment of initially wavy collagen fibres straightening out and bearing the load and (iii) a final linear region which corresponds to the stretch of the tissue when all of the collagen fibres have been recruited [Burton, 1962]. There is great deal of variability in the stress-stretch response of the two tissue types in both the uniaxial and biaxial deformation modes, however, the final slope of the curves can be seen to be very similar for all of the curves (Figures 4.1 – 4.3).

The use of the equibiaxial test device demonstrates the anisotropy of arterial tissue (Figure 4.3). Although an equal load is maintained on the four sides of the tissue the stretch in the longitudinal and circumferential directions are different. No conclusive statement can be made as regards the comparative stiffness of the material in these two directions because of the variability in the stress-stretch curves.

Behaviour similar to that found when a tissue is assumed isotropic has been observed when arterial tissue is physiologically loaded with an axial prestretch corresponding to the *in-situ* length of the vessel [Weisacker *et al.*, 1983]. The biaxial tests conducted in this study are of specimens cut from the vessel wall and are not of

vessels *in-situ* so it is not surprising that the equibiaxial loading produces variable stress-stretch curves. Variability in the tissue specimens could imply that each artery has a different unique *in-situ* prestretch and applying this axial prestretch could produce a more isotropic response. For intact coronary vessels, such as those tested by Carmines *et al.* [1992] and van Andel *et al.* [2003], no significant difference can be seen between the circumferential and longitudinal stiffness of the coronary vessels tested under *simulated* physiological loading conditions although variability is seen in the stress/stretch response between different samples. The axial prestretch applied in the study by van Andel *et al.* [2003] is not specific to each individual vessel's measured *in-situ* axial stretch and hence variability is also seen in the response of the vessels in both the circumferential and longitudinal directions. The existence of a unique prestretch value for each artery *in vivo* might also explain the previous contradictory reports on the comparative stiffness of arterial tissue in the longitudinal and circumferential direction [Weisacker *et al.*, 1988].

Since the variability observed in the mechanical properties of human femoral and porcine coronary arterial tissue would also be present in human coronary tissue then, for the purpose of using arterial tissue for preclinical testing of medical devices or interventional procedures, an isotropic averaged model may be an acceptable approach. It is also widely available in finite element codes used to test medical devices. Whilst an anisotropic model would be more accurate it is clear that the variability in the tissue elasticity would necessitate a host-specific anisotropic model to accurately represent the arterial tissue. The isotropic models outlined here are based on both uniaxial and equibiaxial stress-stretch data. It is therefore proposed that they present an appropriate compromise between the complexity of a host-specific anisotropic model and the simpler approach of using a hyperelastic model based on uniaxial data alone. To account for variability, it is also possible to develop several isotropic models covering the range of arterial tissue elasticity, based on both uniaxial and equibiaxial stress-stretch data [see Lally and Prendergast, 2004; Appendix A].

The Mooney-Rivlin model for the plaque tissue was based on published data but limited to uniaxial data. It is very difficult to obtain human atherosclerotic tissue. However, even if segments of atherosclerotic tissue were obtained it would be very difficult to obtain planar biaxial samples from such small irregularly shaped specimens.

Arterial tissue has also been identified to exhibit viscoelastic properties such as strain rate dependency [Fung, 1993]. The Mooney-Rivlin hyperelastic model does not take account of the viscoelasticity of arterial tissue. The effect of this limitation was minimised by carrying out all of the experimental tests at the same strain rate and preconditioning the arterial tissue. However, this assumes that the same speed of arterial expansion during stent deployment was used for the different stent designs.

5.2.3 Initial and boundary conditions

No residual stresses were included in the model of the artery, based on the opening angle of the vessel in its unloaded state [Fung, 1993] since no data of this nature were available in the literature for coronary arterial tissue. Omitting the residual stresses present in the artery may have affected the stress measures obtained in the vessel wall in the stenting procedures. In the future, testing could be carried out on coronary tissue to establish the opening angles of intact coronary arteries and also of the three layers of the artery, in much the same way as the data obtained for iliac arteries by Schulze-Bauer *et al.* [2003]. Once this data has been obtained future models could then incorporate residual stresses.

No rupture or damage mechanism has been incorporated into our plaque model. The high stresses observed in the calcified plaque are high enough that fracture could occur in this relatively brittle material. An analysis of the fracture process of the plaque is, however, beyond the scope of the present study.

The process of stent expansion is not modelled in our simulations. This limits the study since it cannot be used to analyse the shearing force that an expanding stent could impose on an artery. In this respect, the approach used in this thesis is suitable for studies that aim to look at the influence of stent placement on vessel wall stresses and stent-induced vascular injury after stent deployment since the stent geometry has been obtained from a stent in its expanded state. Neglecting the arterial injury due to shearing during stent deployment may be justified by the fact that in-stent restenosis has been observed to be a more chronic restenotic response than restenosis post angioplasty [Edelman and Rogers, 1998]. Although both procedures cause shearing and endothelial denudation only stenting results in the chronic response to injury of intimal cell proliferation. This is due to the continued presence of the stent in the artery and the high loading on the vessel wall imposed by the stent. This conclusion is

also supported by the many studies which have identified stent design as a major determinant in restenosis post-stenting since all stents cause endothelial denudation during deployment, however, different stent designs induce different loading magnitudes on the vessel wall.

5.2.4 The restenosis models

There is a limitation in the finite element software, Marc/Mentat, whereby a hyperelastic material cannot be thermally activated. This is a necessary requirement for the restenotic tissue in the restenosis algorithm. Due to this limitation the restenotic tissue had to be modelled as a linear elastic material (E=1 MPa). However, restenotic tissue, which is predominantly composed of smooth muscle cells and extracellular matrix, would most likely have non-linear elastic properties similar to the vessel wall and therefore could have been more accurately modelled as a hyperelastic material with properties of arterial tissue. However, this inaccuracy is low since in the restenosis models the newly activated restenotic tissue is only subjected to mean blood pressure of 100 mmHg. Under this low load a hyperelastic material would behave almost linearly. The stress stiffening non-linearity of the arterial tissue is only important when high loads, far beyond physiological loads, are applied to vessel wall such as in the case of stenting.

The damage observed from the fatigue tests to accumulate within arterial tissue causes stress softening in the tissue. This stress softening behaviour of the tissue has not been included in the material model, it has instead been used to determine the degree of restenotic growth. A more accurate material model could be developed which incorporates the stress stiffening behaviour of the tissue, and hence alters the arterial tissue properties, as well as determining the degree of tissue proliferation. In addition, without including this stress softening behaviour of the material, the stresses and strains induced within some areas of the stented vessel are beyond the range of the experimental data obtained. Extrapolation beyond the range of the experimental data may introduce errors in the calculation of stresses in the vessel wall. However, it may be justified in this context where the ultimate goal is to develop a comparative preclinical testing tool for stents which does not rely on the absolute value of the stresses induced in the vessel.

5.2.5 Mechanoregulation in the restenosis algorithm

In this study the development of in-stent restenosis was modelled by the migration and proliferation of cells based on damage within the arterial wall. The migration of cells was represented using the diffusion equation and was therefore the same in every direction. This is not the most accurate representation of the medial cell migration observed during the formation of in-stent restenosis. Cells in the media of the artery have been identified to move to the intima and not in every direction [Edelman and Rogers, 1998]. The high concentration of cells in the arterial wall generated at areas of damage moved to areas of low concentration by diffusion (deactivated restenotic tissue). This closely simulated the cell migration process. It was necessary, however, to remove the cells at the adventitial surface to prevent an artificially high concentration of cells at the outer surface of the artery due to the diffusion of cells to this area of low cell concentration. Applying a convective film coefficient to the outer surface of the artery, as outlined in the Materials and Methods Chapter (Section 3.6.2), removed this potential problem.

The stimulus for restenosis in the models was damage. Arterial tissue, like other soft tissues such as tendons [Ker and Zioupos, 1997], accumulates damage under cyclic loading. This is evident in the reduction in stiffness, which is a measure of damage, observed in the arterial tissue with increasing loading cycles during the fatigue tests. The reduction in the number of cycles to failure of the tissue at higher stress levels also indicates damage is accumulating within the tissue and ultimately causing failure. Since stents induce stresses in the arterial wall that are above the physiological stress levels (Section 4.4.2), the level of damage at this stress level may be sufficient to result in an over zealous healing process which manifests itself as in-stent restenosis. The artery is continuously subjected to cyclic loading from the pulsing of the blood through the artery. This may result in the arterial tissue in a stented vessel accumulating damage at a higher rate due to the high mean stress level induced in the artery by the stent scaffolding open the vessel.

The arterial tissue damage in the restenosis models was calculated based on an *S-N* curve obtained from fatigue tests on the porcine coronary arterial tissue. The fatigue tests were carried out at three load levels: from 10-20%, 10-30% and 10-40 % of the UTS of the coronary arterial tissue. The ratio of the minimum to maximum stress, or the *R*-ratio, in these fatigue tests is, therefore, not the same as that which

would occur during the cyclic loading of a stented vessel. Loading at 10-20%, 10-30% and 10-40 % of the UTS of the arterial tissue correspond to *R*-ratios of 0.5, 0.33 and 0.25, respectively. Blood pressure only fluctuates from 80-120 mmHg, corresponding to an *R*-ratio of 0.67. The reason that the *R*-ratio of 0.67 was not used in the fatigue tests was because of the length of time the tests would have had to run to obtain specimen failure and they were therefore deemed somewhat impractical. However, it has been shown that damage accumulates in arterial tissue when the tissue is cyclically loaded. It has also been shown that this damage is nonlinearly related to the mean stress level at which the cyclic loading takes place. It is therefore proposed that this non-linear relationship may be extrapolated for use in cases where the *R*-ratio is different than that which the coronary arterial tissue samples were tested. Further tests could be carried out in future to obtain additional fatigue data for arterial tissue that include tests carried out at an *R*-ratio of 0.67.

The restenosis model only determined damage as a function of stresses within the artery wall due to stent expansion and did not include the effects of haemodynamic shear stresses. Altered flow patterns in the vessel, initially due to the presence of the stent and later due to restenotic growth, would contribute to the overall restenosis growth pattern. Therefore, a truly accurate model for in-stent restenosis should account for altered tensile and compressive stresses in the artery as well as altered haemodynamic shear stresses, which has shown to influence the activity of cells in stented vessels [Berry *et al.*, 2000, 2002].

5.3 Analysis of stress in stented arteries

5.3.1 Prolapse Study

The tissue within one repeating unit of four different stent designs was modelled to determine the degree of tissue prolapse in the stents. The results of the analyses found that the degree of tissue prolapse was as follows: the least prolapse was in the BeStent 2 unit, next was the TETRA stent, then the NIR, and the highest predicted prolapse was in the unit of the VELOCITY stent, see Figure 5.1.

Binary restenosis rates of 7.4% for direct stenting and 6.8% when stenting occurs following pre-dilation have been found for the BeStent 2 stent[1]. The TETRA

[1] Personal communication with Susanne Hovens, Convertible Trial, Medtronic Bakken Centre, Maastricht, The Netherlands.

stent has been reported to have restenosis rates of 17.9% (versus 31.4% for the Velocity stent) and 17.6 % (versus 28.6% for the NIR stent) [McClean and Eigler, 2002]. Clinical studies using the NIR stent have also reported restenosis rates of 19.3% at 9-months follow-up [NIRVANA trial; Baim *et al.*, 2001] and 19% at 6-month follow-up [FINESS II trial; Rutsch *et al.*, 2000], see Figure 5.1.

From Figure 5.1 it can be seen that the clinical data indicates that the VELOCITY stent is the worst performing stent with the highest rate of restenosis. The simple analyses to investigate prolapse and the stresses surrounding a unit of a stent also found that the VELOCITY stent design had the worst scaffolding properties, allowing up to 0.5 mm prolapse within the stent unit, and also induced the highest stresses in the arterial wall. In these finite element analyses the NIR had the next highest degree of prolapse and the next highest magnitude of stress in the arterial tissue and from the clinical data the NIR has been reported to have a lower restenosis rate than the VELOCITY stent but higher than the TETRA and Bestent 2. The TETRA and Bestent 2 stents were found to have the lowest prolapse and to induce the lowest arterial stresses and they have also the lowest reported restenosis rates of the four stents, particularly the BeStent 2. Therefore, although the prolapse study was relatively simple, it may serve as a simple preclinical test that could aid in improving stent design and preventing in-stent restenosis.

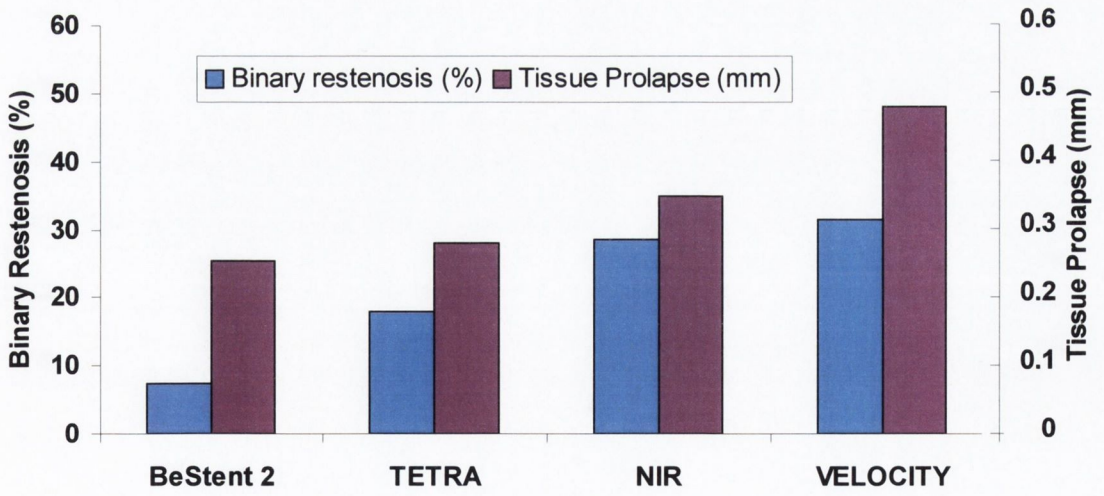

Figure 5.1 *A comparison of clinical binary restenosis data and the predicted maximum prolapse of the vascular tissue within the repeating unit of the four stents analysed.*

5.3.2 Full 3D Models

Application of an axial stretch to the vessel has a major impact on the stresses induced within the artery wall as seen in Figure 4.20 (pg. 106). This indicates the importance of applying longitudinal tethering to the vessel to simulate the boundary condition of a stented artery. Longitudinal tethering values ranging from 1.05-1.23 have been recorded by Schulze-Bauer *et al.* [2003] for aged human iliac arteries. Therefore, the tethering applied to the models here represents the worst case scenario of axial prestretch and hence elevated stresses within a stented vessel. The influence of applying different longitudinal loads and hence different axial stretch values on an idealised cylinder is shown in detail in Appendix A.

For all three geometrical configurations (i.e. cylindrical vessel without stenosis, with stenosis and with a localised stenotic lesion), based on the stresses induced in the vessel wall in these simulations, it is expected that the S7 would cause less vascular injury than the NIR or 'simple' stent. The lower volume of tissue stressed to high levels with the S7 stent compared to the same idealised geometry stented with the NIR and 'simple' stents made from the same material, can be attributed to the greater conformability of the S7 stent to the inner lumen geometry of the vessel. This includes the greater radial recoil observed in the S7 for all three geometrical configurations. By recoiling, the stent maintains the lower stresses on the vessel; however the S7 maintains sufficient patency and superior scaffolding properties, i.e. lower prolapse for all the stented vessels than the NIR or 'simple' stent designs, see Table 5.1. In fact this value of maximum tissue prolapse is also very low compared with other stent designs (BeStent 2, *Medtronic AVE*; VELOCITY, *Cordis*; TETRA, *Guidant*). The maximum tissue prolapse within a repeatable stent unit of each of these designs has been determined for human femoral arterial tissue properties in the prolapse study outlined earlier, see Table 5.2.

	Stent Design		
	NIR	**S7**	**'simple'**
Artery Geometry	Maximum Prolapse (mm)		
(i) Cylinder w/o stenosis	0.053	0.038	0.114
(ii) Cylinder w stenosis	0.121	0.063	0.414
(iii) Cylinder w localised stenosis	0.124	0.056	0.38

Table 5.1 *Maximum tissue prolapse in 3D models of stented vessels.*

Stent Design			
BeStent 2	**VELOCITY**	**TETRA**	**NIR**
Maximum prolapse (mm)			
0.11	0.205	0.117	0.152

Table 5.2 *Maximum tissue prolapse in 'one repeating unit' finite element models.*

Stent recoil is measured by the radial displacement of the stent; however, the tissue prolapse is tissue protrusion between the stent struts and it defines the scaffolding properties of the stent. These results illustrate the coupling that exists between the stresses imposed on the vessel wall and the radial recoil of the stent. The radial recoil observed here is exaggerated as a result of the method used to simulate the stenting procedure, i.e. an expansion of the artery past the stent and the subsequent collapse of the artery around the stent. However, the analyses illustrate that if the two stent designs were deployed using the same pressure in the same vessel, the NIR stent would induce higher stresses in the vessel wall. Clearly, an optimum stent design should retract sufficiently to prevent overstressing the vessel wall but still maintain patency of the vessel and plaque scaffolding. In fact, for a vessel with a localised lesion, and taking account of the differences in magnitude of radial recoil and tissue prolapse for the three stent designs, the minimum lumen diameter was predicted to be 2.79 mm, 2.63 mm and 2.71 mm at the vessel stenosis for the NIR, S7 and 'simple' stents, respectively. It is clear that the marginally higher lumen diameter achieved by the NIR stent is at the expense of large areas of considerably higher stress. These stresses may provoke a greater response to injury by the vessel wall and ultimately restenosis. This demonstrates the high risks associated with choosing an oversized rigid stent design as compared to the use of the more flexible S7 stent.

As stated above, restenosis rates for the NIR stent have been reported of 28.6% [McClean and Eigler, 2002], 19.3% [NIRVANA trial; Baim *et al.*, 2001] and 19% [FINESS II trial; Rutsch *et al.*, 2000]. However, the restenosis rate for the S7 stents has been reported as much lower at 10.1% at 6-months follow-up [Medtronic DISTANCE trial, 2004]. The results of this study offer an explanation for this lower restenosis rate when compared with the NIR stent; the S7 stent would cause less vascular injury to the stented vessel and therefore would be expected to have a lower restenosis rate than the NIR stent. It is important to note that this is achieved whilst

maintaining superior scaffolding properties than the NIR stent. It should also be noted that the S7 achieves high patency (only 4 % stenosis) and excellent scaffolding whilst also having a lower stent/artery contact area (11.3 mm^2 as compared to 13.9 mm^2 for the NIR). Maintaining the metal/tissue contact area low also reduces the thrombotic response of the vessel to the presence of a foreign material [Rogers and Edelman, 1995].

5.4 Analysis of restenosis in stented arteries

The computational model of in-stent restenosis was applied to the NIR, S7 and 'simple' stent designs. Three values of stress were used to calculate the damage within the stented artery wall that subsequently acted as the stimulus for in-stent restenosis. The pattern of restenosis differed depending on which measure of stress was used to calculate damage. The pattern of in-stent restenosis has been identified from animal and human restenosis trials to be concentrated around the stent struts. Also stents induce a different response at different points along the length of the stent. In many studies greater luminal loss after stent implantation has been observed at the edges of stents [Hoffman *et al.*, 1996; Dusaillant *et al.*, 1995; Ikari *et al.*, 1995]. The edges of many stents dilate more than the body during normal inflation. As a result, the stent edges may be more deeply embedded in the vessel wall than the body causing more severe injury to the vessel. Therefore, intimal hyperplasia is most likely greater at the ends of the stents as a response to this injury.

This pattern of restenosis whereby intimal hyperplasia is concentrated around the stent struts and at the ends of the stents is only predicated in the restenosis models when damage is determined based on either minimum principal stress or a combination of maximum and minimum principal stresses within the artery wall, see Section 6.5. The model therefore would support the hypothesis that deviations from physiological circumferential stresses (maximum principal stresses) and physiological radial stresses (minimum principal stresses) in the artery wall induced by the stent cause damage that leads to restenosis.

As outlined in the Literature Review (Chapter 2), in-stent restenosis begins with thrombus deposition where the stent contacts with the artery [Edelman and Rogers, 1998]. This has been modelled by immediately activating a layer of elements in the in-stent restenosis model after stenting. Thrombus deposition is followed by the

migration of surface adherent monocytes, recruited from the circulation and the adventitial vasa vasorum, to the injury site and then into the intima. This migration occurs in the first 7 days whilst proliferation occurs at the same time and continues after the first 7 days to form the restenotic tissue. The restenosis algorithm also models the migration and proliferation of these cells into the intima.

The time course of in-stent restenosis after coronary intervention in humans ranges from 3-18 months after stent implantation, with peak angiographic restenosis typically detected between the first and third month after the procedure [Orford *et al.*, 2000]. The greatest proliferative activity occurs in the first 7 days after stenting [Edelman and Rogers, 1998]. The restenosis model predicts that restenosis occurs in the first month in the NIR and 'simple' stent designs whereas restenosis does not occur in the S7 stent, see Table 5.3. Stenosis of a stented vessel is defined as greater than 50% lumen vessel area stenosis after stenting [Kastrati *et al.*, 2001].

The predominant mechanism of in-stent restenosis is lumen loss from SMC proliferation occurring as a healing response to vascular injury. In order to minimise restenosis, therefore, the optimum stent design should be sufficiently rigid to prevent lumen loss from remodelling whilst minimising injury to the vessel. The in-stent restenosis algorithm predicts that the S7 stent minimises vascular injury whilst achieving vessel patency during stenting and therefore has a lower restenosis rate than the NIR or 'simple' stent designs, see Table 5.3.

It is noted here that the clinical restenosis data most commonly reported in the literature and that used in this study is binary restenosis data. Binary restenosis data only gives information on the number of stented vessel that have been found to have stenoses greater than 50% lumen vessel area. This information is limited since it does not give information on the degree of stenosis in vessels with less than 50% lumen area stenosed or the extent of stenosis in vessels with greater than 50% stenosis. However, binary restenosis data is still deemed a very useful measure in the context of this study in order to comparatively indicate the propensity of different stent designs to cause in-stent restenosis.

	Stent Design								
	NIR	**S7**	**'simple'**	**NIR**	**S7**	**'simple'**	**NIR**	**S7**	**'simple'**
	Final minimum vessel diameter (mm)			*Percent vessel area stenosis based on minimum vessel diameter and the outer stent diameter (3.5 mm)*			*Total volume of restenotic growth (mm^3)*		
(i) Maximum principal stress	2.168	2.966	2.810	62%	28%	36%	29.96	16.96	17.78
(ii) Minimum principal stress	2.284	2.648	1.705	57%	43%	76%	21.28	17.12	29.96
(iii) Maximum and minimum principal stress	2.456	2.810	1.819	51%	36%	73%	29.91	17.80	25.97

Table 5.3 *Final vessel diameters, degree of vessel stenosis and restenotic tissue volume in the stented vessels of the restenosis models. These measures illustrate the higher propensity of the NIR and 'simple' stents, compared with the S7 stent, to cause in-stent restenosis. Stent design and stent vessel converge is clearly a major factor in restenosis. This is particularly evident in the focal nature of restenosis around the stent struts for stimulus (iii) where although the restenosis volume is lower for the 'simple' stent design compared with the NIR stent, the localised formation of restenosis around the struts results in a lower minimum vessel diameter than the NIR stent.*

5.5 Design and preclinical testing of stents

The stress analyses and the in-stent restenosis algorithm both illustrated the high dependence that restenosis has on stent design. Rigid laser cut stents, such as the NIR and the 'simple' stent designs, resist radial recoil and in doing so they cause injury to the vessel wall and subsequently restenosis as a response to that injury. The modular S7, on the other hand, is more flexible and therefore it retracts and bends to conforms to the vessel wall. This is due to the fact that the S7 has welds only at certain points. The S7 has 10 crowns in the circumference yet it only has two welds around the circumference and these welds are offset by 2.5 crowns along the axial direction of the stent, see Figure 5.2. The welds ensure that the stent has sufficient rigidity to resist collapse and maintain patency whilst the lack of welds between every strut allows flexibility and minimises vessel injury. The disadvantage of the modular stent is the presence of welds, which are areas highly susceptible to fatigue and corrosion. To improve on existing modular stent designs it is recommended that the modular type stent geometry be laser cut from a complete cylinder to remove the need for welds but allow flexibility. This can easily be done and would incorporate the advantages of both types of stent.

The localised formation of greatest restenosis at the ends of stents indicates the need for greater recoil of the stent at the ends. This can achieved by machining the stent geometry such that the struts get gradually thinner towards the end of the stent, thereby allowing greater recoil of the stent at the ends. Further work to test this type of design could be carried out in future using the methodologies presented in this thesis. Work has already been carried out to test both the flow characteristics and the

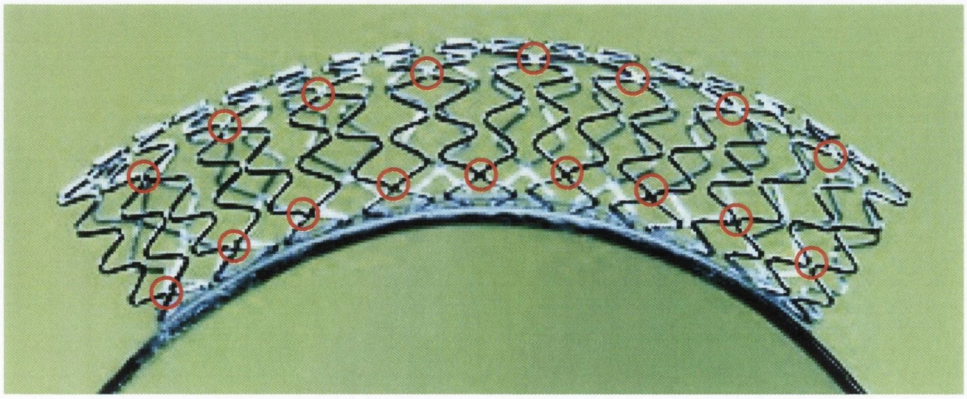

Figure 5.2 *The Medtronic S7 modular stent [Website 4]. The red circles illustrate the position of the welds on the front half of the stent.*

magnitude of wall stresses in a vessel stented with a compliance matching stent [Berry et al., 2002]. This stent is more compliant at the ends and it has shown good *in-vitro* and *in-vivo* results reducing altered flow patterns at the ends of stents. However, this compliance matching stent has not been clinically tested and therefore it has not yet been shown to reduce restenosis.

The methodology established in this thesis can be used as a preclinical tool to test designs such as a 'compliance matching stent' or a laser cut modular stent to optimise the design before expensive time consuming clinical trials take place. This testing tool can also be further developed to incorporate drug coatings on the stent. The restenosis model uses temperature to represent cells and diffusion to simulate cell movement. Drug coatings could therefore be modelled in the in-stent restenosis simulation as a temperature sink on the surface of the stent. Clearly therefore, this testing methodology can be used to ascertain both the optimum biomechanical stent design to minimise injury and also the optimum stent design for drug delivery to the proliferating SMCs in the media and therefore prevent restenosis.

5.6 Achievements of this Study

The main achievement of this study is the development of a preclinical testing tool that can be implemented in commercial finite element codes and used to predict the performance of cardiovascular stents, including the propensity for in-stent restenosis. The methodologies developed here have been tested on actual devices that have been used in clinical service. It is considered an advantage that the procedures can be used in engineering design by stent manufacturers, and provide a framework for including advances in geometric modelling and constitutive material modelling as they occur.

In addition to the development of this preclinical testing tool, hyperelastic constitutive models representing the mechanical properties of human femoral and porcine coronary arterial tissue have been developed which are based on both uniaxial and equibiaxial tensile test data. These constitutive models can now be used to preclinically test other intravascular devices using the finite element method.

Some of the novel experiments conducted were the fatigue tests on arterial tissue. From these tests, a relationship has been established between damage accumulation within arterial tissue and the stress level within the tissue. Although researchers [Ker and Zioupos, 1997] have previously established that damage

accumulates under cyclic loading in tendons, no one has previously determined if this is also true for arterial tissue. This study has established that arterial tissue undergoes stress softening and therefore accumulates damage when subjected to cyclic loading and that this damage accumulates at a higher rate if the stress level at which the tissue is cycled is increased. This finding may have implications in other intravascular procedures also such as at areas of elevated stress due to compliance mismatch in graft artery bypass junctions.

CHAPTER 6

Conclusions

Contents

6.1 Main results of this thesis

The aim of this thesis was to devise a means to preclinically test stent designs and to predict in-stent restenosis. Stress analyses were carried out on stented vessels and a restenosis algorithm was devised. These testing methods were applied to stent designs known to have different restenosis rates. The main conclusions of this study are as follows:

1. Damage accumulates within arterial tissue under cyclic loading and the rate of damage accumulation is dependent upon the mean stress level at which the cyclic loading is carried out.
2. By comparing the results of the simple prolapse study and in the 3D stented vessels to available clinical data, it was found that tissue prolapse within the struts of a stent may be a design feature of stents that can be minimised to prevent restenosis.
3. The in-stent restenosis algorithm would support the hypothesis that it is a combination of damage, generated due to the maximum and minimum principal stresses induced within the artery wall, that acts as the stimulus for restenosis.
4. Because the in-stent restenosis algorithm based on stress/injury predicts higher restenosis for the NIR stent relative to the S7, it confirms the widely accepted view that in-stent restenosis has a biomechanical origin.
5. By comparison to clinical data available on the binary restenosis rates for the two commercially available stent designs (i.e. NIR and S7) to the prediction of restenosis with the algorithm, it has been seen that the in-stent restenosis correctly predicts the stent with the lowest propensity for restenosis. It also successfully predicts the pattern of in-stent restenosis whereby the greatest degree of restenosis occurs at the stent ends and concentrated around the stent struts. This algorithm can now be used to preclinically test new bare-metal stent designs to ascertain the optimum stent design to prevent restenosis.

6.2 Future work

The work presented in this thesis on developing a preclinical test to determine the performance of different stent designs could be significantly enhanced in the future. The following recommendations are made:

1. Patient specific geometrical data of stenosed arteries could be obtained from imaging techniques such as intravascular ultrasound (IVUS) or angiography. These realistic geometries could be used in simulations using the restenosis algorithm for different commercially available stents to determine the most suitable stent for a particular patient.
2. Further advances could be made to improve the accuracy of the constitutive models used. IVUS imaging techniques could also be used to determine the specific material properties of the arterial tissue or plaque in a patient suffering from cardiovascular disease so that a suitable stent could be chosen to account for these properties. The material model could include the collagen fibre orientations and thereby incorporate the anisotropy of the tissue as has been done by Holzapfel *et al.* [2000]. Imaging techniques could be used to establish the fibre orientations *in vivo* and used to develop patient-specific anisotropic constitutive models.
3. The in-stent restenosis algorithm could be developed to simulate the effect of drug elution to reduce restenosis. Stent design in drug-eluting stents is important from a biomechanical point of view but also to ensure even distribution of the drug within the lumen of the vessel to prevent restenosis [Dubini *et al.*, 2004].
4. The accuracy of the in-stent restenosis algorithm could be improved by including the influence of altered blood flow patterns within the stented vessel on restenotic growth. The blood flow patterns within the vessel, and hence the haemodynamic wall shear stresses would alter due to the presence of the stent and also with increasing restenotic growth within the lumen of the vessel and could contribute to the onset and progression of the restenosis disease.
5. Further tests could be carried out in future to obtain additional fatigue data for arterial tissue that include tests carried out at an R-ratio of 0.67. These tests could be carried out to establish both circumferential and axial damage

accumulation under tensile cyclic loading as well as radial damage accumulation under cyclic compressive loading.

6. Further arterial tissue testing could be performed to obtain a measure of the residual stresses in coronary arteries and then incorporated into the preclinical testing tool. Measurements of *in-situ* coronary vessel prestretch could also be obtained and used to improve the accuracy of the finite element models. This could be done by comparing *in-situ* vessel lengths of coronary vessels to harvested vessel lengths.
7. More accurate values of the diffusion coefficient and the constant relating the number of cells and the magnitude of damage, as well as the density of cells within restenotic tissue would contribute to more valid models. These values could be found from experimental tests of deformable membranes seeded with smooth muscle cells and extracellular matrix or endothelial cells. These seeded membranes could be subjected to cyclic loading at elevated stress levels to determine the cell response. Tests of this nature could obtain a range of values to input into the in-stent restenosis algorithm along with diffusion coefficients for drugs applied as stent coatings and their impact on cell activity. In addition, using cells obtained from different sources would allow for the variation in cell response between individuals to be accounted for or the cell response in different anatomical sites, e.g. peripheral versus coronary arteries.
8. In this study cell proliferation was modelled as directly proportional to the damage present in the artery as given in Eqns. 3.16 and 3.17. However, it may have been more realistic to relate damage to the proliferation rate as a function of the cell concentration already present in the artery. Studies of mehanoregulation during tissue differentiation define the relationship between cell number and migration/diffusion as follows:

$$\frac{\mathrm{d}n}{\mathrm{d}t} = \kappa\nabla^2 n + nP(S) - nK(S)$$

where n is the cell concentration, $P(S)$ is the proliferation rate as a function of the stimulus, S, and $K(S)$ is the apoptosis rate as function of stimulus [Kelly and Prendergast, in press].

Preliminary tests were carried out as part of this thesis to represent cell migration and diffusion using the above equation but neglecting apoptosis. The results of the analysis illustrated that excessive proliferation occurs at the stent ends in a matter of a few days in models using this relationship and restenosis occurs prematurely, see Figure 6.1.

This preliminary study indicated that without further information on the complex relationship between damage and cell proliferation as well as apoptosis in arterial tissue after stenting that the study could not be advanced further. Future studies could include these relationships if further cell studies are carried out to establish these complex biological processes more fully.

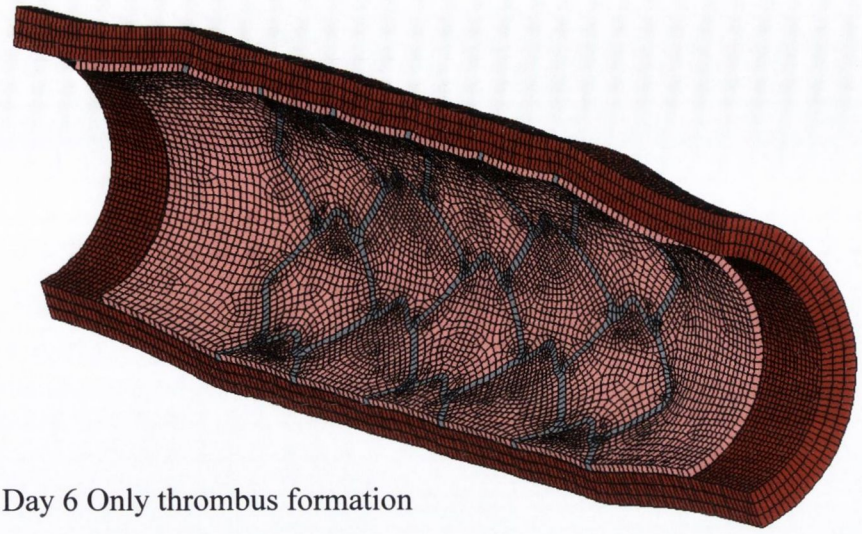

Day 6 Only thrombus formation

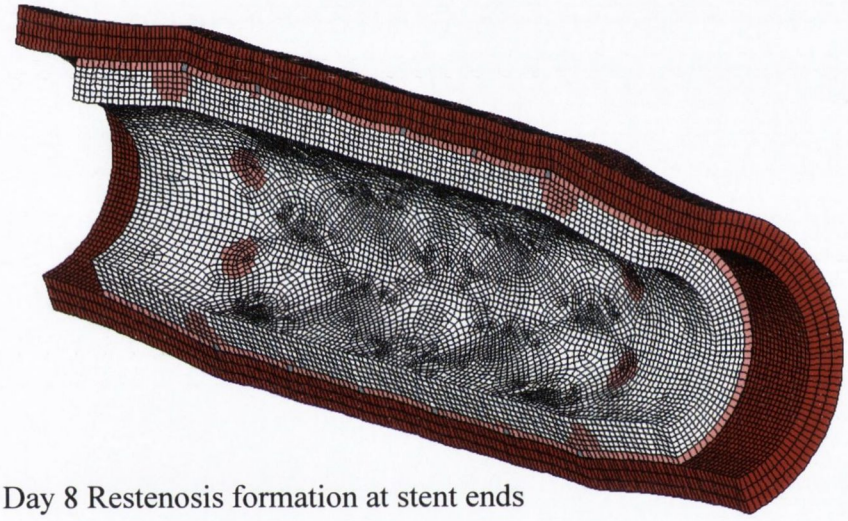

Day 8 Restenosis formation at stent ends

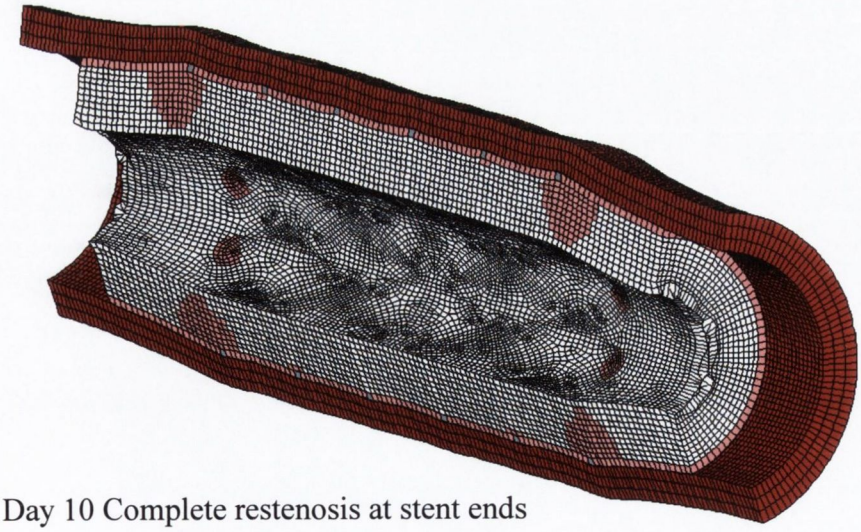

Day 10 Complete restenosis at stent ends

Figure 6.1 *Restenosis growth pattern and time frame when cell generation is proportional to cell concentration present.*

REFERENCES

Arakawa K, Isoda K, Sugiyabu Y, Fukuda M, Nishizawa K, Shibuya T, Nakamura H. Intimal proliferation after stenting reflected by increased stent-to-vessel cross-sectional area ratio: serial intravascular ultrasound study. *Journal of Cardiology*. 1998;32:379-389.

Auricchio F, Di Loreto M, Sacco E. Finite-element analysis of a stenotic artery revascularization through a stent insertion. *Computer Methods in Biomechanics and Biomedical Engineering*. 2001;4:249-263.

Baim DS, Cutlip DE, O'Shaughnessy CD, Hermiller JB, Kereiakes DJ, Giambartolomei A, Katz S, Lansky AJ, Fitzpatrick M, Popma JJ, Ho KKL, Leon MB, Kuntz RE. NIRVANA Investigators. Final results of a randomized trial comparing the NIR stent to the Palmaz-Schatz stent for narrowings in native coronary arteries. *American Journal of Cardiology*. 2001;87:152–6.

Bassiouny HS, White S, Glagov S, Choi E, Giddens DP, Zarins CK. Anastomotic intimal hyperplasia: mechanical injury or flow induced. *Journal of Vascular Surgery*. 1992;15:708–17.

Berry JL, Santamarina A, Moore JE Jr, Roychowhury S, Routh WD. Experimental and computational flow evaluation of coronary stents. *Annals of Biomedical Engineering*. 2000;28:386-98.

Berry JL, Manoach E, Mekkaoui C, Rolland PH, Moore JE Jr, Rachev A. Hemodynamics and wall mechanics of a compliance matching stent: in vitro and in vivo analysis. *Journal of Vascular Interventional Radiology*. 2002;13:97-105.

Billiar KL, Sacks MS. Biaxial mechanical properties of the fresh and glutaraldehyde treated porcine aortic valve: Part I - Experimental results. *ASME Journal of Biomechanical Engineering*. 2000;122:23-30.

Bioscorpio; http:/www. Bioscorpio.com, 2004.

Brands J. Fatigue test of porcine contrary arteries. Internal publication in *Technische Universiteit Eindhoven*, S457818, 2003.

Burton AC. Physical principles of circulatory phenomena: the physical equilibria of the heart and blood vessels". In: *Handbook of Physiology, Section 2*, Circulation 1, American Physiological Society, Washington, D.C., 1962:94.

Carew TE, Vaishnav RN, Patel DJ. Compressibility of the arterial wall. *Circulation Research*. 1968;22:61-68.

Carmines DV, McElhaney JH, Stack R. A piece-wise non-linear elastic stress expression of human and pig coronary arteries tested in vitro. *Journal of Biomechanics*. 1992;24:899-906.

Carter AJ, Laird JR, Farb A, Kufs W, Wortham DC, Virmani R. Morphologic characteristics of lesion formation and time course of smooth muscle cell proliferation in a porcine proliferative restenosis model. *Journal of the American College of Cardiology*. 1994;24:1398-1405.

Chockalingam A, Balaguer-Vintro I. Impending global pandemic of cardiovascular diseases. Barcelona, Spain: Prous Science; 1999.

Central Statistics Office Ireland, cited in www.irishheart.ie.

Choi HS, Vito RP. Two-dimensional stress-strain relationship for canine pericardium. *ASME Journal of Biomechanical Engineering*. 1990;112:153-159.

Chua SND, MacDonald BJ, Hashmi MSJ. Finite element simulation of stent and balloon interaction. *Journal of Materials Processing Technology*. 2003, in press.

Colombo A, Stankovic G, Moses JW. Selection of coronary stents. *Journal of the American College of Cardiology*. 2002;40:1021-1033.

DeScheerder I, Wang K, Zhou XZ, Verbeken E, Ping QB, Yanming H, Jianhua H, Szilard M, Van de Werf F. Neointimal hyperplasia and late pathologic remodelling in a porcine coronary stent model. *Journal of Invasive Cardiology*. 1999;11:9-12.

Dobrin PB, Rovick AA. Influence of vascular smooth muscle on contractile mechanics and elasticity of arteries. *American Journal of Physiology*. 1969;217:1644-1651.

Dubini G, Migliavacca F, Borghi A, Foa E. Numerical simulations of drug release from eluting stents. In *Proceedings of the 14th European Society of Biomechanics*, 's-Hertogenbosch, The Netherlands, 2004.

Duerig T, Pelton A, Stöckel D. An overview of nitinol for medical applications. *Materials Science and Engineering*. 1999;A273-275:149-160.

Dumoulin C, Cochelin B. Mechanical behaviour modelling of balloon-expandable stents. *Journal of Biomechanics*. 2000;33:1461-1470.

Dusaillant GR, Mintz GS, Pichard AD, Kent KM, Satler LF, Popma JJ, Wong SC, Leon MB. Small stent size and intimal hyperplasia contribute to restenosis: a

volumetric intravascular ultrasound analysis. *Journal of the American College* of Cardiology. 1995;26:720-724.

Edelman ER, Rogers C. Hoop dreams: stents without restenosis. *Circulation.* 1996:94:1199-1202.

Edelman ER, Rogers C. Pathobiologic responses to stenting. *American Journal of Cardiology.* 1998;81:4E-6E.

Endo A, Hirayama H, Yoshida O, Arakawa T, Akima T, T. Yamada T, Nanasato M. Arterial remodelling influences the development of intimal hyperplasia after stent implantation. *Journal of the American College of Cardiology.* 2001;37:70-75.

Etave F, Finet G, Boivin M, Boyera J-C, Rioufol G, Thollet G. Mechanical properties of coronary stents determined by using finite element analysis. *Journal of Biomechanics.* 2001;34:1065-1075.

European Cardiovascular Disease Statistics, 2000 Edition, British Heart Foundation.

European Restenosis and Clinical Evaluation in Coronary Arteries Study (RACECAR), http://www.medtronic.com/newsroom/news_20001120.html.

Fronek K, Schmid-Schonbein, G, Fung YC. A non contact method for three dimensional analysis of vascular elasticity in vivo and in vitro. *Journal of Applied Physiology.* 1975;40:634-637.

Fu G, Zeng Y, Xia Z,Lee J. Biorheological features of some soft tissues under a surgical tissue expansion procedure. *Biorheology.* 1997;34:281-293.

Fung YC, Fronek K, Patitucci P. Pseudoelasticity of arteries and the choice of its mathematical expression. *American Journal of Physiology.* 1979;237:H620-H631.

Fung YC. *Biomechanics. Mechanical behaviour of living tissues*, 2nd Edition, Springer, New York, 1993:261-262.

Glagov S, Bassiouny HS, Giddens DP, Zarins CK. Intimal thickening: morphogeneis, functional significance and detection. *Journal of Vascular Investigation.* 1995;1:2-14.

Goldberg SL, Di Mario C, Hall P, Colombo A. Comparison of aggressive versus nonaggressive balloon dilatation for stent deployment on late loss and restenosis in native coronary arteries. *American Journal of Cardiology.* 1998;81:708 –712.

Gottsauner-Wolf M, Moliterno DJ, Lincoff AM, Topol EJ. 1996. Restenosis- an open file. *Clinical Cardiology.* 1996;19:347-356.

Grewe PH, Deneke T, Machraoui A, Barmeyer J, Muller K-M. Acute and chronic tissue response to coronary stent implantation: pathologic findings in human specimens. *Journal of the American College of Cardiology*. 2000;35:157-163.

Gruentzig AR, Senning A, Siegenthaler WE. Nonoperative dilatation of coronary artery stents: Percutaneous transluminal coronary angioplasty. *New England Journal of Medicine*. 1979;301:61-68.

Hayashi K, Imai Y. Tensile property of atheromatous plaque and an analysis of stress in the artherosclerotic wall. *Journal of Biomechanics*. 1997;30:573-579, 1997.

Heart Disease and Stroke Statistics, 2004, American Heart Association, http://www.americanheart.org/.

Hospital In-Patient Enquiry (HIPE) system and the National Perinatal Reporting System (NPRS) Unit, Economic and Social Research Institute, Dublin, Ireland, 2004, http://www.esri.ie.

Hoffmann R, Mintz GS, Dusaillant GR, Popma JJ, Pichard AD, Satler LF, Kent KM, Griffin J, Leon MB. Patterns and mechanisms of in-stent restenosis. A serial intravascular ultrasound study. *Circulation*. 1996;94:1247-1254.

Hoffmann R, Mintz GS, Mehran R, Kent KM, Pichard AD, Satler LF, Leon MB. Tissue proliferation within and surrounding palmaz-schatz stents is dependent on the aggressiveness of the stent implantation technique. *American Journal of Cardiology*. 1999;83:1170-1174.

Hoffmann R, Mintz GS. Coronary in-stent restenosis - predictors, treatment and prevention. *European Heart Journal*. 2000;21:1739-1749.

Hoffmann R, Mintz GS, Haager PK, Bozaglu T, Grube E, Gross M, Beythien C, Mudra H, vom Dahl J, Hanrath P. Relation of stent design and stent surface material to subsequent in-stent intimal hyperplasia in coronary arteries determined by intravascular ultrasound. *American Journal of Cardiology*. 2002;89:1360-1364.

Holzapfel G, Gasser, TC, Ogden, RW. A new constitutive framework for arterial wall mechanics and a comparative study of material models. *Journal of Elasticity*. 2000; 61, 1-48.

Holzapfel G, Stadler M, Schulze-Bauer CAJ. A layer specific three dimensional model for the simulation of balloon angioplasty using magnetic resonance imaging and mechanical testing. *Annals of Biomedical Engineering*. 2002;30:753-767.

Humphrey JD. *Cardiovascular solid mechanics. cells, tissues and organs*. Springer, New York, 2002.

Ikari Y, Hara K, Tamura T, Saeki F, Yamaguchi T. Luminal loss and site of restenosis after Palmaz-Schatz coronary stent implantation. *American Journal of Cardiology*. 1995;76:117-120.

James AG, Green A, Simpson GM. Strain energy functions of rubber. i. characterization of gum valcanizates. *Journal of Applied Polymer Science*, 1972;19:2033-2058.

Kastrati A, Dirschinger J, Boekstegers P, Elezi S, Schühlen H, Pache, J, Steinbeck G, Schmitt C, Ulm K, Neumann F-J, Schömig A. Influence of stent design on 1-year outcome after coronary stent placement: a randomized comparison of five stent types in 1,147 unselected patients. *Catheterization and Cardiovascular Interventions*. 2000;50:290-297.

Kastrati A, Mehilli J, Dirschinger J, Dotzer F, Schühlen H, Neumann F-J, Fleckenstein M, Pfafferott C, Seyfarth M, Schömig A. Intracoronary Stenting and Angiographic Results Strut Thickness Effect on Restenosis Outcome (ISAR-STEREO) Trial. *Circulation*. 2001;103:2816:2821.

Kelly DJ, Prendergast PJ. Mechano-regulation of stem cell differentiation and tissue regeneration in osteochondral defects. *Journal of Biomechanics*. in press.

Ker RF, Zioupos P. Creep and fatigue damage of mammalian tendon and bone. *Comments on Theoretical Biology*. 1997;4:151-181.

Keynton RS, Evancho MM, Sims RL, Rodway NV, Gobin A, Rittgers SE. Intimal hyperplasia and wall shear in arterial bypass graft distal anastomoses: an in vivo model study. *ASME Journal of Biomechanical Engineering*. 2001;123:464–73.

Lally C, Prendergast PJ. An investigation into the applicability of a Mooney-Rivlin constitutive equation for modelling vascular tissue in cardiovascular stenting procedures. *Proc. of the International Congress on Computational Biomechanics*, Zaragoza, Spain, September 24-26, 2003; 542-550.

Lally C, Reid AJ, Prendergast PJ. Elastic behaviour of porcine coronary artery tissue under uniaxial and equibiaxial tension. *Annals of Biomedical Engineering*, October 2004, to appear.

Lally C, Dolan F, Prendergast PJ. Cardiovascular stent design and vessel stresses: a finite element analysis. *Journal of Biomechanics,* in press.

Lanir Y, Fung YC. Two dimensional mechanical properties of rabbit skin. Experimental system. *Journal of Biomechanics*. 1974;7:29-34.

Lepor NE, Madyoon H, Kereiakes D. Effective and efficient strategies for coronary revascularization in the drug-eluting stent era. *Reviews in Cardiovascular Medicine*. 2002;3:S38–S50.

Loree HM, Kamm RD, Stringfellow RG, Lee RT. Effects of fibrous cap thickness on peak circumferential stress in model atherosclerotic vessels. *Circulation Research*. 1992;71:850-858.

Loree HM, Grodzinsky AJ, Park SY, Gibson LJ, Lee RT. Static and circumferential tangential modulus of human atherosclerotic tissue. *Journal of Biomechanics*. 1994;27:195-204.

Manak JJ. The two dimensional in vitro passive stress-strain elasticity relationships for the steer thoracic aorta blood vessel tissue. *Journal of Biomechanics*. 1980;13:637-646.

Marc/Mentat manuals, MSC Software, Santa Ana, CA, USA.

Martini F. *Fundamentals of anatomy and physiology*, fifth edition, New Jersey: Prentice Hall International, 2001:666.

Maurel W, Wu Y, Magnenat Thalmann N, Thalmann D. *Biomechanical models for soft tissue simulation*. Springer, Berlin, 1998.

McClean R, Eigler NL. Stent design: implications for restenosis. *Reviews in Cardiovascular Medicine*. 2002;3:S16–S22.

Medtronic Distance Study, Medtronic AVE, UC200203607EE 6M 5/02.

Meads C, Cummins C, Jolly K, Stevens A, Burls A, Hyde C. Coronary artery stents in the treatment of ischaemic heart disease: a rapid and systematic review. *Health Technology Assessment*. 4:2000.

Migliavacca F, Petrini L, Colombo M, Auricchio F, Pietrabissa R. Mechanical behavior of coronary stents investigated through the finite element method. *Journal of Biomechanics*. 2002;35:803–811.

Miner MA. Cumulative fatigue damage. Transactions, *American Society of Mechanical Engineers*. 1945;67:A159-A164.

Mohan D, Melvin J. Failure properties of passive human aortic tissue: uniaxial tension tests. *Journal of Biomechanics*. 1982;2:887-902.

Mooney M. A theory of large elastic deformation. *Journal of Applied Physics*. 1940; 11:582-592.

Murray JD. *Mathematical biology*, Springer-Verlag, 1989.

Nobuyoshi M, Kimura T, Ohsihi H, Horiuchi H, Nosaka H, Hamasaki N, Yokoi H, Kim K. Restenosis after percutaneous transluminal coronary angioplasty: pathologic observations in 20 patients. *Journal of the American College of Cardiology*. 1991;17:433-439.

Ogden RW. *Nonlinear elastic deformations*, John Wiley & Sons, New York, 1984.

Ogden RW, Schulze-Bauer CAJ. Phenomenological and structural aspects of the mechanical response of arteries. In: *Mechanics in Biology* (Eds. J. Casey, G. Bao), BED2000;46:125-140.

Orford JL, Selwyn AP, Ganz P, Popma JJ, Rogers C. The comparative pathobiology of atherosclerosis and restenosis. *American Journal of Cardiology*. 2000;86:6H-11H.

Palmaz JC. Stents from the past, present, and future. *Endovascular Today*. January 2004:37-41.

Patel DJ, Fry DL. The elastic symmetry of arterial segments in dogs. *Circulation Research*. 1969;24:1-8.

Patel DJ, Vaishnav RN. The rheology of large blood vessels. In cardiovascular fluid dynamics. Bergal DH (Ed).1972;2:2-65.

Peacock J, Hankins S, Jones T, Lutz R. Flow instabilities induced by coronary artery stents: Assessment with an in vitro pulse duplicator. *Journal of Biomechanics*. 1995;28:17-26.

Ponde CK, Aroney CN, McEniery PT, Bett JHN. Plaque Prolapse between the Struts of the Intracoronary Palmaz-Schatz Stent: Report of two cases with a novel treatment of this unusual problem. *Catheterization and Cardiovascular Diagnosis*. 1997;40:353-357.

Prendergast PJ, Maher SA. Issues in pre-clinical testing of implants. *Journal of Materials Processing Technology*. 2001;118:337-342.

Prendergast PJ, Lally C, Daly S, Reid AJ, Lee TC, Quinn D, Dolan, F. Analysis of prolapse in cardiovascular stents: a constitutive equation for vascular tissue and finite element modelling. *ASME Journal of Biomechanical Engineering*. 2003;125:692-699.

Prendergast PJ, Taylor D. Prediction of bone adaptation using damage accumulation. *Journal of Biomechanics*. 1994;27:1067-76.

Rachev A, Hayashi K. Theoretical study of the effects of vascular smooth muscle contraction on strain and stress distributions in arteries. *Annals of Biomedical Engineering*.1999;27:459–468.

Rachev A, Manoach E, Berry J, Moore Jr, JE. A model of stress-induced geometrical remodeling of vessel segments adjacent to stents and artery/graft anastomoses. *Journal of Theoretical Biology*. 2000;206:429-444.

Rogers C, Edelman ER. Endovascular stent design dictates experimental restenosis and thrombosis. *Circulation*. 1995;91:2995-3001.

Rogers C, Tseng DY, Squire JC, Edelman ER. Balloon-artery interactions during stent placement. A finite element analysis approach to pressure, compliance, and stent design as contributors to vascular injury. *Circulation* Research. 1999;84:378-383.

Ross R. Atherosclerosis - an inflammatory disease. *The New England Journal of Medicine*. 1999;340:115-126.

Rutsch W, Kiemeneij F, Colombo A, Macaya C, Guermonprez J-L, Grip L, Hamburger J, Umans V, Gotsman M, Almagor Y, Morice M-C, Garcia E, Chevalier B, Erbel R, Cobaugh M, Morel M-A, Serruys PW. Clinical and angiographic results with the NIR stent: first international NIR endovascular stent study (FINESS-II). *International Journal of Cardiovascular interventions* 2000;3:143-150.

Sacks MS, Chuong C. Orthotropic mechanical properties of chemically treated bovine pericardium. Annals of Biomedical Engineering. 1998;26:892-902.

Sacks MS. Biaxial mechanical evaluation of biological materials. *Journal of Elasticity*. 2000;61:199-246.

Schwartz R. Holmes DR, Topol EJ. The restenosis paradigm revisited: an alternative proposal for cellular mechanisms. *Journal of the American College of Cardiology*. 1992;20:1284-1293.

Schwartz R, Holmes DR. Pigs, dogs, baboons, and man; lessons in stenting from animal studies. *Journal of Interventional Cardiology*. 1994;7:355-368.

Schwartz RS, Chu A, Edwards WD, Srivatsa SS, Simari RD, Isner JM, Holmes DR Jr. A proliferation analysis of arterial neointimal hyperplasia: lessons for antiproliferative restenosis therapies. *International Journal of Cardiology*. 1996;53: 71-80.

Schwartz RS. Pathophysiology of restenosis: interaction of thrombosis, hyperplasia and/or remodelling. *American Journal of Cardiology*. 1998;81:14E-17E.

Schulze-Bauer CAJ, Mörth C, Holzapfel GA. Passive Biaxial Mechanical Response of Aged Human Iliac Arteries, *ASME Journal of Biomechanical Engineering*, 2003;125:395-406.

Serruys PW, Kutryk MJB. *Handbook of coronary stents*, Martin Dunitz: London, 1998.

Sharma MG. Viscoelastic behavior of conduit arteries. *Biorheology*. 1974;11:279-291.

Sprague EA, Luo J, Palmaz JC. Endothelial cell migration onto metal stent surfaces under static and flow conditions. *Journal of Long Term Effects of Medical Implants*. 2000;10:97-110.

Swindle M. *Swine as Models in Biomedical Research*, Iowa State University Press, Ames, Iowa, 1992:165.

Suryapranata H, Boland JL, Pieper M, Legrand VL, Bonnier JJRM, Juliard J-M, Vrolix MCM, Seabra-Gomes R, Hamburger JN, Roguin A, Oosterwijk C, van Es G-A, Beyar R, Serruys PW. Clinical and angiographic results with the BeStent: the registry for optimal BeStent evaluation (ROSE) trial. *International Journal of Cardiovascular Interventions*. 2000;3:21-28.

Taber LA. A model for aortic growth based in fluid shear and fiber stresses. *ASME Journal of Biomechanical Engineering*. 1998;120:348-354.

Tan LB, Webb DC, Kormi K, Al-Hassani STS. A method for investigating the mechanical properties of intracoronary stents using finite element numerical simulation. *International Journal of Cardiology*. 2001;78:51-67.

Tickner E, Sacks A. A theory for the elastic behavior of blood vessels. *Biorheology*. 1967;4:151-168.

Treloar LRG. The elasticity of a network of long-chain molecules. *Transactions of the Faraday Society*. 1943;39:241-246.

Truesdell CA. The mechanical foundations of elasticity and fluid dynamics. *Journal of Rational Mechanics and Analysis*. 1952;1:173-182.

Vaishnav RN, Young JT, Janicki JS, Patel DJ. Nonlinear anisotropic elastic properties of the canine aorta. *Biophysical Journal*. 1973;12:1008-1027.

van Andel CJ, Pistecky PV, Borst C. Mechanical properties of porcine and human arteries: implications for coronary anastomotic connectors. *Annals of Thoracic Surgery*. 2003;76:58-65.

van der Meulen MCH, Huiskes R. Why mechanobiology? *Journal of Biomechanics*. 2002;35:401-414.

Virmani R. The ideal animal model for restenosis. *Cardiovascular Radiation Therapy*. 6-8th February, 2002.

Vito R. The mechanical properties of soft tissues – a mechanical system for biaxial testing. *Journal of Biomechanics*. 1980;13:947-950.

Vito R. The mechanical properties of soft tissues – Part II: The elastic response of arterial segments. *Journal of Biomechanics*. 1980;13:947-950.

Vito RP, Dixon SA. Blood vessel constitutive models 1995-2002. *Annual Review of Biomedical Engineering*. 2003;5:413-439.

Wang XT, Ker RF, McNeill Alexander R. Fatigue rupture of wallaby tail tendons. *The Journal of Experimental Biology*. 1995;198:847-852.

Wentzel JJ, Whelan DM, van der Giessen WJ, van Beusekom HMM, Andhyiswara I, Serruys PW, Slager CJ, Krams R. Coronary stent implantation changes 3-D vessel geometry and 3-D shear stress distribution. *Journal of Biomechanics*. 2000; 33: 1287–1295.

Wentzel JJ, Krams R, Schuurbiers JCH, Oomen JA, Kloet J, van der Giessen WJ, Serruys PW, Slager CJ. Relationship between neointimal thickness and shear stress after wallstent implantation in human coronary arteries. *Circulation*. 2001;103:1740–1745.

Weizsacker HW, Lambert H, Pascale K. Analysis of the passive mechanical properties of rat carotid arteries. *Journal of Biomechanics*. 1983;16:703-715.

Weisacker HW, Pinto JG. Isotropy and anisotropy of the arterial wall. *Journal of Biomechanics*. 1988;21:477-487.

Whitcher FD. Simulation of in vivo loading conditions of nitinol vascular stent structures. *Computers and Structures*. 1997;64:1005-1011.

Wolinsky H, Glagov S. Structural basis for the static mechanical properties of the elastic media. *Circulation Research*. 1964;14:400-413.

Yamada H. *Strength of biological materials*, The Williams and Wilkins Company, Baltimore, 1970:113.

Yang C, Tang D, Liu SQ. A multi-physics growth model with fluid-structure interactions for blood flow and re-stenosis in rat vein grafts: a growth model for blood flow and re-stenosis in grafts. *Computers and Structures*. 2003;81:1041-1058.

Yutani C, Imakita M, Ishibashi-Ueda H, Tsukamoto Y, Nishida N, Ikeda Y. Coronary atherosclerosis and interventions: pathological sequences and restenosis. *Pathology International*. 1999:49:273-290.

Zhou J, Fung YC. The degree of nonlinearity and anisotropy of blood vessel elasticity. *Proceedings of the National Academy of Science USA*. 1997;94:14255-14260.

Website 1: http://www.nlm.nih.gov/medlineplus/ency/imagepages/18050.htm last accessed 19/07/2004

Website 2: http://vascular.mdmercy.com/discoveries/balloon_stent.html last accessed 19/07/2004

Website 3: http://greenfield.fortunecity.com/rattler/46/arteries.htm last accessed 5/07/04

Website 4: http://www.medtronic.com/medtronic_vascular/cs_s7.html last accessed 6/08/04

Appendix A

ICCB Paper
by Lally & Prendergast, 2003

INTERNATIONAL CONGRESS ON COMPUTATIONAL BIOENGINEERING
M. Doblaré, M. Cerrolaza and H. Rodrigues (Eds.)

AN INVESTIGATION INTO THE APPLICABILITY OF A MOONEY-RIVLIN CONSTITUTIVE EQUATION FOR MODELLING VASCULAR TISSUE IN CARDIOVASCULAR STENTING PROCEDURES

Caitríona Lally and Patrick J. Prendergast

Centre for Bioengineering, Department of Mechanical Engineering, Trinity College, Dublin, Ireland.

SUMMARY

Finite element analysis is a tool which can be used to determine the stress distribution caused by different stent designs within arteries. It has the potential to be the basis of a preclinical testing methodology for new stent designs. In order for these simulations to be meaningful however the mechanical properties of the arterial tissue need to be modelled realistically. We investigate if an isotropic model of the artery wall can adequately represent the anisotropic nonlinear elastic characteristics of arterial tissue in stenting procedures.

In this paper, an isotropic hyperelastic Mooney-Rivlin model is developed based on uniaxial and equibiaxial tensile measurements obtained from both human femoral and porcine coronary arterial segments. Finite element models of idealised arteries where the material is defined using the hyperelastic constitutive equations of the two different material types were developed. Comparisons between these models and experimental data from inflation tests on arteries, as well as the results of a recently developed anisotropic model, were made to determine the applicability of the Mooney-Rivlin model for analysis of stent designs.

Based on these comparisons we conclude that a Mooney-Rivlin model can be used to model the arterial tissue for stenting analyses because an initial axial stretch would always be present in arterial vessels. With such initial axial stresses the anisotropic model behaves in the same way as the isotropic material model whereby the artery retracts axially when subjected to a luminal pressure. It is therefore proposed that this less complex isotropic Mooney-Rivlin model may be used for comparative analyses of stents, as it still includes the key features of stress stiffening that would not be simulated by a linear elastic material.

1. INTRODUCTION

Intravascular stents have been developed to maintain vessel patency after balloon angioplasty. The expanded stent remains in the vessel as a buttress for the artery wall. It also scaffolds the atherosclerotic plaque. However, a stent may induce damage within the tissue and provoke a response by the vessel, ultimately causing restenosis of the stented artery [1]. This is called 'in-stent restenosis'. The loss of patency of the vessel is predominantly caused by tissue prolapse between the stent strut interstices and intimal hyperplasia within the vessel lumen [2]. The magnitude of in-stent restenosis has been found to be dependent on stent design [3].

Finite element analysis can be used to determine the stress caused to an artery by a stent. However before finite element analysis can be applied, an appropriate material model of vascular tissue is necessary.

Arterial tissue has been found to be almost incompressible and as such is taken as incompressible for the purpose of numerical modelling [4]. However studies of the elastic response of arteries have found that vessels display curvilinear orthotropy [5]. In addition, arteries undergo large non-linear deformations under loading that are almost completely recoverable, particularly in the preconditioned state existing in the vessel under cyclic loading *in vivo* [6].

A hyperelastic constitutive model may be used to represent the elastic behaviour of incompressible, non-linear elastic materials undergoing finite deformations. Taking the strain energy density function of the material in terms of the principal stretches or the strain invariants and differentiating with respect to the appropriate strain component gives the corresponding stress component. One general form of the strain energy density function in terms of the strain invariants, given by Maurel *et al.* [7] for an isotropic hyperelastic material is:

$$W(I_1, I_2, I_3) = \sum_{i,j,k=0}^{\infty} a_{ijk} (I_1 - 3)^m (I_2 - 3)^n (I_3 - 3)^o, a_{000} = 0$$

where W is the strain energy density function of the hyperelastic material, I_1, I_2 and I_3 are the strain invariants and a_{ijk} are the hyperelastic constants. If the principal stretches of the material are denoted λ_1, λ_2 and

λ_3, then the strain invariants for the material may be defined as:

$$I_1 = \lambda_1^{\,2} + \lambda_2^{\,2} + \lambda_3^{\,2},$$
$$I_2 = \lambda_1^{-2} + \lambda_2^{-2} + \lambda_3^{-2}$$
$$I_3 = \lambda_1^2 \lambda_2^2 \lambda_3^2.$$

$I_3 = 1$ for an incompressible material [7]. Many strain energy functions have been formulated to model incompressible hyperelastic materials. Some of these are summarised below:

Mooney-Rivlin [8]

$$W(I_1, I_2) = \sum_{i,j=0}^{\infty} a_{ij} (I_1 - 3)^m (I_2 - 3)^n, a_{00} = 0$$

Vito [9]

$$W_1 = \sum_{k=1}^{k\leq 4} b_k (I_1 - 3)^k$$

where b_k is a material constant.

Ogden [10]

$$W(\lambda_1, \lambda_2, \lambda_3) = \sum_{p=1}^{N} \frac{\mu_p}{\alpha_p} (\lambda_1^{\alpha_p} + \lambda_2^{\alpha_p} + \lambda_3^{\alpha_p} - 3)$$

where μ_p and α_p are material constants.

Fung [6]

$$W(E_{ij}) = \frac{1}{2} \sum_{i,j,k,l=1}^{3} \alpha_{ijkl} E_{ij} E_{kl} + \beta_0 \sum_{m,n,p,q=1}^{3} \beta_{mnpq} E_{mn} E_{pq} e^{\alpha}$$

$$\alpha = \sum_{i,j=1}^{3} \nu_{ij} E_{ij} + \frac{1}{2} \sum_{i,j,k,l=1}^{3} \gamma_{ijkl} E_{ij} E_{kl} + ...$$

where E is the Green-Lagrange strain tensor. This model also applies to an anisotropic hyperelastic material. (For further strain energy density functions, see [7]).

The experimental parameters of these models, and many similar ones, have been obtained from uniaxial and biaxial tensile tests of arterial tissue. However the application of these models to computational models of cardiovascular stenting and angioplasty procedures is very limited. Many of the computational models to-date represent the vascular wall as linear elastic [11, 12] or isotropic hyperelastic [13], and only one study has modelled the vessel as an anisotropic hyperelastic material [14].

1.1 Mooney-Rivlin model

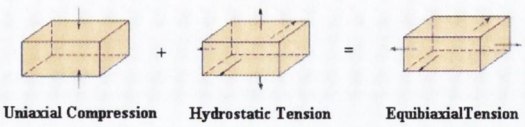

Figure 1 Equivalent modes of deformation for an incompressible material [15].

In this paper we aim to investigate the applicability of the Mooney-Rivlin hyperelastic model when used to simulate the artery behaviour. The advantage of using a Mooney-Rivlin model to generate preclinical testing models is the wide availability of this model, or a derivative of it, in commercial finite element analysis software codes and the ease of implementation of such a model once appropriate experimental data is available. The best deformation modes for testing to determine the constants in a Mooney-Rivlin model are those that are the dominant modes of deformation in the application of interest. A stented vessel undergoes primarily uniaxial and biaxial tension and uniaxial compression; however for an isotropic and incompressible material uniaxial compression is defined by the equibiaxial tension deformation mode, see Fig. 1. Therefore it is not necessary to test the tissue in uniaxial compression if equibiaxial tension tests are carried out. As a result an accurate Mooney-Rivlin model for arterial tissue in cardiovascular stenting applications would be a constitutive equation based on fitting best-fit curves to experimental data from uniaxial tension and equibiaxial tension tests.

Many forms of the generalized Mooney-Rivlin model are available in commercial finite element analysis packages. In fact, the strain energy function W, given by Mooney [8], can be expanded to obtain the special cases of the two, five or nine-parameter strain energy density functions [15]:

$$W = a_{10}(I_1 - 3) + a_{01}(I_2 - 3)$$

$$W = a_{10}(I_1 - 3) + a_{01}(I_2 - 3) + a_{20}(I_1 - 3)^2 + a_{11}(I_1 - 3)(I_2 - 3) + a_{02}(I_2 - 3)^2$$

$$W = a_{10}(I_1 - 3) + a_{01}(I_2 - 3) + a_{20}(I_1 - 3)^2 + a_{11}(I_1 - 3)(I_2 - 3) + a_{02}(I_2 - 3)^2 + a_{30}(I_1 - 3)^3 + a_{21}(I_1 - 3)^2(I_2 - 3) + a_{12}(I_1 - 3)(I_2 - 3)^2 + a_{03}(I_2 - 3)^3$$

These equations represent first, second, and third order models respectively. When the first order model is reduced to $W = a_{10}(I_1 - 3)$ it is called the neo-Hookean form of the strain energy function and it is the simplest hyperelastic constitutive model [16]. The deformation modes of a hyperelastic material, which are highly non-

linear, can be more accurately modelled as the order of the expression for W is increased. When a suitable form of the strain-energy function is chosen, the parameters a_{ij} are found by non-linear regression.

Many of the hyperelastic models available in commercial finite element analysis codes are special cases of the Mooney-Rivlin nine-parameter model, such as the third order model used by Hayashi and Imai [13].

It is known however that the assumption if isotropy for arterial tissue may lead to errors in the analysis of the inflation response of vessels. The objective of this study is therefore to determine the applicability of the Mooney-Rivlin approach or more specifically the third order deformation constitutive model, when established based on both uniaxial and equibiaxial tensile test data obtained from human femoral arterial tissue and porcine coronary arterial segments (to the application of stent design analyses).

To achieve this objective the following deformation plots were generated; for a constant axial load, (a) the internal pressure versus circumferential stretch and (b) the internal pressure versus axial stretch using finite element analysis of a cylinder, where the material was defined using the hyperelastic constitutive equations established from the uniaxial and equibiaxial experimental data. The results are then compared to experimental data and the analytical data of Ogden and Schulze-Bauer [17] for an anisotropic hyperelastic thin-walled membrane model.

Although the isotropic material model may not represent the arterial tissue exactly, it is proposed that if it is established based on experimental data of the deformation modes of interest that it may be used to model arterial tissue in applications where the tissue has an initial prestretch as is the case in stenting procedures.

2. METHODS

2.1 Arterial tissue mechanical tests

Human coronary arteries were not obtained for testing, as the coronary artery is necessary for the embalming process of cadavers and harvesting the coronary arteries is a complicated surgical procedure that requires extensive dissection [18]. The porcine coronary system is the same in most respects to that of humans and is the most similar animal circulatory system in both anatomy and function to that of the human circulatory system [19]. As a result the porcine coronary artery was chosen as the test tissue type to determine the approximate tissue properties for healthy human coronary arterial tissue. Aged human femoral arteries were also tested for comparison as they can easily be obtained from cadavers and are vessels prone to atherosclerosis in the same way as the human coronary arteries. The sizes of the test specimens that can be obtained from human femoral arterial tissue are larger than those that can be obtained from porcine coronary arteries and therefore a different test protocol was developed for each tissue type.

2.1.1 Porcine coronary arterial tissue tests

Porcine left, right and circumflex coronary arteries, which lie on the surface of the heart, were harvested from the hearts of adult pigs and tested in the following experiments.

The arterial tissue samples were stored in antibiotic solution at 4°C prior to testing. All samples were prepared under sterile conditions, and any visible connective tissue was removed from the surface of the vessel before it was cut along its length, pressed flat, and sectioned. Lengths of tissue were prepared for uniaxial testing and areas of 5 mm square were prepared for biaxial testing. The thickness of each sample was measured after mounting the test specimen on a glass slide and by viewing the edge of the sample under a microscope. The tissue thickness was recorded at three different locations along the edge of the sample and an average taken.

2.1.1.1 Uniaxial tissue tests

Pneumatic grips, the gripping faces of which were covered with emery paper to prevent specimen slippage, were mounted on a Zwick Z005 displacement controlled tensile testing machine to grip the arterial tissue in uniaxial tension. Specimens were longitudinal in the *in vivo* orientation and each test section was cut to a width of 3.5 mm using a custom made cutter comprising of two scalpel blades 3.5 mm apart. Extension of the specimen was taken to be the crosshead displacement. Five preconditioning cycles were performed before the tissue was tested to failure. A strain rate of 60%/min, of the initial gauge length prior to preconditioning, was used to test the sample to failure after the preconditioning cycles. The test specimens were maintained moist throughout the test with 0.9% saline solution.

2.1.1.2 Biaxial tissue tests

The biaxial loading device consists of a balanced set of levers which ensures equal force is applied to the four sides of a square test specimen, as reported earlier [20].

Test specimens, 5 mm square, were cut using a cutter comprising of two scalpel blades 5 mm apart. Each sample was marked using vegetable dye to indicate its *in vivo* circumferential/longitudinal orientation. For biaxial testing, dots were printed on the inner surface of the blood vessel using a pin and water resistant, oil-based, quick drying ink to enable strain measurement using image analysis. In the case of the porcine coronary artery specimens the loading bracket of the biaxial device transferred the loads from the line to the specimen via threads with fishing hooks attached, see Fig. 2. A specially designed gripping jig was used to

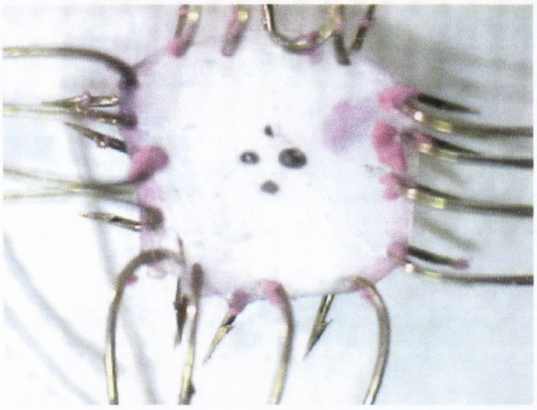

Figure 2 Porcine coronary artery test specimens were gripped with fishing hooks, four on each side. The four dots shown are used for strain measurement.

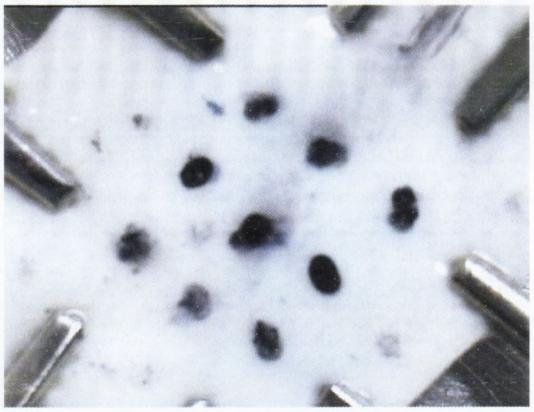

Figure 3 Human femoral artery test specimens were gripped with crocodile grips, with screws added to the clamps to grip the specimens. The markers shown were used for strain measurement.

ensure that the hooks were placed an even distance apart when gripping the small tissue specimens.

Five preconditioning cycles were performed after which the tissue was loaded at a constant strain rate of 60%/min of the initial gauge length and stopped when the tissue began to tear at the fishing hooks. The test specimens were moistened throughout the test with 0.9% saline solution.

A high-resolution colour digital camera (JAI CV-950, Vortex Vision, UK) mounted above the test specimen was used to take an image of the tissue every second during the test. Each image was thresholded in Scion Image (Maryland, USA) and the vertical and horizontal distance between two pairs of central markers was determined for each image. The strain of the tissue in the principal directions was then determined from the increase in distance between the markers on the specimen, in both the vertical and horizontal directions, from picture to picture as the load increased. The gauge length for stress and strain calculations was taken as the distance between the hooks in the direction orthogonal to the loading direction and an average value was found for the two principal directions using image analysis. For the biaxial tests, to obtain the parameters of the Mooney-Rivlin models, it was necessary to establish just one biaxial stress-stretch curve since the Mooney-Rivlin model assumes the material to be isotropic – therefore an average stress-stretch curve was determined from the stress-stretch curves in both the circumferential and longitudinal directions.

2.1.2 Human femoral arterial tissue tests

The method used for testing the human femoral arterial tissue in uniaxial and biaxial tension has been reported earlier [20]. Briefly, it comprises harvesting and storing the human femoral arterial tissue, preparing longitudinal strips of tissue for uniaxial testing and square specimens for equibiaxial testing as described above. The uniaxial tissue specimens were gripped between stainless steel grips and the gripping of the biaxial samples was done with crocodile grips (Fig. 3), which were deemed suitable for the larger biaxial tissue samples, i.e. 25 mm square. The tissue specimens in all of the tests were tested to failure.

2.2 Constitutive modelling

A third order deformation model, a specific form of the nine-parameter Mooney-Rivlin hyperelastic material model is available in MARC/mentat (MscSoftware, Santa Ana, CA, USA) along with a non-linear regression routine to determine the parameters, a_{ij}, of this third order model. It is given by the following equation:

$$W = a_{10}(I_1 - 3) + a_{01}(I_2 - 3) + a_{20}(I_1 - 3)^2 + a_{11}(I_1 - 3)(I_2 - 3) + a_{30}(I_1 - 3)^3 \qquad \text{Eqn. (1)}$$

In some cases it may be found that the predicted non-linear elasticity is unaffected by a particular parameter and therefore that parameter is redundant and may be set to zero. However, the final set of parameters must satisfy the requirement for positive definiteness of the elastic behaviour, and these conditions can be violated if insufficient data is used in the regression [21].

It is worth noting that if uniaxial data alone were used to determine the hyperelastic constitutive equation, the predicted biaxial stress-stretch relationship of the material could be totally unlike that which would occur *in vivo*. This can be explained by the fact that one hyperelastic constitutive equation describes all modes of deformation of the hyperelastic material and although it may be determined based on only one mode of deformation it also predicts the other modes of deformation.

This is illustrated in Fig. 4, where the constants of the hyperelastic constitutive equation were established

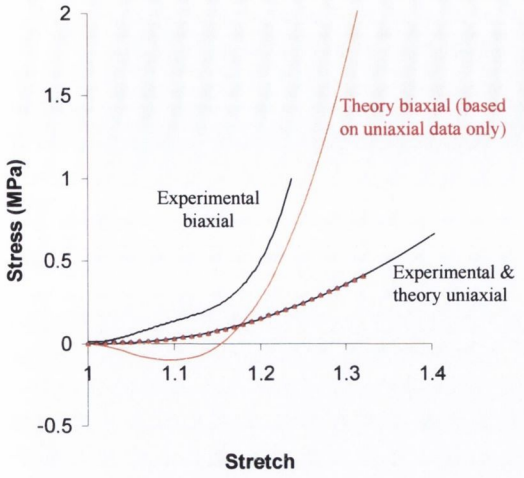

Figure 4 Uniaxial and equibiaxial experimental data curves for human femoral arterial tissue and the regression curve fit using only the uniaxial stress-stretch curve shown.

based on the uniaxial stress-stretch data shown using the non-linear regression routine available in MARC/mentat. Although the curve fit predicts the uniaxial behaviour precisely, the biaxial behaviour is totally unrealistic. It is necessary to ensure that the stress-strain curves continue to be positive definite within the range of experimental data obtained and on extrapolation beyond the experimental data. This is clearly not the case for the hyperelastic constitutive model shown in Fig. 4.

Therefore, by obtaining a curve that is a best fit to both the uniaxial and the biaxial stress-stretch data and ensuring that it is positive definite, one hyperelastic constitutive equation can be obtained which most accurately represents the uniaxial and biaxial stress-stretch properties of the arterial tissue.

2.3 Finite element modelling

Finite element models of an idealized artery, represented by a cylinder, were generated to determine the deformation characteristics of the two materials defined by the experimental data. The dimensions of the cylinder were the following: an outside diameter of 4 mm, length of 10 mm and wall thickness of 0.5 mm. Eight-node, isoparametric, arbitrary hexahedral elements were used. The loading conditions which were applied to an intact artery, given in Ogden and Schulze-Bauer [10], were reproduced in the finite element models. One end of the vessel was fixed in the axial direction and a constant axial load was applied by means of a rigid contact body at the other end to ensure uniform application of the axial load. The axial load ranged from 0 to 9.9 N. Circumferential constraints were applied to the vessel at the four quadrant points at both ends of the vessel to ensure uniform expansion of the vessel. A luminal pressure was applied ranging from 0 kPa to 35 kPa.

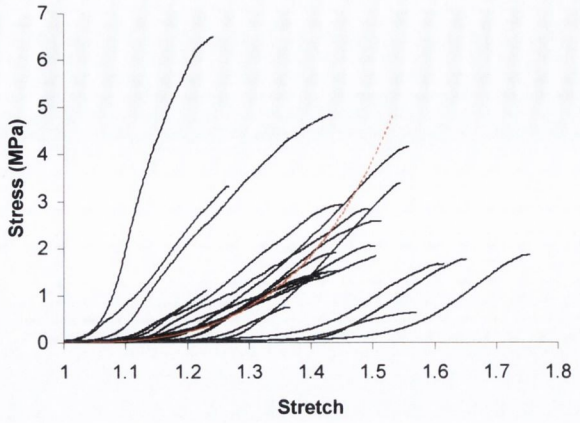

Figure 5 Uniaxial stress-stretch data (solid lines, n=20) for porcine coronary arterial tissue and the regression curve fit to the data (dashed line).

3. RESULTS

3.1 Arterial tissue mechanical tests and hyperelastic constitutive equations

3.1.1 Porcine coronary artery

The uniaxial stress-stretch data obtained for the porcine coronary tissue samples clearly illustrate the non-linear stress-stretch characteristics of arterial tissue, see Fig. 5. There is a great deal of variation in the stress-stretch data particularly in the initial stretch of the tissue after preconditioning. However the final slopes of the curves, which represent the stiffness of the tissue once all of the collagen fibres have been recruited, along with the elastin, to bear the load [22], are not at all dissimilar.

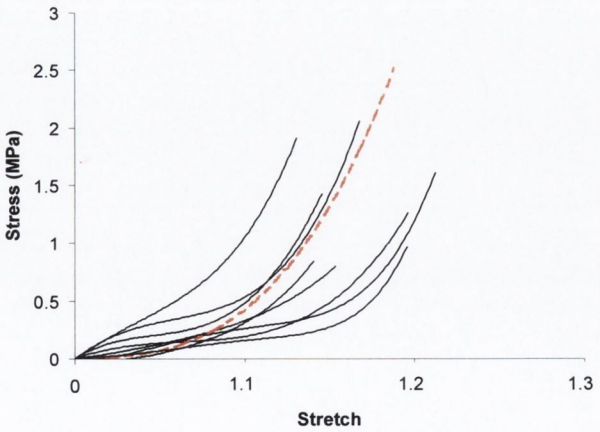

Figure 6 Biaxial stress-stretch data (solid lines, n=8) for porcine coronary arterial tissue and the regression curve fit to the data (dashed line)

Using a single central lying curve from each set of data to represent the uniaxial and biaxial data the hyperelastic constants were obtained for a best fit to this uniaxial and biaxial data, shown in Table 1. The uniaxial regression curve fit is shown in Fig. 5 as a dashed line and it can be seen that it represents the majority of uniaxial data reasonably well.

The equibiaxial experimental data for the porcine coronary test specimens again shows nonlinear stress-stretch characteristics (Fig. 6). However the tissue is clearly stiffer in equibiaxial tension than in uniaxial tension.

The regression curve fit to the biaxial data (dashed line), also shown in Fig. 6, indicates a good fit to the biaxial data especially at higher values of stretch.

3.1.2 Human coronary artery

The uniaxial and equibiaxial data obtained for the human femoral arterial tissue are shown in [20] and also given in Fig. 7 with additional stress-stretch data given here. The same characteristics are seen for this arterial tissue whereby the tissue is stiffer in equibiaxial tension than in uniaxial tension alone. The regression curve fits the uniaxial data very well. The biaxial data shows a great deal of variation, however the biaxial curve fit can be seen to fit one set of biaxial experimental data very well.

The hyperelastic constants of Eqn. (1) above, found to best fit the experimental data for each tissue type, are given below in Table 1. To ensure positive definiteness, the hyperelastic constants had to be restricted to positive values only.

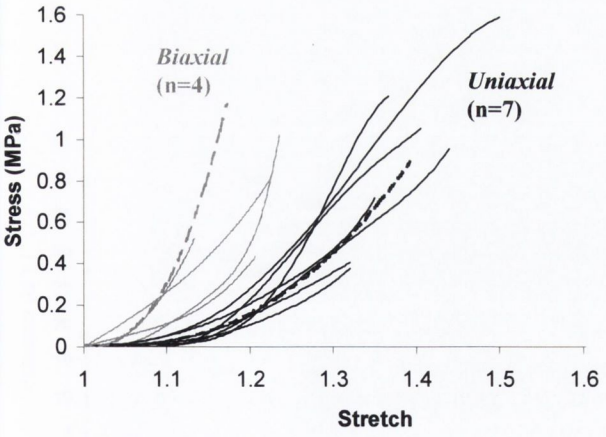

Figure 7 Uniaxial and biaxial stress-stretch data (solid lines) for human femoral arterial tissue and the regression curve fit to the data (dashed lines)

	Porcine coronary artery parameters (kPa)	Human femoral artery parameters (kPa)
a_{10}	7.31	18.90
a_{01}	12.99	2.75
a_{20}	845.15	590.42
a_{11}	0	857.18
a_{30}	825.46	0

Table 1 Hyperelastic constants to describe human femoral and porcine coronary tissue using the third order deformation hyperelastic material model

3.2 Finite Element models

Using the FE model of an idealised artery the circumferential and axial stretch of the vessel with a constant axial load of varying magnitude were determined as the luminal pressure increased from 0 to 35 kPa. This is identical to the loading mode applied by Ogden and Schulze-Bauer [17] both experimentally and to their model that had anisotropic properties.

The luminal pressure versus the circumferential stretch in the model with the material properties based on those for porcine coronary arterial tissue illustrate that as the axial load is increased the tissue becomes stiffer, see Fig. 8.

The non-linear response of the artery wall is clearly seen where no axial load is applied to the ends of the vessel whereby the artery is initially of lower stiffness than at higher values of luminal pressure. However with an axial load of 9.9 N applied, the vessel experiences very little deformation in the circumferential direction as the pressure increases because the tissue is so stiff.

The axial stretch however decreases, i.e. the vessel shortens, as the luminal pressure increases, as shown in Fig. 9. This is due to the circumferential expansion of the artery and the nature of the material, which is incompressible and isotropic. As the load increases however the axial stretch alters very little for the given increase in luminal pressure, illustrating the stiffening of the vessel material in the axial direction when the vessel is subjected to an axial load.

The same stiffening features are evident when the circumferential and axial stretch are plotted versus the applied luminal pressure, where the artery material is defined by the hyperelastic constitutive equation established from the human femoral arterial tissue, see Figs. 10 and 11.

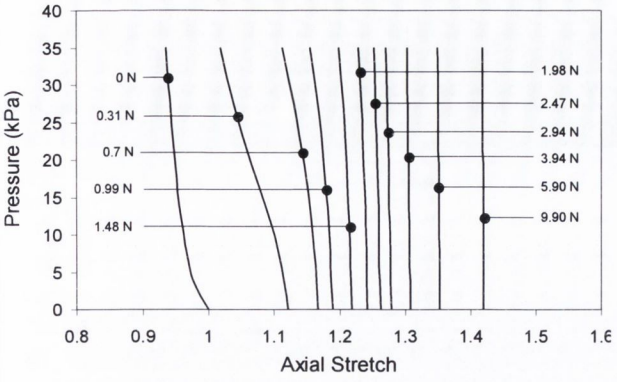

Figure 8 Dependence of circumferential stretch on internal pressure, as a function of axial load (porcine coronary tissue)

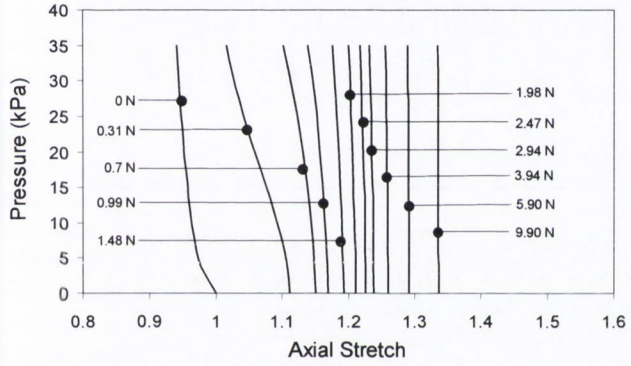

Figure 9 Dependence of axial stretch on internal pressure, as a function of axial load (porcine coronary tissue)

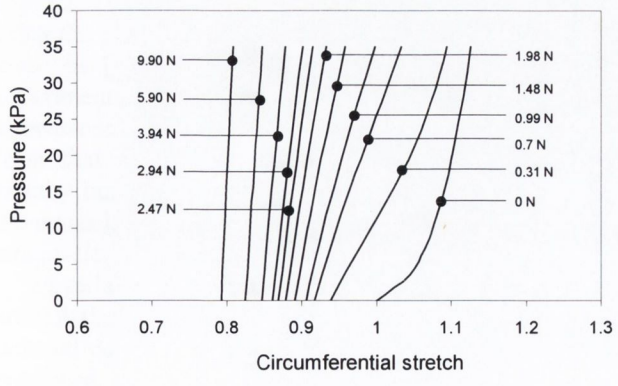

Figure 10 Dependence of circumferential stretch on internal pressure, as a function of axial load (human femoral tissue)

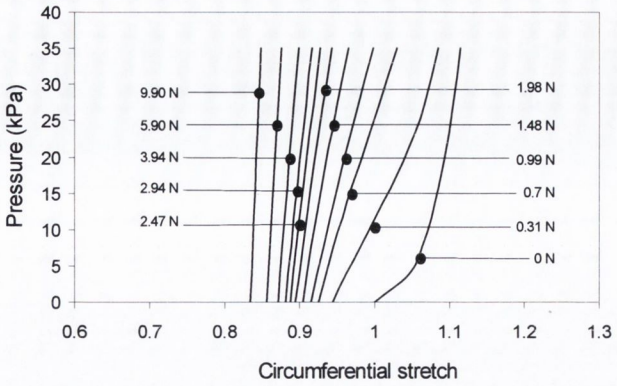

Figure 11 Dependence of axial stretch on internal pressure, as a function of axial load (human femoral tissue)

4. DISCUSSION

The arterial tissue modelled using the porcine coronary arterial test data is stiffer than that of the human femoral artery model as was seen in the experimental data. This is evident also in the finite element models where the circumferential stretch is lower and the axial stretch higher, for the greatest axial load applied, in the human material model compared with the porcine coronary model. This would be expected, as the coronary artery is a more muscular vessel than the femoral artery.

Previous experimental observations of the deformation characteristics of an artery with an applied constant axial load have yielded some similar and some differing results to that which we see for our hyperelastic isotropic materials in the finite element models. The experimental data and the anisotropic model in [17] showed similar results for the relationship between the circumferential stretch and the internal pressure applied. However, the axial stretch was initially found to increase (rather than decrease) on application of an internal pressure for low values of axial load, see Fig. 12.

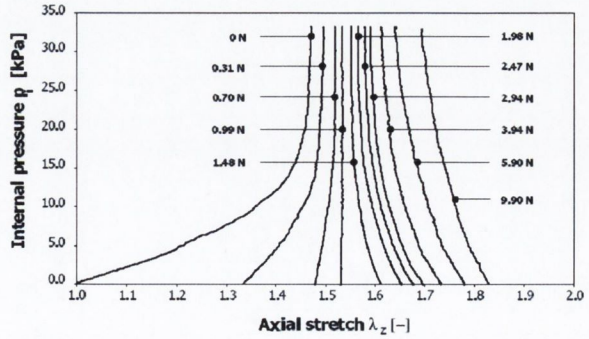

Figure 12 Dependence of axial stretch on internal pressure, as a function of axial load for an intact human iliac artery, taken from Ogden and Schulze-Bauer [17]

In fact an inversion point was found in the axial stretch versus internal pressure plot whereby the axial stretch remained constant with increasing internal pressure at a particular value of the axial load. For all axial loads below this critical value the artery elongated as the internal pressure increased and retracted for axial loads greater than this critical value, see Fig. 12.

Ogden and Schulze Bauer [17] found the value of the inversion point to be between 1.07 and 1.25 for the arteries tested, with the exception of one, for which a value of 1.53 was recorded, which is shown in Fig. 12. This characteristic of arteries whereby the artery elongates axially at low values of luminal pressure has been seen previously in experimental tests [23, 24]. It has been proposed by Weizsacker et al. [23] that this critical value of axial stretch is in fact the *in situ* length of the vessel, as it was found to be very close to the *in situ* length of the vessel under average physiological conditions of the vessel.

The Mooney-Rivlin model detailed in this paper does not include this characteristic of the deformation of arteries observed *in vitro*, therefore it can be asked whether or not it can be legitimately used in simulations of cardiovascular stenting procedures. However, for all simulations of stenting procedures the longitudinal tethering of the vessel would have to be simulated. This is achieved by applying an axial prestretch of 1.2 to replicate the initial stretch in the coronary artery wall. Although this is below the value of 1.53, found for the iliac artery shown in Fig. 12, it is in the range of the average values for the inversion points obtained by Ogden and Schulze-Bauer [17]. By applying this value of prestretch and thereby simulating the in situ length of the vessel the artery would behave as modelled by the isotropic hyperelastic model and only deform in the manner that the experimental and anisotropic model do when they are above the critical axial stretch value.

The other difference between the model data shown here and that of the anisotropic model is the magnitudes of the deformations under the same internal pressure applied. The magnitudes of the deformations are lower using the models described in this paper compared with those in [17]. The dimensions of the vessels tested experimentally are not given in [17] and hence the dimensions of the idealised vessel modelled may be far from that of the iliac artery tested. In addition the healthy human iliac artery would be more elastic than the muscular porcine coronary artery and the less elastic atherosclerotic human femoral artery tested here.

Material test data is widely available on many human arterial tissue types, however it is primarily limited to uniaxial data. In addition, very little test data has been published on the vessel of most interest in terms of cardiovascular stenting, the human coronary artery. In fact, the only available data are the results from uniaxial tensile tests carried out on segments of human coronary arteries [25] and a test, which investigates the relationship between lumen pressure and axial and circumferential strain for an intact coronary artery, for three fixed values of axial extension [26]. Although tests which have been carried out on intact arteries offer valuable information on the deformation modes of arteries *in vivo* they cannot easily be used to define the constitutive model parameters within any currently available numerical material model. In addition, test data available, although very limited, has shown that the porcine coronary artery has very similar mechanical properties to the human coronary artery [26].

5. CONCLUSIONS

It is necessary to define the isotropic Mooney-Rivlin constitutive model based on both the uniaxial and biaxial deformation modes to ensure realistic deformation in a stented vessel. Certain differences are found between the deformation characteristics of a vessel simulated using an isotropic model and that using an anisotropic model; namely axial contraction on inflation at low luminal pressure. However the isotropic and anisotropic models are found to behave in a similar manner if the axial stretch is higher than some critical value. This critical value is generally below that which is applied initially in computational models to simulate the *in vivo* stretch conditions. Therefore, in respect of the phenomenon of vessel elongation during increasing luminal pressure, this is not expected to be a critical issue in stress analysis of stented vessels. Therefore an isotropic Mooney-Rivlin hyperelastic model, established based on both uniaxial and equibiaxial tensile test data, may be used for analysis of cardiovascular stents to determine the stress distribution and hence tissue responses within stented vessels.

6. ACKNOWLEDGEMENTS

Project funded by an Applied Research Grant awarded by Enterprise Ireland to Medtronic AVE, Galway, Ireland, and the Programme for Research in Third Level Institutions, administered by the HEA.

7. BIBLIOGRAPHY

[1] Hoffman, R. and G.S. Mintz, "Coronary in-stent restenosis - predictors, treatment and prevention", *European Heart Journal,* 21, pp. 1739-1749, 2000.

[2] Hoffman, R., G.S. Mintz, G.R. Dusaillant, J.J. Popma, A.D. Pichard, L.F. Satler, K.M. Kent, J. Griffin and M.B. Leon, "Patterns and Mechanisms of in-stent Restenosis. A serial Intravascular Ultrasound Study", *Circulation*, 94, pp. 1247-1254, 1996.

[3] Colombo, A., G. Stankovic and J.W. Moses, "Selection of coronary stents", *Journal of the American College of Cardiology*, 40, pp. 1021-1033, 2002.

[4] Carew, T.E., R.N. Vaishnav and D.J. Patel, "Compressibility of the vascular wall", *Circulation Research,* 27, pp. 105-119, 1968.

[5] Patel, D.J. and R.N. Vaishnav, "The Rheology of Large Blood Vessels" In: *Cardiovascular Fluid Dynamics*, Vol. 2, pp. 2-65, 1972.

[6] Fung, Y.C., *Biomechanics. Mechanical Behaviour of Living Tissues*, 2nd Edition, Springer, New York, 1993.

[7] Maurel, W., Y. Wu, N. Magnenat Thalmann and D. Thalmann, *Biomechanical Models for Soft Ttissue Simulation*, Springer, Berlin, 1998.

[8] Mooney, M., "A theory of large elastic deformation", *Journal of Applied Physics,* 11, pp. 582-592, 1940.

[9] Vito, R., "The mechanical properties of soft tissues – Part II: The elastic response of arterial segments", *Journal of Biomechanics*, 13, pp. 947-950, 1980.

[10] Ogden R.W., *Nonlinear Elastic Deformations*, John Wiley & Sons, New York, 1984.

[11] Loree, H.M, R.D. Kamm, R. G. Stringfellow and R.T. Lee, "Effects of fibrous cap thickness on peak circumferential stress in model atherosclerotic vessels", *Circulation Research*, 71, pp. 850-858, 1992.

[12] Rogers, C., D.Y. Tseng, J.C. Squire, and E.R. Edelman, "Balloon-artery interactions during stent placement. A finite element analysis approach to pressure, compliance, and stent design as contributors to vascular injury". *Circulation Research,* 84, pp. 378-383, 1999.

[13] Hayashi, K. and Y. Imai, "Tensile property of atheromatous plaque and an analysis of stress in the artherosclerotic wall", *Journal of Biomechanics,* 30, pp. 573-579, 1997.

[14] Holzapfel, G., M. Stadler and C.A.J. Schulze-Bauer, "A layer specific three dimensional model for the simulation of balloon angioplasty using magnetic resonance imaging and mechanical testing", *Annals of Biomedical Engineering*, 30, pp. 753-767, 2002.

[15] ANSYS 5.5 theory manual, ANSYS Inc. HQ, Canonsburg, PA, USA.

[16] Treloar, L.R.G., "The elasticity of a network of long-chain molecules", *Transactions of the Faraday Society*, 39, pp. 241-246, 1943.

[17] Ogden, R.W., and C.A.J. Schulze-Bauer, "Phenomenological and structural aspects of the mechanical response of arteries", In: *Mechanics in Biology* (Eds. J. Casey, G. Bao), BED-Vol. 46, pp. 125-140, 2000.

[18] Personal communication from Prof. Clive Lee, Professor of Anatomy, Royal College of Surgeons in Ireland, Dublin, Ireland.

[19] "Information Resources on Swine in Biomedical Research",see; http://www.nal.usda.gov/awic/pubs/swine/cardio

[20] Prendergast, P.J., C. Lally, S. Daly, A.J. Reid, T.C. Lee, D. Quinn and F. Dolan. "Analysis of prolapse in cardiovascular stents: a constitutive equation for vascular tissue and finite element modelling", *ASME Journal of Biomechanical Engineering,* 125, pp. 692-699, 2003.

[21] Truesdell, C.A., "The mechanical foundations of elasticity and fluid dynamics", *Journal of Rational Mechanics and Analysis*, 1, pp. 173-182, 1952.

[22] Burton, A.C., "Physical principles of circulatory phenomena: the physical equilibria of the heart and blood vessels" in: *Handbook of physiology*, Section 2, Circulation, 1, pp. 85-106, American Physiological Society, Washington, D.C. 1962.

[23] Weizsacker, H.W., H. Lambert and K. Pascale, "Analysis of the passive mechanical properties of rat carotid arteries". *Journal of Biomechanics*, 16, pp. 703-715, 1983.

[24] van Loon, P., W. Klip and E.L. Bradley, "Length-force and volume-pressure relationship of arteries", *Biorheology*, 14, pp. 181-201, 1977.

[25] Yamada, H., *Strength of Biological Materials,* The Williams and Wilkins Company, Baltimore, 1970.

[26] Carmines, D.V., J.H. McElhaney and R. Stack, "A piece-wise non-linear elastic stress expression of human and pig coronary arteries tested in vitro", *Journal of Biomechanics*, 24, pp. 899-906, 1991.

Appendix B

Preparation Of Antibiotic Solution Protocol

The antibiotic solution should be prepared before the tissue samples are harvested and stored at 4°C. Every effort should be made to ensure that the antibiotic solution is sufficiently chilled before being used to store the samples.

Equipment and ingredients required for the implementation of the protocol

Gloves, eye protection, disposable apron
Plastic Graduated cylinder – 1000 ml with spout
Plastic container- 1000 ml capacity
pH colour coded paper
Spatula or magnetic stirrer

Normal Saline at 0.9 %	– 500 ml
Gentamicin sulphate	– 100 mg
Metronidazole	– 100 mg
Flucloxacillin or cloxacillin	– 100 mg

Procedure

1. 500 ml of 0.9 % saline solution is prepared.

2. 100 mg of Gentamicin, 100 mg of Metronidazole and 100 mg of Flucloxacillin is added to the 500 ml 0.9% saline solution.

3. Antibiotic solution is thoroughly mixed/stirred for 15 minutes.

4. pH of solution is measured using pH paper and noted.

5. Antibiotic solution is poured into plastic container (1000 ml capacity) and sealed.

6. Plastic container is labelled, time, date and content.

7. Container is placed in a laboratory refrigerator and maintained at a constant temperature of 4 °C.

8. Graduated cylinder, spatula and workbench are thoroughly cleaned.

9. Any remaining ingredients are stored away for further use.

The specimens should be stored in the antibiotic solution, in plastic sealed containers and transported to a refrigerator. The specimens should be used in mechanical testing within 3-6 weeks of preservation.

Appendix C

Mesh Convergence for Models of Tissue Prolapse

Four mesh densities were analysed for one of the stent designs (the Velocity Stent). The peak stress was determined in each case. It was found that eight elements through the thickness of the vessel was an adequate mesh density. The maximum prolapse did not alter for any of the mesh densities shown, see Figure A.1 below.

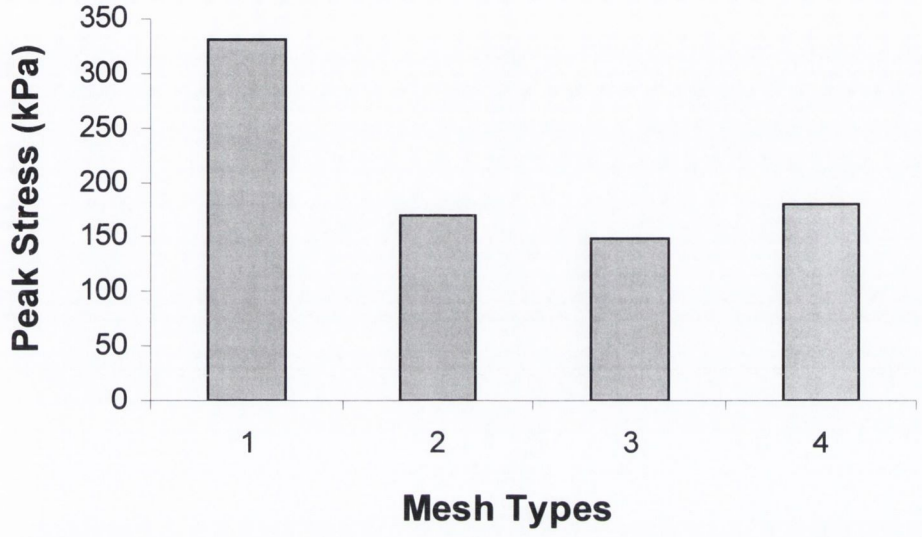

Figure A.1 *Peak stress vs. mesh type.*

Mesh type 1: *4 elements through vessel wall;*

Mesh type 2: *8 elements through vessel wall;*

Mesh type 3: *12 elements through vessel wall;*

Mesh type 4: *12 elements through vessel wall, with double the mesh density shown in Figure 3.9.*

Appendix D

Application Of Symmetry To The Stenting Procedures

The following appendix explores the use of symmetry conditions to simulate a stenting procedure. An artery stented with a NIR stent design is simulated. The NIR stent design has 7 repeating units in the circumference. It was necessary to initially carry out the stenting procedure in a complete vessel so as to ascertain the suitability of using a segment of the vessel and symmetry constraints to adequately model the full stented vessel. The stenting procedure was generated using the method outlined in Section 3.5.3. The complete vessel was simulated along with the complete 7-unit NIR stent, see Figure D.1. The stent scaffolds open the vessel thereby radially displacing the vessel wall. The magnitude if the radial displacement of the vessel wall for the complete stented vessel is shown in Figure D.2(a). The radial displacements in one seventh segment of the complete vessel wall is also shown in Figure D.2(b) and Figure D.2(c). These illustrate the radial displacement of the vessel wall by the stent for each circumferentially repeating segment of the stenting procedure.

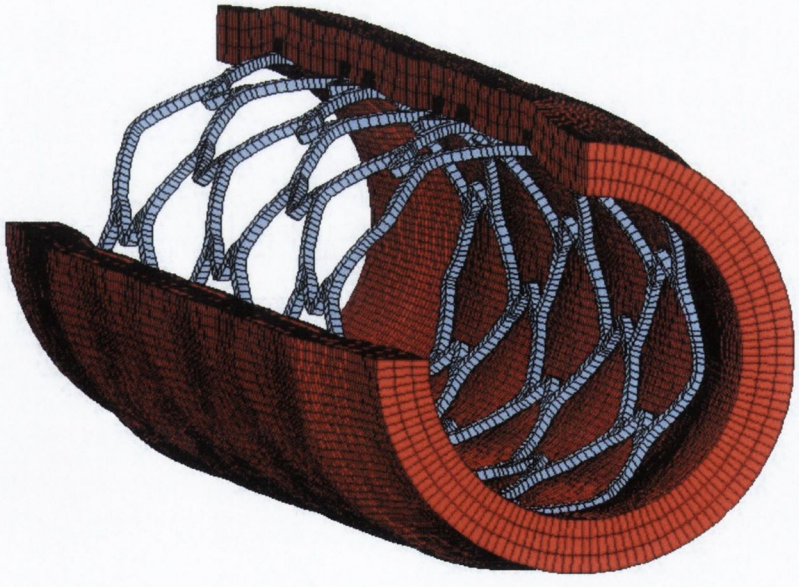

Figure D.1 *Deformed geometry of complete NIR stented vessel.*

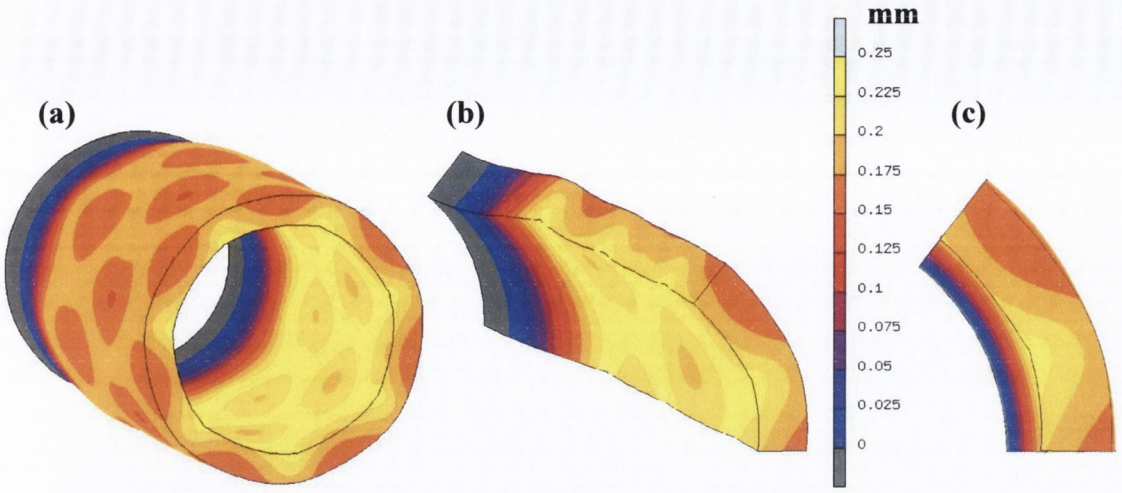

Figure D.2 *Full NIR stented vessel (a) radial displacements in complete vessel, radial displacement in one seventh segment of the complete stented vessel, (b) isometric view and (c) end view.*

The stented vessel was then represented by one seventh segment of the vessel wall and one seventh segment of the stent. Boundary conditions were applied in a similar manner to the complete stent procedure, however planar symmetry constraints were applied to the symmetry planes as shown in Figure D.3(b). The radial displacements that resulted in the segment of the vessel in the simulated stenting procedure are shown in Figure D.3.

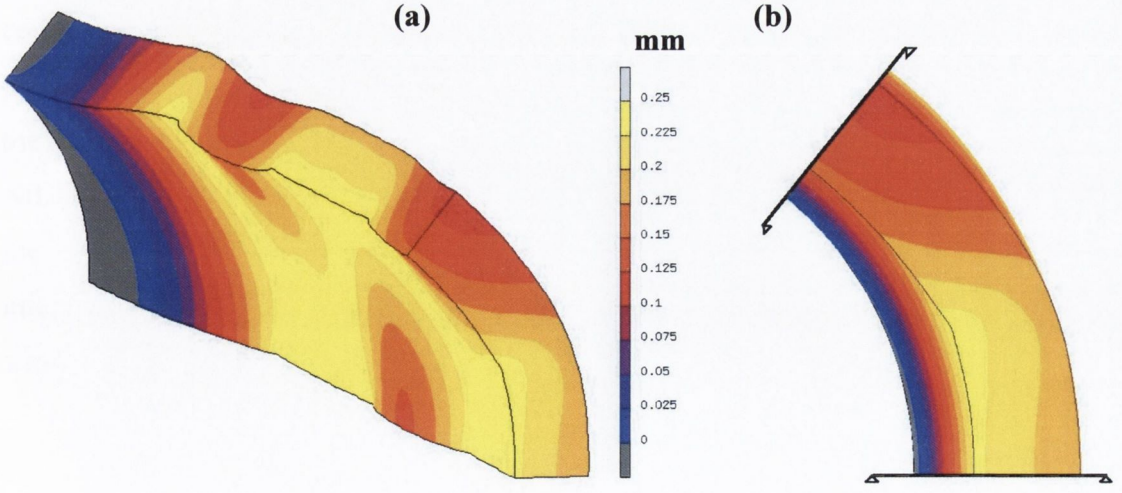

Figure D.3 *Radial displacements in NIR stented one seventh vessel segment using planar symmetry constraints, (a) isometric view and (b) end view.*

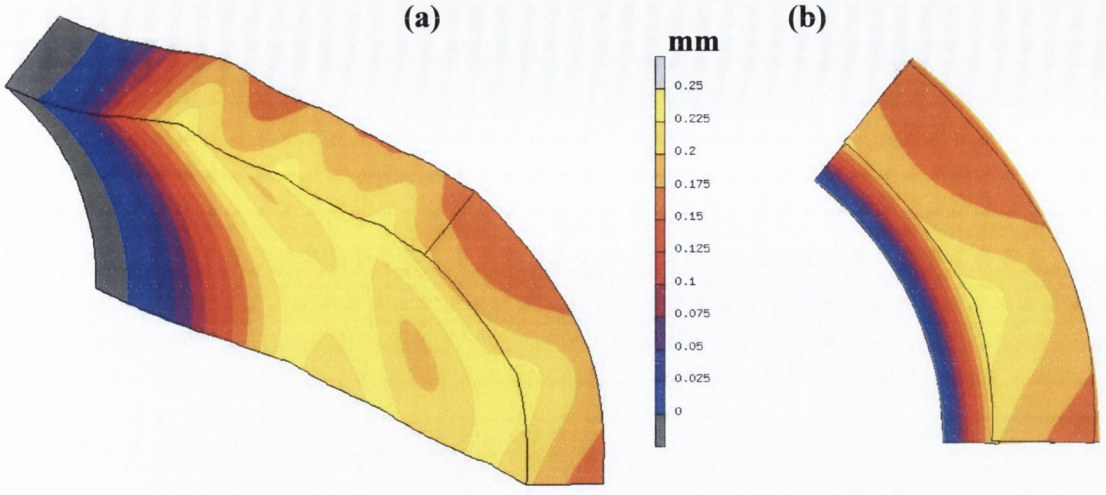

Figure D.4 *Radial displacements in NIR stented vessel; one seventh segment using cyclic symmetry constraints, (a) isometric view and (b) end view.*

The stented vessel was also represented by one seventh segment of the vessel wall and one seventh segment of the stent, however, cyclic symmetry constraints were applied to the symmetry planes. The cyclic symmetry capability is available in Marc/Mentat and has the ability to tie/couple two symmetry faces of a segment of a cylindrical model. The radial displacements that resulted in the vessel segment of the stenting procedure using cyclic symmetry constraints are shown in Figure D.4.

It is clear. by comparing of the radial displacements for the two symmetry models to that of the complete model, that only by applying cyclic symmetry constraints can the complete model be represented accurately. The failure of the planar symmetry constraints to model the stenting procedure is the assumption that the vessel is also symmetric in the axial direction and therefore no out of plane motion will occur, however this is clearly not the case for the complex designs of the S7 and the NIR stents. Clearly planar constraints are inadequate at representing the complex interaction between the stent and the artery and the stenting procedure can only be simplified to a segment of the stent and vessel if cyclic symmetry constraints are used.